



City Research Online

City, University of London Institutional Repository

Citation: Coward, D. P. (2001). Cracking of Laminated Glass Initiated by Low Velocity Impacts. (Unpublished Doctoral thesis, City, University of London)

This is the accepted version of the paper.

This version of the publication may differ from the final published version.

Permanent repository link: <https://openaccess.city.ac.uk/id/eprint/30818/>

Link to published version:

Copyright: City Research Online aims to make research outputs of City, University of London available to a wider audience. Copyright and Moral Rights remain with the author(s) and/or copyright holders. URLs from City Research Online may be freely distributed and linked to.

Reuse: Copies of full items can be used for personal research or study, educational, or not-for-profit purposes without prior permission or charge. Provided that the authors, title and full bibliographic details are credited, a hyperlink and/or URL is given for the original metadata page and the content is not changed in any way.

**Cracking Of Laminated Glass Initiated By Low
Velocity Impacts**

by

David Paul Coward

Thesis presented for the degree of Doctor of Philosophy

The City University
School of Engineering
October 2001

Contents

	Page
1 Introduction	
1.1 Historical Perspective	1.3
1.2 Glass and Glazing	1.4
1.3 The Role Of Glazing In The Post Office	1.6
1.4 The Aim Of The Current Work	1.8
2 Literature Review	
2.1 The nature of Silica Glass	2.2
2.2 Polyvinyl butyral (PVB)	2.7
2.2.1 The Dynamic Mechanical Properties of PVB	2.8
2.3 Impact	2.11
2.4 Contact	2.21
2.5 Crack Initiation and Failure Prediction.	2.26
2.6 Weibull Analysis	2.27
Figures	
3 Theoretical Considerations	
3.1 Beams in Bending	3.2
3.1.1 Monolithic Beams	3.2
3.1.2 Superimposed Beams	3.5
3.1.3 Sandwich Beams	3.5
3.2 Plate Analysis	3.8
3.2.1 Quasi-static Loading of plates	3.8
3.3 Stress waves	3.13
3.3.1 Reflection of Elastic Waves at a Boundary.	3.16
3.3.2 Oblique Impinging of Stress Waves.	3.18
3.3.3 Stress Wave Propagation in a Solid-Solid Impact	3.19
3.3.4 Release Wave	3.24
3.3.5 Additional Stress Waves	3.30
3.4 Contact Mechanics	3.32
3.5 Fracture Mechanics	3.34

3.6	Strain Rate	3.38
	Figures	
4	Experimental Equipment and Methodology	
4.1	Industry Standard Impact Tests	4.2
4.2	Test Rig Design and Construction	4.5
4.3	Experimental Procedure	4.7
4.4	Controllable variables	4.9
	4.4.1 Nominal Velocity of the ram	4.9
	4.4.2 Pre-set deflection	4.9
	4.4.3 Contact area	4.9
4.5	Non-controllable variables	4.10
	4.5.1 Flow through valve	4.10
	4.5.2 Actual Velocity Of Ram	4.10
	4.5.3 The Material Characteristics	4.10
4.6	Instrumentation	4.11
	4.6.1 Force Transducer	4.11
	4.6.2 Linear Variable Differential Transformer	4.11
	4.6.3 Laser Velocity Transducer	4.12
	4.6.4 Strain Gauges	4.12
4.7	Effectiveness of the Test Rig Design	4.13
	Figures	
5	Results	
	5.1.The relationship between the deflection at failure and the velocity at failure.	5.2
	5.2. The relationship between the deflection at failure and the velocity at failure divided by the deflection at failure (v/d).	5.6
	5.3 The relationship between the deflection at failure and the total number of impacts.	5.7
	5.4 The relationship between the velocity at failure and the velocity at failure divided by the deflection at failure (v/d).	5.8
	5.5 The relationship between the velocity at failure and the total number of impacts.	5.8

5.6 The relationship between the velocity at failure divided by the deflection at failure (v/d) and the total number of impacts.	5.9
5.7 The Influence of Relative Humidity.	5.9
5.8 The Influence of Temperature	5.11
5.9 The comparison between the measured stress and the calculated stress.	5.12

Figures, at the rear of the thesis

6 Discussion of results

6.1 General Discussion	6.2
6.1.1 Impact of different materials	6.4
6.2 The influence of the PVB interlayer.	6.5
6.3 Full Data Set	6.7
6.3.1 The Deflection At Failure Versus The Velocity At Failure	6.7
6.3.2 The Deflection At Failure, And The Velocity At Failure Divided By The Deflection At Failure (V/D).	6.9
6.3.3 The Relationship Between The Deflection At Failure And The Total Number Of Impacts To Failure For Each Sample.	6.9
6.3.4 The Relationship Between The Velocity At Failure And The Velocity At Failure Divided By The Deflection At Failure.	6.10
6.3.5 The Relationship Between The Velocity At Failure And The Total Number Of Impacts To Failure.	6.11
6.3.6 The Relationship Between The Velocity At Failure Divided By The Deflection At Failure And The Total Number Of Impacts.	6.12
6.3.7. The Influence Of Relative Humidity.	6.13
6.3.8. The Influence Of Temperature.	6.14
6.4 Reduced Data Set	6.15
6.5 Weibull Analysis.	6.21
6.6 Stress intensity factor	6.24

6.7	Strain rate dependency	6.26
6.8	The Influence of the stress history	6.28
7	Conclusions and Recommendations for future work	
7.1	Test Rig And Testing Process.	7.2
7.2	Weibull Analysis	7.2
7.3	Stress Intensity Factor	7.3
7.4	Strain Rate Dependency	7.4
7.5	The Influence Of Relative Humidity	7.4
7.6	The Influence Of Temperature	7.4
7.7	The influence of lamination and PVB	7.5
7.8	The Nature Of The Stress Combination Factor f	7.5
7.9	Future Work	7.6

Acknowledgements

The work presented here was started under the supervision of Dr. H.R. Harrison, so I would like to express my thanks to him for his support and direction. For the majority of the project, the work was supervised by Dr. P.A. Lush, and I am extremely grateful to him for his valuable help, guidance, and time.

I'd like to thank my wife and family for their support and encouragement throughout the period of my study.

I should like to thank my colleagues at the Post Office's Technology Centre in Swindon for their support, especially to Simon King for his help with the experimentation and to Paul Senior for his help with the construction of the test rig.

I should also like to thank the Post Office for the financial support for this project.

I grant powers of discretion to the University Librarian to allow this thesis to be copied in whole or in part without further reference to me. This permission covers only single copies made for study purposes, subject to normal conditions of acknowledgement.

Abstract

The work presented in this thesis is concerned with the determination of the relationship between low velocity impacts and the failure by cracking of 420mm square, 6.4 mm thick, three ply, laminated glass. An hydraulic test rig has been constructed which allows tests involving impacts with pre-determined velocities, up to 7 m/s, and deflections, up to 4.6mm, to be conducted upon the glass samples.

Weibull's approach to describing the failure of brittle materials has been adopted. A Weibull cumulative distribution, which relates the probability of failure to the applied stress, has been generated from the experimental data, and the Weibull modulus or flaw density parameter has been determined to be 3.5.

The stress intensity factor, K or fracture toughness value, is an indication of the toughness of a material. Glass, as a brittle material would be expected to have a low fracture toughness. Values for K can be determined experimentally, and as a material characteristic should not vary widely, however the value of $0.46 \text{ MPa m}^{1/2}$ for the fracture toughness, obtained dynamically in this work, appears to differ from those figures determined by others, using quasi-static loading, of between 0.7 and $0.8 \text{ MPa m}^{1/2}$. If the value for K determined during quasi-static loading is applicable to this work, then the length of surface cracks in the glass is calculated to be between 55 and $72 \times 10^{-6} \text{ m}$.

The stresses generated during the dynamic loading of glass by an impact can be divided into two distinct elements, the stresses produced by the bending of the glass, and the stresses generated during the impact. However, although the resulting stresses can be described separately, they have a combined effect upon the glass. The stress combination factor f , is used to describe how the bending stresses and the impact stresses combine to occasion a micro-crack (which may be found on all exposed glass surfaces) to propagate and cause a fracture in the glass. The value of f is considered to be between 0.7 and 0.8 .

Notation

a	length of rectangular plate, crack length
A	Amplitude of wave, Area
b	Breadth of beam or plate
c	Thickness of sandwich core, subscript for sandwich core, velocity of propagation of waves, intercept of a straight line
c_0	Velocity of longitudinal waves in a bounded medium
c_1	Velocity of longitudinal waves in an unbounded medium
c_2	Velocity of transverse waves in an unbounded medium
c_L	Velocity of one dimensional longitudinal wave
c_p	Phase velocity
d	Depth of beam or plate, distance between the centre lines of the upper and lower faces of a sandwich
D	Flexural rigidity
E	Young's Modulus
f	Subscript for sandwich face, shape factor, stress combination factor
g	Shape factor
h	Thickness of sandwich, shape factor
I_x, I_y	Moments of inertia with respect to x and y axes
I	Subscript for incident
K	Stress intensity factor
l	Length of bar
L	Length of plate
m	Slope of a straight line, Weibull modulus

M	Bending moment
n	Rate effect fitting parameter
N	Number of cycles to failure
p	Subscript for projectile, pressure
P	Load, Probability of failure
q	Uniformly distributed load
r	radius of concentrated load, radius of contact circle, correlation coefficient
R	Radius of bending of a beam, acoustic impedance, subscript for reflected
s_f	Failure stress
S	Failure stress
t_f	Time to failure
t	Thickness of a plate, subscript for target
T	Subscript for transmitted
u	Particle velocity
v	Velocity
V	Volume of stressed material
w	Deflection
W	Load
y	The distance from the neutral axis to the outer fibres of a beam
x,y,z	Rectangular coordinates
α	numerical factor for deflection of a plate, angle of incidence for a wave
β	numerical factor for stress of a plate, angle of reflection of a wave

Δ	Deflection, dilatation
ϵ	Strain
∇^2	Laplacian operator
λ	Lamé's constant, wavelength
μ	Lamé's constant
$\sigma_x, \sigma_y, \sigma_z$	Normal Components of Stress parallel to x, y and z axes
σ	Stress
σ'	Stress at which there is a zero probability of failure
σ''	Weibull normalising factor
ν	Poisson's ratio
ξ	Co-ordinate of concentrated load on a plate
η	Co-ordinate of concentrated load on a plate
ρ	Density
γ	Surface energy

Chapter 1

1 Introduction

- 1.1 Historical Perspective**
- 1.2 Glass and Glazing**
- 1.3 The Role Of Glazing In The Post Office**
- 1.4 The Aim Of The Current Work**

1 Introduction

During low velocity impacts on glass plates, stresses are generated which will cause the plates to fracture, once a critical load is reached. The bending of beams and flat plates has been investigated in some depth over a number of years, as described by Love (1927). Timoshenko et al (1951,1959) described later developments in the theory of elasticity, the analyses of beams and plates, and their application to the solution of engineering problems. Love (1927) also described the early investigations into the propagation of waves in elastic solids, and in his book Kolsky (1963) reflected upon developments in understanding wave propagation, because of improved experimental techniques, and the importance of understanding the properties of solids at high rates of loading.

Many workers have explored the bending of plates, and stress waves in elastic solids, but few have investigated the transitional region where the quasi-static loading of glass plates merges with impact or dynamic loading. It was considered that this transitional region was worthy of further investigation. When a glass plate deflects due to a quasi-static load, bending stresses are generated which can be determined. Following an impact, stresses propagate through a material, and these stresses can also be determined. Although the two stresses can be described and calculated separately, it is considered likely that it is the combination of the stresses that determines the failure.

1.1 Historical Perspective

Addis (1999) states that the first window glass to be used in Rome was in c.100 AD manufactured by the Romans using captured Egyptian technology, and that the first laminated glass was developed by the French chemist Benedictus for use in car windscreens. Addis states that Benedictus used a sandwich of two sheets of glass and an inter-layer of Celluloid. Addis further indicated that toughened glass was developed by Saint Gobin in 1930, also for use in car windscreens, and that PVB was developed in 1940 as an improved laminating interlayer.

In the late 19th century Hertz (1882) investigated the contact between glass lenses and observed the cone cracks that now bear his name. The Hertzian fracture, or Hertzian cone crack, begins as a ring, at, or just outside, the circumference of elastic contact. Once a critical load has been reached, the crack propagates into the material, and in sufficiently thick glass, continues by flaring outward into a truncated cone. Auerbach (1891) extended this early work into mechanics of cone crack initiation, and developed what is now known as Auerbach's law, which describes the empirically observed linear relationship between the critical load and the impacting sphere size. Griffith (1921) produced a seminal paper which demonstrated that in most brittle materials, fracture begins at pre-existing flaws, with the further consideration that a larger stressed area has a greater chance of including a particularly weak flaw.

In the early part of the twentieth century Weibull (1939) published his thoughts on strength of materials, and developed a probabilistic approach to the failure of materials, which has been subsequently used for brittle materials.

When consideration is given to impacts, the nature and propagation of elastic waves generated as a result of the impact is important. The propagation of elastic waves is comprehensively described by Kolsky (1963), building on the work on acoustics developed by Rayleigh (1887).

1.2 Glass and Glazing

Silica glass has been used as a building material for many years. It is demonstrably hard wearing, has good transparency and is cheap. However, it has relatively low resistance to impact, because of its brittle nature.

Glass is used in three basic forms for most applications, annealed, toughened, and laminated. The main constituent of practically all commercial glass is sand, however very high temperatures ($\sim 1700^{\circ}\text{C}$) are needed to fuse sand to produce glass, so other chemicals are added to reduce the fusion temperature. Traditionally, soda ash (Na_2CO_3) was used to reduce the fusion temperature to about 800°C , but this resulted in a glass that was water soluble, so other chemicals such as calcium oxide (CaO) were added to provide stability.

In the U.K. and in the west of Europe annealed glass is manufactured using the float glass process developed by Pilkington Brothers Ltd., introduced in 1959. Float glass is produced by heating the glass in a furnace until it is molten ($\sim 1000^{\circ}\text{C}$) and then pouring the molten glass onto a large bed of molten tin. The glass floats on the tin, spreading out until it reaches the edges, forming flat parallel surfaces. The thickness of the glass is controlled by the speed at which the solidifying glass “ribbon” is drawn off the tin bath. The hot glass then passes into an annealing area where it cools down in precisely controlled conditions. Float glass is the basic product of the glass manufacturing industry and is used as the basis for the other two forms, toughened and laminated glass.

Toughened or tempered glass is produced by heating a panel of float glass until it reaches approximately 600°C , and then rapidly cooling it with blasts of cool air. The rapid cooling of the outer surfaces causes compressive forces to be induced at the surface which are balanced by tensile forces in the centre. Glass normally fails in tension, and fractures usually start at the surface, so the surface compressive forces prevent the surface cracks propagating, and increase the strength of the glass approximately fourfold. When toughened glass breaks, the release of the forces tends to cause the glass to fracture into small, relatively innocuous, pieces, hence its use as

safety glazing. Toughened glass also tends to have an improved thermal stability. An alternative toughening method, known as chemically toughening, is to immerse the glass in a potassium nitrate bath which causes ion exchange to occur. The sodium ions are exchanged for potassium ions, whose larger size causes the surface to be in compression.

Laminated glass is produced by bonding two pieces of glass together with an interlayer. There are two alternative methods for producing laminated glass, Polyvinyl Butyral (PVB) laminating, and resin laminating. In PVB laminating two or more sheets of glass are assembled together with thin sheets of extruded PVB. (PVB is normally supplied in rolls with a sheet thickness of 0.38mm, but if a thicker interlayer is required then multiple thicknesses of PVB are used.) The resulting sandwich is then passed through a pre-heating oven which raises the temperature of the sandwich to 70°C. The heated sandwich is passed through a set of rollers which squeeze the materials together, excluding air bubbles and providing an initial light adhesion. The laminate is then placed into an autoclave and is heated up to a temperature of 140°C and a pressure of 8 bar. Once removed from the autoclave, and having cooled down, the laminate is permanently bonded together and is transparent.

Resin laminating uses a measured amount of liquid polymer resin which is poured into the space between two pieces of glass, held apart at an appropriate distance. Once the resin has been poured, the glass laminae are pressed together until all air bubbles have been displaced, and then clamped until the resin has cured. Resin laminating results in a product that does not have the bonding performance of PVB laminated glass, but one that can be used for difficult shapes, or for patterned and textured glass.

1.3 The Role Of Glazing In The Post Office

The Post Office is one of the largest cash carriers in the United Kingdom, and additionally, has large sums of money held in vaults and behind the counters at Post Offices. The criminal fraternity have sought to exploit this fact, so the Post Office continues to suffer attacks from robbers, armed or otherwise, and burglars. Both types of attack are on the increase, both within and outside the Post Office.

The Post Office needs to have a good communications interface with its customers, the general public, thus transparent materials have an important role to play. Additionally, in security vehicles, normal windscreen glass will not provide the level of protection required, so glazing with an improved attack performance is an important requirement.

Security glazing is used in a variety of applications, anti-vandal, anti-bandit, and ballistic resistant. Vandal resistant glazing is often required to resist a low level of attack, such as a brick or bottle thrown at a window at relatively low velocity. For this application a simple 3 ply laminate is used consisting of 2 laminae of 3mm glass, with an interlayer of 0.38mm PVB.

The anti-bandit glazing systems would be expected to resist a more concerted and prolonged attack; pre-meditated and often using hand tools of one form or another, and with an impact velocity of between four and ten metres per second. Anti-bandit glass would normally be thicker than vandal resistant glazing, often an 11.5 mm 3 ply laminate would be used, consisting of two sheets of 5mm glass and an interlayer of 1.5mm thick PVB. A better performance can be achieved if more glass laminae are used, for a laminate with a similar thickness and mass; a 5 ply laminate, 11.3 mm thick, consisting of 3 pieces of glass, 3 mm thick, and two PVB interlayers each 1.15 mm thick is often used. The Post Office developed an anti-bandit 7 ply glass, called "Secutex" which was 14 mm thick. The design of Secutex is unusual because it is not symmetric, and uses chemically toughened glass as the rear layer to provide protection to staff against spall in the first one or two blows during an attack. Secutex

also has a very thick penultimate PVB layer which is difficult to penetrate during a manual attack.

Ballistic resistant glazing is obviously designed to resist a different type of threat and consequently has to deal with a different type of dynamic loading over considerably different time scales. For example, in a typical ballistic attack the glazing is struck by a 10 gram lead slug travelling at speeds in excess of 450 m/s. Ballistic resistance requires a thick glass laminate of between 35mm and 50mm, depending upon the threat, with thick individual glass laminae which dissipate the energy of the bullet. In the construction there may be thicker layers of PVB, and thinner pieces of glass towards the rear of the laminate, which help to reduce the spall effect.

The majority of laminate designs in this important field are based upon empiricism, so the various elements of design are not always rigorously linked with the performance of different glass laminates.

Within the Post Office, a number of projects have been conducted in an attempt to understand the performance of glazing systems and to improve both the ballistic and manual attack performance. A study using high speed video techniques (Sobey 1990) indicated that a falling weight is not sufficiently representative of the loading that occurs during a manual bandit attack. An attacker does not merely take a "free swing"; like a pendulum, during an attack, in the case of a sledgehammer attack, the attacker uses his body to maintain the pressure between the sledgehammer head and the glass laminate. The hydraulic test rig, described in chapter four, was designed to simulate, in part, the action of an assailant when conducting an attack, in that the hydraulic ram maintains the pressure between impactor head and glass sample, in a similar fashion to the way an attacker would maintain pressure on the sledgehammer handle.

1.4 The Aim Of The Current Work

The damage caused to the glass over the whole impact history of a bandit attack, when the glazing suffers repeated blows, is evidently quite complex. To understand how fractures start, and then how the material responds to further blows is obviously important if designs of glazing systems are to be designed to respond effectively to an attack. The initiation of the cracking of glass when subjected to a sledgehammer speed impact, i.e. at low velocity (up to 7 m/s) is considered to be an important step towards building a model of the failure of glass when subjected to the attacks mentioned above.

As part of this project an hydraulic impact test rig, mentioned above, was designed and built to explore the failure of glass at low velocity impacts. The test rig allowed controlled velocity and deflection impacts to be applied to 6mm thick, 420 mm square, glass laminate samples, with velocities up to 7 metres per second, and deflections up to 4.6 mm.

The work reported here is intended to identify the relationship between low velocity impacts and the fracture initiation of simple three ply glass laminate panels. The results of the failures at the various impact velocities and deflections were analysed using the approach that Weibull (1939) developed for brittle materials which produced a cumulative distribution function.

During an impact, stress waves are generated at the point of impact which propagate through the material, are reflected at boundaries, and then decay because of internal friction. The stress waves may cause tensile fields to be created which cause failure of the glass if the fracture stress is exceeded. Deflection of the plate, by an external load, will cause bending stresses to be generated in the plate and may also lead to failure if the conditions for failure are exceeded. Although the two types of stresses are described and calculated separately, it is likely that the combination or superposition of the two stresses will determine the failure of the glass. The superposition of the stresses has been characterised in this work as the “stress combination factor”, f .

Two material characteristics investigated during the project were the stress intensity factor, and the strain rate dependency. The stress intensity factor is a measure of the fracture toughness of a material, whilst the strain rate dependency describes the phenomenon whereby a material fails at different loading levels depending upon the duration of the applied load. Both characteristics can be derived from experimental results, and the figures obtained were compared with those identified previously by others.

Other considerations addressed during this work were the influence of relative humidity and temperature upon the glass failures.

Chapter 2

2 Literature Review

2.1 The nature of Silica Glass

2.2 Polyvinyl butyral (PVB)

2.2.1 The Dynamic Mechanical Properties of PVB

2.3 Impact

2.4 Contact

2.5 Crack Initiation and Failure Prediction.

2.6 Weibull Analysis

2 Literature Review

2.1 The nature of Silica Glass

The term "glass" is normally used to describe the ordinary silicate glasses which are used to produce common household products such as bottles and window glasses. Glass was defined in 1945 by the American Society for Testing and Materials in the following way "Glass is an inorganic product of fusion which has been cooled to a rigid condition without crystallising"; Scholze (1990). This description encapsulates the most significant feature about glass when considering its mechanical properties, which is that it is non-crystalline. There are countless other types of glass, both organic and inorganic, but the present work is concerned with the fusion product of silicon, and to a lesser degree, other substances. Glasses do not normally have a sharp melting or solidification point, and they do not fracture in "preferred" directions in the way that crystalline materials do. A glass can be considered to reflect some of the characteristics of crystalline materials, such as exhibiting elastic behaviour comparable to crystalline materials, but also retain some of the characteristics of the liquid state for example; the ability to flow under a shear stress, but only when the shear stress is very high, such as that generated during a Vickers Hardness test (Paul 1990).

Paul (1990) suggests that glass formation is a kinetic phenomenon, so that a material's ability to form a glass appears to be related to its viscosity at the freezing point, thus a good glass forming material is one where the rate of crystallisation is slow compared to the rate of cooling. At ordinary room temperatures silica glass acts as if it were a mechanically rigid solid, and in the majority of cases can be considered to be a perfectly elastic material, i.e. any deformation, due to an applied load, within the elastic limit, is completely recovered when the load is removed. Scholze (1990) illustrated the difference between crystalline materials and glasses when he discussed the dependence of volume on temperature. Generally, a liquid decreases in volume with decreasing temperature at a constant rate, until crystallisation occurs, during which the volume decreases at a constant temperature. A further reduction in volume as the temperature reduces occurs at a different rate. When a glassy material cools, no

crystallisation occurs at the melting point, instead the volume decrease occurs at the same rate, this portion of the graph is described as the “supercooled” region, figure 1 illustrates this phenomenon. The supercooled liquid is still in thermodynamic equilibrium. The curve shown in figure 1 does not decrease at the same rate indefinitely, at a certain temperature, the transformation temperature, the rate changes so that the curve is parallel to that for the crystal form. The deviation between the glass and the crystal graphs is caused by loss of equilibrium of the glass form. As the supercooled liquid continues to cool, the viscosity increases. The attainment of equilibrium of the liquid at each temperature reduction takes longer at each step, until the viscosity becomes so high that with further cooling it is not possible to reach the equilibrium state. At this point the liquid has become a solid.

Scholze (1990) states that there are several hypotheses about the structure of glass. If a glass can be considered as a liquid with its characteristics "frozen in" then the inherent disordered structure of a liquid should be reflected in the structure of a glass. Zachariasen (1932) established that the energy differences between glass and crystal of the same composition are very small and concluded that in the glass state the same type of bonding structure must occur as in the crystal state; in silicates the bonding structure is the SiO₂ tetrahedron. Zachariasen hypothesised that in the crystal these tetrahedrons are arranged regularly, but in the glass they form a random network. Warren's (1941) work on X-ray diffraction patterns of glasses appeared to confirm this hypothesis. Figure 2, from Scholze (1990), illustrates the difference between an ordered and a random SiO₂ network.

The normal type of glass used for windows, and for laminating into panels is float glass, typical values for the constituents are given in table 1. Various compounds can be added to alter the physical characteristics. Lead oxide and Boron oxide are good examples.

Compound	Percentage
Silicon Oxide	71-73 %
Sodium Oxide	12-14 %
Calcium Oxide	8-10 %
Magnesium Oxide	1-4 %
Aluminium Oxide	0.5-1.5 %

Table 1. Chemical composition of float glass used for windows.

Data supplied by Colvin of Pilkington Glass Ltd. (1993) indicate that the appropriate value for the material characteristics of industry standard annealed float glass are as given in table 2.

Material Characteristic	Value
Young's Modulus, E	$73 \times 10^9 \text{ N/m}^2$
Poisson's ratio ν	0.23
Density ρ	2500 kg/m^3

Table 2. Material characteristics of industry standard annealed float glass.

Glass is normally considered to be strong in compression ($\sim 10 \text{ GN/m}^2$) but weak in tension ($40\text{-}80 \text{ MN/m}^2$), however, precise figures are rarely quoted because of the wide spread of results normally observed in strength tests. The measured tensile strength of glass is often several orders of magnitude lower than the theoretical value, because failure is apparently controlled by the stress concentrations caused by micro-cracks on the surface.

Early and fundamental work on the identification of the causes of the variation in the tensile strength of glass was performed by Griffith (1921) at the Royal Aircraft

Establishment. Griffith's paper highlighted the difference between the theoretical strength and observed experimental results, and has formed a central plank in later work investigating the characteristics of glass. Griffith was able to prepare samples that, when tested, approached the theoretical strength of glass, but he observed that the strength reduced spontaneously until it reached a lower steady value some hours later. Another of Griffith's observations was that his results demonstrated that the observed strength of his glass samples was less than one tenth of that suggested by indirect deduction from physical data, and that the strength was no greater than if the surface of the glass had been covered in cracks several thousand molecules long. Thus Griffith's work indicated that brittle bodies such as glass contain a multitude of flaws which cause cracks to start, and propagate, once the material is subjected to significant tensile loads. Ernsberger (1962) argued that whilst the micro-cracks suggested by Griffith (1921) were important, not all the strength controlling structures within glass were "crack like". Ernsberger identified that inclusions of refractory material and gas bubbles influence the strength of glass when they are present. Ernsberger also made a number of observations on the practical strength of glass:

- (i) The measured strength is lower than the theoretical maximum by two or three orders of magnitude.
- (ii) Fractures originate at the surface.
- (iii) Measured strength increases as the size of the area tested decreases.
- (iv) The scatter of results during experiments is high, with mean deviations of fifteen to twenty percent.
- (v) The strength of glass is strain rate dependent, and increases as the strain rate rises, i.e. a static fatigue effect exists (static fatigue is the delayed failure of a material under a static load).
- (vi) There is a threshold for static fatigue.
- (vii) Static fatigue appears to be linked to moisture; the effect disappears in vacuum, dry gases and at low temperature.
- (viii) The strength increases as the fresh abrasions age.
- (ix) Dynamic fatigue is not observed.
- (x) The strength is at a minimum between one hundred and two hundred degrees Celsius.

Ernsberger (1962) investigated the cause of micro-cracks and concluded that micro-cracks in glass are always traceable to mechanical damage of one form or another. The mechanical damage did not take the form of gross cracks visible to the naked eye, the cracks were more subtle, and the cumulative damage was described by Ernsberger as micro-abrasion.

2.2 Polyvinyl butyral (PVB)

Polyvinyl butyral (PVB) is a polymer manufactured primarily for use in the laminated glass industry, although it does have other miscellaneous applications in textile and metal coatings and in adhesive formulations. It has been used in laminating glass, because of its high adhesion properties, toughness, light stability and clarity. PVB is rarely used in isolation, so the mechanical properties of the bulk material may not be of great interest. Table 3 gives figures for a mid-range PVB resin.

Different grades of PVB are used for different purposes, for example the PVB used in the manufacture of windscreens has a lower peel strength (to provide the required absorption properties), than that used for architectural applications, and both have plasticizing compounds added to modify the characteristics.

Property	Value
Tensile strength, yield	40-47 MPa
Tensile strength, break	32-39 MPa
Elongation, yield	8 %
Elongation, break	110 %
Apparent modulus of elasticity	1.9-2.0 GPa
Flexural strength, yield	72-79 MPa

Table 3 Mechanical properties of Butvar B-76 Polyvinyl butyral resin.

David and Wittberg (1984) have demonstrated that the adhesion of the PVB to glass is so high that during peel tests the adhesion is greater than the cohesive forces keeping the material whole.

PVB is normally regarded as a visco-elastic material which has a low modulus of elasticity, and is capable of sustaining deformations in the order of 400% depending

upon the grade and the manufacturer. Rubber like polymers, such as PVB, are not, generally speaking perfectly elastic, they often exhibit internal damping, and the stiffness is frequency dependent. In most instances the modulus of elasticity is not used to describe the material behaviour because of the tendency of PVB to creep, instead a definition for an alternative modulus is used, normally referred to as the 100% (or possibly 200%) modulus. This figure is the tensile strength of a polymer at a specified elongation. If a normal tensile strength is quoted it is usually in the region of 20-40 MN/m².

2.2.1 The Dynamic Mechanical Properties of PVB

During quasi-static loading the deformation characteristics of a material can be described using the shear modulus G , and the bulk modulus B . The bulk modulus, B is normally used to describe the deformation of a body that does not change shape, and the shear modulus used to describe a shear deformation in which the body does not change volume. Snowdon (1968) states that the mechanical behaviour of a rubber like material, such as PVB, is governed primarily by the bulk modulus when the lateral dimensions of the sample are very large in comparison with the sample thickness. It is likely that a panel of laminated glass conforms to these requirements. In this circumstance, the material changes in both shape and volume, and the modulus M , which describes the ratio of stress to strain in the material in this type of situation approximates to the bulk modulus. The resilience that would normally be expected from rubber like material is not exhibited in this situation, because the bulk modulus, is much greater in value than the shear modulus. If resilience is required then a practical approach would be to use strips of PVB in the sandwich, or perforate the sheet of PVB, to allow the material to expand laterally when subjected to an orthogonal compressive load.

Snowdon (1968) indicated that the modulus, M , determines the characteristics of the propagation of longitudinal elastic waves in the material, provided that the frequency is high enough to ensure that the panel dimensions are large when compared with the wavelength of the elastic wave.

The above discussion concerns the quasi-static case. When a linear visco-elastic material is subjected to a time varying stress or strain, the fundamental volume deformation of the material is no longer governed by a simple relationship defined by the bulk modulus, instead the relationship is far more complex and may be described in the general case by a linear partial differential equation.

Snowdon (1968) demonstrated that it was possible to show that the mechanical characteristics of materials vary with the frequency of the applied load, and that the stress and strain relationships may be represented using complex numbers that have elements which are functions of the frequency. The ratio of the complex stress to complex strain can be represented by a complex elastic modulus which has real and imaginary parts that are functions of frequency. The bulk modulus and the shear modulus can also be described in frequency dependant complex terms.

The imaginary part of the equation is a measure of the mechanical loss associated with shear deformation in the material, and is usually known as the damping factor. The real part of the equation is normally described as the dynamic shear modulus. The dynamic shear modulus has been found experimentally to increase with frequency and decrease with temperature. The relationship between temperature, frequency and the damping factor is not so obvious. Nolle (1950) indicated that at sufficiently high frequencies, or sufficiently low temperatures, the dynamic modulus becomes so high that the characteristic resilience of the rubber like materials is no longer exhibited. The point at which the material changes from its normal state to the new inextensible or glasslike state is known as the rubber-to-glass transition, and at this point the damping factor passes through a maximum value.

PVB is normally considered to be a high damping material. This type of material has a rubber-to-glass transition frequency at room temperature that is of the same order of frequency as those normally of interest in vibration problems. The dynamic modulus of PVB increases rapidly with frequency, however, the damping factor of PVB is large, but varies relatively slowly with increasing frequency at room temperature. For example at a loading frequency of 1000 Hz, the dynamic shear modulus is 9×10^8 Dynes/cm² but at 10 Hz falls to 2×10^8 Dynes/cm².

2.3 Impact

Kolsky (1963) identified that the underlying theory for the propagation of elastic waves in solids was, in the main, developed during the last century by Stokes, Poisson, Rayleigh, Kelvin, and others to deal with two things, (i) the issues surrounding the vibration of bodies, which was an extension to the theory of elasticity, and (ii) to assist in their studies of the transmission of light when treated as vibrations in the "ether".

The response of materials and structures to both impulsive and time varying dynamic loads is complex. A number of analytical approaches have been used for establishing the response of various materials and structures when subjected to a range of loading conditions. However, the analysis becomes even more complex when real problems are considered, with strikers and targets which have finite boundaries that can have a significant effect upon the result of the analysis.

Raman (1920) investigated the problem of the transverse impact of a solid sphere on an elastic plate of finite thickness but infinite breadth and width. Raman developed a relatively simple relationship for the coefficient of restitution which was a function of the material constants of the sphere and plate, the thickness of the plate, the diameter of the sphere and the impact velocity. Raman's experimental work established that for thicker plates the variation in coefficient of restitution was two to three percent lower than indicated by theory, for moderate thickness' of plates, and for very thin plates, theory and experiment agreed very well. However, for intermediate cases, where the thickness of the plate is in the order of half (or less) the diameter of the impacting sphere, the observed values of the coefficient of restitution were somewhat larger than the calculated values.

In the early thirties Preston (1931) presented a paper to the American Ceramic Society in which he attempted to clarify and correct the use of an impact modulus formula, known as the Tuckerman formula. Preston demonstrated that the static "modulus of rupture" could be obtained using a strain energy approach (and experiments using glass laths supported on two knife edges) Preston identified that the modulus of

rupture was the maximum stress produced in the beam, and suggested that, for reason of uniformity, the impact modulus should relate to the maximum stress produced in the beam. However, he concluded that the theoretical basis for the extension of the principles used in the static case to the dynamic case were not valid.

Tillett (1954) investigated the impact of steel spheres on glass and plastic plates to establish the coefficient of restitution for the plate materials. Tillett stated and used the assumption of Hertz (1882); that in the region near the point of contact, the stress and strains may be computed at any instant, as though the contact were static, provided that the distance travelled by the elastic waves during the impact is very large compared with the area of impact.

Tillett (1954) concluded that when the plates are thick relative to the diameter of the ball, (i.e. between one and two orders of magnitude greater) the variation of the coefficient of restitution with the velocity of the impacting sphere was quite small, in the order of one half of a percent. Conversely, when considering plates that are thinner, with a thickness similar to the sphere diameter, the variation was much larger; 12 % variation of the coefficient of restitution with velocity in the case of a 2 mm plate and a 1.25 mm sphere.

When the thickness of the plate was described in terms of the number of times a longitudinal wave could be reflected from rear and front surfaces of the plate during the time that the ball is in contact with it, then the figure for the coefficient of restitution for glass was reduced to approximately half of its infinite thickness value when the thickness of the plate was reduced to a thickness that corresponded to 30 reflections of the longitudinal wave. The thickness of the plate was considered to be effectively infinite when the time of contact was greater than the time required for the elastic waves to return to the point of impact after having been reflected from the rear surface.

Tillett (1954) suggested that the reason the coefficient of restitution was not observed to be unity in a plate considered to be effectively infinite was because of the relaxation

of stress in the material and because a small amount of energy goes into the elastic waves set up in the plate.

Tillet measured the time of contact of the spheres impacting with the plates and concluded that the variation of the time of contact with the velocity of impact in the case of thick plates of glass was in agreement with the prediction of Hertz; the time of contact is inversely proportional to the fifth root of the impacting velocity.

Hunter (1957) discussed the reason for the energy loss mentioned by Tillett (1954), and developed a relationship for the energy absorbed by the transient elastic waves set up during the impact. For thick plates of glass Tillett quoted a figure for the coefficient of restitution of 0.986 at the approach velocity of 90 m/s. The figures Hunter obtained are given in table 4

Approach Velocity m/s	Coefficient of Restitution
1	0.999
9	0.996
30	0.993

Table 4. Variation of coefficient of restitution with approach velocity.

Hunter (1957) considered that the reason that the experimental figures for the coefficient of restitution, for the impacts where glass was the target, were close to the theoretical estimate, compared with other materials, was that there was relatively little viscous damping effects in the glass, unlike materials such as steel.

Glathart and Preston (1968) recognised, and addressed, the two different means by which glass can fail under impact, with particular reference to the failure of bottles and similar glassware. If a glass beam with a thickness that is small compared to a spherical indenter, supported at each end, is loaded quasi-statically by the spherical steel indenter with a large enough force, then the beam will deform under the load and

fail in bending. A crack will develop at the centre on the underside of the beam opposite the point of loading. If the load is maintained the initial crack will propagate through the beam until the structure fails. If the thickness of the beam is increased so that it is large compared to the indenter, and provided that the supports are not too sharp, then when the load is high enough, the initial crack will form as a hyperboloid fracture which emerges in a circle adjacent to the contact region. These fractures are often described as 'percussion cones' or 'Hertzian conoids' and can be considered as failures under localised bearing stresses. The two methods described above for static failure are also applicable for dynamic failure when the glass beam is subjected to impact. Glathart and Preston further describe the dynamic failure; the flexural stresses can be considered to be essentially the same irrespective of the nature of the impact provided that the striking energy of the impactor is equal. The same cannot be said in the case of the bearing stress failures, the likelihood of failure if the impactor is soft and deformable (e.g. a leather bag) is different to the case when the impactor is hard and rigid (e.g. a steel sphere). If the impactor is too soft to initiate a percussion flaw, then an increase in the flexibility of the target does not improve the strength; the stiffer the glass the more able it is to withstand flexural stresses. If the impactor is made from a hard material which is able to cause a percussion failure, then there is a certain optimum target flexibility. The optimum flexibility is one where it is equally likely that a crack will be initiated on the impact surface near to the impactor as a bearing stress crack, or as a crack initiated on the non-impacted surface as a flexural stress crack. The optimum flexibility is significantly affected by the material and the shape of the impactor, even in the case of an impactor made of the same material and with the same shape, for example a sphere, a change in the diameter of the sphere will cause a notable change in the bearing stress with a consequential variation in the likelihood of a crack initiation.

Glathart and Preston (1968) believed that there should be a quantitative method of expressing the difference between an impact of a large soft impactor upon a target and a small hard impactor upon the same target, since in either case the failure is a result of the surface tensile strength of the glass being exceeded locally. They suggested that the theory underlying the explanation of the flexure failure was well established and relatively simple. The theory of bearing stresses was developed by Hertz, and is

relatively complex. Subject to the modification of the analysis to cater for the duration of the stress, and the size of the area affected in the two different cases, the problem of impact could be reduced to the question; which of the two stresses, that due to flexure or that due to bearing, will locally exceed the tensile strength of the glass. To establish the answer to this question Glathart and Preston suggested that it would be necessary to calculate the tension first in the area directly affected and then in areas indirectly affected. The glass will fail at the point and at the time at which the local stress is greater than the failure stress. The calculation for the area directly affected by the bearing stresses can be made using the theory established by Hertz, the calculation for the flexural stress can be made if it is assumed that the deflection shape during impact is similar to the quasi-static case; i.e. a simple bow.

Glathart and Preston (1968) considered the analysis for the stresses in the bending case first. It is assumed that the deformation shape is similar to that of the quasi-static case, so that the bending stresses in all areas of the beam are determined by the value of the maximum deflection and the shape of the deformed beam. The stresses determine the elastic energy contained within the beam, and if the supports and the impacting sphere are considered to be rigid, then when the velocity of the sphere has reached its minimum figure, the impact energy is equivalent to the elastic energy contained within the beam. A low mass sphere dropping from a large distance could have the same elastic energy as a large mass sphere falling from a small distance.

Using an energy approach Glathart and Preston established that the reciprocal of the stress in the lower face is proportional to root of the beam thickness. and that the relationship holds provided that the surface deformation is not excessive compared to the overall deformation, and that the duration of the impact is sufficiently long to allow the beam to bend to the quasi-static shape.

A further conclusion was that for a particular glass the shape of the beam can be altered significantly without affecting the energy needed to fracture it provided that the beam can still be regarded as a beam up until failure.

Glathart and Preston proceeded to discuss the Hertzian bearing stresses; the causation of a percussion cone requires a relatively hard material, this view is supported by the fact that the Young's modulus for the impactor forms part of Hertz's mathematical approach to the problem.

Glathart and Preston (1968) indicate that to develop the critical stress at the perimeter of the contact area in order to initiate the percussion cone, the ratio of the pressure divided by the diameter squared must be constant, consequently the square of that ratio must also be constant. If the physical characteristics of a beam are kept constant, such as the material, the beam dimensions, the support conditions, then to develop the critical stress at the periphery of the contact area the properties of the impacting sphere must be kept constant, so that the height the sphere is dropped, divided by the sphere diameter must be constant. The implications of this ratio is that a large sphere has to be dropped from a greater height to create the same conditions for a percussion failure as a smaller ball dropped from a lower height.

Glathart and Preston discuss two approaches to establish the bearing stresses during impact. The first uses the approach developed by Hertz, the second uses the principle of similitude. The Hertzian approach considers the quasi-static case where a sphere constructed from a hard material, for example steel, comes into contact with a massive piece of glass. When the contact force is sufficiently high, the notional contact point expands to a circle whose diameter is defined by the load and the elastic properties of steel and glass. Using Hertz's theory Timoshenko (1934) established that the pressure, between the two surfaces is a maximum at the centre of the contact area. Glathart and Preston (1968) identified that the pressure reduces to zero in an area adjacent to the perimeter and that the deformation of the glass surface produces a radial tensile stress adjacent to the edge of the contact circle perimeter.

A crack initiated as a result of the radial stress must be nominally tangential to the circle of maximum stress, so that a crack forms at one point on the circle and extends itself around the circle until it joins. The crack extends vertically into the material of the glass for a short distance, and then flares out to form a conoid. The crack may not start on the circle of maximum stress, it may be initiated a short distance outside of

the circle if the surface conditions are more favourable, because the radial stress is maintained at a significant level for short distances outside of the circle.

Glathart and Preston (1968) used Timoshenko's analysis for the determination of the contact circle radius, and found that in practice, the initiating crack does not start when the ratio of the diameter of the impacting sphere to the diameter of the contact area is the same for both impacting spheres. Glathart and Preston identified that when a crack is initiated this ratio, and the ratio of pressure divided by the square of impacting sphere diameter, both increase when the sphere diameter decreases, i.e. the smaller the area tested, the higher the value the breaking stress.

Glathart and Preston examined the case of massive glass under impact by developing their consideration from the case of a "dead load" or static sphere. A semi-infinite specimen would have a flat top surface, and extend to infinity in both the horizontal and vertical planes. A piece of glass could be considered to be semi-infinite if it extends a significant distance in all directions and is suitably supported.

If a sphere rests upon the piece of glass, it exerts a force upon the glass that is equal to the weight of the sphere. The stress is proportional to the force divided by the square of the diameter, so that the larger the sphere, the greater the stress. A depression or "dimple" will be formed by the sphere.

In the special case of the "live load", a sphere is lowered onto the surface of the glass until it makes contact, the sphere is then released. The depth of the dimple will oscillate but the maximum value of the depth will be twice that of the dimple which formed during the static loading. Using the principles of similitude, Glathart and Preston established that if two different spheres are to induce the same stress in the glass then their densities and their diameters must be inversely related, to keep the product of density multiplied by sphere diameter constant.

The more general case is impact loading. From Hertz, an expression can be obtained for the mutual compression of the glass and the sphere, using the undisturbed top surface of the glass as the datum. A relationship can be established which relates the

total energy absorbed to the maximum reaction force and the deflection. The result obtained using the Hertzian approach is different to that identified for flexible impacts.

The last aspect that Glathart and Preston (1968) consider in their paper is the duration of contact on massive and flexible glass samples. They indicate that the duration of the stress is likely to have an influence on whether or not the glass will fracture.

Glathart and Preston argue that it can be shown that the contact time is very insensitive to the height of the drop, the height has to be reduced by three orders of magnitude before the duration of contact doubles. The contact time was discovered to be in the order of 10^{-4} multiplied by the radius, i.e. approximately 10 μs for each millimetre of radius of the impacting sphere. Additionally, it is likely that the contact time is insensitive to the value of Poisson's ratio, and is moderately sensitive to the density of the impactor, and Young's modulus of the impactor and target.

The contact time is sensitive, however, to the radius of the sphere, so if the duration of contact is related to the likelihood of fracture then because the contact time increases with increasing diameter, the glass would be more likely to fail if the spheres were larger. Glathart and Preston discuss the effect of the contact duration on the breaking strength and suggest that the effect is not great unless the duration is increased by one or two orders of magnitude, however it was also suggested that the duration of stress is relatively more important at short durations. Mould (1961) was quoted as commenting that "...at extremely short durations the strength is independent of duration".

Glathart and Preston (1968) indicated that impacts on flexible beams of glass could be considered in a similar fashion to massive beams, but with the added consideration of the deformation of the beam. They indicated that the contact time is not dependent upon the height from which the sphere drops, but it is dependent upon the shape of the beam and the mass of the sphere. The assumption during the analysis that the beam deforms during impact to a bow shape requires that the contact duration is

significantly larger than the time required for an elastic wave to travel from the impact to the beam supports.

Langitan and Lawn (1969) discussed the interpretation of the empirically determined Auerbach's law (i.e.; that the critical load for the production of a Herzian cone fracture is proportional to the radius of the indenting sphere) and its use in determining the validity of brittle fracture criteria, and as a means to measure surface fracture energies. The two alternative approaches to explain Auerbach's law are the flaw statistical view, and the energy balance concept.

Langitan and Lawn (1969) found it difficult to accept that a distribution of flaws would always have the appropriate occurrences to fit with a simple power law and also that a smaller scatter of results would occur with a decreasing radius of indenter sphere, which was not observed during experimentation. They argue that an extension to Roesler's approach viz. that Auerbach's law follows from the Hertz equations, in that the total loss in strain energy following a crack is equal to the total gain in surface energy of the new crack surface, was more acceptable. Langitan and Lawn developed a stepwise application of the Griffith's energy balance criterion to the growth of a cone crack predicting strict adherence to Auerbach's law within limits of indenter size.

Tsai and Kolsky (1967) studied the fractures produced by steel balls after impacting glass blocks at different velocities, ranging from 1.5 m/s to 34 m/s. Tsai and Kolsky investigated four aspects during the study. Firstly, they identified the relationship between the appearance of cracks and the velocity of an impacting sphere. The Hertzian cone fracture grew and penetrated further into the body of the glass plates as the velocity increased, a further increase in the velocity resulted in two or more Herzian cracks forming, and at the highest velocities used during the tests, a powdering of the glass surface was observed underneath the area of impact.

The second element of Tsai and Kolsky's work concerned the coefficient of restitution, they discovered that the formation of small cracks during impact had little effect upon the rebound height, but at higher velocities the damage caused to the glass

dissipated more energy and thus resulted in a lower rebound height. Additionally, the experimental scatter at higher velocities was more marked.

The third part of the work recorded the surface waves produced on the glass blocks by the impact of steel spheres. Strain gauges were used to measure the stress waves. The gauges were placed in three different sets of positions for three different aspects of the experimentation. Fractures were identifiable because they caused large jumps in the output of the strain gauges. When fracture occurred the shape of the strain gauge output pulse was different in different radial directions. When the velocity of impact was increased, the fractures occurred earlier in the impact process, and the amplitude and number of jumps in the strain gauge output increased. For impacts of half inch steel spheres, the strain gauge output pulse shape did not vary to any great extent with the distance travelled, and at radial distances greater than one and a half inches, the pulse amplitude decreased approximately with the square root of the radial distance travelled.

The final part of Tsai and Kolsky's paper described a simplified mathematical approach to the propagation of waves produced by Herzian impacts on an elastic half space which produced a close agreement to the observed operational pulse shapes.

Schonberg, Keer and Woo (1987) investigated low velocity impact of a cylindrical impactor upon beams and plates using a numerical approach. They concluded that impact force, the maximum transverse displacement and the duration of impact were directly proportional to the plate mass, and inversely proportional to the bending stiffness of the area, whilst the contact area was inversely proportional to the transverse stiffness of the plate.

2.4 Contact

In his book, Johnson (1987) states that the first satisfactory theory describing the stresses generated during contact between two elastic solids was developed by Hertz (1882) when he was considering the influence of elastic deformation on the surfaces of the lenses due to the static contact pressure between them.

Raman (1920) mentions that one of the premises that Hertz used during the development of his theory was that during the collision of two elastic solids, the strains developed in the region of the contact area at any instant, are determined by the pressure between the bodies and are very close to those developed under static conditions.

As mentioned above, Tillet measured the time of contact for a variety of materials and conditions and concluded that the time of contact was in agreement with the prediction of Hertz; the time of contact is inversely proportional to the fifth root of the impacting velocity. The measured contact times for a 6.35mm steel sphere impacting on different materials at 9 m/s are given in table 4.

Material	Time of Contact <i>s</i>
Perspex	73×10^{-6}
Glass	32×10^{-6}
Steel	21×10^{-6}

Table 4. Measured contact times for impacting 6.35mm sphere, from Tillet (1954).

Frank and Lawn (1966) discuss the stresses generated in the contact region during the impact of spherical indenters and brittle solids, and the subsequent generation of cracks in the stress field surrounding the contact area. Using the Hertzian approach to loading (Hertz 1882) they produced a diagram of a steel indenter striking a large flat steel specimen that illustrated the greatest tensile stress as a function of position

through the axis of symmetry (see figure 3). In the zone underneath the area of contact, all three principal stresses are compressive. Outside of the immediate contact area the greatest tensile stress is quite low, and rises to a maximum at the circle of contact. Frank and Lawn noted, however, that the chief empirical inconsistency with their analysis was that a crack generally formed outside the circumference of the contact circle, instead of on it.

Tsai and Kolsky (1967) investigated the flaw distribution on glass surfaces subjected to stresses generated by small spherical indenters pressed into the surface. Tsai and Kolsky indicate that during this type of loading a ring crack develops and encircles the contact region. They point out that, according to theory, the tensile stress is at a maximum at the boundary of the contact area, but that the circular ring cracks were found to have radii slightly in excess of the circle of contact. Tsai and Kolsky note that approaching the boundary of the contact area from the centre the radial stress is compressive, whilst approaching the boundary from outside of the contact area the stress is tensile. Theoretically, therefore, the stress changes rapidly near the boundary. The rapidly changing stress gradients are likely to be smoothed out in practice in a way which may be related to the frictional forces between the spherical indenter and the glass plate. Tsai and Kolsky suggest that the smoothing could explain the observation that the circular crack is always found to have a diameter greater than that of the contact boundary circle.

Glathart and Preston (1968) discuss the bearing stresses induced in glass plates by spherical steel impactors, and using relationships established by Hertz (1895) and later by Timoshenko (1934) describe a result similar to Frank and Lawn whereby the pressure of contact produces a tensile stress which has a maximum value at the edge of the contact circumference. Glathart and Preston establish that the maximum value of the tensile stress is related to the force of contact, the geometry of the contact area, and Poisson's ratio for glass.

Tsai (1971) investigated the theoretical dynamic contact stresses generated during an impact between an axi-symmetrical projectile and an elastic half space by solving three dimensional equations of motion. Tsai calculated the contact stresses for various

values of the contact time and the maximum contact radius, and concluded that the Hertz theory is an acceptable approximation for establishing the total force produced by the projectile when impacting upon a half space, but that the Hertz approach for calculating maximum radial surface stress, is limited to moderate impact velocities when the contact time is more than approximately 40 μsec . Tsai concluded that the discrepancy between the established Hertzian analysis and his approach increases with decreasing contact time and increasing contact radius, and is more noticeable at the beginning of the contact time than in the middle.

Johnson, O'Connor and Woodward (1973) indicated that Hertz's theory should be modified to take into account interfacial frictional stresses. Their work indicated that the initiation of cracks outside of the circumference of contact can be explained by the result that the maximum radial tensile stress occurs outside of the contact circle if there is a mismatch in the elastic constants of the impactor and target plate (i.e. the modulus of the impactor is greater than that of the impact plate).

Chaudhri and Walley (1978) considered the damage to glass surfaces caused by the impact of small spheres, and indicated that if the impactor is small, (i.e. the radius of the impactor is small), and the loading sufficiently high, then plastic deformation will occur, thus Hertz's approach will not be appropriate for the analysis. They state that the nature of the surface stresses change during plastic deformation of the substrate; the radial stress eventually becomes compressive, whilst conversely, the circumferential stress becomes tensile. The tensile circumferential stresses cause the radial cracks around plastic deformations.

Chaudhri and Yoffe (1981) investigated the apparent disagreement in published results between the theoretical diameter of the Hertzian contact area, and the diameter of the ring crack noted during experimental studies. Their studies, using small steel and tungsten carbide spheres impacting upon 3mm thick glass discs, fused silica and sapphire, indicated that there was good agreement between the Hertzian theory and the experimental results produced by the steel ball and glass impact combination. The material properties used by Chaudhri and Yoffe (1981) are given in table 5.

Material Properties	Soda-lime Glass	Steel
ν	0.25	0.3
E/Nm^{-2}	69×10^9	205×10^9
$(1 - \nu^2)/E$	13.6×10^{-12}	4.44×10^{-12}

Table 5. Properties of material used for Hertzian analysis of area of contact, Chaudhri and Yoffe (1981).

Hamilton and Rawson (1970) conducted some indentation experiments on float and plate glass that had been etched with hydrofluoric acid, and analysed the results in terms of the theory of flaw statistics generated by Weibull (1939). They concluded that an acceptable degree of similarity was obtained between their experimental results, and the results predicted using simple flaw distribution functions for the five surfaces investigated. They identified that the tin-bath surface of the float glass is significantly weaker than the top surface exposed to air, and the results for the upper surface are very similar to those obtained for 7 minute etching of plate glass, whilst the results for the tin-bath surface are similar to 4 minute etching of the plate glass. The results were represented by two straight lines intersecting at a point, when the logarithm of the median fracture load is plotted against the logarithm of the indenter radius. The range of the indenter size below the point of intersection is usually termed the Auerbach range. Hamilton and Rawson identified that the upper limit of the Auerbach range decreased significantly as the strength of the glass increased, and that the slope of the median fracture load versus indenter radius on a log-log plot was sensitive to variations in the condition of the surface. Thus, the statement that the mean fracture load is linearly proportional to the indenter radius in the Auerbach range is not generally correct. In the final part of their paper Hamilton and Rawson discuss the objections raised to the application of flaw statistics analysis to their type of experimentation by Roesler (1956) and by Frank and Lawn (1967), they concluded that the objections were not justified.

2.5 Crack Initiation and Failure Prediction.

Cottrell (1964) discussed brittle fracture and indicated that brittle solids often fail at approximately $E/1000$ (the ideal strength of $E/10$ only achievable in specially prepared samples such as fibres). Cottrell indicated that brittle solids are weak in normal use because sharp notches, cracks, rapid changes in geometry, etc., will produce localised concentrations of applied stress. Doremus (1994) discussed the nucleation of cracks, and suggested that when a glass sample is loaded, cracks will start at pre-existing flaws, and will then propagate. However, an existing flaw is not always necessary, Doremus stated that indenting a flaw-free surface of fused silica will nucleate a ring crack if the load is high enough. Doremus indicated that median cracks are formed by the need to accommodate strains at the intersection of two flaw lines, whilst lateral and radial cracks start at the boundary between a faulted region and the rest of the glass and nucleate by unloading residual compressive stresses.

Cottrell (1964) indicated that materials are considered to be “stronger” when they have a greater fracture toughness. Fracture toughness is often determined empirically by measuring the breaking strengths of a large number of samples, and fitting the results to an appropriate curve to provide suitable figures for fracture toughness. Lawn (1993) indicated that the presence of cracks does not necessarily cause a failure. Fracture will occur when, in a material subjected to stress, a crack reaches a critical size, or when a material containing cracks of a critical size is subjected to a critical stress. The combination of stress and crack length is often described using the stress intensity factor, and the combination at which the fracture commences is called the critical stress intensity factor. The value at which the stress intensity factor becomes critical is often described as the fracture toughness.

Overend et al (1999) discussed the Beason and Morgan failure prediction model which forms the basis of the US and Canadian codes of practice for glass design. The Beason and Morgan model uses a two parameter Weibull curve with an average maximum stress based upon a sixty second equivalent maximum principal stress. Overend et al extended the failure prediction model to any load, support or plate geometry arrangement.

2.6 Weibull Analysis

Weibull (1939) discussed how in classical theory the ultimate strength of a material is determined by the internal stresses, and that the value of those stresses should be definitively decisive in judging whether the ultimate strength has been reached, and consequently when failure will occur. However, Weibull indicated that many experimental results did not appear to correspond with the classical theory. Weibull claimed that using elementary probability as a starting point it was possible to reconcile the apparent difference between classical theory and measured results.

Weibull (1939) used as an example, a simple tensile test on a rod, where the breaking load was not exactly the same but distributed around the computed mean with some amount of dispersion. Weibull argued that although it was not possible to indicate an absolute value for the breaking load, it was possible to indicate a definite probability of failure occurring at a given stress level. Weibull suggested that if S were the probability then $S = f(\sigma)$ would be a continuously increasing function of the stress, σ . For very low stresses, $S = 0$, and for very high stresses, $S = 1$. Weibull demonstrated that an “s” shaped distribution curve can be generated which illustrates the relationship between the probability of failure and the stress.

Weibull (1939) concluded that the distribution function m could be determined empirically by plotting the relationship between the probability and the stress after suitable manipulation of the equation (taking logarithms, and re-arranging), so that m was the slope of the rearranged linear relationship.

A number of others have used the approach that Weibull (1939) developed, for example, Oh and Finnie (1967) investigated the ring cracking of glass by spherical indenters, whilst as mentioned above, Hamilton and Rawson (1970) used Weibull's approach to analyse the differences between glass samples with different polished and acid etched surfaces; they determined some simple flaw distribution functions for the various specimens, and compared the experimental results with those predicted.

Chapter 3

3 Theoretical Considerations

3.1 Beams in Bending

3.1.1. Monolithic Beams

3.1.2 Superimposed Beams

3.1.3 Sandwich Beams

3.2 Plate Analysis

3.2.1 Quasi-static Loading of plates

3.3 Stress waves

3.3.1 Reflection of Elastic waves at a boundary.

3.3.2 Oblique Impinging of stress waves.

3.3.3 Stress wave propagation in a solid-solid impact

3.3.4 Release Wave

3.3.5 Additional Stress Waves

3.4 Contact mechanics

3.5 Fracture Mechanics

3.6 Strain rate

3 Theoretical Considerations

3.1 Beams in Bending

The glass samples used in the experimentation were square plates, clamped on all four edges. The analysis of plates for point loads is complex, so consideration was given to a simplified approximation using beam theory.

3.1.1. Monolithic Beams

When a simply supported beam is subjected to lateral loads, the response to that loading across a section of the beam can be described using bending moments and shear forces, Case and Chilver (1971). The load on the beam causes distortions to occur; for a load acting downwards on a simply supported beam, the material forming the lower sections of the beam will be stretched so that tensile stresses are induced. Similarly, compressive stress will be induced in the upper sections of the beam. The variation in stresses through the depth of the beam also has the effect of distorting the cross section.

Consider a beam bent in one of its principal planes by two equal and opposite moments (figure 4), according to Timoshenko and Goodier (1951) the stress components given by the elementary theory of bending (provided that the boundary condition requirements are satisfied) are;

$$\sigma_z = \frac{Ex}{R} \quad (1)$$

The bending moment is given by;

$$M = \int \sigma_z x dA = \int \frac{Ex^2}{R} dA = \frac{EI_y}{R} \quad (2)$$

which leads to the more general case;

$$\frac{M}{I} = \frac{\sigma}{y} = \frac{E}{R} \quad (3)$$

where y is the distance from the neutral axis to the outer edge of the beam.

The test samples under consideration were clamped along all edges. If the clamping were considered perfect then the representative beam could be considered as being “built in”. If the samples were resting upon a support frame, then they would be considered to be simply supported. However, it is likely that the real situation is some way between a built in beam and a simply supported beam. Consequently both approaches will be considered.

The samples used for this work were 420mm wide, 420mm long, and 6.4mm thick. Using simple beam theory, approximations can be made as to the expected deformations and stresses in the plate.

From Young (1989), for a built-in beam, for a given load, the maximum deflection,

$$\Delta_m = \frac{WL^3}{192EI} \quad (4)$$

$$\text{thus, } W = \frac{192EI\Delta_m}{L^3} \quad (5)$$

$$\text{for a rectangular beam, } I = \frac{bd^3}{12} \quad (6)$$

which in this case = $9.2 \times 10^{-9} \text{ m}^4$.

For the case of a built-in beam,

$$M_m = \frac{WL}{8} \quad (7)$$

From equation (3),

$$\sigma = \frac{My}{I} = \frac{WLy}{8I} \text{ and substituting using equation (5),} \quad (8)$$

$$\sigma = \frac{24Ey\Delta_m}{L^2} \quad (9)$$

Assuming that the maximum deflection $\Delta_m = 3\text{mm}$, substituting appropriately gives a value of 95.3 MPa for the stress.

Similarly, from Young (1989), for a simply supported beam,

for a given load, W the maximum deflection,

$$\Delta_m = \frac{WL^3}{48EI} \quad (10)$$

$$\text{and } M_m = \frac{WL}{4}, \quad (11)$$

substituting as before gives

$$\sigma = \frac{12Ey\Delta_m}{L^2} \quad (12)$$

with a value of 47.7 MPa for the stress.

Figures 5 and 6 are graphs which illustrate the relationship between deflection and stress for the two cases described above.

3.1.2 Superimposed Beams

Laminated glass is constructed from three layers of material, two layers of glass with an interlayer of PVB. If the interlayer was considered to play no part in resisting applied loads, and allowed the free movement of one glass layer with respect to the other, then the two glass layers could be considered as a superimposed beam, Pye and Leadbetter (1999).

If a superimposed beam were to be loaded laterally, then the laminae would slide over each other once the beam started to distort. The strength of the superimposed beam is the sum of the strength of the two separate lamina.

If the natural tendency of the laminae to slide over each other is wholly resisted, the superimposed beam acts as if it were a monolithic beam.

Case and Chilver (1971) indicate that the maximum bending moment able to be sustained by the superimposed beam with a rigid shear connection is twice that of the beam with no sliding resistance. A laminated glass beam is likely to be closer to the former case than the latter because the PVB has high adhesion with glass, and because the PVB does not appear to allow significant movement of one glass lamina with respect to the other.

3.1.3 Sandwich Beams

The laminated glass beam may further be considered to be a sandwich beam in which case not only does the PVB act as a “glue” between two layers of glass, but it responds to the loading, in which case the flexural rigidity of the beam is the sum of the flexural rigidities of the component parts measured about the centroidal axis of the entire cross-section. Allen (1969) indicated that in the general case the flexural rigidity D of a sandwich beam is given by

$$D = E_f \frac{bt^3}{6} + E_f \frac{btd^2}{2} + E_c \frac{bc^3}{12} \quad (13)$$

where E_f and E_c are the moduli of elasticity for the faces and the core, respectively, and d is the distance between the centre lines of the upper and lower faces, as illustrated in figure 7, so that

$$d = \frac{h+c}{2} \quad (14)$$

Allen's approach to beams has been developed to deal with sandwich beams used, for example in the aerospace industry, where the core is usually thick in comparison to the outer faces.

Allen (1969) indicates that in the right hand side of equation (14), the first term represents the stiffness of the faces bending around their own centroidal axes, the second term represents the stiffness of the faces bending around the centroidal axis of the sandwich, and the third term represents the bending stiffness of the core. If values for laminated glass are used in equation (14) the third term in the equation is significantly less than the first two terms indicating that the core material, in this case PVB, contributes little to the stiffness of the structure.

Provided that the sections remain plane and perpendicular to the longitudinal axis, the strain, at a point a distance z below the centroidal axis, is given by Mz/D . The strain may be multiplied by the relevant modulus of elasticity to give the stress at the distance z , so that

$$\sigma_f = \frac{Mz}{D} E_f \quad \text{where} \left(\frac{c}{2} \leq z \leq \frac{h}{2}; -\frac{h}{2} \leq z \leq -\frac{c}{2} \right) \quad (15)$$

and

$$\sigma_c = \frac{Mz}{D} E_c \quad \text{where} \left(-\frac{c}{2} \leq z \leq \frac{c}{2} \right) \quad (16)$$

The maximum stress in the face and the core can be determined by substituting for z , $\pm h/2$ and $\pm c/2$ respectively, to give,

$$(\sigma_f)_{\max} = \pm \frac{ME_f}{D} \cdot \frac{h}{2} \quad \text{and} \quad (\sigma_c)_{\max} = \pm \frac{ME_c}{D} \cdot \frac{c}{2} \quad (17)$$

The bending moment, M , for sandwich beams with thick faces is not simple. Allen (1969) determined that the maximum stress in a thick faced simply supported sandwich beam with a central point load was given by

$$\sigma_{\max} = \frac{WL}{4} \left\{ \frac{c+2t}{2I} \psi_3 + \frac{t}{2I_f} (1-\psi_3) \right\} \quad (18)$$

where ψ_3 is related to the ratio of the core shear stiffness to the local bending stiffness of the faces. However, as the core becomes stiffer, the sandwich acts more like a single composite beam, and hence ordinary bending theory is applicable.

3.2 Plate Analysis

3.2.1 Quasi-static Loading of plates

Timoshenko and Woinowsky-Krieger (1959) address in some depth the analysis of stresses and deflections of circular and rectangular plates subjected to a variety of loading and support conditions.

Using the approach developed by Navier in 1820, Timoshenko and Woinowsky-Krieger demonstrated that deflection w in a simply supported rectangular plate can be represented using an infinite trigonometrical or Fourier series;

$$w = \sum_{m=1}^{\infty} \sum_{n=1}^{\infty} A_{mn} \sin \frac{m\pi x}{a} \sin \frac{n\pi y}{b} \quad (19)$$

For a given load distribution the coefficients of the series can be obtained.

To approach the problem for a rectangular plate with built in edges, Timoshenko and Woinowsky-Krieger solved the problem for a simply supported plate and then superposed on the deflection of such a plate, the deflection of the plate by moments distributed along the edges. They then adjusted the moments in such a manner so as to satisfy the condition that the deflection is equal to zero at the boundary of the clamped plate.

Megson (1990) uses the above in his discussion of solutions to thin plate problems using the energy method. Using this approach Megson demonstrated that the deflection of a simply supported rectangular plate, of length a and width b which carries a uniformly distributed load q_0 is given by;

$$w = \frac{16q_0 a^4 b^4}{\pi^6 D (a^2 + b^2)^2} \sin \frac{\pi x}{a} \sin \frac{\pi y}{b} \quad (20)$$

where $D = \frac{Et^3}{12(1-\nu^2)}$

and since at the centre of the plate w is a maximum,

$$w_{\max} = \frac{16q_0 a^4 b^4}{\pi^6 D (a^2 + b^2)^2} \quad (21)$$

Megson (1990) extended this approach to show that the energy method can be used to consider the deflected shape of a simply supported rectangular plate, of length a , and width b , carrying a concentrated load at a position (ξ, η) . The term A_{mn} in the Navier equation, (19) can be shown to be;

$$A_{mn} = \frac{4W \sin \frac{m\pi\xi}{a} \sin \frac{n\pi\eta}{b}}{\pi^4 D ab [(m^2/a^2) + (n^2/b^2)]^2} \quad (22)$$

For a square plate with a central concentrated load, $\xi = \frac{a}{2}$, $\eta = \frac{b}{2}$,

and $a = b$, so that,

$$A_{mn} = \frac{4W \sin \frac{m\pi}{2} \sin \frac{n\pi}{2}}{\pi^4 D (m^2 + n^2)/a^2} \quad (23)$$

the deflection at the centre is;

$$w = \sum_{m=1}^{\infty} \sum_{n=1}^{\infty} A_{mn} \sin \frac{m\pi}{2} \sin \frac{n\pi}{2} \quad (24)$$

and considering the leading terms in the series, so that $m = n = 1$,

i.e., neglecting m, n greater than 1, the maximum deflection can be shown to be,

$$w = A_{11} = \frac{Wa^2}{\pi^4} \frac{12(1-\nu^2)}{Et^3} \quad (25)$$

In his discussion on bending of thin plates, Megson (1990) indicates that the direct stresses are given by,

$$\sigma_x = \frac{Ez}{1-\nu^2} \left(\frac{\partial^2 w}{\partial x^2} + \nu \frac{\partial^2 w}{\partial y^2} \right) \quad (26)$$

and

$$\sigma_y = \frac{Ez}{1-\nu^2} \left(\frac{\partial^2 w}{\partial y^2} + \nu \frac{\partial^2 w}{\partial x^2} \right) \quad (27)$$

If the general expression for w is differentiated, this gives,

$$\frac{\partial^2 w}{\partial x^2} = \sum \sum A_{mn} \left(\frac{-m^2 \pi^2}{a^2} \right) \sin \frac{m\pi x}{a} \sin \frac{n\pi y}{b} \quad (28)$$

and

$$\frac{\partial^2 w}{\partial y^2} = \sum \sum A_{mn} \left(\frac{-n^2 \pi^2}{b^2} \right) \sin \frac{m\pi x}{a} \sin \frac{n\pi y}{b} \quad (29)$$

Putting $a = b$, $x = y = a/2$, and $m = n = 1$,

$$\sigma_x \text{ at centre} = \frac{Ez}{1-\nu^2} \left(A_{11} \frac{\pi^2}{a^2} + \nu A_{11} \frac{\pi^2}{a^2} \right) \quad (30)$$

$$\sigma_y \text{ at centre} = \frac{Ez}{1-\nu^2} \left(A_{11} \frac{\pi^2}{a^2} + \nu A_{11} \frac{\pi^2}{a^2} \right) \quad (31)$$

i.e. $\sigma_x = \sigma_y$

Since, in this case, $A_{11} = w$ then

$$\sigma_x = \frac{Ez}{1-\nu^2} \cdot \frac{w\pi^2}{a^2} (1+\nu) = \frac{\pi^2 Ez}{(1-\nu)a^2} w \quad (32)$$

The maximum stress occurs at the outer fibres of the plate where $z = t/2$,

so

$$\sigma_{x \max} = \frac{\pi^2}{2(1-\nu)} \frac{Et}{a^2} w \quad (33)$$

In terms of the load W ,

$$\sigma_{x \max} = \frac{6(1+\nu)W}{\pi^2 t^2} \quad (34)$$

An alternative approach to the bending of rectangular plates, with two sides supported, was developed by Levy (1899). Levy transformed the double series of the Navier solution to a simpler series which has the advantage of being more suitable for numerical computation.

A number of numerical factors for different loading conditions can be obtained using the approaches discussed above. Young (1989) lists formulas for the two conditions of interest.

For a rectangular plate, with all edges built in, and with a load, W , concentrated over a small circle of radius r , the maximum deflection w is given by

$$w = \frac{\alpha Wb^2}{Et^3} \quad (35)$$

Where α is dependent upon the ratio of width and breadth of the rectangle, and for a square is equal to 0.0611.

The stress σ at the centre of the plate is given by;

$$\sigma = \frac{3W}{2\pi t^2} \left[(1 + \nu) \ln \frac{2b}{\pi r} + \beta \right] \quad (36)$$

Where β is dependent upon the ratio of width and breadth of the rectangle, and for a square is equal to -0.238.

Similarly, for a simply supported rectangular plate, with a uniform load over a small concentric circle of radius r the value for α is equal to 0.1267, and the value for β is equal to 0.435.

In comparisons between theoretical calculations and measured stress, the approach suggested by Megson (1990) appeared to give a reasonable fit (figure 8).

3.3 Stress waves

In the introduction to his book, Kolsky (1963) indicated that in rigid dynamics, it is assumed that should a force be applied to any point on a body, then all points of that body act as if the resultant stresses and strains occur instantaneously, thus every point is set in motion at the same time resulting in a linear acceleration of the whole body, together with an angular acceleration about the centre of gravity. The theory of elasticity requires that the body be considered to be in equilibrium under the action of the applied forces, and any elastic deformations are assumed to have reached their static values. Kolsky concluded that the above approaches are acceptable for problems where, the time between the imposition of forces, and the time for equilibrium to have been effectively reached, are short compared with the time during which the observations are made. However, when the reverse is the case and consideration is given to forces which are applied for short lengths of time, or are varying rapidly, then the effects should be considered in terms of the propagation of stress waves.

Section 3.2 concentrated upon the quasi-static effects of bending, which is unlikely to provide the full picture when considering the impact history. When investigating impact, it is necessary to consider the response of the material and the structure to a rapidly varying, or an impulsive load. Zukas (1982) suggests that for low intensity excitations, both the physical nature of the whole structure and the characteristics of the material from which the structure is built play a major role in resisting the externally applied load. Zukas indicated that as the intensity of the loading increases the material characteristics tend to dominate the structural considerations, because the response of the system becomes more and more localised. For loads that do not cause the resultant stresses to exceed the elastic limit, it is appropriate to restrict the analysis to elastic considerations. The present work is concerned with both the elastic case and also situations when the stresses exceed the elastic limit, but it is considered that the elastic case is an appropriate starting point.

Johnson (1972) defines a stress wave or pulse as a transient effect that results from an external load causing different parts of a body not to be in equilibrium, and because of the material characteristics, the disequilibrium takes a finite time to travel to remote

areas of the body, i.e. there is a calculable time delay before the stress is "felt" by the more remote parts.

Zukas (1982) comments that elastic theory indicates that there are two wave types that travel through an extended solid medium, these are longitudinal, (dilatational, irrotational, or primary) and transverse (distortional, shear, equivoluminal, or secondary). In a longitudinal wave the particle motion induced by the disturbance is parallel to the direction of propagation of the wave, (i.e. normal to the wave front) and the strain is pure dilatation, whilst in a transverse wave the particle motion induced by the disturbance is at right angles to the direction of the propagation of the wave (i.e. parallel to the wave front) and the strain is a shearing strain.

Kolsky (1963) demonstrated that the equations of motion of an isotropic elastic solid are;

$$\begin{aligned}\rho \frac{\partial^2 u}{\partial t^2} &= (\lambda + \mu) \frac{\partial \Delta}{\partial x} + \mu \nabla^2 u \\ \rho \frac{\partial^2 v}{\partial t^2} &= (\lambda + \mu) \frac{\partial \Delta}{\partial y} + \mu \nabla^2 v \\ \rho \frac{\partial^2 w}{\partial t^2} &= (\lambda + \mu) \frac{\partial \Delta}{\partial z} + \mu \nabla^2 w\end{aligned}\tag{37}$$

$$\text{where } \nabla^2 = \left(\frac{\partial^2}{\partial x^2} + \frac{\partial^2}{\partial y^2} + \frac{\partial^2}{\partial z^2} \right)$$

and λ and μ are Lamé's constants. This equation (37), may be shown to correspond to the propagation of two types of wave through the unbounded medium. Using the equations of motion, Kolsky showed that the wave equation was;

$$\rho \frac{\partial^2 \Delta}{\partial t^2} = (\lambda + 2\mu) \nabla^2 \Delta\tag{38}$$

The wave equation shows that the dilation Δ , travels through the medium with a velocity c_1 where,

$$c_1^2 = (\lambda + 2\mu) / \rho = \frac{E(1 - \nu)}{\rho(1 + \nu)(1 - 2\nu)} \quad (39)$$

Thus the propagation speed of longitudinal waves depends upon the density, Poisson's ratio, and Young's modulus.

It can be further shown that transverse waves travel with a velocity c_2 , where,

$$c_2^2 = \frac{\mu}{\rho} = \frac{E}{2\rho(1 + \nu)} \quad (40)$$

Kolsky (1963) considered the propagation of stress waves in any bounded isotropic solid and showed that the propagation of longitudinal waves along a bar with a velocity c_0 can be given by;

$$c_0 = \sqrt{\left(\frac{E}{\rho}\right)} \quad (41)$$

Kolsky states that this relationship is approximate, because an assumption is made that plane transverse sections of the bar remain plane whilst the stress waves pass through the section, and that the stress acts uniformly over each section. Provided that the length of an elastic wave is large compared to the lateral dimensions of the bar, this approximation is acceptable.

Kolsky (1963) showed that there is a linear relationship between the stress at any point and the particle velocity, so that;

$$\sigma_{xx} = \left(\frac{E}{c_0} \right) \frac{\partial u}{\partial t} = \rho c_0 \frac{\partial u}{\partial t} \quad (42)$$

The ratio between them corresponds to the characteristic or acoustic impedance, R , where,

$$R = c_0 \rho \quad (43)$$

The two materials of prime interest in this work are glass and steel. Glass has a Young's Modulus of $73 \times 10^9 \text{ N/m}^2$ a Poisson's ratio of 0.23, and a density of 2400 kg/m^3 , whereas steel has a Young's modulus of $200 \times 10^9 \text{ N/m}^2$, a Poisson's ratio of 0.3, with a density of 7850 kg/m^3 .

The longitudinal wave speed for glass and steel can be calculated, and are as follows;

The "bar" longitudinal wave speed, c_o for steel = 5048 m/s

The "bar" longitudinal wave speed, c_o for glass = 5515 m/s

The "bulk" longitudinal wave speed c_l for steel = 5856 m/s

The "bulk" longitudinal wave speed c_l for glass = 5938 m/s

3.3.1 Reflection of Elastic waves at a boundary.

All media propagate stress waves, and when a stress wave impinges upon the interface between two different media, part of the wave is reflected, and part is transmitted (Kolsky (1963)). If the second medium is the special case of a vacuum (which obviously cannot transmit an elastic wave), then the stress wave is completely reflected within the body. For most engineering applications air is considered to be analogous to a vacuum as far as the transmission of stress waves is concerned.

Achenbach (1975) showed that if an incident stress wave can be denoted by

$$\sigma_I = f\left(t - \frac{x}{c_L}\right) \quad (44)$$

where f is a shape factor, and t time, then the reflected and transmitted waves may be represented by;

$$(\tau_x)_r = g\left(t - \frac{a}{c_L} + \frac{x-a}{c_L}\right) \quad (45)$$

and

$$(\tau_x)_t = h\left(t - \frac{a}{c_L} - \frac{x-a}{c'_L}\right) \quad \text{respectively,} \quad (46)$$

where g and h are shape factors.

Using the relationship that relates the stress to the particle velocity,

$$\sigma = -\rho c_L u$$

Achenbach (1975) goes on to show that the reflection coefficient C_R , and the transmission coefficient C_T , are given by;

$$C_R = \frac{\rho'c'_L/\rho c_L - 1}{\rho'c'_L/\rho c_L + 1} \quad (47)$$

and

$$C_T = \frac{2\rho'c'_L/c_L}{\rho'c'_L/\rho c_L + 1} \quad (48)$$

The above equations indicate that the character of the reflection and transmission waves are determined by the ratio of the mechanical impedences (i.e. $\rho'c'_L/\rho c_L$). If

$\rho'c'_i/\rho c_i = 0$, as for a free surface, then the reflection coefficient = -1 and the transmission coefficient = 0, as discussed above. The negative sign of the reflection coefficient shows that the sign of the stress pulse changes upon reflection, so that a tensile wave is reflected as a compression wave, and vice versa. It can be seen that since $\rho'c'_i/\rho c_i$ approaches 0 for air, then air can be considered to approximate to a vacuum in this instance.

If $\rho'c'_i/\rho c_i = 1$, i.e. the mechanical impedances of the two media are identical, then the stress wave is completely transmitted. The transmitted wave is invariably the same sign as the incident wave.

Zukas (1982) demonstrated that at a free surface, the result of the reflection of a stress wave is that the net stress becomes zero, whilst the net displacement and particle velocities have values which are doubled. Similarly, the reflection of a stress wave at a fixed boundary results in a doubling of the total stress, with a particle speed of zero, assuming in both cases that no transmission of the stress wave takes place.

3.3.2 Oblique Impinging of stress waves.

The section above concentrated upon stress waves that were normal to a boundary, should either a longitudinal wave or a transverse wave impinge upon a boundary at an angle, then waves of both types would be reflected.

Kolsky (1963) has shown that when a longitudinal wave impinges on a free surface a longitudinal wave is reflected at the same angle as the angle of incidence, and a transverse wave is reflected at an angle, β , similar to that for the refraction of light. The refractive index is given by the ratio between the velocities of the longitudinal and transverse waves, i.e.

$$\beta = \sqrt{(2 + \lambda/\mu)} \quad (49)$$

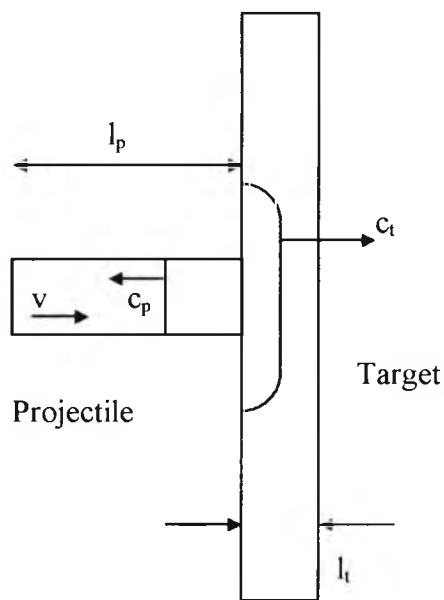
Similarly when a transverse wave impinges upon a free surface, a transverse wave is reflected at the angle of incidence and a longitudinal wave is reflected at an angle β' , where

$$\frac{\sin \alpha'}{\sin \beta'} = \frac{c_1}{c_2} \quad (50)$$

and α' is the angle of incidence.

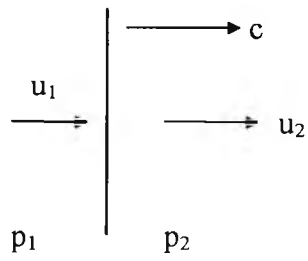
3.3.3 Stress wave propagation in a solid-solid impact

In the case of the impact shown in the following diagram,

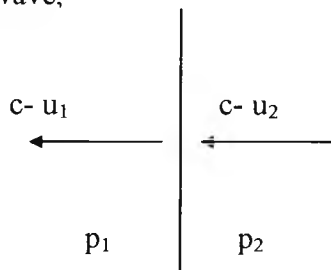


a steel projectile of length l_p impacts upon a glass target of thickness l_t , at a velocity, v of up to 7 metres per second. The above illustration represents the simplified one dimensional approach which is discussed further in section 3.3.4.

Lush (1999) discussed the relationship between pressure and particle velocity for a wave. For a right going wave,



Relative to the wave,

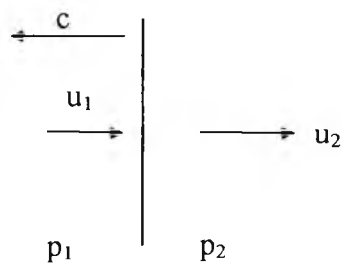


Using the principle of conservation of momentum,

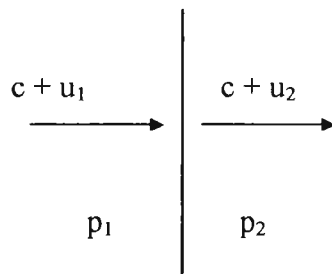
$$p_2 - p_1 = \rho(c - u_2)(c - u_1 - c + u_2) \quad (51)$$

$$\text{i.e. } p_2 - p_1 = \rho c(u_2 - u_1) \quad \text{for } c \gg u_2 \quad (52)$$

Consider a left going wave



Relative to the wave,



Applying the momentum principle,

$$p_1 - p_2 = \rho(c + u_2)(c + u_1 - c - u_2) \quad (53)$$

$$\text{i.e. } p_2 - p_1 = -\rho c(u_2 - u_1) \quad \text{for } c \gg u_1 \quad (54)$$

Thus, $\Delta p = \pm \rho c \Delta u$ which is positive for a right going wave, and negative for a left going wave.

Solid-solid impacts have been described using Lagrangian diagrams, or x-t plots, (Johnson (1972), where x is the spatial co-ordinate and t is time. Figure 9 is a Lagrangian diagram for an impact of steel on glass in the case where the length of the impactor is far greater than the thickness of the target. Considering the same example, figure 10 is another Lagrangian diagram which illustrates the early part of the impact history in more detail, and illustrates the stresses and particle velocities. Given that the acoustic impedance of the projectile R_p is equal to $\rho_p c_p$ and the acoustic impedance of the target, R_t is equal to $\rho_t c_t$, Lush (1999) showed that solving for pressure and velocity from the impact gives

$$-p_1 = -R_p(v - u_1) \quad (55)$$

$$\text{and } p_1 = R_t u_1 \quad (56)$$

$$\text{hence } p_1 \left(\frac{1}{R_p} + \frac{1}{R_t} \right) = v \quad (57)$$

$$\text{or } p_1 = \frac{R_p R_t v}{R_p + R_t} \quad \text{and} \quad u_1 = \frac{R_p v}{R_p + R_t} \quad (58)$$

Using appropriate values for the steel impactor and the glass target, with an impact velocity of 7 m/s, a figure of 73.3 MPa for p_1 is obtained.

For the incident wave,

$$p_1 = -R_t(u_1 - u_2) \quad (59)$$

for the transmitted wave,

$$p_1 - p_3 = -R_p(u_1 - u_3) \quad (60)$$

and for the reflected wave,

$$p_3 = R_t(u_3 - u_2) \quad (61)$$

Eliminating u_3 from the 3 equations above, gives

$$-\frac{p_1}{R_p} + p_3 \left(\frac{1}{R_p} + \frac{1}{R_t} \right) = u_1 - u_2 \quad (62)$$

$$\text{i.e.} \quad = -\frac{p_1}{R_t} \quad (63)$$

$$\text{so } p_3 \left(\frac{1}{R_p} + \frac{1}{R_t} \right) = p_1 \left(\frac{1}{R_p} - \frac{1}{R_t} \right) \quad (64)$$

$$\text{therefore, } \frac{p_3}{p_1} = \frac{R_t - R_p}{R_t + R_p} \quad (65)$$

If the acoustic impedance of the projectile is greater than that of the target, then p_3 would be negative, the interface between the projectile and target would be in tension and they would separate.

If p_3 is equated to zero, so that $u_2 = u_3$ and solving for u_3 in the target medium gives

$$p_1 = -R_t(u_1 - u_3) \quad (66)$$

and similarly, solving for u_3 in the projectile medium gives

$$p_1 = -R_p(u_1 - u_3) \quad (67)$$

Hence, for the target medium,

$$u_3 = \frac{p_1}{R_t} + u_1 = \frac{2p_1}{R_t} \quad (68)$$

$$= \frac{2R_p v}{R_t + R_p} \quad (69)$$

For the projectile medium,

$$u_3 = \frac{p_1}{R_p} + u_1 = \frac{p_1}{R_p} + \frac{p_1}{R_t} \quad (70)$$

$$= p_1 \frac{R_p + R_t}{R_p R_t} = v \quad (71)$$

When $\frac{2R_p}{R_t + R_p} > 1$ i.e. $R_p > R_t$ the target will separate from the projectile.

The separation velocity is given by

$$\frac{R_p - R_t}{R_p + R_t} v \quad (72)$$

So, for a glass target and a steel projectile travelling at 7 metres per second, the separation velocity is equal to;

$$\frac{39.6 - 13.6}{39.6 + 13.6} \cdot 7 = 3.4 \text{ m/s}$$

However, in the experiments under consideration, the target glass sample is restrained and the projectile or in this case the hydraulic impactor continues to move forwards, driven by the flow through the hydraulic cylinder. Consequently, the situation existing just prior to the original impact reoccurs, so that further impacts will take place.

If the acoustic impedance of the target were to be greater than that of the projectile, i.e. $\rho_t c_t > \rho_p c_p$ then p_3 would be positive, so that the interface would not be in tension and the projectile and target would not separate, consequently further reflections of the stress wave in the target would occur.

3.3.4 Release Wave

Once the stress wave has reached a boundary, part of the stress wave will be reflected, and part will be transmitted. If the boundary is a free surface, all of the wave will be reflected, Kolsky (1963). The reflected element is often called the release or unloading wave. If the impactor were a plain cylindrical bar, as is normally the case in Hopkinson bar experiments, then the release wave would take time $2l/c$ to return to the impact point where l is the length of the bar, and c is the stress wave velocity. However, the impactor under consideration has a more complex shape, thus the nature and timing of the release wave is more involved.

Figure 10 et seq illustrate how the stress waves may interact as they propagate through the material of the target and the impactor. Figure 11 shows the projectile, - the steel impactor, and the glass target at the point of impact. The impact is not considered to be a point contact because the radius of the impactor is such that there exists an essentially flat region of contact during the impact. Investigation into this aspect of the impact indicated that the contact area was in the order of 6mm. In figure 12, starting from the contact area, plane stress waves start to move through the material at the appropriate wave velocities. At the edge of the contact area, i.e. at the free surface boundary, a release wave starts, and as shown in figure 13, the release waves propagate into the material, following the initial impact stress waves. In 13, the release waves have just met at the centreline of the impact.

In figure 14, the incident waves have moved well into the material, and the release waves have overlapped. The conditions in the overlapped area have therefore been affected by the incident wave and both reflected release waves. In order for one dimensional theory to apply to this impact, and for bar type conditions to apply, the release waves must die away in, at least, the projectile before the incident wave is reflected from the rear face of the glass target, i.e. once the release wave has traversed the front of the projectile, it behaves as a bar, (Lush (1999)). (Johnson (1972) indicated that a bar should have a length one magnitude greater than any cross-sectional dimension.) It takes approximately one micro-second (6.0×10^{-3} m divided by 5938 m/s) for a wave to cross the contact area and approximately one micro-second (6.4×10^{-3} m divided by 5938 m/s) for the stress wave to reach the rear of the target, thus it is possible that the conditions described above are met, at least for the initial stage of the impact.

In the simplified one dimensional bar approach illustrated in figure 15, the projectile may be considered to be a stepped bar with a minor diameter of 6mm (equating to the contact area) and a major diameter of 60mm. Johnson (1972) indicates that, for the general case of a bar having a discontinuity in both cross sectional area and material, an incident elastic wave of intensity σ_I , moving leftwards (see figure 15) with velocity v_I , will be partially reflected with intensity σ_R , velocity v_R and partially transmitted

with intensity σ_T , velocity v_T at the boundary A B. If both σ_R and σ_T are taken to be compressive then

$$A_1(\sigma_I + \sigma_R) = A_2\sigma_T \quad (73)$$

where A_I is the cross sectional area of the steel impactor to the left of section AB, and A_2 is the cross sectional area of the steel impactor to the right of section AB.

The incident and reflected waves are travelling in opposite directions, so that

$$v_I - v_R = v_T \quad \text{or} \quad \sigma_I - \sigma_R = \sigma_T \quad (74)$$

substituting for σ_R gives

$$\sigma_T = \frac{2A_1\rho_2c_2}{A_2\rho_2c_2 + A_1\rho_1c_1} \sigma_I \quad (75)$$

and substituting for σ_T gives

$$\sigma_R = \frac{A_2\rho_2c_2 - A_1\rho_1c_1}{A_2\rho_2c_2 + A_1\rho_1c_1} \sigma_I \quad (76)$$

For a bar with a cross sectional discontinuity, and no difference in material composition, (the change of section leads to a mismatch in the acoustic impedance, and hence a virtual boundary) equations (68) and (69) can be simplified to give

$$\sigma_T = \frac{2A_1}{A_2 + A_1} \sigma_I \quad (77)$$

and

$$\sigma_R = \frac{A_2 - A_1}{A_2 + A_1} \sigma_I \quad (78)$$

substituting appropriate values into equation (78) gives a figure for the intensity of the reflected stress wave of

$$\sigma_R = 0.82 \sigma_I \quad (79)$$

Johnson (1972) noted that ;

- (i) if $A_2/A_1 \rightarrow 0$, then the end of the bar is effectively free so $\sigma_R \rightarrow -\sigma_I$, and $\sigma_T \rightarrow 2\sigma_I$, and,
- (ii) if $A_2/A_1 \rightarrow \infty$, then the end of the bar is effectively fixed so $\sigma_R \rightarrow \sigma_I$, and $\sigma_T \rightarrow 0$.

Johnson also noted that complicated stress wave interactions occur in the vicinity of the cross sectional discontinuity and for a length equal to about the first diameter.

Equation (72) indicates that if the initial stage of the impact can be considered to be one dimensional, and also if the simplified approach as illustrated in figure 15 is reasonable, then a release wave of approximately 82% of the intensity of the incident wave will propagate back towards the contact zone causing unloading. The release wave would generate a tension when interacting with the reflected wave from the rear face of the glass target.

In the discussions above on the stress wave propagation in a solid-solid impact, illustrated by figure 9, it can be seen that during the impact of a steel projectile whose thickness is large compared to that of the glass target, many reflections of the stress wave occur in the glass before the release wave in the steel projectile reaches the impact boundary. The multiple reflections in the glass are likely to lead to a reduction in the peak stresses due to internal friction effects, (Kolsky (1963)), which consequently are likely to lead to reduced tensile stress in the glass. However, if the release wave follows quite closely behind the loading wave, as illustrated by figures 11

to 14, and as indicated by the approach illustrated in figure 15, then the analysis is more akin to that derived for a target that is of the same order of thickness as the projectile.

In a similar fashion to the approach discussed above, in section 3.3.3, Lush (1999) showed that, for this case, starting with the solution described by equation (58), and illustrated in figure 16, for the incident wave,

$$0 - p_1 = R_p(u_3 - u_1) \quad (89)$$

for the reflected wave,

$$0 - p_4 = -R_p(u_3 - u_4) \quad (90)$$

and for the transmitted wave,

$$p_4 - p_1 = R_t(u_4 - u_1) \quad (91)$$

Dividing through by R_p and R_t gives

$$\frac{p_1}{R_p} = u_1 - u_3 \quad (92)$$

$$\frac{p_4}{R_p} = u_3 - u_4, \text{ and} \quad (93)$$

$$\frac{p_4 - p_1}{R_t} \quad (94)$$

Eliminating velocities by adding or subtracting gives

$$\frac{p_1 + p_4}{R_p} + \frac{p_4 - p_1}{R_t} = 0 \quad (95)$$

thus

$$p_4 \left(\frac{1}{R_p} + \frac{1}{R_t} \right) = p_1 \left(\frac{1}{R_t} - \frac{1}{R_p} \right) \quad (96)$$

hence,

$$p_4 \left(\frac{R_p + R_t}{R_p R_t} \right) = p_1 \left(\frac{R_p - R_t}{R_t R_p} \right) \quad (97)$$

so;

$$\frac{p_4}{p_1} = \frac{R_p - R_t}{R_p + R_t} \quad (98)$$

If the acoustic impedance of the projectile is greater than that of the target, then p_4 is positive.

$$\frac{p_5}{p_1} = \frac{p_4 - p_1}{p_1} = \frac{-2R_t}{R_p + R_t} \quad (99)$$

Using appropriate values

$$p_1 = \frac{39.6 \times 10^6 \times 14.25 \times 10^6}{39.6 \times 10^6 + 14.25 \times 10^6} \times 7 = 73.4 \text{ MPa}$$

$$p_4 = 73.4 \times \frac{39.6 \times 10^6 - 14.25 \times 10^6}{39.6 \times 10^6 + 14.25 \times 10^6} = 34.5 \text{ MPa}$$

and $p_s = 34.5 - 73.4 = -38.9$ MPa

13 Additional Stress Waves

Kolsky (1963) indicated that along the surface of an elastic isotropic body, two additional wave types may propagate; Rayleigh waves and Love waves. Lord Rayleigh (1887) investigated surface waves in liquids, and showed that the effect of the waves decreases rapidly with depth, and that the wave propagation velocity is lower than that of the two body waves. Rayleigh waves have a significant amplitude at the surface only, but decay far more slowly than the body waves. The ratio between the velocity of Rayleigh waves and the velocity of distortional waves has been shown by Kolsky (1963) to be dependent only upon the elastic characteristics of the material. Observations of seismic phenomena by Love (1927) indicated that Rayleigh waves were not the only surface waves propagating after a seismic event. Love suggested that waves with horizontal components parallel to the wave front can be explained by the difference between the material characteristics of the outer layer of the earth and the inner. Love demonstrated that such waves can propagate through the outer layer of a body without penetrating into lower layers, hence this type of wave (a Love wave) could be of interest in layered materials, such as laminated glass.

Torsional waves and flexural waves may appear under certain loading conditions. Torsional waves are a special subset of distortional waves. Johnson (1972) states that flexural waves or bending waves have a speed of propagation that is dependent upon their wavelength, and hence no simple expression can be used to derive the wave speed, thus the simple results and values used for compressive longitudinal pulses cannot be used.

Johnson derives an expression for the elastic wave equation of the form,

$$\frac{\partial^2 w}{\partial t^2} = -c_0^2 k^2 \frac{\partial^4 w}{\partial x^4} \quad (100)$$

where $c_0 = \sqrt{\frac{E}{\rho}}$ and $k^2 = \frac{I}{A}$

Johnson suggests, as a solution,

$$w = A \sin \frac{2\pi}{\lambda} (x - c_p t) \quad (101)$$

where A is the wave amplitude, λ , the wavelength, and c_p the phase speed.

Johnson states that a solution to the wave equation is found if,

$$c_p = c_0 \frac{\pi a}{\lambda} \quad (102)$$

It can be seen that the wave speed is inversely proportional to the wavelength and infinitely short waves will travel with infinite speed, which is clearly not possible, so some limiting factor will come into play. This equation is valid as long as the wavelength is much greater than any lateral dimension of the beam.

3.4 Contact mechanics

The bearing stresses can be determined using Hertz's approach, for a steel sphere pressing with a load P onto a flat plate of glass, one form of the approach, Lawn (1993), gives the radius of the contact circle, a , as;

$$a = \sqrt[3]{\frac{4krP}{3E}} \quad (103)$$

where

$$k = \frac{9}{16} \left(\frac{(1-\nu_p^2)}{E_p} + \frac{(1-\nu_t^2)}{E_t} \right) \quad (104)$$

and r is the radius of the sphere.

The mean contact pressure is given by

$$p_0 = \frac{P}{\pi a^2} \quad (105)$$

Lawn (1993) indicates that the dimpling of the glass surface produces a radial tensile stress, which is a maximum at the edge of the contact area and is given by

$$\sigma = \frac{1}{2}(1-2\nu_t)p_0 \quad (106)$$

substituting for p_0 gives

$$\sigma = \frac{(1-2\nu_t)P}{2\pi a^2} \quad (107)$$

Although no measurements of the indentation load were taken, a value for P of 4000N would yield a maximum tensile stress of 34 MPa.

3.5 Fracture Mechanics

Uhlmann and Kreidl (1980) indicate that at an atomic level fracture occurs because a force exists that is large enough to break the bonds between atoms in the material being subjected to a load. Figure 17 indicates the relationship between the atomic separation and the stress created by an applied load.

As Figure 17 illustrates, the stress needed to cause a separation between the atom planes rises to a maximum, where fracture is considered to occur, and then falls. For a particular material it is possible to calculate the stresses required to cause fracture by consideration of the stress-displacement function. Uhlmann and Kreidl (1980) state that the stress-displacement curve can be approximated by a sine curve having a wavelength λ as indicated on figure 17, so that

$$\sigma = \sigma_c \sin\left(\frac{2x\pi}{\lambda}\right) \quad (108)$$

where x is the displacement from equilibrium. Given that at small displacements, x is approximately equal to $\sin x$, equation (71) can be re-written as

$$\sigma \cong \sigma_c \left(\frac{2x\pi}{\lambda}\right) \quad (109)$$

If it is assumed that the solid is completely elastic, then

$$\sigma = E \epsilon = \frac{Ex}{a_0} \quad (110)$$

where ϵ is the strain, and a_0 is the equilibrium atomic spacing, so that

$$\sigma_c = \frac{E\lambda}{2a_0\pi} \quad (111)$$

Two new surfaces are created each time the atomic bond is broken, so the surface energy can be obtained by calculating half the area under the stress-displacement curve, i.e.;

$$\gamma_s = \frac{1}{2} \int_0^{\lambda/2} \sigma_c \sin \frac{2\pi x}{\lambda} dx = \frac{\lambda \sigma_c}{2\pi} \quad (112)$$

combining the two equations gives;

$$\sigma_c = (E\gamma_s/a_0)^{1/2} \quad (113)$$

Typical values suggested by Uhlmann and Kreidl (1980) of $E=7 \times 10^4$ MPa, $a_0= 30\text{nm}$, $\gamma_s= 5 \text{ J/m}^2$, are used then,

$$\sigma_c \approx \frac{E}{7} \text{ or } 1 \times 10^4 \text{ MPa}$$

However, glass strengths of this order of magnitude are normally only encountered in special circumstances, such as in pristine glass fibres. Normally, the strength of the glass is reduced by several orders of magnitude because of the presence of the Griffith flaws which are thought to be processing, machining, or handling induced flaws. The flaws occur as small surface cracks, and the intensification of the applied load by the cracks can lead to stresses of 10^4 MPa or greater in the vicinity of the crack tip, (Uhlmann and Kreidl (1980)).

Inglis (1913) discussed the stress concentration at a crack tip when a structure is loaded. He demonstrated that for an elliptical crack with length $2c$ and minor axis $2h$, the maximum tensile strength σ_{\max} is given by;

$$\sigma_{\max} = \sigma [1 + (2c/h)] \quad (114)$$

When $\sigma_{\max} = \sigma_c$, crack growth will occur, the result being that the cracks will propagate, and failure will occur at much lower stresses than those indicated by the theoretical analysis.

In his experimental work on glass rods Griffith (1921) showed that the stored elastic strain energy could be equated to the surface energy formed by the propagation of a crack, so that

$$4c\gamma_s = \pi\sigma^2 c^2/E \quad (115)$$

and hence

$$\sigma = (2E\gamma_s/c\pi)^{1/2} \quad (116)$$

Irwin (1958) defined the stress intensity factor, K as the product $\sigma c^{1/2}$. K is a measure of the intensification of the applied stress due to the presence of a crack. For a crack in an infinitely wide plate, K is given by

$$K = \sigma(\pi c)^{1/2} \quad (117)$$

Ashby and Jones (1996) indicate that a reasonable value for K for glass is between 0.7 and 0.8 MN/m^{3/2}.

3.6 Strain rate

Dalgliesh and Taylor (1989) discuss the dependence of window glass strength upon the loading duration and rate, and also indicate that moisture entering the micro-cracks was considered by Michalske and Bunker (1987) to influence the strength loss as glass weathers and ages. Dalgliesh and Taylor suggest that the randomly distributed “Griffith” micro-cracks grow slowly under a tensile stress until a critical level is achieved at which point the cracks propagate at high speed, and that the number of cracks formed increases with the amount of elastic energy stored in the glass just before failure. They describe this effect as stress corrosion and suggest that stress corrosion explains the fluctuating pressures, load duration and varying loading rate noted during different tests. Dalgliesh and Taylor indicate that one way of describing the duration or rate effect is to fit a straight line to a logarithmic plot of failure stresses, s_f vs. time to failure, t_f , so that ;

$$\ln(s_f) = C_1 - (1/n)\ln(t_f) \quad (118)$$

where C_1 is a constant.

The fitting parameter n was found to be 16 or 17 for soda-lime glass in small specimen tests and in many tests of large panels as well, but some large panel tests resulted in larger values of n and hence indicated a weaker dependence on load duration.

Chapter 4

4 Experimental Equipment and Methodology

- 4.1 Industry Standard Impact tests.**
- 4.2 Test Rig Design and Construction**
- 4.3 Experimental Procedure**
- 4.4 Controllable variables**
 - 4.4.1 Nominal Velocity of the ram**
 - 4.4.2 Pre-set deflection**
 - 4.4.3 Contact area**
- 4.5 Non-controllable variables**
 - 4.5.1 Flow through valve**
 - 4.5.2 Actual Velocity Of Ram**
 - 4.5.3 The material characteristics**
- 4.6 Instrumentation**
 - 4.6.1 Force Transducer**
 - 4.6.2 Linear Variable Differential Transformer**
 - 4.6.3 Laser Velocity transducer**
 - 4.6.4 Strain gauges**
- 4.7 Effectiveness of the Test Rig Design**

4 Experimental Equipment and Methodology

The purpose of the test rig was to create the right conditions to enable a thorough investigation of the transitional region between quasi-static loading and low velocity impact loading to be conducted.

4.1 Industry Standard Impact tests.

The British Standards Institute publish two standards that are relevant to the impact of glass, and at present, CEN have a standard advancing through the drafting process; prEN356:1990. The first BSI standard is BS 6206:1981; Impact performance requirements for flat safety glass and safety plastics for use in buildings, the second is BS5544:1978; Anti-bandit glazing (Glazing resistant to manual attack).

BS 6206 describes a test procedure that utilises a pendulum type impactor. The pendulum consists of a 3mm stranded steel cable and a leather "bag" which is intended to represent a 45 kg child. The leather bag is filled with lead shot and is swung from set heights. The pivot point of the pendulum is arranged so that the bag strikes the centre of a test specimen 865 mm wide, by 1930 mm high. The objective of the test is to classify the samples tested into satisfactory (no breakage, or breaks safely) and unsatisfactory (breaks dangerously). The three specified drop heights of 305mm, 457mm and 1219mm correspond to impact energies of 135 J, 202 J, and 538J.

BS5544 describes a simple free drop ball test, where a 2.26 kg, 82 mm diameter steel ball is dropped from 3m and 9m onto an horizontal 590 mm² test piece. If the ball passes completely through the test piece during the impact, or within five seconds, then the test piece is failed.

European standard prEN 356:1990 describes two tests; the first is a drop ball test similar to BS5544, but with a 100mm diameter steel sphere (4.11 kg), dropped from four different heights ; 1500 mm, 3000 mm, 6000 mm, and 9000 mm. The second test

is a spring driven axe impact test, with impact velocities of 11 m/s for a cutting strike and 12.5 m/s for a blunt strike.

There are other impact tests that are in general use in industry, for example the Izod test and the Charpy test, but these tests are undertaken to test material properties such as fracture toughness and do not normally use glass as a sample material.

The principle of the falling weight tests was considered to be unrepresentative of the loading history encountered by a glazing panel when subjected to a manual attack (such as a sledgehammer). Studies undertaken at the Royal Mail Research Centre Sobey (1990), using high speed video recording of manual attack tests indicated that there were a number of key differences between an actual sledgehammer impact and falling mass tests. Consequently, it was necessary to design a test rig that simulated, as far as was possible, the type of impact that glass panels suffered during an actual attack. The design and fabrication of the test rig formed the first part of the research activity.

Blows in a drop test are normal to the surface, whilst in a sledgehammer impact the blows are oblique, and the head has a translational motion across the face of the panel. Secondly, during a drop test the impactor is effectively free, but the rebound of a sledgehammer head during a manual attack is constrained by the handle and thus by the attacker. The high speed video results confirmed the intuitive view that an attacker continues to expend effort on the strike during and immediately after the impact, and appears to "relax" only when the head has started to rebound away from the panel. Thirdly, drop test samples are normally horizontal (the British pendulum tests and the European axe tests have vertical samples), which on a repeated attack might be significant if the material breaks up and cannot move away from the impact site.

When the design of the test rig was undertaken the second element described above was considered to be the most significant, thus the test rig was designed with a loading system that allowed the load to be maintained for a short period of time after the initial impact had taken place.

After the test rig had been completed, it was established that Kamal et al (1987) evaluated an hydraulic ram impact tester; the Rheometrics variable-speed impact tester (RVSIT). The RVSIT is a linear displacement, velocity controlled, system which drives a penetrating rod into contact with the material, in the case investigated by Kamal, the material was polyurethane panels. They concluded that there were inaccuracies between the set impact speed and the speed actually measured, and poor reproducibility of information generated by the load cell at high speed. However, they concluded that the RVSIT provided a flexible impact testing system for flat and formed polymeric materials.

4.2 Test Rig Design and Construction

The test rig used to conduct the experiments was constructed in the main from mild steel box and angle sections and consisted of two parts; the sample holder, and the impactor structure, see figure 18.

The impactor structure consisted of a framework constructed from mild steel box section fixed to the floor, a horizontal aluminium alloy “table”, and the actuator support structure as shown in figure 19. The actuator was bolted to a mild steel box section frame which could be rotated around the nominal impact point to represent oblique impacts.

The impactor head was a 60mm hemi-sphere mounted onto a high response hydraulic actuator. The hydraulic actuator was manufactured by Avon Controls of Tewkesbury, and had a 22mm bore, a 16mm rod, and a stroke of 120mm, as shown in figure 20. A Model 25 servo valve manufactured by Dynamic Valves of California was used to control the hydraulic oil supply to the actuator, and the servo valve, in turn, was controlled by an Avon Controls linear servo drive amplifier. Figure 21 is a schematic diagram of the hydraulic circuit and components. The amplifier had the capability to be used in either positional control mode or velocity control mode. In all the experiments velocity control mode was selected. A Linear Variable Differential Transformer (LVDT) was installed inside the actuator which enabled the relative position of the actuator rod to be determined during its stroke. Figure 22 illustrates the hydraulic pump, and the fast response hydraulic accumulator .

The sample holder consisted of a square structure manufactured from mild steel box section with a ledge to support the sample in an upright position, see figure 23. A ring frame was used to hold the sample in position using appropriate spacers, and eight fixing bolts, two on each side of the ring frame. The bolts were tightened with a torque wrench in a sequence determined to reduce mis-alignment of the ring frame as the bolts were tightened. Correct tightening procedures minimised the number of glass panels that cracked during initial installation. The bolts were tightened to a torque of 10 Nm.

Aluminium spacers (or ring frames) were used to set the relative position of the sample and the impactor head, and thus were the device by which it was possible to pre-set the maximum displacement of the glass panel. The relative position between the actuator and the frame support structure was fixed, however it was possible to introduce a variable into the experiments by placing an aluminium ring frame between the sample support structure and the front face of the sample.

The servo drive amplifier was set to the velocity control mode for all the tests, thus disabling the positional control for the actuator. Since it was not possible to set the position of the actuator, the actuator ram moved through the full extent of its possible travel, i.e. until the ram end stop was reached, for each test. The instrumentation and servo drive amplifier are shown in figure 24.

4.3 Experimental Procedure

During the early part of the project (the first 50 or so results) impact velocity and pre-set deflections were selected randomly. For the majority of the project the tests were arranged so that gradually increasing stresses were generated in the glass samples as the test progressed. For each new sample, the test cycle commenced with both the minimum deflection and the minimum velocity. If the sample survived the first set of ten impacts at the lowest velocity, then the velocity was increased whilst keeping the pre-set deflection constant. The velocity continued to increase up to the maximum, or until the sample failed. If the sample did not fail at the maximum velocity then it was removed, and a new spacer fitted which incrementally increased the pre-set deflection. Once the spacer had been fitted a new set of tests commenced at the lowest velocity, and again increased until either failure occurred or the maximum velocity was reached. The incremental increase of both pre-set deflection and velocity increased until the sample failed.

The procedure was as follows:

The appropriate pre-set was determined, and the aluminium ring frame selected, and checked for flatness and damage.

A glass laminate sample was selected and checked for damage, both on the surface and around the edges.

The sample was loosely placed onto the sample support structure behind the ring frame. The bolts were inserted into the clamping plate, and tightened up in the correct sequence, using the correct torque.

The appropriate adjustment was made to the servo drive amplifier to provide the required hydraulic actuator ram velocity.

Instrumentation output was selected and enabled.

The hydraulic actuator ram was activated and once the ram struck the panel, the ram was withdrawn back to its rest position.

The sample was checked for cracks. A breakage was considered to be a failure of the sample, so that if a crack was observed the sample was removed, the result noted, and the procedure re-initiated. If no crack was observed the result was noted, and the sample re-tested with the next velocity or displacement.

The output from the instrumentation was noted manually, printed at the time or stored on a computer.

4.4 Controllable variables

4.4.1 Nominal Velocity of the ram

The required test velocity was selected using a vernier adjustment potentiometer as an input to the servo drive amplifier, which controlled the servo valve. The vernier dial was used to pre-set the ram velocity by selecting the resistance corresponding to the required velocity. The hydraulic ram is supplied via the servo valve by an hydraulic accumulator. The hydraulic accumulator ensures that the flow of oil to the hydraulic ram is sufficient to maintain the velocity of the ram over its full travel.

4.4.2 Pre-set deflection

As described above, ring frame spacers are used to pre-set the maximum deflection that the test panel experiences. Choice of an appropriate ring frame therefore determines the maximum deflection that the panel would undergo during the dynamic test, provided that the loading capabilities of the hydraulic ram exceeded the stiffness and bending resistance of the test panel.

4.4.3 Contact area

The impact test rig has 6 interchangeable heads, but all of the impact tests conducted during this work used the same impactor head; the 60 mm diameter hemispherical impact head. The impact head was machined from mild steel, and is affixed to the hydraulic ram centre rod with an internal screw thread and a conical bearing surface. The contact area described by the Hertzian approach should be consistent throughout the tests, however it is possible that the effective change in geometry during tests where the deflection is large, i.e. where the panel could be considered to be curved, may cause a change in the contact area.

4.5 Non-controllable variables

4.5.1 Flow through valve

The flow of oil through the valve starts when the electronic control system allows current to flow in the coil of the servo valve which then allows the valve spool to move. Variations in timing of the electronic circuit, variations in the electric field in the servo coil and delays in the movement of the spool will all cause variations in the flow of the hydraulic fluid. Minor variations in the positioning of the vernier potentiometer, will also influence the electronic control circuit.

4.5.2 Actual Velocity Of Ram

The variations discussed in section 4.5.1 will have an impact upon the repeatability of the ram velocity, as will variations in the ram response caused by friction, turbulence in the hydraulic fluid, and temperature.

4.5.3 The material characteristics

The steel impactor was not changed during the experimentation, and no significant changes to the material of the steel were identified.

All glass samples were purchased at the same time from the same glass laminate manufacturer. The glass laminate was examined to establish which surface of the glass lamina were uppermost; "tin side" or "air side". Variations in temperature and humidity were noted during the experimental procedure.

4.6 Instrumentation

The determination of the forces generated during impact is problematical. The results derived from the use of transducers physically attached to the striker can lead to problems arising from stress waves within the striker and transducer assembly. The interfaces between the striker, the transducer and the hydraulic actuator central shaft will also add noise to the output from the transducer. Other noise can be introduced from electrical and electronic sources, such as induced voltages in cables and leads and control electronics amplifiers. It is possible to filter the output from transducers electronically at the time of measurement, or mathematically after the information has been captured, but because filtering, by its nature, affects the signal form, appropriate filtering must be used.

Four sets of instrumentation were used during the work, a force transducer, a linear variable differential transformer (LVDT), a laser velocity transducer, and strain gauges.

4.6.1 Force Transducer

The force transducer is a Kistler 9041a "load washer" mounted between the impact head and the actuator shaft, thus it is 47.5 mm away from the actual impact point when the 60mm large hemispherical impactor is used. The load washer has a range of 0 to 90 kN, and has a resonant frequency of 65 kHz. The load washer is connected to a type 5007 Kistler charge amplifier, which has a cut off frequency of 180 kHz. The output from the Kistler charge amplifier is connected to a Gould digital storage oscilloscope, which had a sampling rate of 200 Msamples/second. Figure 25 is an example of the output from the load washer.

4.6.2 Linear Variable Differential Transformer

The displacement measurement was made using the linear variable differential transformer (LVDT) which was fitted internally to the actuator ram. The LVDT was an Avon Controls type MTN/DL50 which had a linearity better than 0.5%. The output

signal from the LVDT was stored on a Gould digital storage oscilloscope. Figure 26 illustrates a typical output from the LVDT device.

4.6.3 Laser Velocity transducer

The velocity is measured at the rear of the impact panel, opposite the impact point, using a Bruel and Kjaer laser velocity transducer, type 3544. The output from the signal processor was stored by the oscilloscope. An example is shown in figure 27.

4.6.4 Strain gauges

The strain gauges used were standard pattern 120° rosettes, with thermal characteristics that matched those of glass. A typical Wheatstone bridge amplifier manufactured by Measurement Systems was used. The output was recorded on a Gould storage oscilloscope.

4.7 Effectiveness of the Test Rig Design

As discussed above, the design of the test rig attempted to replicate, as far as was possible with a relatively simple approach, the loading that a glass panel would experience when subjected to a physical attack. It was considered that the design was reasonably representative of an idealised sledgehammer strike, but that the shape of the impact head, and the “angle of attack” between the sledgehammer head edge and the glass, were areas where the test rig was probably not representative of a real attack.

The instrumentation did not appear to be as successful as it might have been. Both the Kistler “load washer” force transducer and the Bruel and Kjaer laser velocity transducer did not have a dynamic range capable of recording the very high speed phenomena occurring. However, the Bruel and Kjaer laser velocity transducer was capable of recording the relatively slow vibration of the panel after the impact had occurred.

The strain gauges were not used very often because of the time required to install the gauges, but the few results obtained appeared to indicate that they would be more responsive than either the laser velocity transducer or the Kistler force transducer. However, the output from the gauges was quite “noisy” , making interpretation difficult.

The output from the LVDT appeared to be quite accurate and demonstrated that the velocity of the hydraulic ram was repeatable.

The use of aluminium spacers to provide a pre-set maximum deflection was quite time consuming each time the deflection needed to be changed, but was considered to be accurate and repeatable.

Chapter 5

5 Results

5.1. The relationship between the deflection at failure and the velocity at failure.

5.2. The relationship between the deflection at failure and the velocity at failure divided by the deflection at failure (v/d).

5.3 The relationship between the deflection at failure and the total number of impacts.

5.4 The relationship between the velocity at failure and the velocity at failure divided by the deflection at failure (v/d).

5.5 The relationship between the velocity at failure and the total number of impacts.

5.6 The relationship between the velocity at failure divided by the deflection at failure (v/d) and the total number of impacts.

5.7 The Influence of Relative Humidity.

5.8 The Influence of Temperature

5.9 The comparison between the measured stress and the calculated stress.

5 Results

The main series of experiments yielded a summary data set of 329 rows. The summary data were generated by logging each of the test impacts recorded on the test sheets. Each row corresponds to a single glass sample. For each test set the following were noted, the sample number, the pre-set deflection, the temperature, the relative humidity, the velocity pre-set, and the total impacts for the set of tests, or to failure.

5.1 The relationship between the deflection at failure and the velocity at failure.

Figure 28 is the graph of the deflection at failure versus the velocity at failure. A linear regression analysis was conducted upon the full data set. The correlation coefficient, r , was calculated to be -0.435. When considering the significance of r , and whether the observed correlation coefficient is significantly different from zero, Chatfield (1983) states that the statistic

$$r\sqrt{(n-2)} / \sqrt{(1-r^2)} \quad (1)$$

has a t-distribution with $n-2$ degrees of freedom, provided that both variables are normally distributed. Thus, to be considered significant the value of the statistic above must be greater than the value given in the Student's t-distribution table for the appropriate degrees of freedom, and significance level. For large samples, and for a significance level of 5%, the value is close to 2. (The critical points for the absolute value of the correlation coefficient at the 5 per cent level for a number of sample sizes were determined by Pearson and Hartley (1966). For degrees of freedom values greater than 120, the minimum value to demonstrate significance is 1.960.)

For figure 28 the value for the significance test is 7.6, i.e. significant at the 5 per cent level. Chatfield (1983) indicated that for a sample size of 100, the critical value of the correlation coefficient, r , to show a significant correlation is 0.20. Consequently, the

correlation coefficient can be considered to be statistically valid, but the relationship that the regression line is illustrating is, at best, of medium strength.

In chapter 3, equation (33) indicates that the stress in a square plate is given by,

$$\sigma_{x_{\max}} = \frac{\pi^2}{2(1-\nu)} \frac{Et}{a^2} w_{\max} \quad (2)$$

so that for a test pieces of the same size and material, the deflection at failure is representative of the maximum bending stress in the glass plate.

In chapter 3, equation (58) indicates that the impact stress is obtained using

$$\sigma_g = \frac{R_g R_s \nu}{R_g + R_s} \quad (3)$$

so that for test pieces of the same material, in similar experiments, the velocity at failure may be representative of the impact stress in the plate, although it should be noted that the impact stress is initially compressive, whereas tensile stress is required for the glass to fail.

As discussed above, Figure 28 indicates that there is a weak to medium strength relationship between the velocity and deflection when the samples fail. It was not possible to de-couple the two variables during the low velocity impact experiments, but if the correlation is an accurate portrayal of the relationship, then it is reasonable to infer that it is the combination of both the impact velocity and the size of the deflection which leads to the failure. As the impact velocity decreases, the deflection needs to increase to achieve the failure of the sample, and conversely, as the deflection decreases, the velocity of impact needs to increase.

It is not apparent from figure 28 that some of the data points represent multiple occurrences. Although the tests are representative of a continuous distribution, the experimental procedure created a discrete distribution, so that, for example, three

failures at the same velocity and impact are coincident when plotted. Figure 29 illustrates this aspect of the experiments by illustrating the number of occurrences at each data point with a third dimension, which is drawn as a circle whose diameter is related to the number of occurrences.

The data in Figure 28 are widely scattered so a sub-set of graphs was constructed which partitioned the x axis to establish if there were any variation in the slope of the correlation line, and consequently to identify points at which the behaviour of the material changed.

Figure 30

The data for figure 28 were separated into two different groups, a deflection at failure of 3mm and above, and below 3mm deflection. The regression was plotted and the correlation coefficient calculated. For the portion of the graph below 3mm, the correlation coefficient was -0.36, a medium to low, but significant correlation. For the portion of the graph including and above the 3mm deflection point, the correlation coefficient was -0.09 , a low figure.

Figure 31

The data for figure 28 were separated into two different groups, a deflection at failure of 2.5 mm and above, and below 2.5mm deflection. The regression was plotted and the correlation coefficient calculated. For the portion of the graph below 2.5 mm, the correlation coefficient was -0.31, a medium to low correlation. For the portion of the graph including and above the 2.5 mm deflection point, the correlation coefficient was -0.18, a low figure.

Figure 32

The data for figure 28 were separated into two different groups, a deflection at failure of 2.0 mm and above, and below 2.0 mm deflection. The regression was plotted and the correlation coefficient calculated. For the portion of the graph below 2.0 mm, the

correlation coefficient was -0.22, a low correlation. For the portion of the graph including and above the 2.0mm deflection point, the correlation coefficient was -0.21, also a low figure.

Figure 33

The data for figure 28 were separated into two different groups, a deflection at failure of 1.5 mm and above, and below 1.5 mm deflection. The regression was plotted and the correlation coefficient calculated. For the portion of the graph below 1.5 mm, the correlation coefficient was -0.003, a low, insignificant correlation. For the portion of the graph including and above the 1.5 mm deflection point, the correlation coefficient was -0.25, a low figure.

Figure 34

The data for figure 28 were separated into two different groups, a deflection at failure of 1.0 mm and above, and below 1.0 mm deflection. The regression was plotted and the correlation coefficient calculated. For the portion of the graph below 1.0 mm, the correlation coefficient was -0.29, a low correlation. For the portion of the graph including and above the 1.0 mm deflection point, the correlation coefficient was -0.4, a low to medium figure.

None of the sub-sets of data described above gave a significant indication that there were any step changes in material behaviour when considering changes in the deflection at failure.

5.2. The relationship between the deflection at failure and the velocity at failure divided by the deflection at failure (v/d).

If as, discussed above, the deflection at failure is representative of the bending stress, and the velocity of the impact is representative of the impact stress, then it may be considered that the velocity divided by the stress for any one impact is representative of the rate of strain, i.e.,

$$\frac{m}{s} \cdot \frac{1}{m} = \frac{1}{s} \quad (4)$$

Figure 35 is the graph of deflection at failure versus the velocity at failure divided by the deflection at failure. An exponential regression line of the form

$$y = ae^{-bx} \quad (5)$$

was fitted to the data, giving values of 67.4 for a , and 4.4 for b with a correlation coefficient of -0.91.

Figure 36

If equation (5) is rearranged to give

$$\ln y = \ln a - bx \quad (6)$$

then values for $\ln a$ and b can be determined by plotting the deflection versus the natural log of the velocity at failure divided by the deflection at failure.

The data points in figure 35 are concentrated towards the axes, especially the x axis, the deflection at failure. Figure 36 uses the same data as figure 35, but with the linear y axis replaced by a natural logarithm axis. The regression correlation coefficient was calculated to be -0.86 for this graph.

5.3 The relationship between the deflection at failure and the total number of impacts.

If the deflection at failure is indicative of the bending stress, then Figure 37 which is the graph of deflection at failure versus the total number of impacts may illustrate the influence that the bending stress has upon the distribution of the number of impacts to failure. The total number of impacts for each test piece may be analogous to a fatigue characteristic in glass, in that the stress required to cause failure after a test piece has suffered a large number of impacts would be comparatively lower if some form of fatigue phenomenon was occurring. The data points appear to be quite widely distributed, but with a cluster of points in the medium deflection, (between 1.5mm and 3.5mm) low number of impacts, (less than 10), region of the graph. The linear regression correlation coefficient was calculated to be -0.17, with a Student t-test significance value of 2.6, which is significant at the 5 per cent level.

Figure 38

Re-plotting the data for figure 37 using a natural logarithmic scale for the y axis, the total number of impacts, reduced the scatter to a certain extent, and increased the correlation coefficient to -0.47. However, the improvements were not considered to be significant.

The data used for figure 37 were divided up into sets by keeping one of the variables, velocity, constant. Figures 39 to 58 show the relationship between the deflection at failure, and the total number of failures whilst keeping the velocity constant for each graph. The first figure in each set (i.e. 39,41,43, etc.) shows the frequency curve, whilst the second graph in each set (i.e. 40,42,44, etc.) shows the cumulative distribution function.

5.4 The relationship between the velocity at failure and the velocity at failure divided by the deflection at failure (v/d).

Figure 59 is a graph of the velocity at failure plotted against the velocity at failure divided by the deflection at failure, (v/d), the latter term is considered representative of the rate of strain as discussed above. Most of the data points are positioned at the lower part of the graph, but there are recognisable lines of data points away from the main concentration of points. On a linear plot the correlation coefficient was calculated to be 0.417. The Student significance test gives a value of 7.2, higher than the value required to indicate significance level at the 5% level.

Figure 60

Figure 60 uses the same data as figure 59, but replaces the linear axes with natural logarithm axes. The regression correlation coefficient was calculated to be 0.81 for this plot, but the data appear widely scattered.

5.5 The relationship between the velocity at failure and the total number of impacts.

Figure 61 is a graph of the velocity at failure versus the total number of impacts. The data at the lower section of the graph (below 100 total impacts to failure) are close to the regression line. The points between 100 and 200 total impacts are approximately on a line parallel to the regression line, whilst those points above 200 total impacts appear to be randomly distributed. The Student significance test gives a value of 5.97, higher than the value required to indicate significance level at the 5% level.

The data used for figure 61 were divided up into sets by keeping one of the variables, deflection, relatively constant (i.e. within uniformly spaced intervals). Figures 62 to 77 show the relationship between the velocity at failure and the total number of failures, whilst keeping the deflection constant for each graph. The first figure in each set (i.e. 62,64,66, etc.) shows the frequency curve, whilst the second graph in each set (i.e. 63,65,67, etc.) shows the cumulative distribution function.

5.6 The relationship between the velocity at failure divided by the deflection at failure (v/d) and the total number of impacts.

Figure 78 is a graph of the velocity at failure divided by the deflection at failure plotted versus the total number of impacts. The data points on the graph are quite widely scattered, and, in the main, are clustered adjacent to the y axis (the total number of impacts). When plotted on linear axes, the linear regression analysis produced a low figure of 0.15 for the correlation coefficient.

Figure 79

Figure 79 was plotted using the same data, but using natural log axes. The data were located in a broad band with a positive slope, around the regression line. The correlation coefficient for this graph was found to be 0.63.

5.7 The Influence of Relative Humidity.

Figure 80

Figure 80 uses the same data as used for the Figure 61 graph, but the data have been divided into three sub-sets depending upon the value of the relative humidity at the time that the tests were conducted. There does not appear to be a large difference between the three regression lines. The correlation coefficient for the 40-60% relative humidity line is 0.44, for the 26-39% line, 0.23, and for the 10-25% regression line, 0.56. The Student significance test gives a value of 5.03 for the 10-25% relative humidity data, 2.37 for 26-39%, and 4.63 for the 40-60% relative humidity data, all of which exceed the critical value for significance at the 5% level.

Figure 81

Figure 81 is a similar graph to figure 80, but a reduced data set has been used. The information for the first 53 samples, considered to be distorted by a variation in

experimental procedure (see chapter 6) have been removed. The correlation coefficients for 10-25%, 26-39%, and 40-60% relative humidity were 0.78, 0.28 and 0.47, respectively.

Figure 82

Figure 82 uses the same data as used for the Figure 28 graph, but as above, the data have been sub-divided into three sub sets depending upon the value of the relative humidity at the time that the tests were conducted. The data are widely scattered, and there does not appear to be a strong relationship indicated by the graph. The correlation coefficient for the three regression lines is fairly low. There appears to be little difference between the 40-60% RH regression line and the 26-39% RH regression line. The regression correlation coefficient for the two lines is also similar with a value of -0.40 for the former, and -0.43 for the latter. The regression line for the 10-25% relative humidity data is at a steeper angle, with the data points mostly residing in the central part of the x (deflection at failure) axis. The data points for the other two data sets are more widely scattered. The correlation coefficient is -0.52 for the 10-25% relative humidity data. The Student significance test gives a value of 4.5 for the 10-25% relative humidity data, 4.7 for 26-39%, and 4.1 for the 40-60% relative humidity data, all of which exceed the critical value for the 5% significance test.

5.8 The Influence of Temperature

Figure 83

Figure 83 uses the same data as used for the Figure 61 graph, but the data have been sub-divided into three sets depending upon the value of the temperature at the time that the tests were conducted. In a similar fashion to the analysis for the relative humidity discussed above, the regression lines for two of the sub-sets are close together with the 15-19.9 °C data having a regression line similar to the line for the 20-23.9 °C data. The regression correlation coefficient for the 15-19.9 °C data was 0.97,

and for the 20-23.9 °C data was 0.90, with significance test figures of 27.3 and 23.7 respectively. The regression correlation coefficient for the 24-28 °C data was 0.62, with a significance test figures of 6.23, indicating that the data were more scattered in this temperature bracket.

Figure 84

In a similar fashion to figure 81, a reduced data set was used for figure 84; the information for the first 53 samples has been removed. The correlation coefficient for 15-19.9 °C, 20-23.9 °C, and 24-28 °C was calculated to be 0.988, 0.994 and 0.988 respectively.

Figure 85

Figure 85 uses the same data as used for the Figure 28 graph, but the data have been sub-divided into three sub sets depending upon the value of the temperature at the time that the tests were conducted. As with figure 82, the data are widely scattered, and there does not appear to be any clear pattern to the behaviour at different temperatures. The regression lines were similar for all three sets of data, but with differing correlation coefficients and statistical significance. The regression correlation coefficient for the 15-19.9 °C data was -0.3, for the 20-23.9 °C data was -0.51, and for the 24-28 °C data was -0.46. The 15-19.9 °C data had a fairly low significance test value of 2.3, whilst the 20-23.9 °C and 24-28 °C data had significance figures of 6.6 and 4.2 respectively.

5.9 The comparison between the measured stress and the calculated stress.

Figure 86

Figure 86 is a graph showing the difference between the measured bending stress (derived from the strain) and the calculated bending stress for the glass samples under consideration. The stress (strain) measurement was made with a rectangular strain

gauge rosette fixed to the rear of the glass sample. The plate was incrementally loaded at the centre. The regression correlation coefficient for the measured stress relationship was 0.97, and the Student significance test gave a value of 15.76, which indicates that the regression is statistically significant. The measured stress appears to lie on two separate lines, however, as the stress was measured at various levels whilst the plate was being loaded, and at similar points whilst the plate was being unloaded, it is considered that the two lines observed in figure 86 are indicative of an hysteresis effect.

Figure 87

Figure 87 is a graph showing the maximum principal stress, derived from measurements made with a strain gauge rosette fixed to the rear of the glass, to illustrate the levels of bending stress as the vibration of the panel decays after the impact.

Chapter 6

6 Discussion of results

6.1 General Discussion

6.1.1 Impact of different materials

6.2 The influence of the PVB interlayer.

6.3 Full Data Set

6.3.1 The Deflection At Failure Versus The Velocity At Failure

6.3.2 The Deflection At Failure, And The Velocity At Failure Divided By The Deflection At Failure (V/D).

6.3.3 The Relationship Between The Deflection At Failure And The Total Number Of Impacts To Failure For Each Sample.

6.3.4 The Relationship Between The Velocity At Failure And The Velocity At Failure Divided By The Deflection At Failure.

6.3.5 The Relationship Between The Velocity At Failure And The Total Number Of Impacts To Failure.

6.3.6 The Relationship Between The Velocity At Failure Divided By The Deflection At Failure And The Total Number Of Impacts.

6.3.7. The Influence Of Relative Humidity.

6.3.8. The Influence Of Temperature.

6.4 Reduced Data Set

6.5 Weibull Analysis.

6.6 Stress intensity factor

6.7 Strain rate dependency

6.8 The Influence of the stress history

6 Discussion of results

6.1 General Discussion

As indicated in the introduction, the intention of this work was to establish the nature of the initiation of fracture caused by low velocity impacts, and to identify the difference in importance between the dynamic impact effects and the bending of the glass plate during the transitional region where the quasi-static loading of glass plates merges with impact or dynamic loading.

The test rig consisted of a hemi-spherical impactor which came into contact with the glass test sample. At the first instant of contact neither the material in the steel impact head nor the material of the silica glass test sample has been subjected to any increase of stress. As the impactor starts to penetrate the surface of the glass, stress fields start to build in the glass and the steel impactor. The glass and the steel both deform at the point of contact, and the stress effects start to propagate away from the point of impact at the appropriate sonic velocity for the stress wave characteristic. A Lagrangian diagram can be used to explore the timings of the important moments during the impact history.

The Lagrangian diagram has distance as the horizontal, x , axis, and time as the vertical, y , axis. Referring to figure 9, the point of impact is marked A. The steel impactor approaches the glass test piece at velocity, v . Starting at the point of impact, A, the two stress waves propagate through each material at the respective sonic velocities. The slope of the line, with reference to the y axis, is equivalent to the velocity of the stress wave. The determination of the velocity of the stress waves in the steel impactor and the glass target was discussed in chapter 3. It was established that the velocity of the stress wave in the steel impactor was in the order of 5050 m/s, and that the velocity of the stress wave in the glass sample was in the order of 5515 m/s, hence on the Lagrangian diagram, the slope of the glass stress wave is steeper than that of the steel stress wave.

At point B the elastic compressive wave reaches the rear face of the glass panel and is reflected at the same velocity, but now travels as a tensile wave, until it reaches point C. As it travels, the tensile wave acts as an unloading wave, “cancelling” the stress produced by the original impact compressive wave. When the tensile wave reaches the interface it is likely that at that time, or shortly afterwards, the plate and the impactor will separate. However, since the impactor is not a dropped weight that will rebound, but is driven by a hydraulic ram, the impactor will continue moving forwards and will then come back into contact with the restrained glass test piece re-initiating the impact and the consequential stress waves.

If the impactor were to be considered a plain bar, then it would be significantly thicker than the glass target so the compressive wave travelling through the steel would not reach the rear of the impactor (at point D) until after the stress wave in the glass has reached point C. Consequently, it is some time, relatively speaking, before the release wave in the steel reaches the interface between the impactor and the target. Thus, it is likely that the stress wave in the glass travels backwards and forwards a number of times until the release wave in the steel impactor reaches the interface. The stress wave in the glass takes approximately 2.3×10^{-6} seconds to travel to the rear of the glass and return, and approximately 7.4×10^{-5} seconds to reach the edge of the glass and return. The stress wave produced in the steel is likely to take in the order of 1.2×10^{-5} seconds to travel through the steel and return to the interface between the two materials. Thus, in that time, the incident stress wave in the glass is likely have traversed the glass back and forth many times. As discussed above, when the compressive wave in the glass is reflected from the rear surface of the glass it becomes a tensile wave, as does the stress wave reflected at the rear face of the steel. When the two tensile stress waves intercept each other, tension in the material is generated, which if it exceeds the local failure stress, will result in a crack forming.

If the glass panel suffers repeated impacts, as appears likely, the stress history of the glass over the whole of the impact event is likely to be complex. Although the stress history will contain peaks of tensile stress able to cause a fracture in the glass, it is considered that only when those peaks coincide with an appropriate Griffiths micro-crack at or near the surface, or a flaw within the body of the glass, will a failure crack

in the glass be initiated. It is considered that part of the explanation for the wide variation in the failure of glass, and in the experiments discussed in this work, are caused by transient peak stresses coinciding (or, often, not coinciding) with susceptible micro-cracks, or internal flaws.

6.1.1 Impact of different materials

The analysis in chapter 3 concentrated upon a projectile of steel impacting a target of glass and indicated that if the acoustic impedance of the projectile R_p was greater than that of the target R_t , then the interface between the projectile and target will be in tension and thus the projectile and target will separate when the compressive wave is reflected from the free surface of the glass. Wood is a material which has a wide range of material properties, but for the purposes of illustration it is considered that a figure of $3.2 \text{ Kg/m}^2\text{s}$ for the acoustic impedance is reasonable. Substituting the value of acoustic impedance for wood into the equations in chapter 3 indicate that a wooden projectile and a glass target would not separate when the initial stress wave reflected from the glass surface reaches the boundary, furthermore, from equation (58), the initial compressive stress would be 18 MPa and from equation (65) the tensile stress resulting from the reflected stress wave would be 11 MPa. This result reflects the intuitive conclusion that; a glass sample is less likely to fail when struck by a wooden object than a steel one.

If the impact of a piece of flint is considered, then the following results can be obtained. The material characteristics of flint are very similar to that of glass, so that if appropriate figures are used for equation (58) then the initial compressive stress generated by the impact would be 46.2 MPa, but the reflected tensile wave as described in equation (65) would be close to zero. If the tensile stress is calculated after the release wave from the impacter passes into the glass target, then using equation (99) the same figure of 46.2 MPa is obtained for the tensile stress. The result of this is that, although a steel projectile is likely to result in a higher compressive stress following an impact, for a similar impact from a flint projectile, the tensile stress will be higher, thus the likelihood of a flint projectile initiating a fracture is greater.

6.2 The influence of the PVB interlayer.

In chapter 2 two important aspects of PVB were discussed, viz., that although the damping factor is large, it decreases as the frequency increases, especially through the range of frequencies likely to be of interest for impact problems. Secondly, the physical characteristics of the PVB observed when unconstrained are likely to be significantly different when the material is constrained between two sheets of glass. Since the damping effect is minimised by both the PVB being constrained, and the frequency of vibration being high, it is considered that the stress wave will pass through the PVB with little dispersion. The physical characteristics of constrained PVB have not been assessed, all data relate to the material in its unconstrained state, (although PVB is a soft, plastic elastomer, some text books quote an “apparent” modulus of elasticity of 2.7-3.1 GPa). So, although it is likely that the velocity of the stress wave as it passes through the PVB is lower than that of the glass or the steel, it has not been possible to quantify the resultant reduction in time for the stress wave to pass from the impact point to the rear of the glass.

Achenbach (1975) states that when a stress wave strikes the interface between two media of different material properties, part of the wave is reflected and part is transmitted. The reflection and transmission characteristics are determined by the ratio of acoustic, or mechanical, impedances;

$$\frac{R_t}{R_p} \quad (1)$$

When the ratio is equal to 1, the stress wave is completely transmitted, when the ratio is equal to 0, which corresponds to a free surface, the stress wave is completely reflected. Using the values for the unconstrained PVB, the ratio was calculated to be 0.14, with a transmission coefficient of approximately 0.24. However, as discussed above, the PVB is constrained between the two layers of glass, consequently, the effective stiffness of the PVB is likely to be significantly greater than the apparent modulus of elasticity quoted. If the constrained PVB is considered to have a value of

Young's Modulus approximating to half that for glass, then the transmission coefficient rises to 0.7.

6.3 Full Data Set

6.3.1 The Deflection At Failure Versus The Velocity At Failure

Figure 28 is the graph of deflection at failure versus the velocity at failure. The deflection at failure represents the maximum bending stress, whilst the velocity represents the impact stress in the plate. To compare the experimental results with previous work or analytical considerations, it would be desirable to map similar relationships. However, to produce an effective comparison, it may also be necessary to include the variation in the results described by the Weibull distribution.

If the regression line is indicative of the nature of the relationship, then the failure of the glass panels appears to be a response to the combination of the different loading conditions. As the deflection increases, the impact velocity at which failure occurs decreases. Conversely, as the velocity of impact increases, the deflection at which failure occurs decreases. The impact and bending stresses can be calculated using the equations for stress wave propagation and bending discussed in chapter 3.

The regression line generated for figure 28 is of the form;

$$y = mx + c \tag{2}$$

where the slope of the line, $m = -7.4$, and the intercept, $c = 4.5$.

However, the regression line may not be indicative of a direct relationship between the velocity at failure and the deflection at failure. If the variables are changed to the deflection stress at failure versus the impact stress at failure (figure 88) the graph looks the same, but the values for the regression line change to reflect the different values for the variables. The value for the slope, m , becomes -0.522 , and the intercept, c , changes to 44.96 . The regression line on this graph would be, in effect, the boundary between failure and survival if all points were located upon it, (see figure 89) however, the correlation coefficient is quite low, with a value of -0.51 , (although it is statistically

significant) so the regression line could be considered to be the mid line of a broad boundary between failure and survival, as shown in figure 90. The broad boundary reflects the variability in failure loads for glass. The boundary between failure and survival is equivalent to a failure stress in the material, so the combination of the impact stress and the bending stress should equate to the failure stress. Merely adding the value for impact stress to the value for bending stress is probably not suitable and gives a value for the total stress that appears to be too high. Furthermore, the impact stress appears to be the dominant influence (see below) so it was considered appropriate to apply a modification factor, the stress combination factor, f , to the bending stress, to reduce its contribution to the total stress, and also to reflect the apparent lesser importance of the bending stress to the initiation of failure of the glass sample.

It would be expected that the combined impact and bending stress would follow a normal type distribution, albeit with a fairly large standard deviation, in common with other brittle materials. Figure 91 illustrates the distribution for the combined bending and impact stress for all failures, for both the $f = 1$ and the $f = 0.7$ cases. A Gaussian distribution has been fitted to both curves. The “noisy” nature of both curves may be indicative of the experimental procedure, in that both the velocity at impact, and the deflection at impact were discrete values.

One feature of figure 28 that is worthy of further discussion is the apparent contradiction between the reasonably high correlation coefficient and the appearance of widely scattered data points on the graph. The experimental procedure results in a number of points that are coincident, so the graph does not give a true indication of the distribution of all the points. Figure 29 is a “bubble graph” which shows a third dimension, the number of occurrences at each data point, as a circle at each point, with the diameter of each “bubble” related to the number of occurrences. This graph illustrates that, whilst the data are quite scattered, there is a concentration of points at the lower part of the graph, and in the middle section of the graph.

6.3.2 The Deflection At Failure, And The Velocity At Failure Divided By The Deflection At Failure (V/D).

Figure 35 illustrates the relationship between the deflection at failure, and the velocity at failure divided by the deflection at failure (v/d). The former term can be considered to represent the bending stress in the plate, whilst the latter, the rate of strain. If v/d is an accurate description of the strain rate then the graph appears to indicate that at the comparatively high rates of strain (within the context of the experimentation) the deflection and hence stress necessary to cause failure was low, and vice versa. Following tests conducted upon glass rods Oliver (1975) indicated that stress levels required to cause failure fell as the duration of the load increased, i.e. apparently a result contradictory to figure 35. Ruiz (1989) reached similar conclusions to Oliver. If the inverse of the strain rate term used in figure 35 is plotted, as in figure 92 i.e. a graph indicative of the duration of load, the relationship is again apparently different to that determined by Oliver. It is possible that the velocity term is dominant and that figure 35 illustrates the relationship that high velocities cause failures even when the deflection is quite small.

As a comparison to Oliver's results, a theoretical analogue was generated using the calculated values for the total stress loading plotted against the deflection divided by the velocity to provide a figure for loading time; figure 93. The resulting graph did not appear to be conclusive.

6.3.3 The Relationship Between The Deflection At Failure And The Total Number Of Impacts To Failure For Each Sample.

Figure 37 is a graph which plots the deflection at failure versus the total number of impacts to failure for each sample. There is a significant amount of scatter on the graph, and the regression analysis indicated that the relationship between the two variables was fairly weak. If the regression model is indicative of a valid relationship then, as the deflection increased, fewer impacts were necessary to cause the glass to fail, and conversely, larger number of impacts were required to cause failure when the deflections were small. Figure 38 which used the same data, but plotted the total

number of impacts on a natural log axis appeared to reduce the concentration effect towards the lower area of the total number of impacts axis. Although different in appearance, the scatter did not appear to have significantly reduced.

The implication of the relationship described in the paragraph above is that the likelihood of failure of a particular sample or test piece is not a simple relationship between load and failure stress. Test results on brittle materials have shown the wide variation in results that occur. Thus the failure of the glass is likely to be influenced by a material characteristic - surface cracks, as well as the propagation of stress waves and the impact conditions at a “micro” scale as well as at the macro-scale. The Weibull distribution recognises the material variability by ascribing a power term, m , the flaw density parameter, to the material. The Weibull distribution describes the probability of a test piece failing at a certain stress level, so at small deflections, the impacts need to be repeated until the conditions for failure have been satisfied. At higher deflections it is more likely that the stress field is higher than that required for failure, hence the probability of failure is raised.

6.3.4 The Relationship Between The Velocity At Failure And The Velocity At Failure Divided By The Deflection At Failure.

Figure 59 is a graph of the velocity at failure versus the velocity at failure divided by the deflection at failure. The latter term is representative of strain rate, whilst the first term is indicative of impact stress. As mentioned in chapter 5, although the majority of the data are concentrated near the x-axis, there are two distinctive areas that do not appear to be associated with the majority of the data. There is one line of data at approximately 45° , and another at approximately 22° . It is considered that the lines are an artifice of the experimental procedure, the deflection at failure variable is not a continuous variable, different ring frames were used to provide the variation in deflection (see chapter 4). Additionally, there were a small number of failures at low deflections; seven at 0.1, and five at 0.2. Considering that the failures at low deflections happened at various velocities, and that the velocity appears on both axes, the effect of the relatively few low deflection failures was to create a few data points

that appeared on the 45° and 22.5° line, i.e.; x v. $x/0.1$, and x v. $x/0.2$. The relatively minor significance of these data points is indicated by the reasonably strong correlation coefficient of 0.417 for the whole data set, and the fact that the regression line is close to the majority of the data points at an angle to the x axis of approximately 10°.

If the regression line is indicative of a real relationship, it appears to indicate that the likelihood of failure increases as both the velocity increases and as the rate of strain increases, but that the relationship appears more sensitive to the increase of velocity than the increase of rate of strain.

As discussed above, Oliver (1975) and Ruiz (1989) concluded that the stress levels required to cause failure fell as the duration of the load increased, which appears to agree with the results illustrated by figure 59. If the inverse of the strain rate term in figure 59, i.e. a term which is indicative of the load duration, is used (see figure 94) the relationship is similar to that obtained by Oliver (1975). Figure 94 appears to indicate two things, the first that most of the failures appear to occur at a low loading time period, and secondly, that impacts at a velocity of 1 m/s seem to be relatively insensitive to the loading duration. The correlation coefficient of -0.76 indicates a reasonable correlation, even though the regression line doesn't appear to fit the data points particularly well. Using natural logarithm axes leads to a regression line that appears to be more well behaved (see figure 95), and which has a slightly better correlation coefficient of -0.81.

6.3.5 The Relationship Between The Velocity At Failure And The Total Number Of Impacts To Failure.

Figure 61 is a graph of the velocity at failure versus the total number of impacts to failure. The apparent relationship illustrated by the graph is that the number of impacts required to fracture the glass increases as the velocity of impact increases. It is considered that this result has occurred because of the method used for the experimentation, and the nature of the material being tested. The majority of the samples were tested using the same approach; (see chapter 4). After the sample had

been mounted with the appropriate maximum deflection, the minimum velocity was set before the hydraulic ram was activated. The impact was repeated nine more times at that velocity, provided that the glass had not fractured. If after the set of impacts had been completed, the glass remained unbroken, the velocity pre-set was increased to the next point. The procedure continued until either the glass broke or the set of tests had been completed. As discussed above, glass does not fail at a specific stress level, the distribution of flaws on the surface lead to a broad distribution of failure loads. Consequently, this characteristic of glass, when combined with the experimental procedure used, is likely to lead to the failure of “weak” samples at low velocities, and “strong” samples at higher velocities, i.e. as soon as the velocity is high enough to create a stress field that is higher than the glass can withstand, the sample fails.

It can be seen that data are arranged in three regions of interest. The first region is for data points between 0 and 100 total impacts to failure. The data in this region are approximately aligned along two lines; the first line adjacent to the regression line, the second line at a lesser angle. It is considered that the line adjacent to the regression line is a result of the experimental methodology, as discussed above. The line of data points close to the x axis correspond to the early set of tests (approximately 50) which employed a different experimental procedure.

In the second region of interest, between 100 and 200 total impacts to failure, the straight line represents the second phase of the experimental process, whereby if a sample does not fail after 100 impacts the pre-set deflection is incremented, and the experimentation restarts at the minimum velocity.

The third region of interest, between 200 and 500 total impacts, illustrates the performance of a small number of samples with a high failure stress.

6.3.6 The Relationship Between The Velocity At Failure Divided By The Deflection At Failure And The Total Number Of Impacts.

Figure 78 is a graph of the velocity at failure divided by the deflection at failure (representing strain rate) versus the total number of impacts. With linear axes, the

graph doesn't appear to illustrate any strong relationship. The majority of the data points are positioned towards the y axis (total number of impacts), and the lower portion of the x axis, but there appears to be a significant amount of scatter. When the axes are changed to logarithmic axes, (figure 79) the data appear to be better aligned, at approximately forty-five degrees, but there is still a significant amount of scatter. The correlation coefficient for figure 79 is 0.63.

6.3.7. The Influence Of Relative Humidity.

Overend et al (1999) discussed the failure prediction of glass and indicated that when the micro cracks present on the surface of the glass are exposed to water vapour, whilst the sample is subjected to a tensile load, the flaws grow more rapidly in depth than in width, leading to higher stress concentrations, and thus potentially a failure at a lower stress level. Overend described this effect as static fatigue.

Figure 80 was intended to identify any relationships that could be attributed to changes in the relative humidity of the atmosphere at the time of testing. The lower line of figure 80 consists mainly of the 10-25% relative humidity data points, but there appear to be a significant number of points in this sub-set also scattered at the higher end of the graph. Both the set of points in the 26-39% relative humidity range and the set in the 40-60% range are close together and appear to lie close to a straight line at approximately 45 degrees. The indication is, therefore, that above 25% the relative humidity does not appear to be a contributing factor to the failure of the glass samples, but that below 25% the relative humidity may be a contributing factor in the resistance of glass to impact, or may cause some variation in the results. However, if the reduced data set is used (see below), the relative humidity does not appear to influence the relationship at all.

Figure 82 graphs the relationship between the deflection at failure and the velocity at failure, but again the data points are separated into different relative humidity regions. As before, the data points in the 26-39% relative humidity range and the points in the 40-60% range have similar regression lines. The regression line for the 10-25% relative humidity data points deviates from the previous two cases but is still close enough to

indicate a similar relationship. As before, the variation in the graphs may be an indication of greater experimental scatter at the lower end of the relative humidity scale, or it may just be a general feature of the widely scattered data set.

6.3.8. The Influence Of Temperature.

Figure 83 was intended to illustrate any relationship that could be attributed to variations in temperature. Most of the data points in the 15-19.9 °C range, and in the 20-23.9 °C range lie on a line, similar in position and angle to the regression line. The data points for the temperatures above that, the 24-28 °C band, appear more scattered, and the regression correlation coefficient concurs with that perception. The reduced data set did not indicate any variation in the relationship with a variation in temperature. Figure 85 was analogous to figure 82 discussed above, in that the data were separated into ranges of temperature. The lower temperature band data points appear to occupy an area close to the left hand end of the graph, viz., at low deflection but at a variety of velocities. The regression lines for all three sets of data are reasonably consistent, but have fairly weak correlation coefficients.

6.4 Reduced Data Set

In the early stages of the experimentation the samples were tested using a vaguely random approach to determination of the impact velocity and the pre-set deflection. The intention was to test the full range of permutations of deflection and velocity options by selecting the combinations of impact velocity and deflection that had not been previously tried. It became clear that the approach was unlikely to be rigorous enough for a full understanding of the problem when apparent inconsistencies appeared, viz.; a test piece failed to fracture even though a similar sample had fractured at a lower impact velocity or pre-set deflection. A revised experimentation procedure was implemented which commenced the testing of each sample at the same point; the minimum deflection and the minimum impact velocity, and then progressively increased both the deflection and the velocity, as described in chapter 4. Unfortunately, it has not been possible to accurately identify when the experimentation procedure was changed, because the original records were destroyed by fire, but it is considered that the change was introduced after approximately fifty samples had failed.

The following part of the chapter considers the relationships for the reduced data set, i.e., with the first fifty results removed.

The graphs shown on figures 28, 35, 37, 59, 61, and 78 were re-plotted with the reduced data set, as figures 96 to 101 respectively.

Most of the graphs have an improved result for the correlation figure as illustrated in table 6.1, below, as would be expected if the revised experimental procedure had been an improvement resulting in reduced experimental scatter. However, the graph shown in figure 100 is worthy of further discussion

Figure	r	Figure	r
28	0.435	96	0.505
35	0.55	97	0.568
37	0.165	98	-0.159
59	0.417	99	0.475
61	0.355	100	0.432
78	0.147	101	0.129

Table 6.1 Comparison of correlation coefficients.

As discussed above in the section on figure 61, figure 100 illustrates the relationship between the impact stress represented by the velocity at failure, and the total number of impacts, and indicates that the graph illustrates a feature of the experimental approach in that “weak” test pieces fail first, i.e. when the impact stress has exceeded a “low” threshold. However, the velocity at impact is not the only contribution to the stress history experienced by the test piece, the bending stress as represented by the deflection at failure also makes a contribution. If the bending stress produced a similar effect, then the graph of deflection at failure versus the total number of impacts (figure 98) would be expected to indicate a similar relationship, viz., that “weak” test pieces would fracture once the test piece reached a relatively low bending stress threshold. This is not the case, the data points are quite widely scattered, and the regression line has a low correlation coefficient of -0.159. It is possible that the velocity at impact is more important in determining the likelihood of failure than the deflection, but because the two variables are linked during the experimental procedure it is not possible to divorce one from the other. If the graphs are re-plotted, but keeping one of the variables constant (or at least within a narrow band) whilst varying the other, the following results are obtained.

The following table lists the variation in correlation coefficient for each constant velocity.

Figure	Constant Velocity m/s	Correlation Coefficient
102	1.05	0.24
103	1.9	0.26
104	2.6	0.11
105	3.3	-0.29
106	3.8	-0.22
107	4.3	-0.03
108	4.75	0.33
109	5.3	0.76
110	5.85	-0.24
111	6.6	0.39

Table 6.2. Comparison of Correlation coefficients for varying deflections at constant velocity.

The table below lists the variation in correlation coefficient for each band of deflections.

Figure	Deflection, mm between;	Correlation Coefficient
112	0-0.5	0.09
113	0.6-1.0	0.59
114	1.1-1.5	0.70
115	1.6-2.0	0.60
116	2.1-2.5	0.21
117	2.6-3.0	0.88
118	3.1-3.5	0.84
119	3.6-4.0	0.71

Table 6.3. Comparison of Correlation coefficients for varying velocities at constant deflection.

Table 6.2 highlights the scattered nature of the data when plotted using the two variables deflection at failure and total number of impacts.

Table 6.3 indicates that the relationship between velocity at failure and the total number of impacts to failure in most cases appears reasonably strong, and does not appear to be sensitive to the variation in bending stress.

The above discussion would appear to indicate that, generally speaking, on its own, the value for the pre-set deflection does not greatly influence the probability that the glass will fail, but that the impact velocity does tend to influence the probability of failure. If a series of plots for the set of fixed velocities (figures 102 to 111) are drawn on the same graph (figure 120) the broadly stratified nature of the graph can be observed, although there is significant scatter. When examined together with the series of graphs at fixed deflections, (figures 112 to 119) it is considered that these graphs illustrate an

artifice of the experimental procedure, as discussed above viz.: The nature of the experimentation is one of exposing the glass samples to an ever increasing stress level. At the beginning of the process the pre-set impact was low, and the velocity was low. If, after a number of tests the glass had not failed, the velocity was gradually increased. If the glass sample remains undamaged, the pre-set impact was increased and the test cycle restarted with a low velocity. The consequence of this approach is that “weak” glass samples will fail early in the procedure, equating to a low number of total impacts, whilst “strong” glass samples will fail late in the procedure, equating to a high number of total impacts. This would lead to a graph which would have a positive correlation at approximately 45 degrees if the scales for the axes were similar, and if the relationship was linear, which is indeed, broadly speaking, what can be observed in figures 112 to 119. However, no similar conformity can be seen in figures 102 to 111, and consideration of the stratified nature of figure 120 leads to the conclusion that the impact velocity is the predominant influence, and that the probability of failure is not sensitive to the pre-set deflection figure, except perhaps at velocities lower than 1.9 metres per second.

If the stress combination factor, f is used to plot a total combined failure stress versus the total number of impacts, then the sensitivity of the experimental “artifice” discussed above to the combined stress can be investigated. Although the data are reasonably well ordered when a stress combination factor of 1 is used (Figure 121), figures 122 to 130 illustrate that as the stress combination factor is reduced, the data points are less scattered and the correlation coefficient for the regression line improves. It is possible that this result is an alternative way of illustrating the apparent predominance of the impact stress over the bending stress when considering the failure of the glass sample.

Table 6.4 and figure 131 show the variation in the correlation coefficient as the stress combination factor reduces.

Stress combination factor, f	correlation coefficient, r
1.0	0.28
0.9	0.31
0.8	0.34
0.7	0.37
0.6	0.39
0.5	0.41
0.4	0.43
0.3	0.43
0.2	0.44
0.1	0.44

Table 6.4 Comparison of stress combination factor and correlation coefficient.

6.5 Weibull Analysis.

Weibull (1939) indicated that some materials, did not appear to have a unique ultimate strength, but that the failure load was distributed around a computed mean with an amount of dispersion. Weibull argued that although it was not possible to determine an absolute value for the breaking load, it was possible to calculate a definite probability of failure occurring at a given stress level.

The failure of glass samples has been identified by Oh and Finnie (1967), amongst others, as following a Weibull distribution, hence there is no unique strength or fracture stress for glass. The Weibull distribution relates the probability of failure, P , to the applied stress with the relationship;

$$P = 1 - \exp\left[-V\left(\frac{\sigma - \sigma'}{\sigma''}\right)^m\right] \quad (3)$$

(from Harris (1998)) where V is the volume of stressed material, σ is the applied stress, σ' is the stress at which there is zero probability of failure, σ'' is a normalising factor, and m is the Weibull flaw density parameter.

The distribution reflects the nature of the material, and with glass is dependent upon the interaction between the tensile stress and the microscopic surface flaws. The Weibull flaw density parameter, m , is related to the coefficient of variation (the ratio of standard deviation to mean failure stress), and would be preferably high, because a high figure would produce a low scatter for test results, a lower safety factor for practical usage and would require fewer test results to identify a satisfactory figure. For glass fibres, m has been quoted as varying between 5 and 10. For steel this figure would be nearer to 60. Norville et al (1991) indicate that for weathered glass samples tested at Glass Research Testing Laboratory at Texas University, values of m were estimated to be between 4.0 and 6.0, but they also state that the ASTM Task Group E06-51.13 has agreed that the value for m for new window glass lights should be 7.

However, the value of m used by Norville et al (1991) for their investigations of thermally tempered window glass was 3.0.

Using appropriate values for equation 6.3 for the volume of the test pieces, and the stress levels discussed in chapter three, a theoretical graph of applied stress versus the probability of failure can be drawn, (figure 132). This graph illustrates the nature of the theoretical Weibull distribution for glass, and more specifically the glass test pieces currently under consideration.

To establish the Weibull cumulative probability of failure for the experimental data, illustrated in figure 133, the range of the combined stress values (impact stress plus bending stress) was divided up into 20 intervals. Next, the number of times a failure occurred in each stress range was noted. The frequency of failure was used to determine the likelihood of failure, which was then normalised with respect to the total number of failures. The cumulative probability of failure was then calculated by summing the appropriate values.

It should be noted that the shape of the graph in figure 133 is influenced by the stress combination factor, f , and the Weibull flaw density parameter, m , the nature of this variation is discussed below.

By rearranging equation (3), to give

$$\ln(-\ln(1-P)) = m \ln \left(V \left(\frac{\sigma - \sigma'}{\sigma''} \right) \right) \quad (4)$$

it is possible to obtain values for m by plotting

$$\ln(-\ln(1-P)) \text{ versus } \ln \left(V \left(\frac{\sigma - \sigma'}{\sigma''} \right) \right)$$

Using these axes, the graph of the experimental results (with a value for the stress combination factor of 0.75), was plotted, and the slope of the graph was calculated, which was equivalent to the value for the Weibull flaw density parameter, m . The slope of the graph, and hence the value for m was calculated to be 3.456. Figures 134 to 138 show the differences between the experimental results and a range of theoretical results, varying the theoretical flaw density parameter between 2.0 and 7.0.

Figures 139 to 144 are a similar set of graphs, but the theoretical Weibull flaw density parameter was fixed at 3.456, whilst the experimental stress combination factor was varied between 0.4 and 1.0. The best fit between the graph of the experimental results and the graph of the theoretical calculation appears to be with a stress combination factor of 0.75, and a flaw density parameter of 3.456.

The figure for the flaw density parameter, or Weibull modulus is lower than figures identified by previous studies, Norville et al (1991), but this may be caused by the combination of loading conditions, the impact and the bending. The figure for the Weibull modulus is often obtained using a distributed, or pressure loading methodology, not a dynamic point load such as an impact. A pressure loading approach may be more consistent, and hence result in higher values for the Weibull modulus, which would imply a reduced experimental scatter.

Figure 145 illustrates the way that the flaw density parameter, m , changes with the variation of the stress combination factor, f . Using Student's t-distribution the 95 % confidence intervals were also shown on the graph. Figure 145 appears to indicate that for values for f of 0.5 and above, m is not related to f , but that for values of f below 0.5, m reduces as f reduces.

6.6 Stress intensity factor

Scholze (1990) discusses the response of a material to the stresses generated around the tip of a crack, and defines the stress intensity factor K as a measure of the intensification of the applied stress due to the presence of a crack. K is normally determined using;

$$K = \sigma\sqrt{\pi a} \quad (5)$$

where a the crack length, and σ is the applied stress, with units of MPa m^{1/2} for K .

Figure 146 is a graph which illustrates the frequency of a number of values of K , derived from the total stress, with a value of the stress combination factor of 1, and a value for the crack depth of 5×10^{-6} , m, which was the value indicated by Griffith (1921) for fibres. The figures 147 to 150 illustrate the same relationship, but with varying values for the stress combination factor, f .

Figures 151 to 155 are similar to the graphs described above, but a value of 30×10^{-6} m, which has been used for bottle and bulk glass previously, Frechette (1990), and is considered more appropriate for this application, has been used for the crack length.

The critical stress intensity factor K_c is the value for K at which a crack occurs. Since the values for K discussed above are calculated once the glass test piece has failed, all the values for K obtained are effectively the critical values.

A Gaussian curve was fitted to each of the distributions plotted in figures 151 to 155, and the arithmetic mean of the values for critical stress intensity factor calculated. The table below lists the figures and the values for the correlation coefficient for the Gaussian fit, and for the mean K . It can be seen that the fit is best for the stress combination factor of 0.7, and that the correlation coefficient is high. For this graph, the value for K occurring at the peak of the Gaussian curve is between 0.4 and 0.5. with a value for the arithmetic mean of 0.46. Ashby and Jones (1996) quote a range of

0.7-0.8 for K . Substituting a value of $0.45 \text{ MPa m}^{1/2}$ for K into equation (5) gives a critical stress value of 47.4 MPa.

Figure	f	mean value of $K \text{ MPa m}^{1/2}$	r
151	1	0.55	0.94
152	0.8	0.49	0.95
153	0.7	0.46	0.97
154	0.5	0.40	0.91
155	0.3	0.35	0.77

Table 6.5 Variation of the correlation coefficient, r , mean value of K with stress combination factor, f , in figures 151 to 155.

The approach above assumes that the value for the crack dimension used is accurate and representative of the majority of cases. However, if the range of values for K used by Ashby and Jones (1996) is applicable for dynamic loading, and is a material constant which does not vary, then equation (5) can be used to determine the corresponding range of crack lengths. Using the mean value for the failure stress of 53MPa, (with a stress combination value of 0.7), gives a range for the crack length of between 55 and $72 \times 10^{-6} \text{ m}$.

6.7 Strain rate dependency

In section 6.3.2 the relationship between the deflection at failure (d) and the velocity at failure divided by the deflection at failure (v/d), is discussed. It was suggested that (v/d) was indicative of strain rate, and that the results appeared to indicate that at high strain rates, the failure bending stress was low, and vice versa.

In section 6.3.4, the relationship between velocity and (v/d) was considered, and again, if (v/d) can be considered to be representative of strain rate then the results appeared to indicate that at high strain rates, the samples failed at high impact stresses, and at low strain rates, the samples failed at lower impact stresses.

Oliver (1975) indicated that as the duration of the load decreased, the stress at which the glass failed increased, or in other words, as the strain rate increased, the stress at which the glass failed increased. Thus, the relationship between the velocity (or impact stress) and the strain rate, discussed above, appears to be consistent with Oliver (1975), but the relationship between deflection (or bending stress) and Oliver (1975) does not appear to be consistent.

Dalgliesh and Taylor (1989) described the duration or rate effect of glass failure using the equation

$$\ln(s_f) = C_1 - (1/n)\ln(t_f) \quad (6)$$

where C_1 is a constant, s_f is the failure stress, t_f is the time to failure, and n is a fitting parameter that is often 16 or 17 for large panel tests.

The loading duration that Dalgliesh and Taylor (1989) used for their tests on 107 panes of new glass was 60 seconds, or normalised to equivalent 60 second pressures. Dalgliesh and Taylor assumed that under constant pressure the stresses are constant and produced a graph effectively showing $\ln(s_f)$ versus $\ln(t_f)$ to determine the values of C_1 and n . Using this approach Dalgliesh and Taylor fitted a straight line to their data,

the slope of which was -0.067, giving a value for the fitting parameter, n , of 14.9. Dalglish and Taylor indicated that the negative slope of the graph showed that the strength of the glass plates decreased as the loading rate decreased, i.e., as the load duration increased.

Figure 156 is a graph illustrating the relationship between the load duration, (as indicated by dividing the deflection at failure by the velocity at failure) and the total combined stress (with a stress combination factor of 1.0). The data appear quite widely scattered. The slope of the linear regression line is slightly positive but the correlation coefficient is very low, indicating a weak, or statistically insignificant, relationship between the two variables. However, as the stress combination factor reduces, the correlation coefficient increases, rising to 0.69 when the stress combination factor is 0.2, as illustrated in the table below.

f	slope	fitting parameter	r
1	0.023	43.4	0.098
0.8	-0.019	52.6	0.08
0.7	-0.04	22.8	0.18
0.6	-0.071	14.08	0.29
0.4	-0.141	7.1	0.51
0.2	-0.24	4.17	0.69

Table 6.6 Comparison of the fitting parameter, n and the correlation coefficient, r with varying values of the stress combination factor, f .

Table 6.6 indicates that a stress combination factor of 0.6 produces a figure for the fitting parameter that is very close to that obtained by Dalglish and Taylor, but that the statistical significance is weak. Table 6.6 also indicates that for values of the stress combination factor of less than one, a negative slope is produced, thus indicating that the strength of the glass samples decreased as the loading rate decreased, which is consistent with the findings of Oliver (1975) and Ruiz (1989) discussed above.

6.8 The Influence of the stress history

Some materials, such as steel and aluminium, fail under fluctuating load at a level lower than their normal static failure stress. The response of materials to fluctuating stress is often illustrated using S-N graphs, which plot the number of cycles to failure, N , versus the failure stress, S . An S-N graph is a description of the idealised case, Megson (1990) discusses the use of a linear cumulative damage law to establish a practicable fatigue failure prediction relationship. This approach reflects the practical situation where the fatigue failure of a component is caused by many different stress amplitude cycles. The appropriate S-N graph can be obtained by testing a large number of small specimens.

Figure 37 illustrates the relationship between the deflection at failure, and the total number of impacts experienced by a test piece before failure. There does not appear to be a significant relationship between the total number of impacts and the deflection recorded at failure. Figure 61 does appear to illustrate a meaningful relationship, but, as discussed above, this is considered to be a natural result of the experimental process. An alternative approach is to consider the number of failures at specific impact velocities and deflections. Figures 39 to 58 show the relationship between the number of failures and the pre-set deflection at impact, whilst the velocity remains constant, the first figure in each set (i.e. 39, 41, 43, etc.) shows the distribution of the failures, whilst the second figure (i.e. 40, 42, 44, etc.) shows the cumulative result. There does not appear to be any strong relationship that can be deduced from the figures. In addition, the sample size is small and may not be statistically valid. Similarly, figures 62 to 77 are graphs illustrating the relationship between the number of failures and the velocity at impact, whilst keeping the pre-set deflection constant. There does not appear to be any strong relationship illustrated by the latter graphs either, which would seem to indicate that a stress history of the kind experienced by test pieces during the experimentation described is not significant.

It is conceivable that the surface micro-cracks that form on the surface of silica glass could grow when the material is subjected to a repeated loading cycle, and consequently could exhibit some form of fatigue failure. The nature of the experimental

process used for this work caused an incrementally increasing load to be applied to the test pieces, and then removed. If the test piece did not fail during a series of ten repeated impacts at the same velocity and deflection, then the velocity of impact was increased and another set of impact tests conducted. Thus, the test pieces were subjected to what was effectively a cyclic loading of low frequency. The total number of impacts for each test piece may be analogous to a fatigue characteristic in glass, in that the stress required to cause failure after a test piece has suffered a large number of impacts would be comparatively lower if some form of fatigue phenomenon was occurring. No suggestion that silica glass is vulnerable to fatigue failure has been identified, so a linear cumulative damage law approach, such as Miner's Rule, Ashby and Jones (1996), is unlikely to be appropriate. Paul (1990) discusses both static and dynamic fatigue, but in the context of variation in loading rate, as opposed to the material response to cyclic loading. Consequently, it is assumed that the failure of the glass test pieces is determined by the stress level alone, and that the history of the impacts to failure is irrelevant.

Chapter 7

7 Conclusions and Recommendations for future work

- 7.1 Test Rig And Testing Process.**
- 7.2 Weibull Analysis**
- 7.3 Stress Intensity Factor**
- 7.4 Strain Rate Dependency**
- 7.5 The Influence Of Relative Humidity**
- 7.6 The Influence Of Temperature**
- 7.7 The influence of lamination and PVB**
- 7.8 The Nature Of The Stress Combination Factor f**
- 7.9 Future Work**

7 Conclusions and Recommendations for future work

7.1 Test Rig And Testing Process.

As part of this project an hydraulic test rig was designed and constructed which simulated the early impact phase of an attack upon a laminated glass panel by an assailant. The test rig was used to obtain a set of measurements of deflection and velocity at which the 420mm by 420mm, 6.4mm thick, glass laminate samples failed. Concurrent to the deflection and velocity measurements, relative humidity and temperature measurements have also been taken.

In the early stages of this work the testing procedure was to randomly select a pre-set deflection and an impact velocity and then to conduct the test and note the result. In the latter, and main part of the project, the pre-set deflection and velocity were incrementally increased from a low starting point, with repeated impacts at the same level, until failure occurred.

7.2 Weibull Analysis

The strength of a glass panel subjected to an impact is largely determined by the number and severity of the flaws on its surface. When comparative tests are made on a number of nominally identical samples there is normally a considerable spread in the results, the coefficient of variation (the standard deviation divided by the mean) is often fifteen percent or more. Weibull showed how the features of the strength of brittle materials, in this case glass, could be predicted quantitatively, once a function was specified which describes the flaw distribution on the surface of the material. The Weibull cumulative distribution function is crucial to the correct prediction of material response, and is obtained using experimental results. The cumulative distribution function relates the probability of failure to the strength. The Weibull modulus, or flaw density parameter, is a dimensionless shape parameter which is determined by measuring the slope of the cumulative distribution graph after the natural logarithm of the original expression has been taken twice. The Weibull cumulative distribution function may be regarded as a skewed Gaussian distribution, with a skewness determined by the value of the Weibull modulus. The loading

conditions for the impact tests discussed in this work meant that the stress normally used for a cumulative distribution function was a combined stress, with an element of bending stress and an element of impact stress. Values used by others for the Weibull modulus were identified as normally being between four and seven for flat panels, and between five and ten for glass fibres. The best fit for the data generated during this work gave a statistically significant figure of 3.456 for the Weibull modulus. It is considered that this relatively low figure reflects the variation in results caused by the combined impact and deflection stresses, and the point loading, compared with the quasi-static, uniformly distributed loading that has often been used to establish the Weibull modulus of between four and seven.

7.3 Stress Intensity Factor

The stress intensity factor, K , or fracture toughness value, is an indication of the toughness of a material. Glass is a brittle material, so it would be expected to have a low fracture toughness. Using a value for a surface crack length of 30×10^{-6} m, the stress intensity factor was calculated from the experimental results using different critical stress values (determined by varying the stress combination factor) and subsequently plotted. The best fit for a Gaussian distribution was for a value of the stress combination factor of 0.7, with a value for the arithmetic mean of the stress intensity factor of $0.46 \text{ MPa}^{1/2}$. This figure is lower than the $0.7\text{-}0.8 \text{ MPa}^{1/2}$ determined by others quoted in chapter 6. However, if the range of values for K used by Ashby and Jones (1996) is an appropriate material characteristic, then using a mean value for the failure stress of 53 MPa , gives a range for the crack length of between 55 and 72×10^{-6} m.

The stress intensity factor is a measure of the fracture toughness, and hence is a material characteristic which should not change, however, the stress intensity factor is normally determined using quasi-static loading and as Anderson (1995) states, the dynamic fracture toughness may be drastically different from the quasi-static case, because the reflecting stress waves influence the local crack tip stress and the strain fields. This project has focussed upon point impact loads, and since the combined

impact and bending stresses have been used to generate the stress intensity factor this may result in a difference between that derived, and figures quoted by other workers.

7.4 Strain Rate Dependency

The level of stress at which glass fails is dependent upon the rate at which the glass is loaded. This phenomenon is described as strain rate dependency and has been discussed in chapter 6. A value of 16 or 17 for a fitting parameter, n , which relates the failure stress with the time to failure has been identified in work on quasi-static, (normalised for sixty seconds) loading of large panels of glass. In this study a range of values for the fitting parameter between 4.17 and 43.4 was obtained, as the stress combination factor was varied, with a wide range of statistical certainty about these values. So it is considered that either the term used for the loading duration (the deflection at failure divided by the velocity at failure i.e. v/d) is not appropriate, or that the relationship utilised for strain rate dependency is not pertinent for impact loading.

7.5 The Influence Of Relative Humidity

Glass has been described as being vulnerable to a static fatigue condition because the micro-cracks present on the surface of the glass grow when subjected to a tensile load in the presence of water vapour, but the data obtained in this work did not appear to show any relationship between failure and relative humidity. The tests covered a range of relative humidity from 12 % to 50 %, thus it is possible that the influence of relative humidity is only discernible outside of this range, or that its significance was not apparent.

7.6 The Influence Of Temperature

Silica glass is a non-crystalline “glass”, and as such its properties will change as the temperature changes, however examination of the experimental data indicates that the temperature effects in the range of the experimentation, 15° C to 27° C, are not large enough to influence the experimental results.

7.7 The influence of lamination and PVB

The tests pieces used were constructed from laminated glass. The PVB interlayer between the two glass laminae can be considered as flexible and incompressible. During bending the glass laminate will act as a composite beam, which will be some way between the response of a layered beam (i.e. two beams on top of each other with no adhesive medium joining them) and a monolithic beam. During impact it is likely that the stress wave at the PVB interlayer will be partially reflected and partially transmitted. Unfortunately, it has not been possible to investigate the influence of the PVB in any great depth.

7.8 The Nature Of The Stress Combination Factor f

It was suggested in the discussion of the results that the dynamic loading of the glass plate can be divided into two distinct elements, the stress generated by the bending of the glass, and the stress generated by the impact. However, although the stresses can be described separately, they have a combined effect upon the glass, and consequently need to be superposed when considering the conditions for failure. Consideration of the relationship between impact velocity, the pre-set deflection and the total number of impacts to failure indicated that the impact stress was more significant than the bending stress so a less than unity multiplier, the stress combination factor, f , was applied to the bending stress.

When considering the Weibull distribution, it was established that altering the value of the stress combination factor affected the shape of the distribution, and the fit of the experimental data with the theoretical analysis. Using an iterative approach, a value for f of 0.75 was obtained that gave a good fit between the experimental and theoretical models. The correlation coefficient for the best fitting regression line was equal to 0.973, and was statistically valid, using Student's t-test at the 99% level.

Consideration was given to the relationship between the Weibull modulus or flaw density parameter, m , and the stress combination factor, f . It was established that for the experimental data, for values for f of 0.5 and above, m was not related to f , but that

for values of f below 0.5, m reduces as f reduces. Since the region of interest for the stress combination factor is greater than 0.5, this result is not considered to be significant.

The stress intensity factor K was determined using the quasi-static approach, and did not appear to be consistent with figures obtained by others, but, as discussed above, this deviation may be explained by the differences between the static and dynamic response of the material. The best fit for the data was obtained using a value for the stress combination factor of 0.7

As discussed above, the values obtained for the fitting parameter for the strain rate dependency relationship have dubious statistical validity, but a value of 0.6 for the stress combination factor produced a figure for the fitting parameter close to that obtained by others.

In conclusion, it is considered that there is sufficient evidence identified to justify the hypothesis that during low velocity impacts the stresses from the impact, and the stresses from the bending, combine to occasion a micro-crack to propagate and cause fracture, and that the combination of stresses can be described using a stress combination factor, f , whose value is between 0.7 and 0.8.

7.9 Future Work

During the course of this work there were two areas that were explored, but not pursued in any great depth, they were finite element analysis, and crack measurement. In the early part of the study some work was conducted to compare the experimental results with those achieved using a non-linear, dynamic finite element package (FEA Lusas). Unfortunately, at that time, the computer power available, both in terms of processor speed and storage, made the running of repeated, detailed, non-linear dynamic models unrealistic. Recent expansion in computational power has made the analysis of glass computationally feasible. Secondly, the material characteristics for the finite element modelling of PVB had not been fully developed, but recent developments in the modelling of visco-elastic materials should improve the analysis.

Some work was conducted using digital image processing to establish the position and length of all cracks on a failed sample in an attempt to establish if there was a relationship between the energy applied to the system by means of an impactor, and the energy dissipated in initiating and growing the crack pattern. The work was abandoned because no practicable way of automating the measurement of the crack length was identified.

In addition to the above, it is considered that one area of worthwhile investigation would be the very high speed filming of the first stage of the crack initiation and propagation. Such an investigation would shed more light on the interaction between the bending stress and the impact stress, and may identify at what time the applied stress exceeds the fracture stress for the sample.

Finally, although it was considered that the design of the test rig was reasonably representative of an idealised sledgehammer strike, work on improving the instrumentation used would provide a better picture of the loads and stresses generated during the impacts.

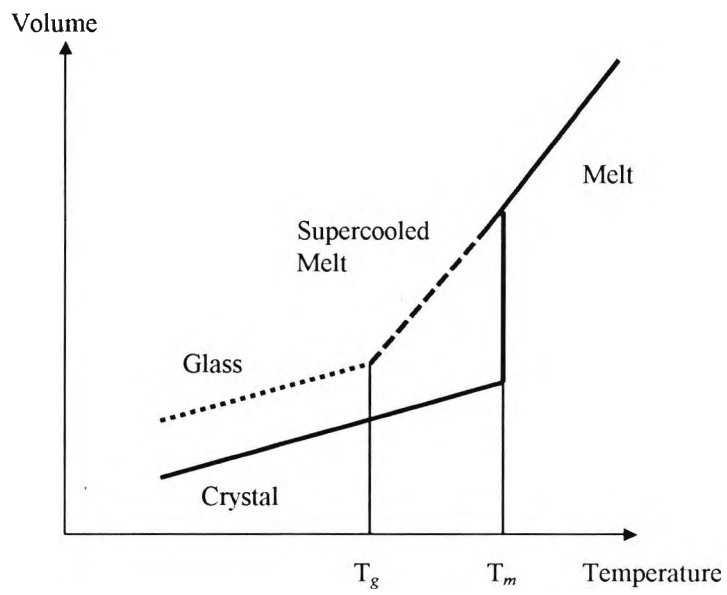
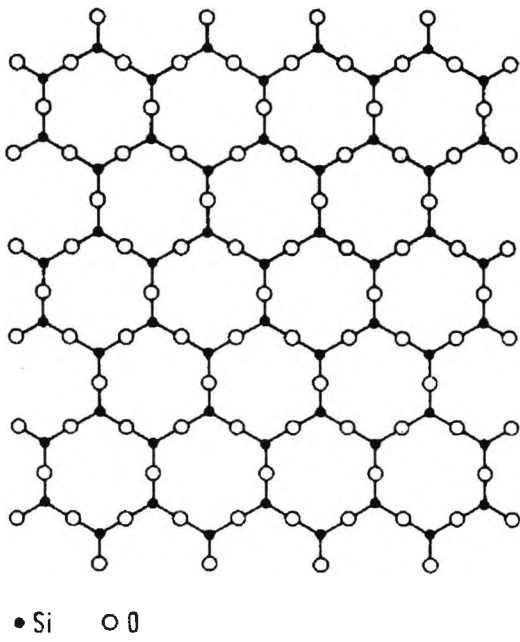
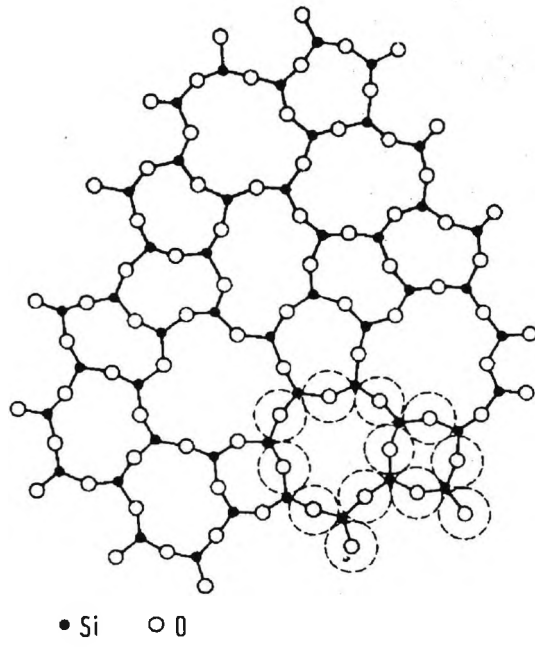


Figure 1 Schematic diagram of the temperature dependence of volume from Scholze (1990)



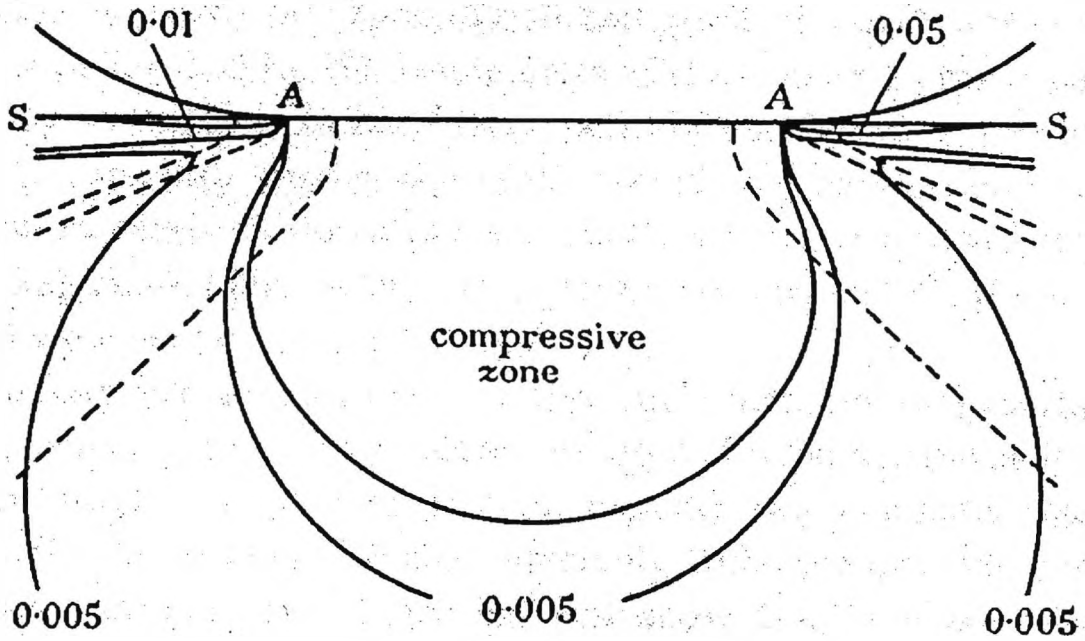
Two dimensional diagram
of an ordered SiO₂ network



Two Dimensional diagram of
a random SiO₂ network

From Scholze (1990)

Figure 2



Contours of greatest principal stress in a semi-infinite elastic media in contact with a spherical indenter. From Frank and Lawn (1967).

Note: The contour numbers relate to the unit of stress, the mean pressure acting between the indenter and specimen.

Figure 3

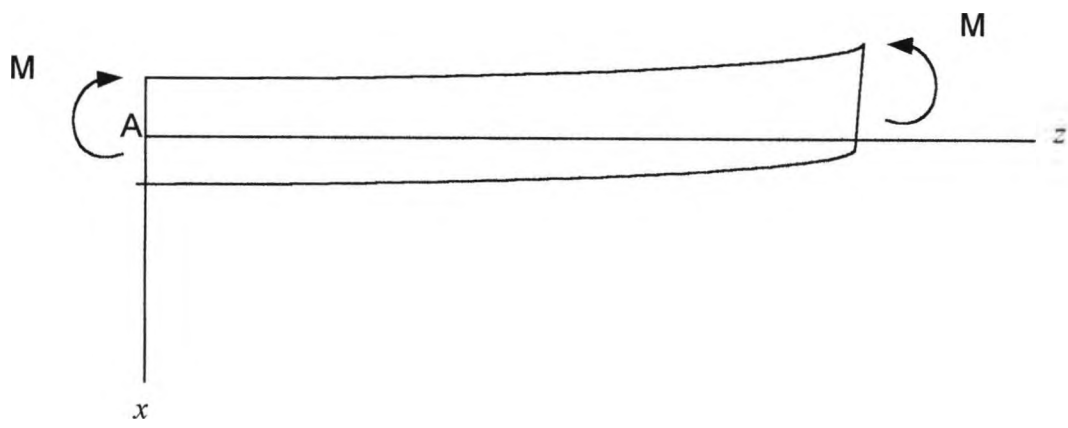


Figure 4

Deflection versus Stress for a built in beam

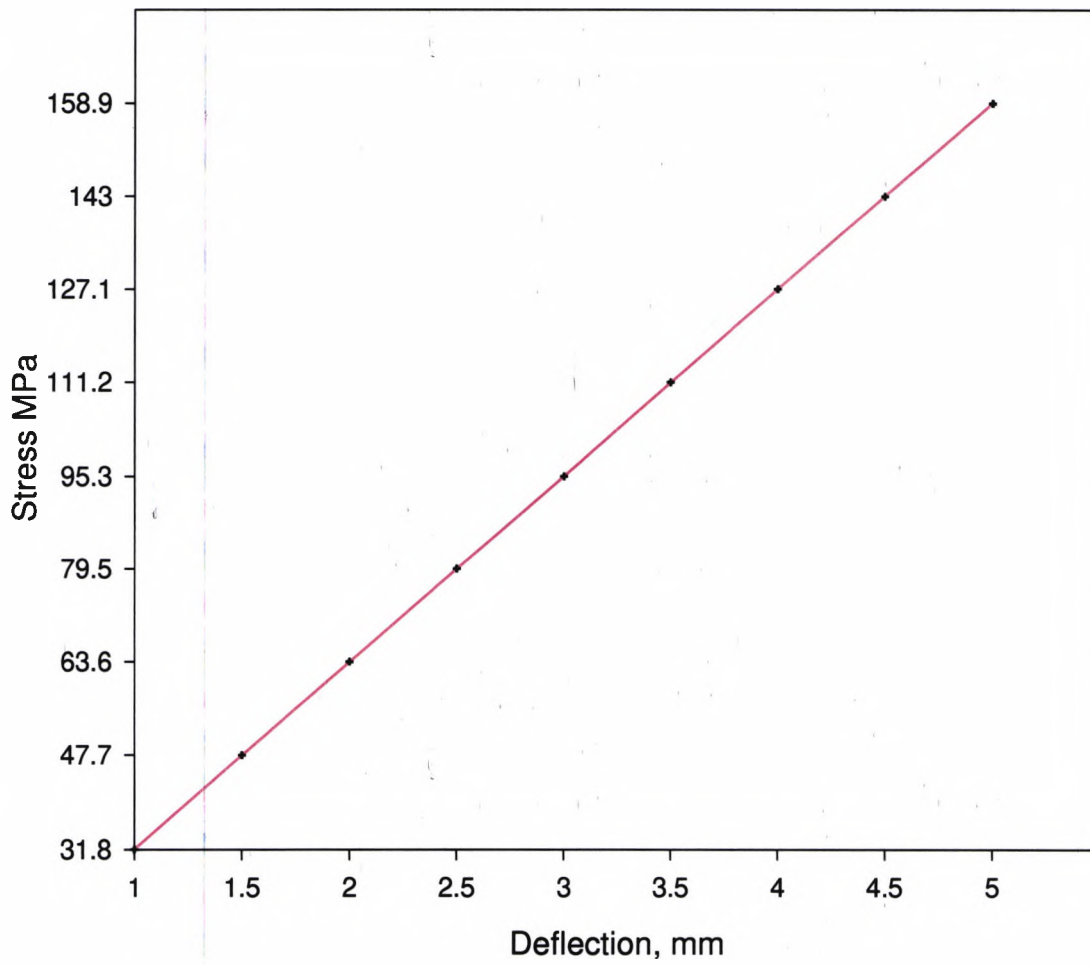


Figure 5

Deflection versus Stress for a simply supported beam

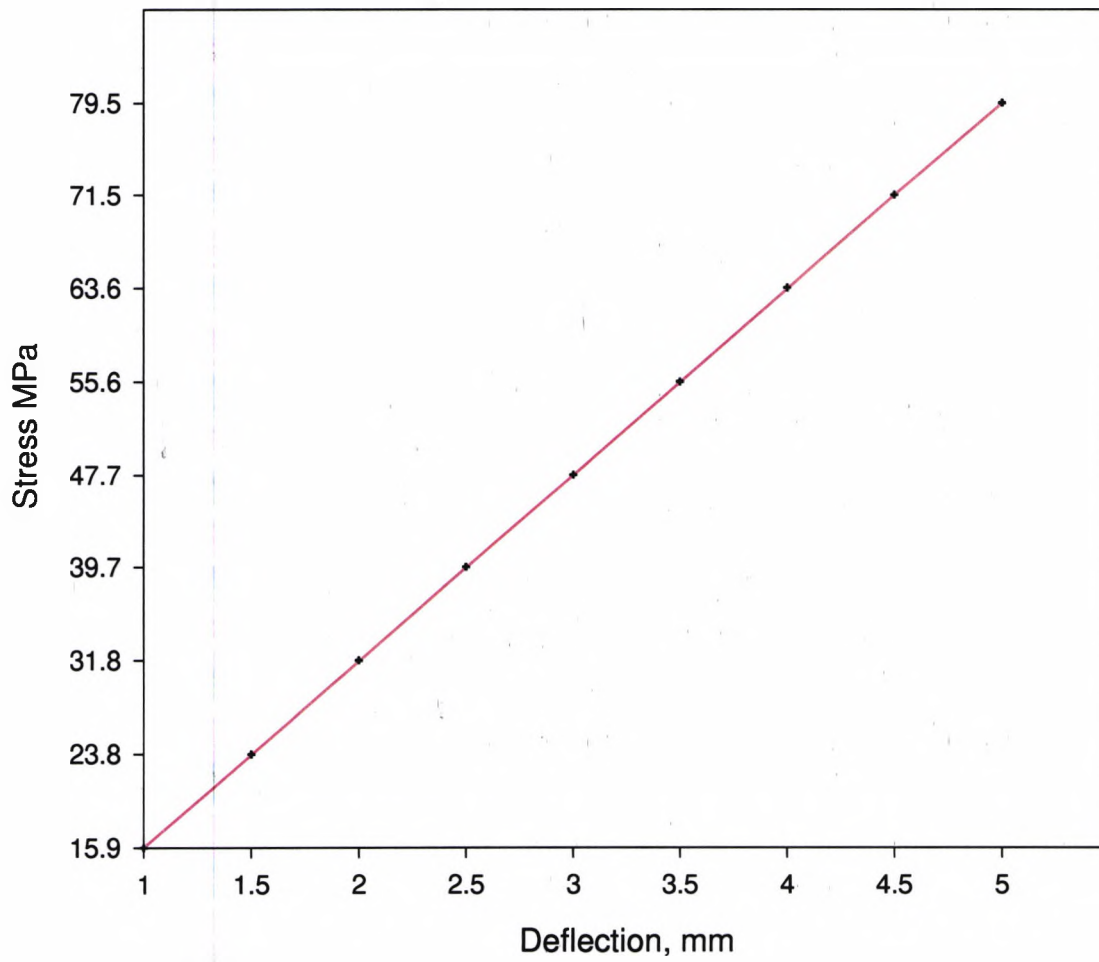


Figure 6

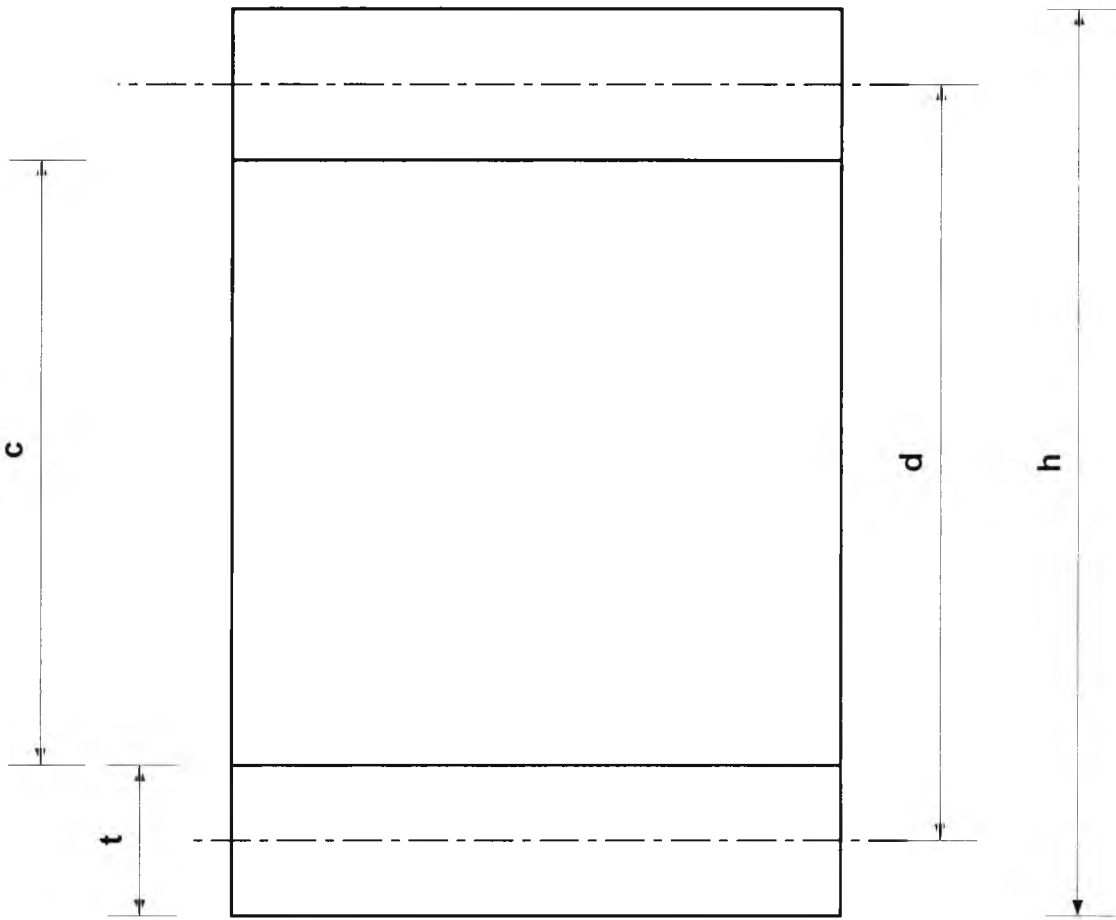
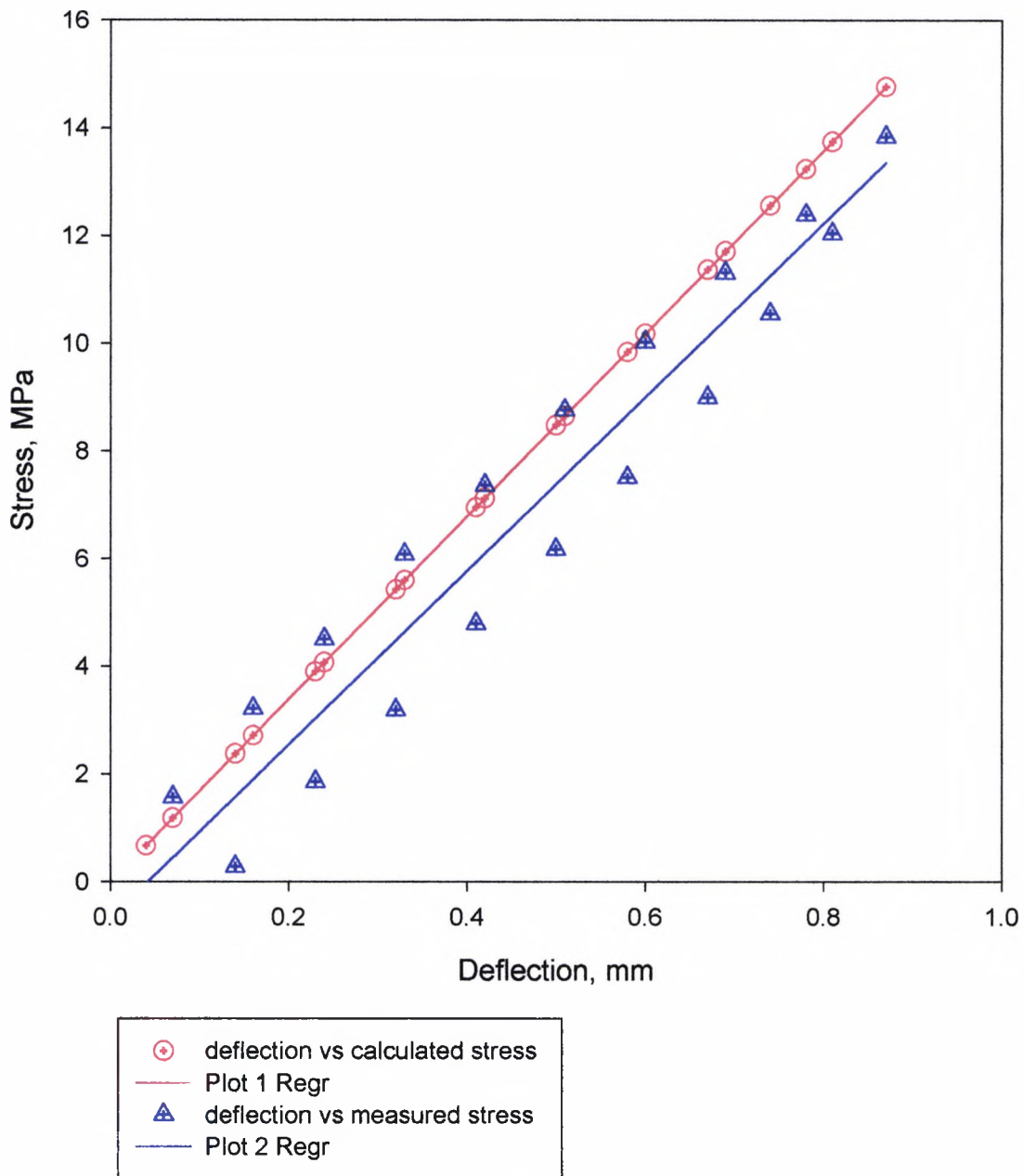


Figure 7 Dimensions of a section of a sandwich beam

Comparison between measured and calculated stress on sample loaded centrally.
Figure 8



Lagrangian Diagram

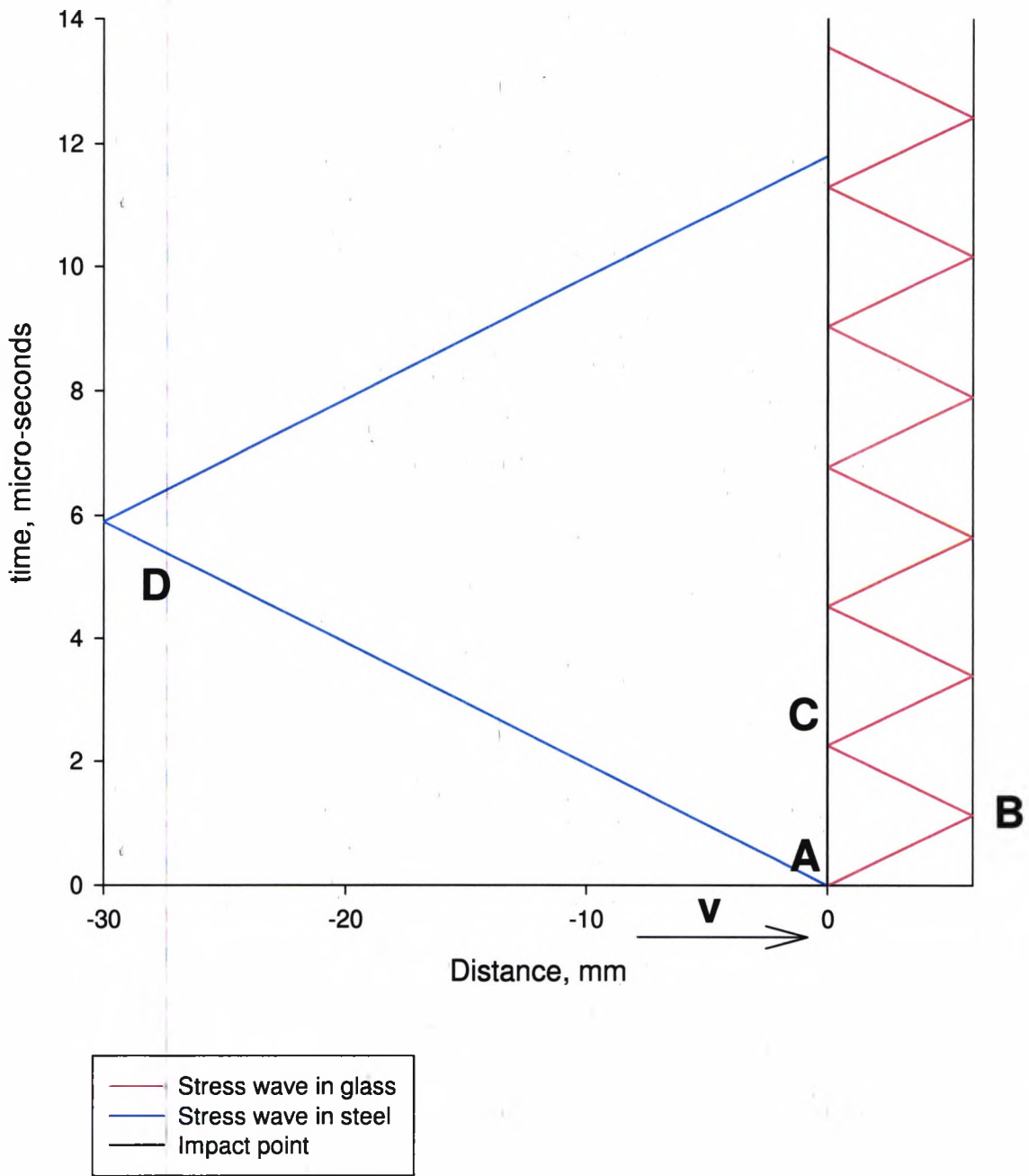


Figure 9

Langrangian Diagram
illustrating stresses and particle velocities

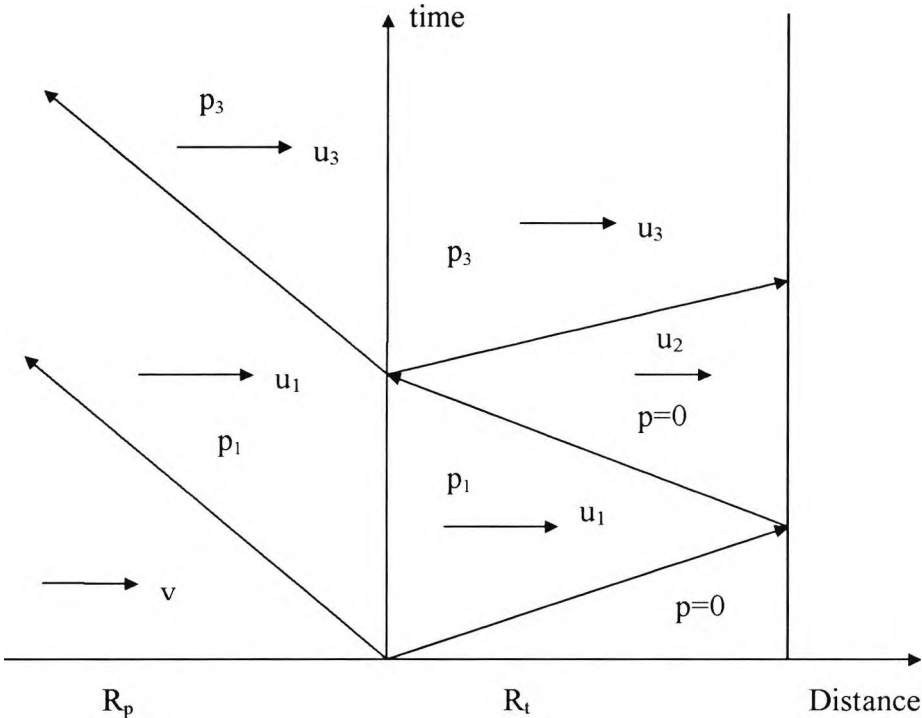


Figure 10

At Point of Impact

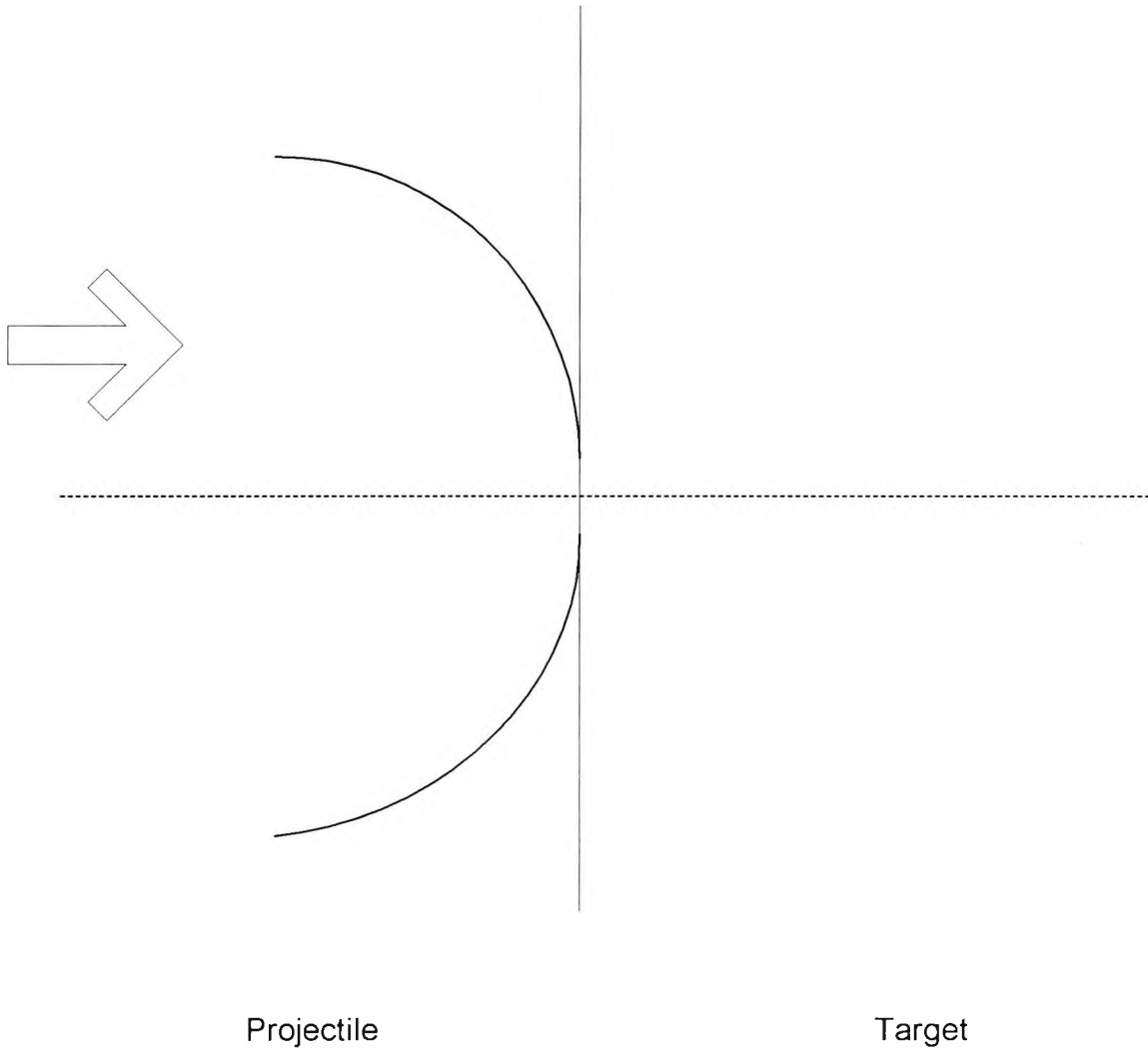


Figure 11

Stress waves start to
move into material,
and release waves start
at the edge of the contact area

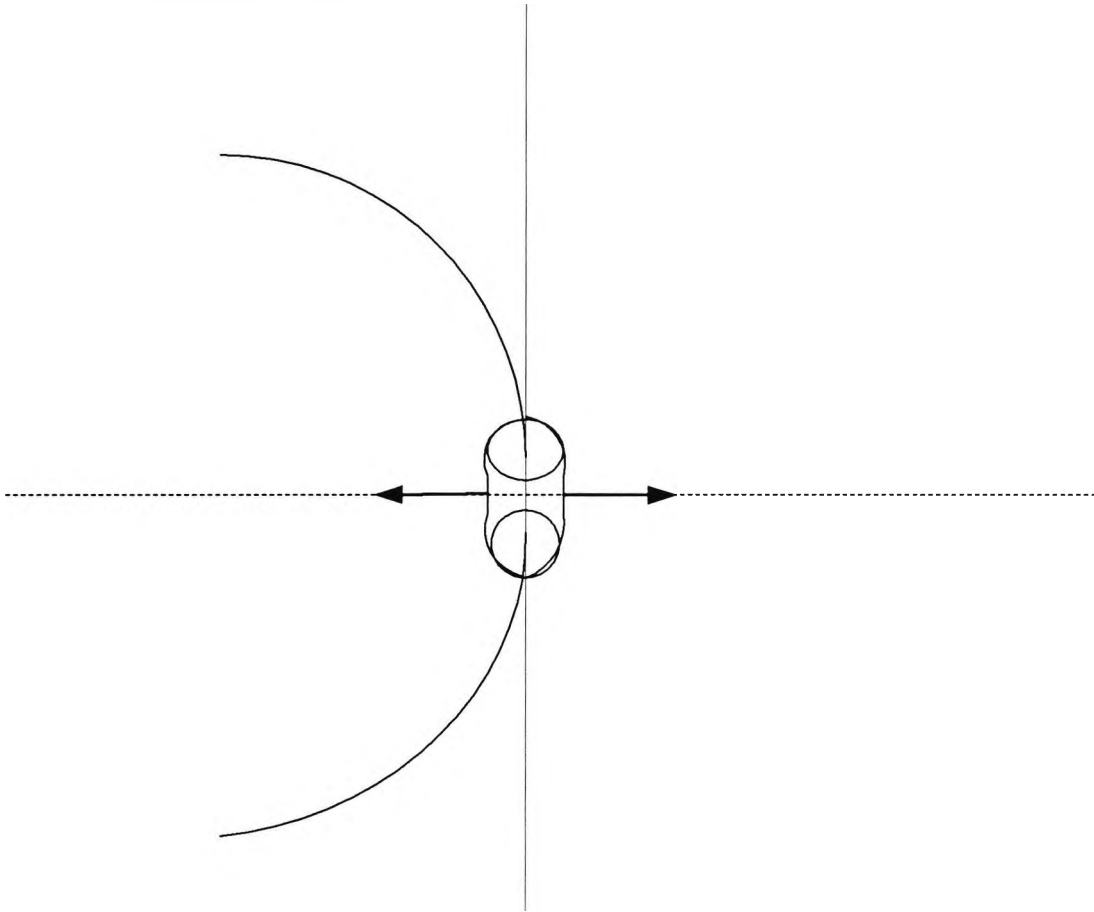


Figure 12

Release waves from
contact edge follow initial
waves

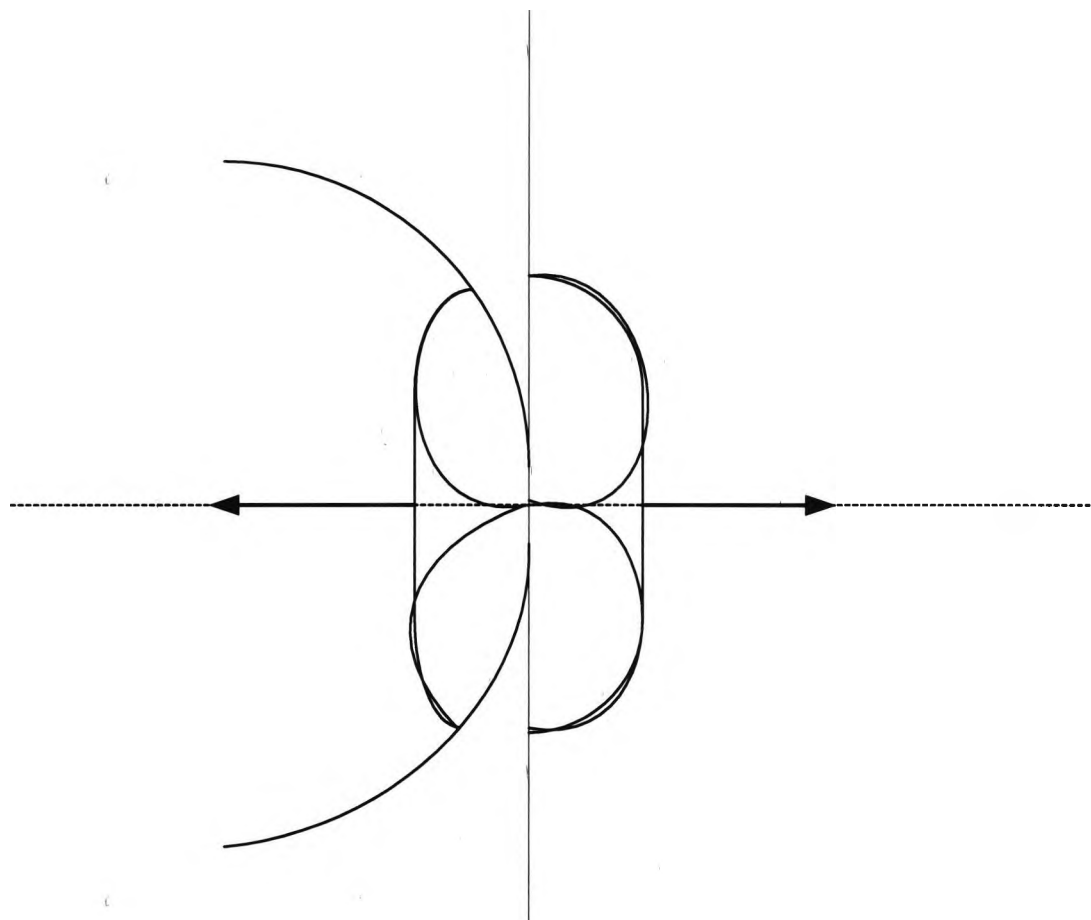


Figure 13

Release waves overlap

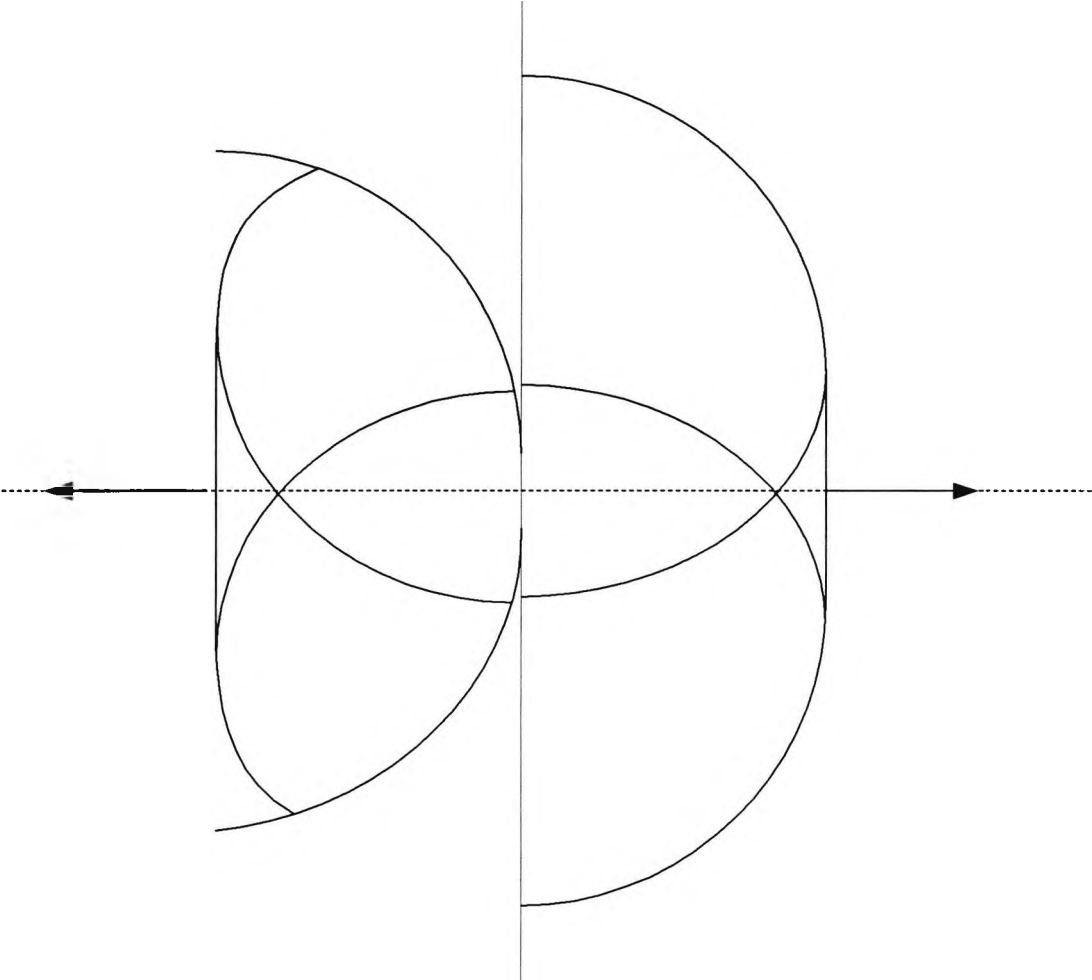


Figure 14

Illustration of an Idealised Impactor with the Minor Diameter
Corresponding to the Impact Contact Area

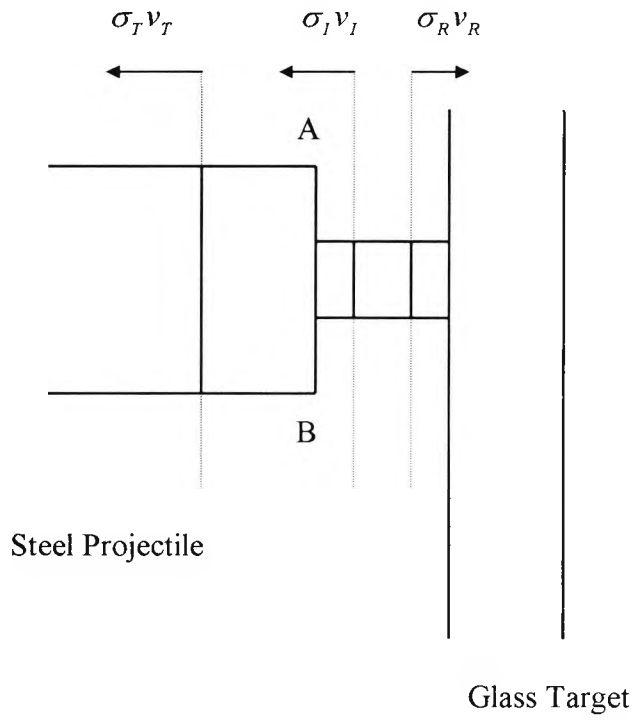


Figure 15

Langrangian Diagram
 illustrating stresses and particle velocities

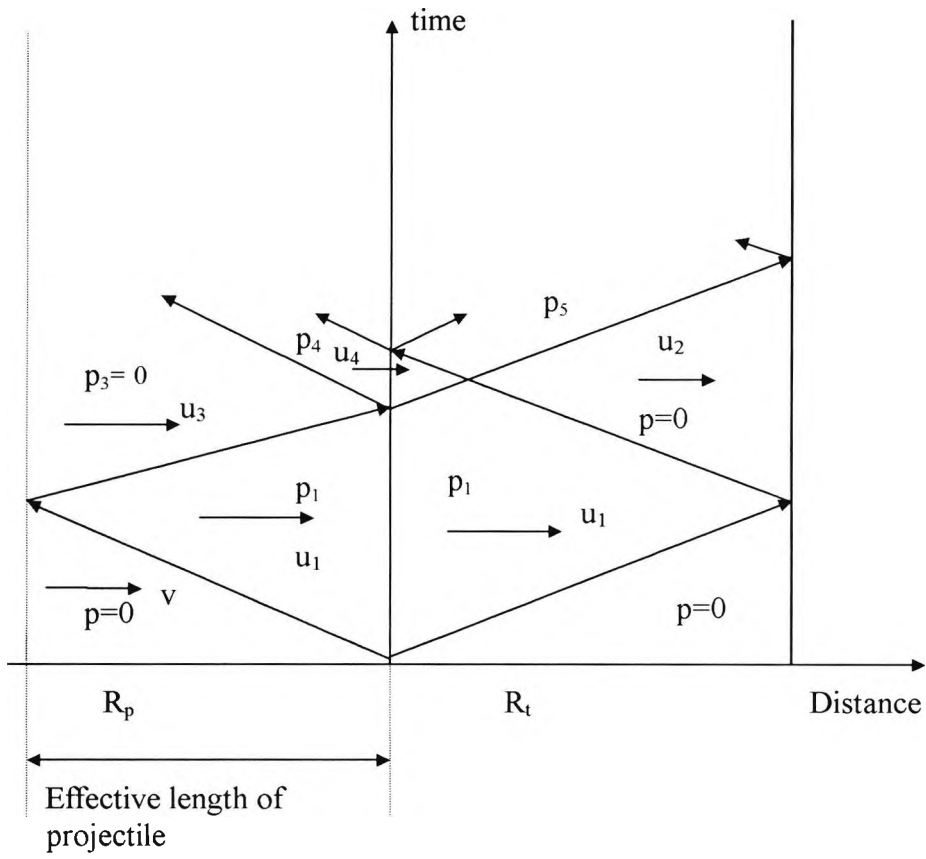


Figure 16

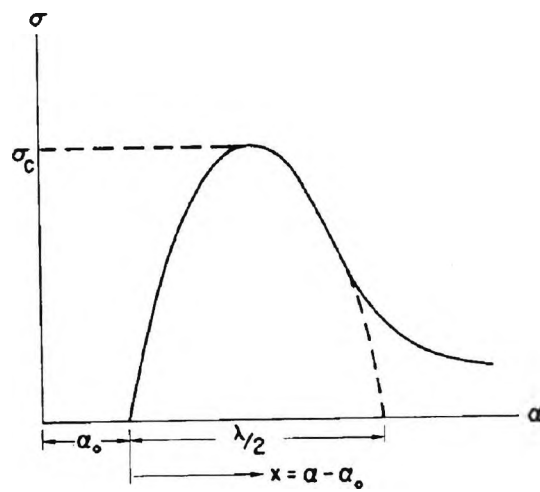


Figure 17 The stress required to separate atomic planes; a_0 is the equilibrium separation at zero stress. (From Uhlmann and Kreidl (1980))

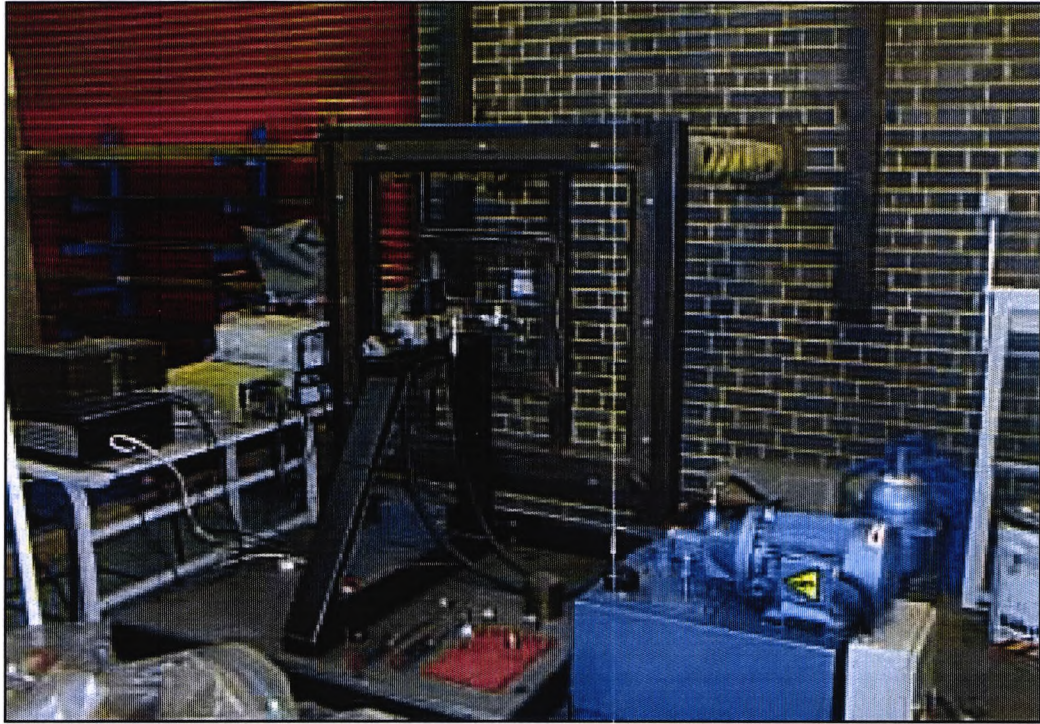


Figure 18

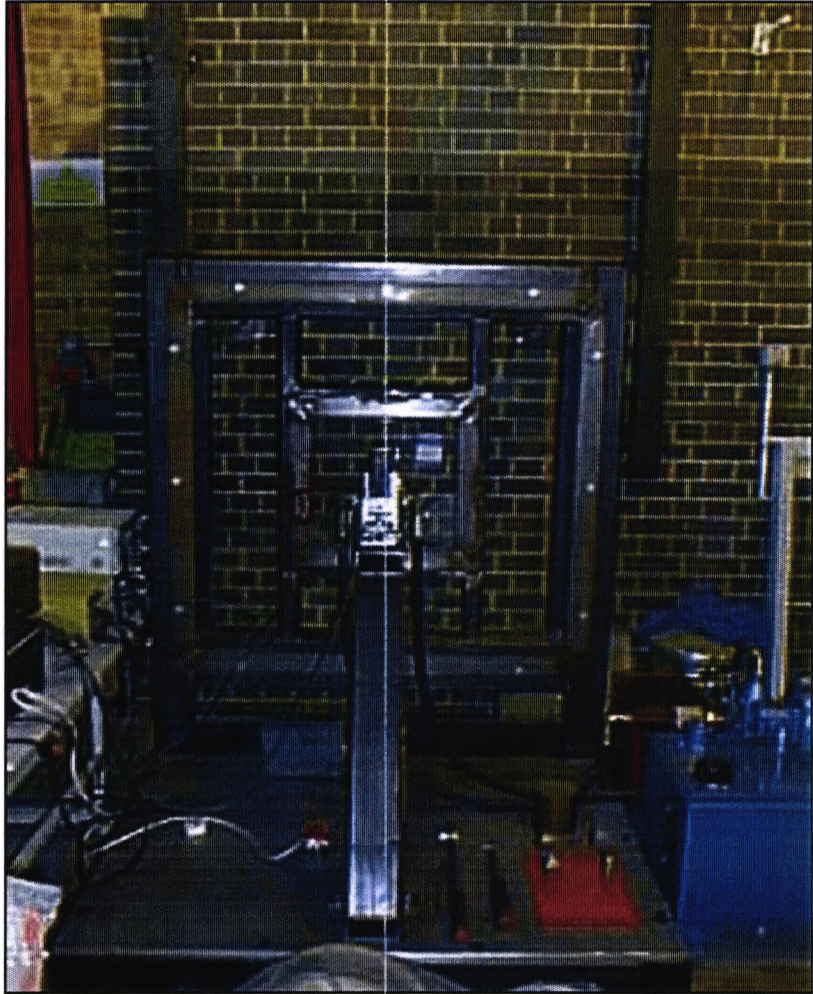


Figure 19

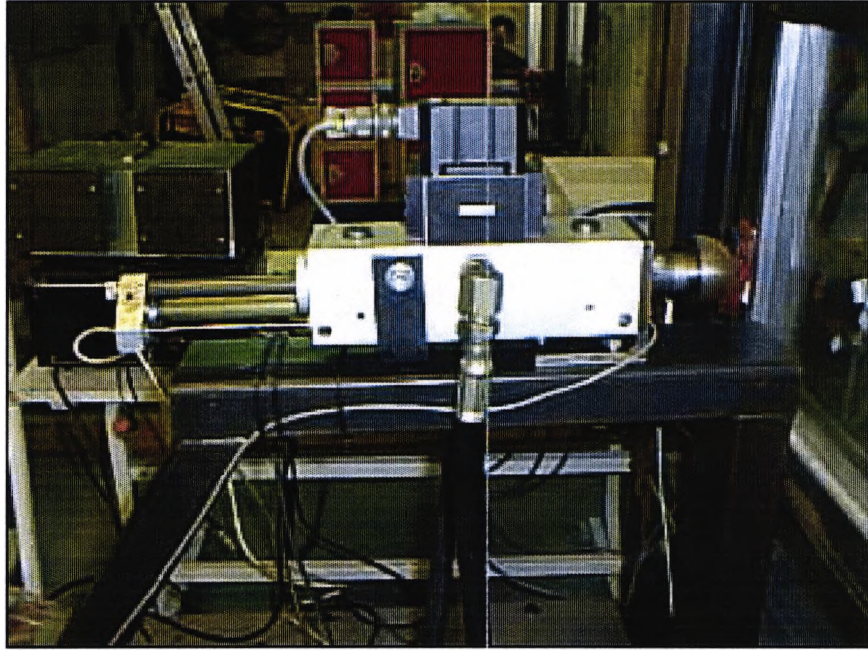


Figure 20

Schematic of Hydraulic Arrangements

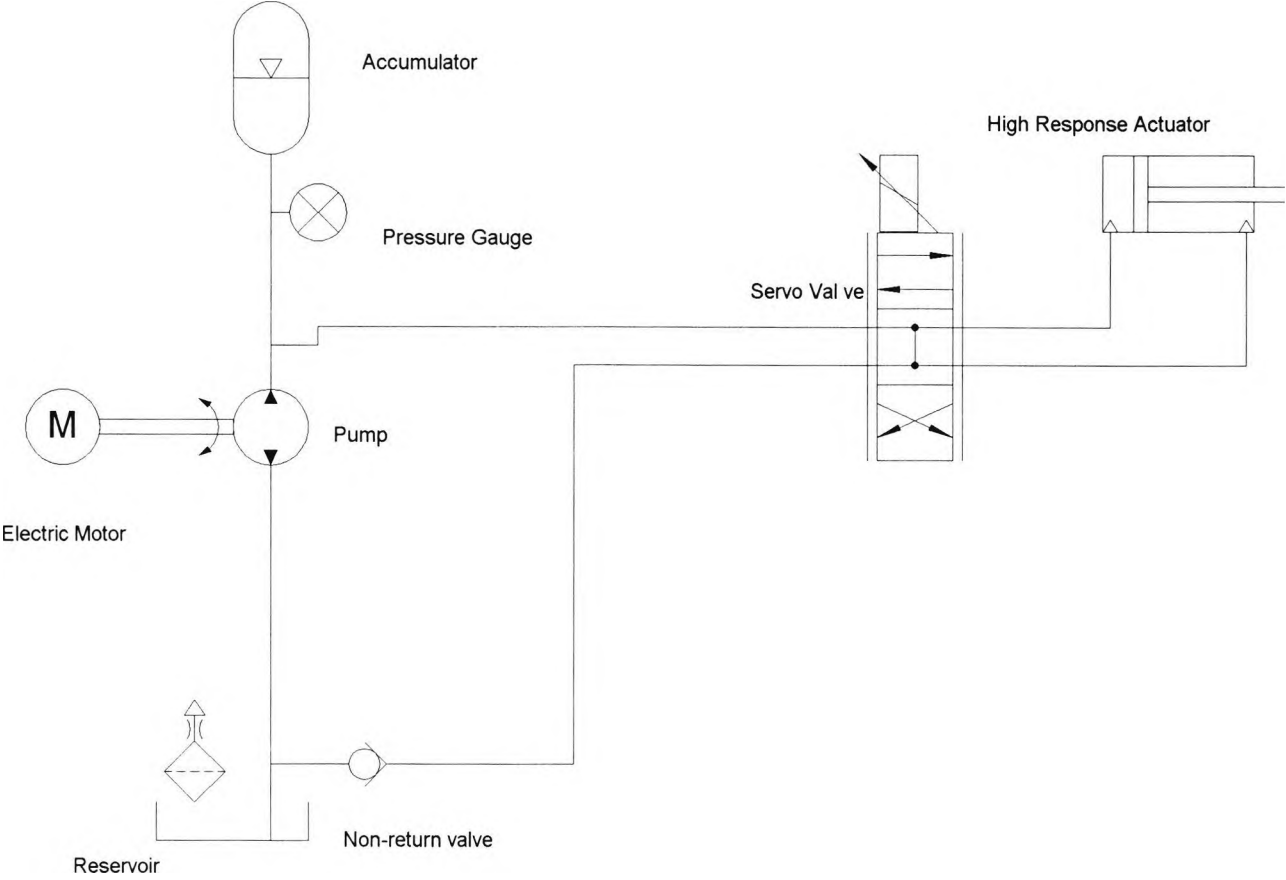


Figure 21

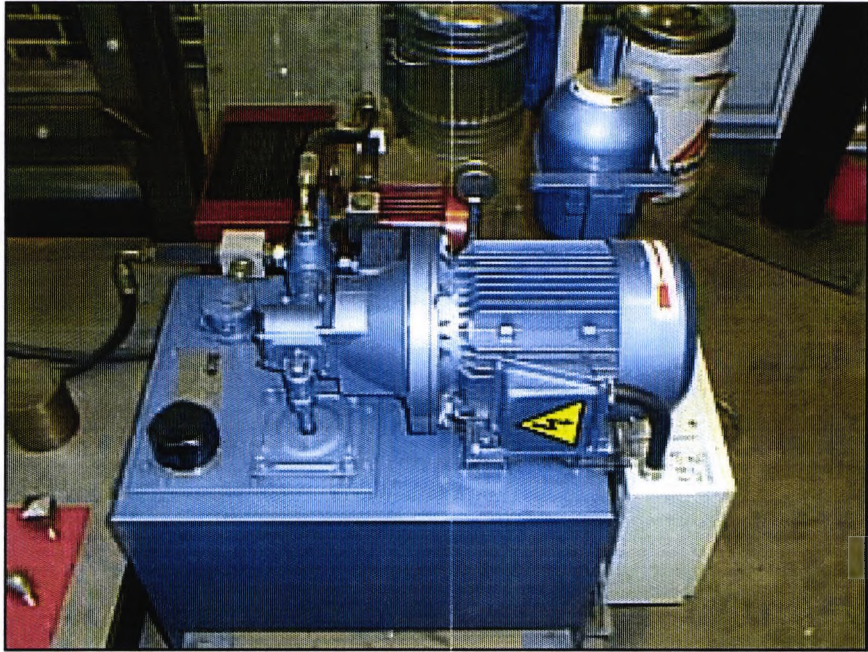


Figure 22

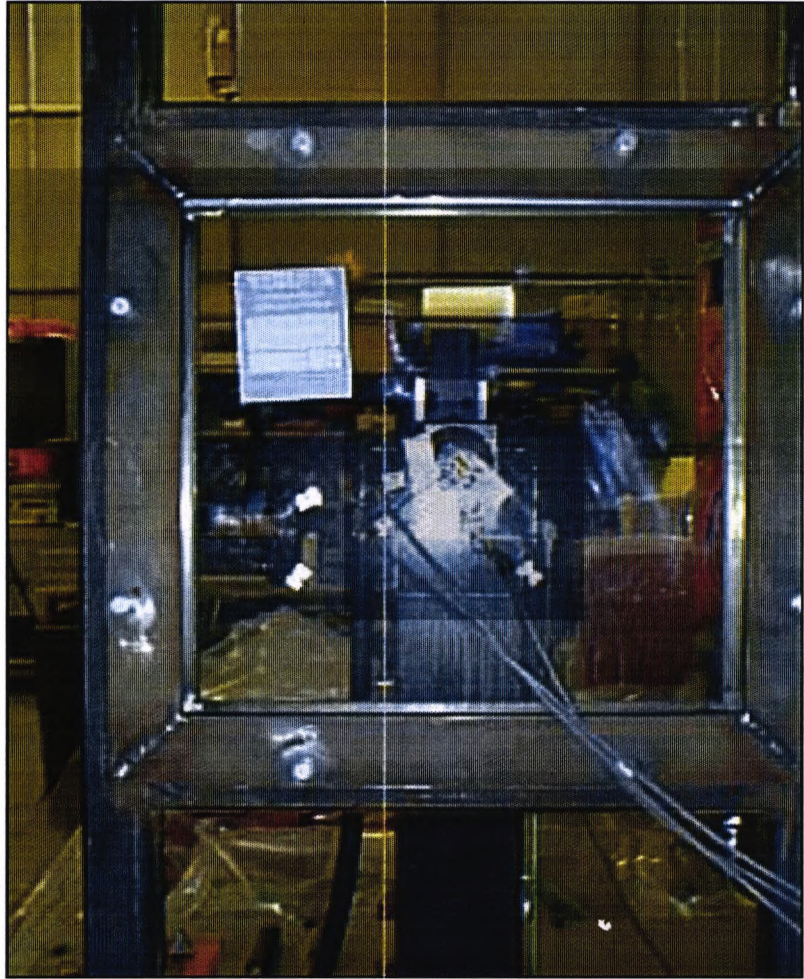


Figure 23

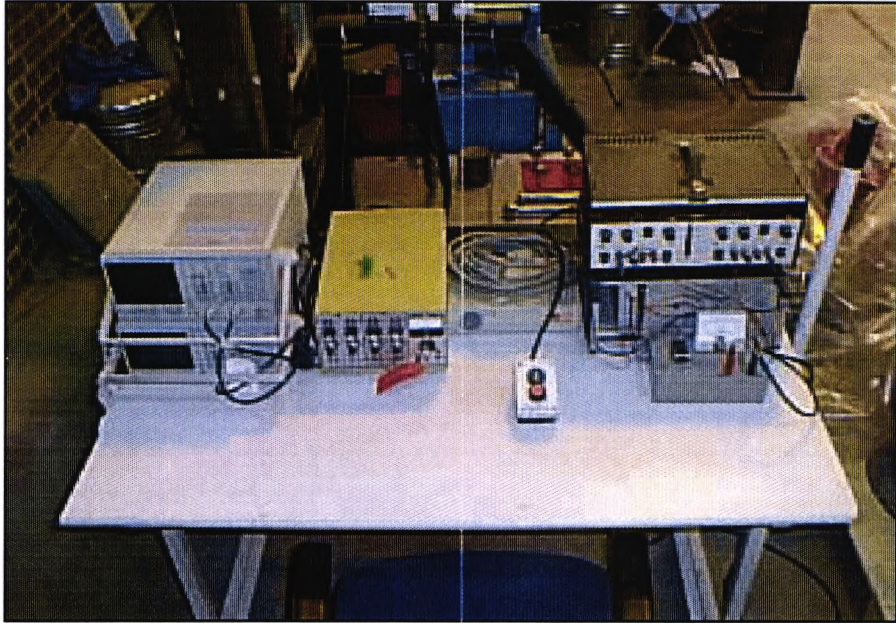
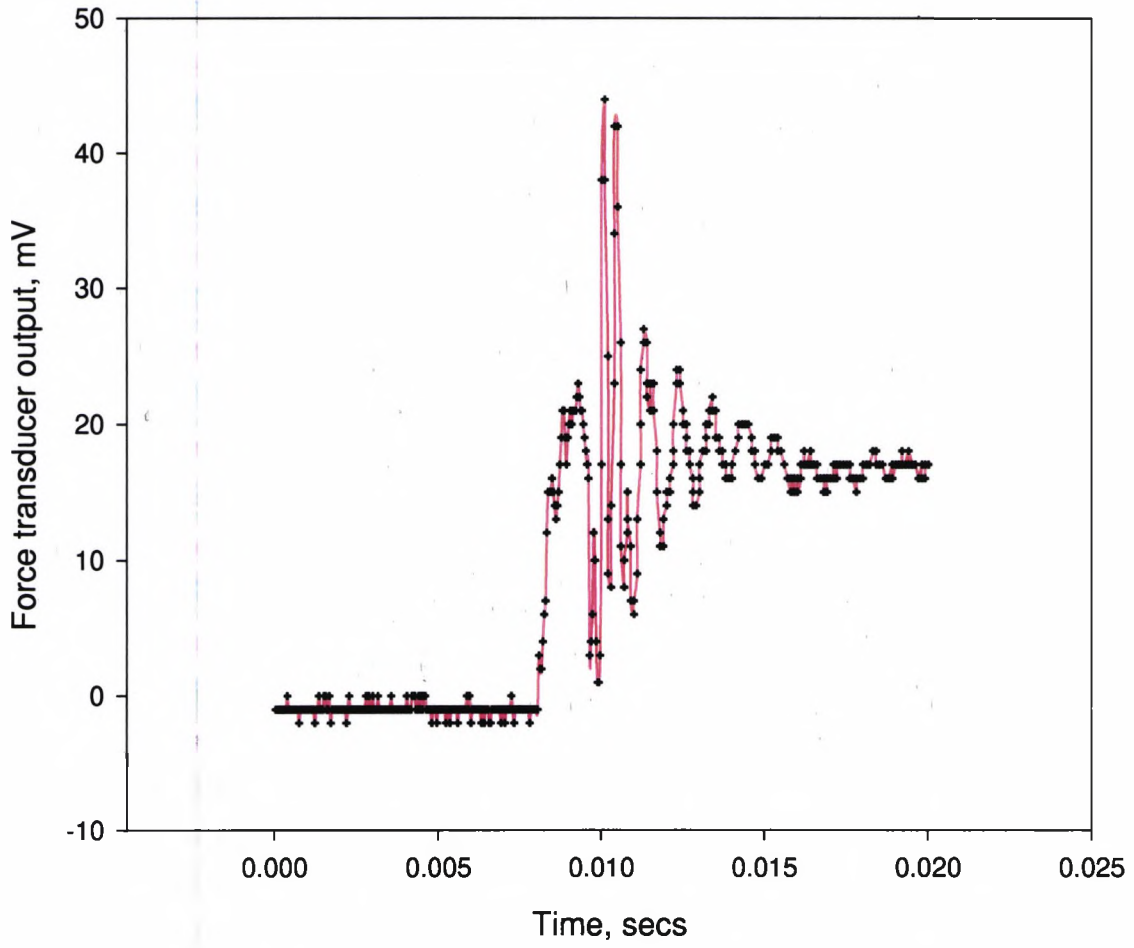


Figure 24

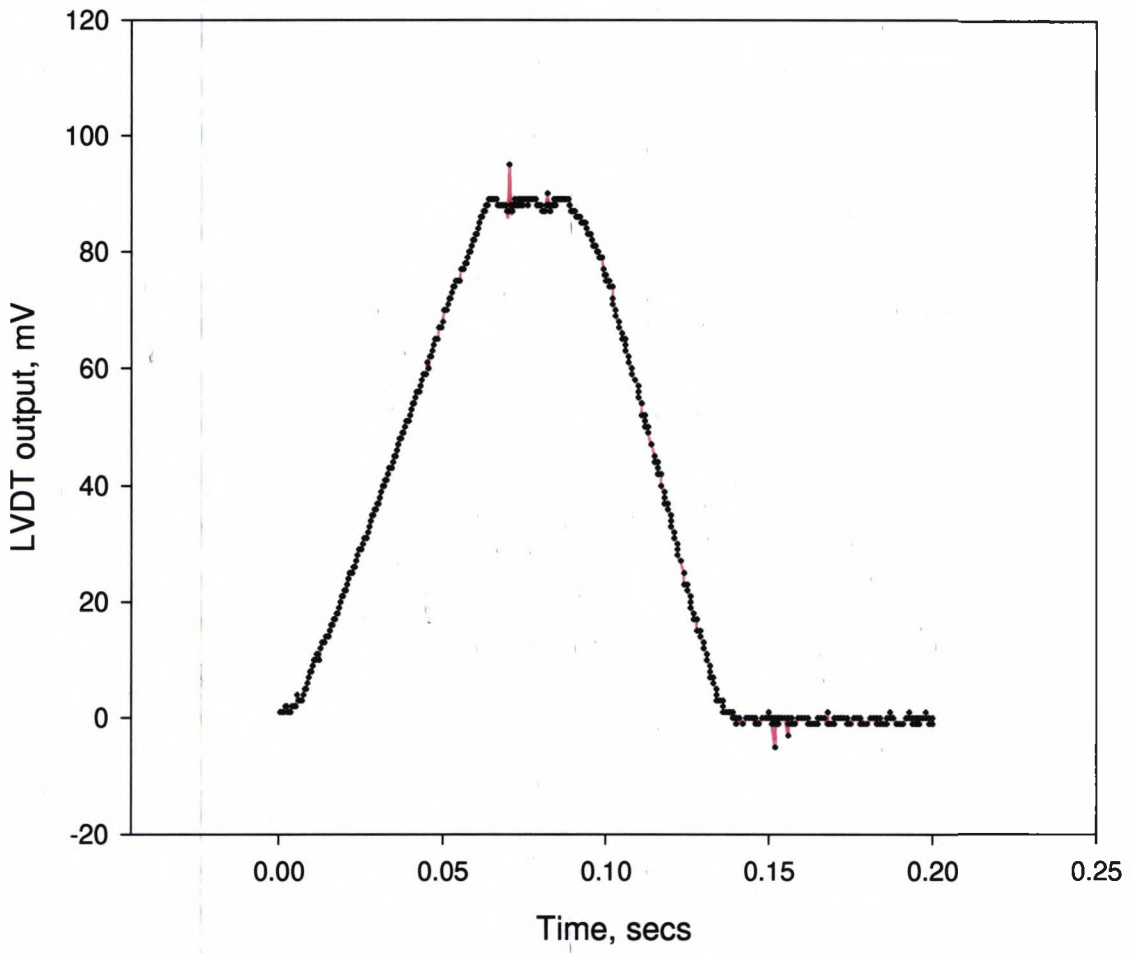
Force Transducer



Sample 35, test 89

Figure 25

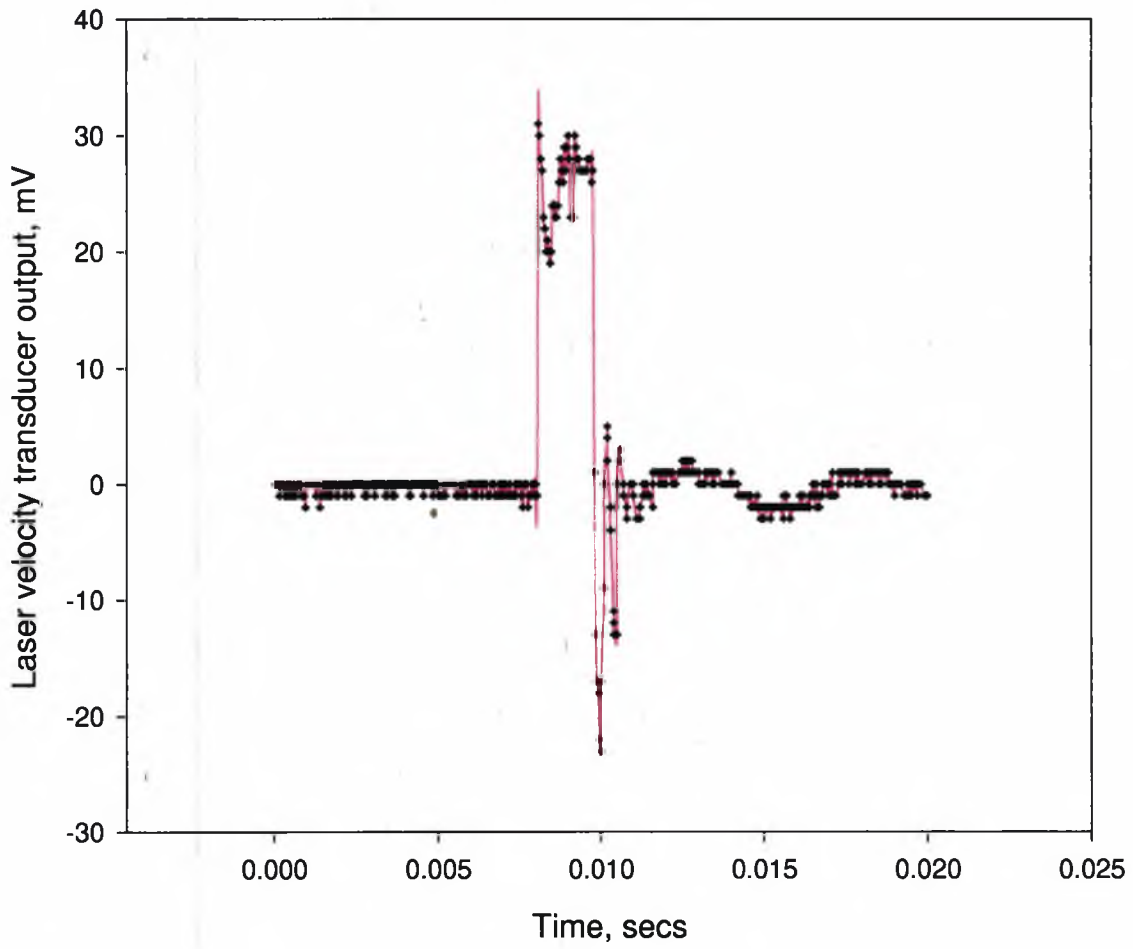
LVDT



Sample 35, test 89

Figure 26

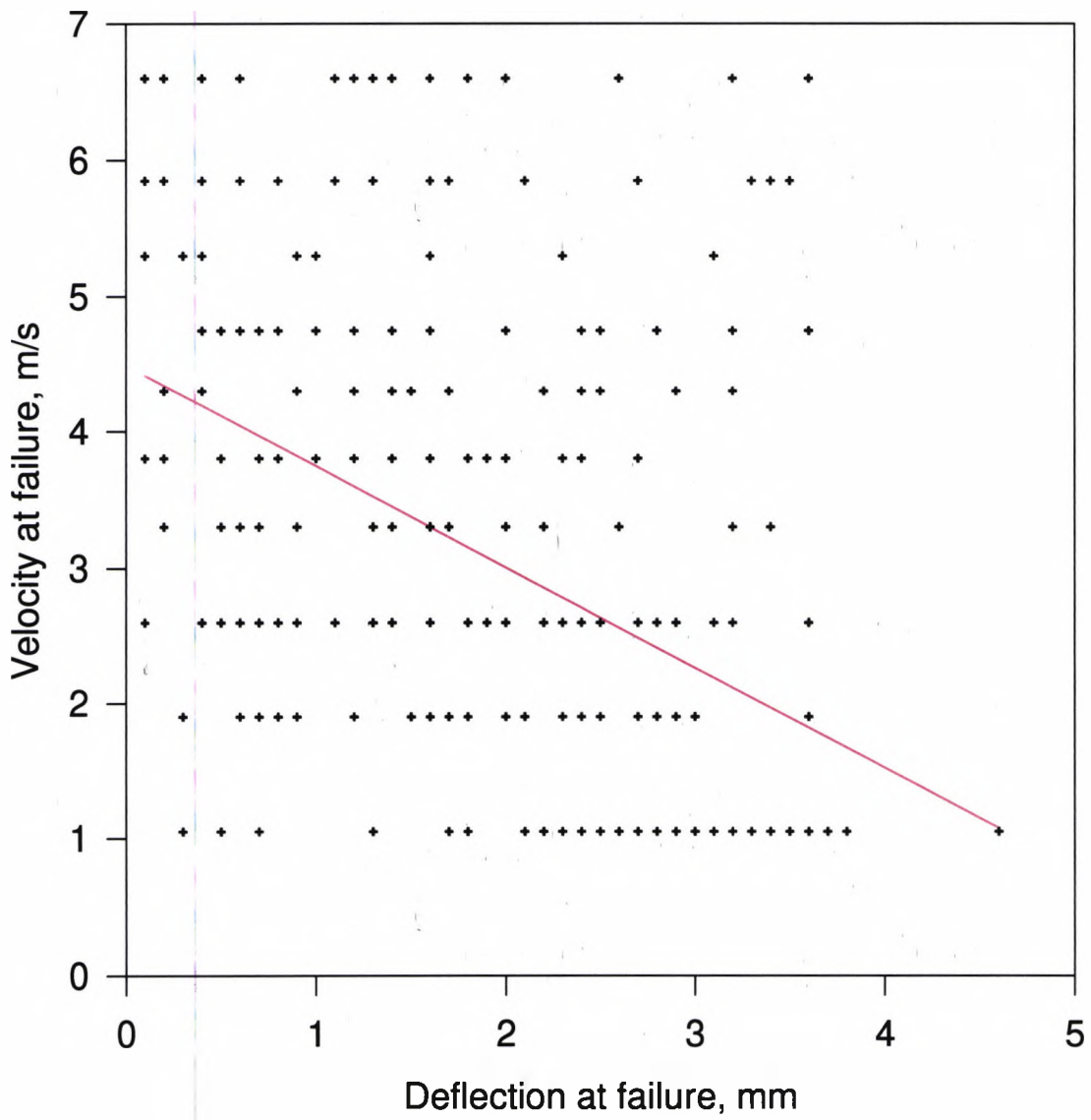
B&K Laser Velocity Transducer



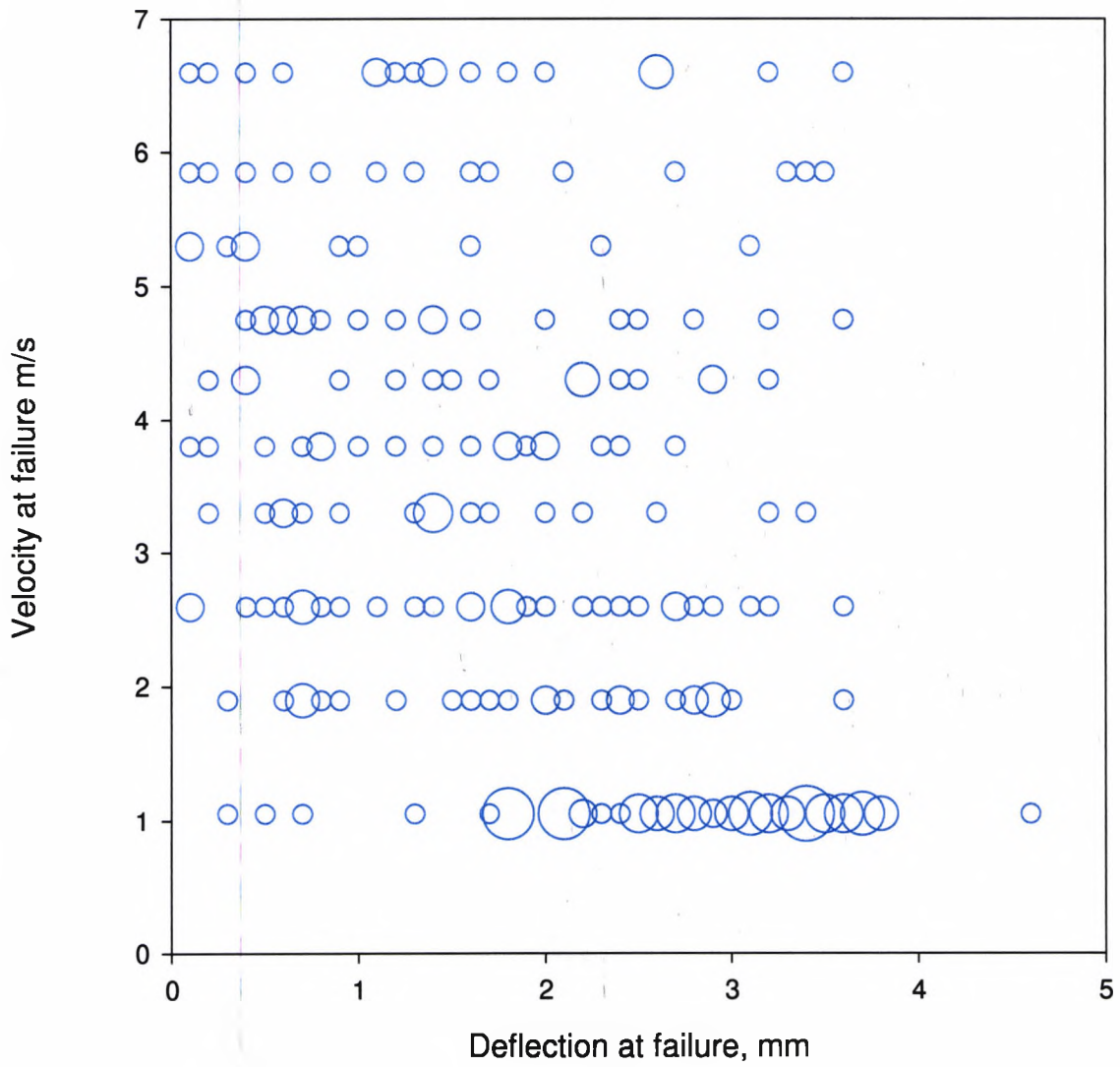
Sample 35, test 89

Figure 27

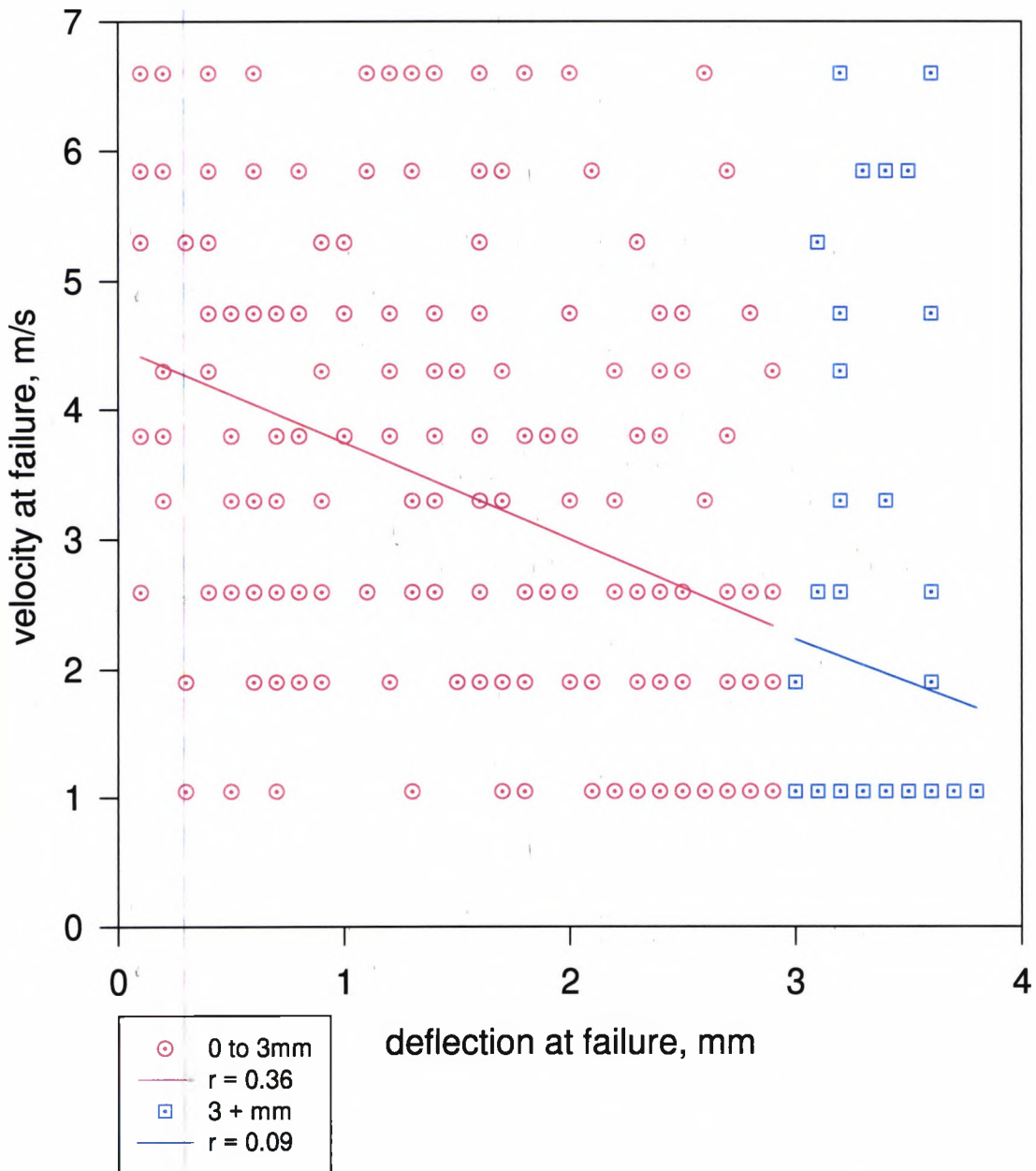
Deflection at failure v. Velocity at failure Figure 28



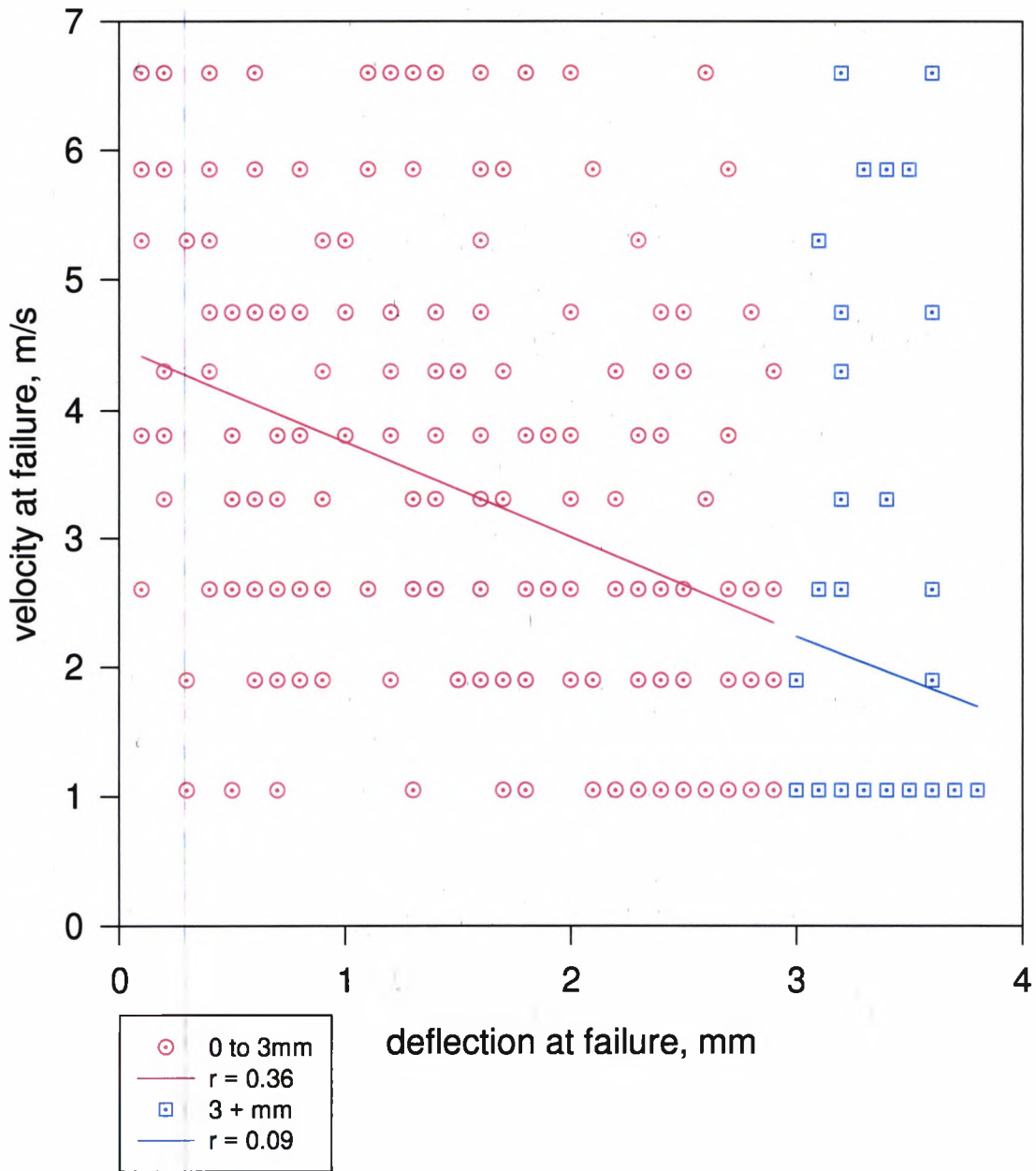
Deflection at Failure v. velocity at failure
Figure 29



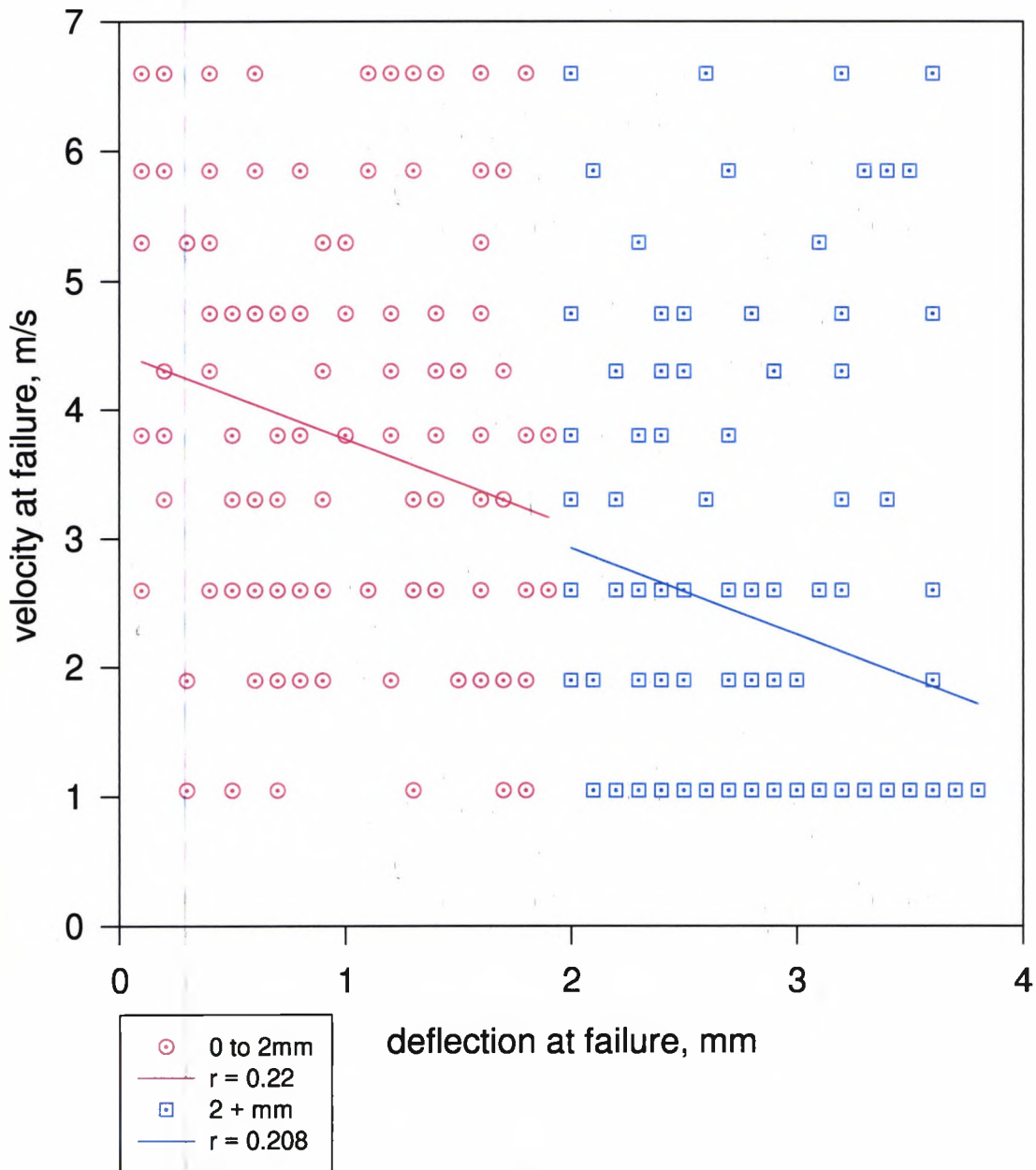
Regressions for two segments of Deflection v Velocity
Figure 30



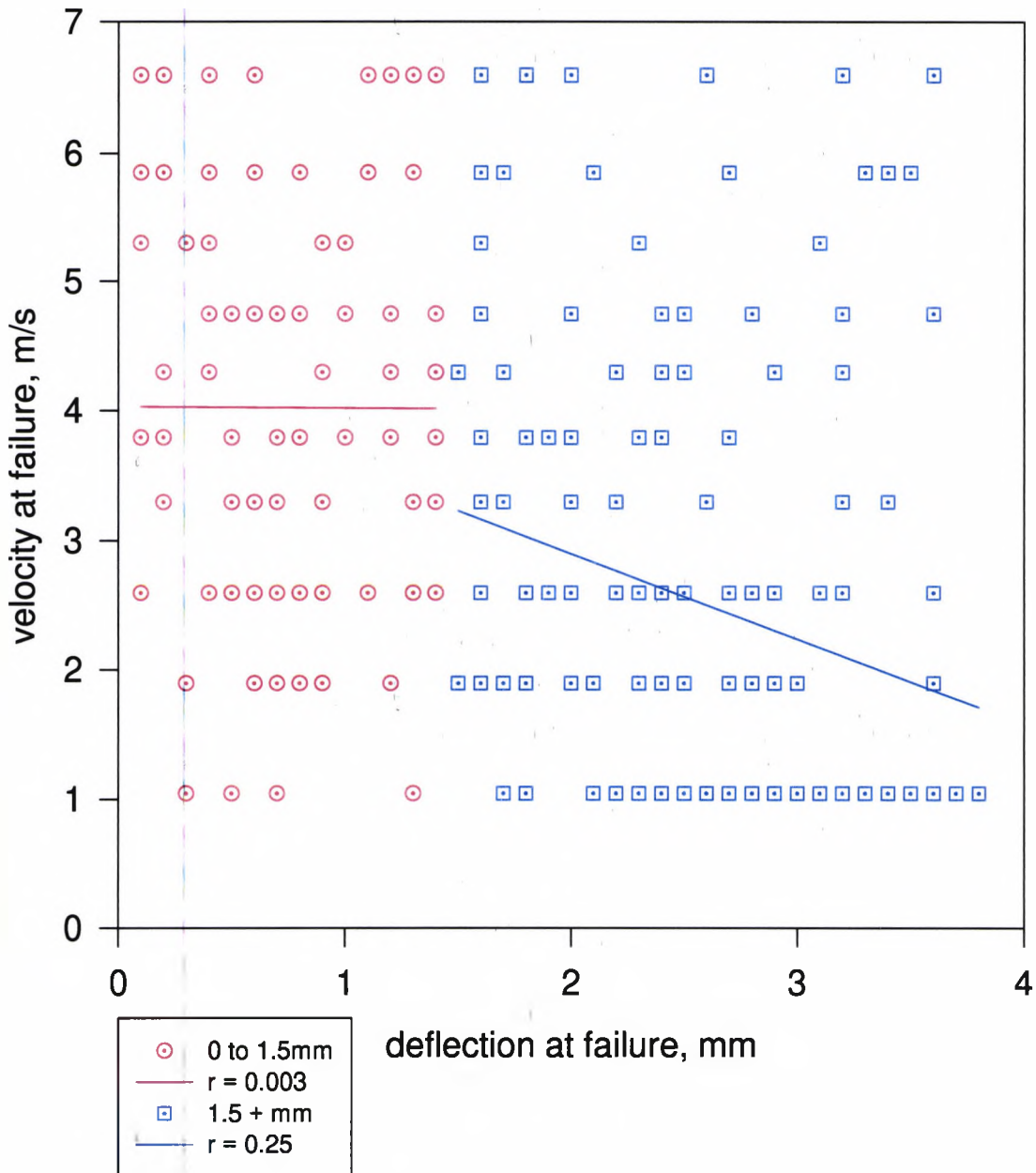
Regressions for two segments of Deflection v Velocity
Figure 31



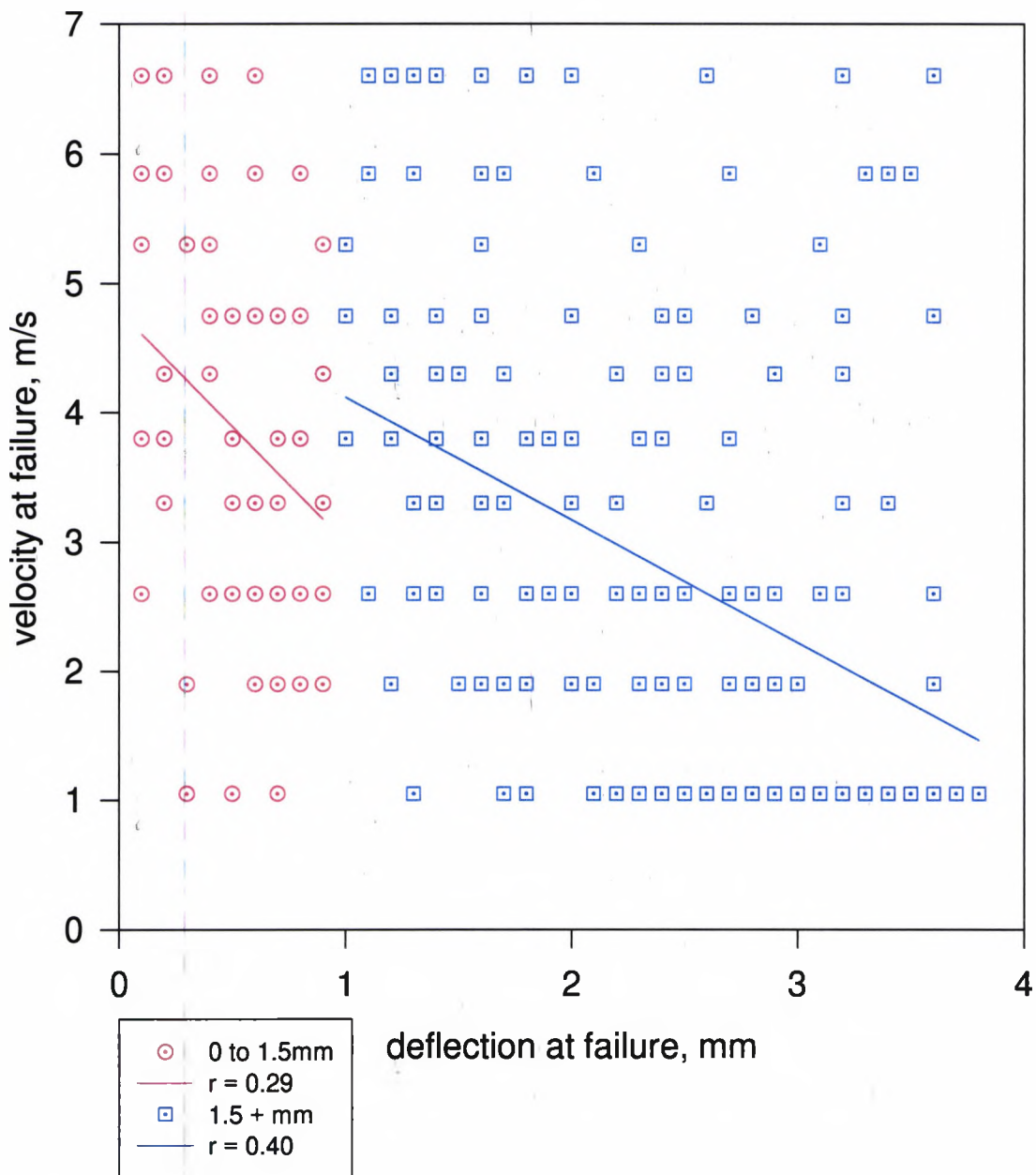
Regressions for two segments of Deflection v Velocity
Figure 32



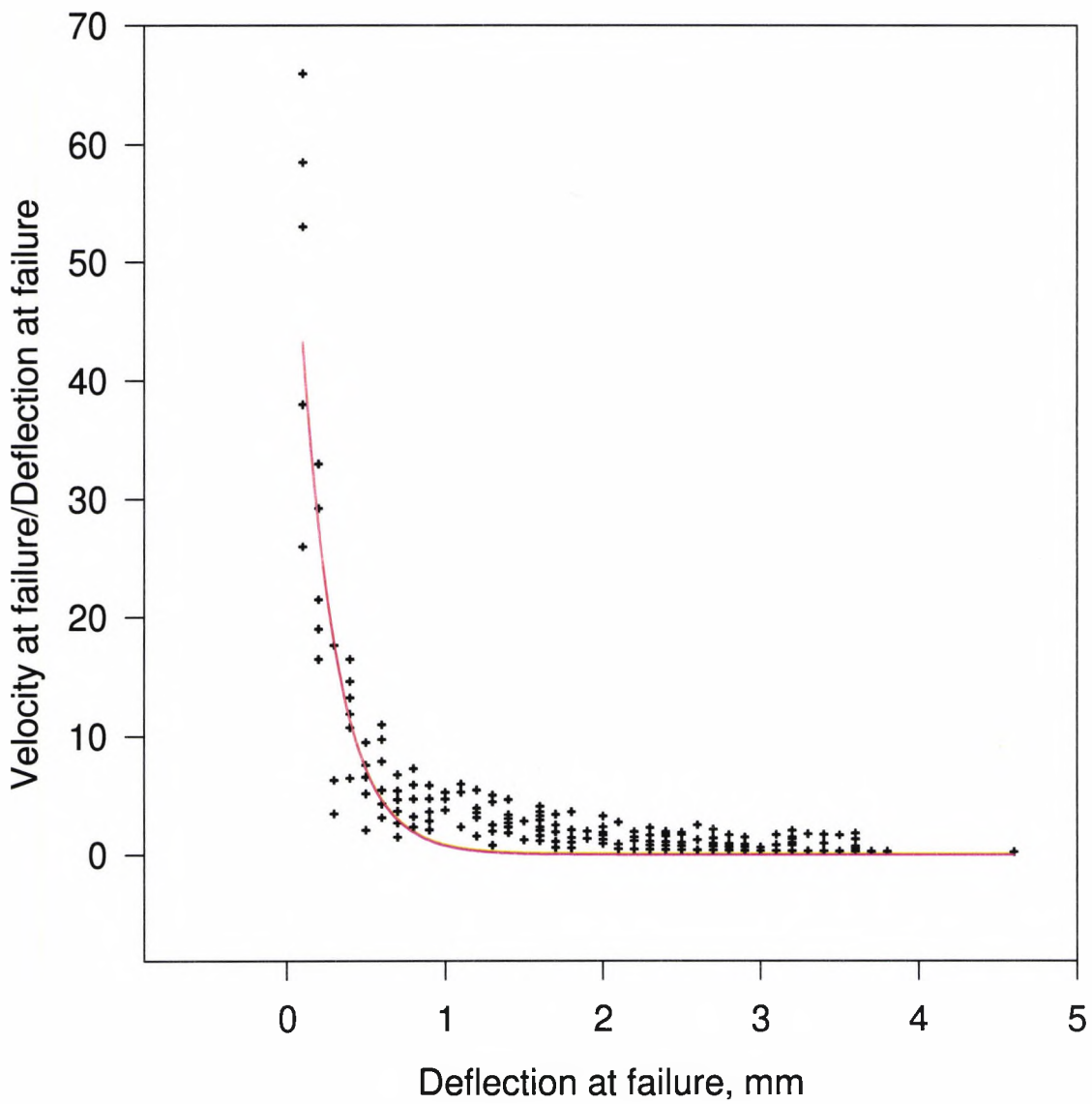
**Regressions for two segments of Deflection v Velocity
Figure 33**



Regressions for two segments of Deflection v Velocity
Figure 34

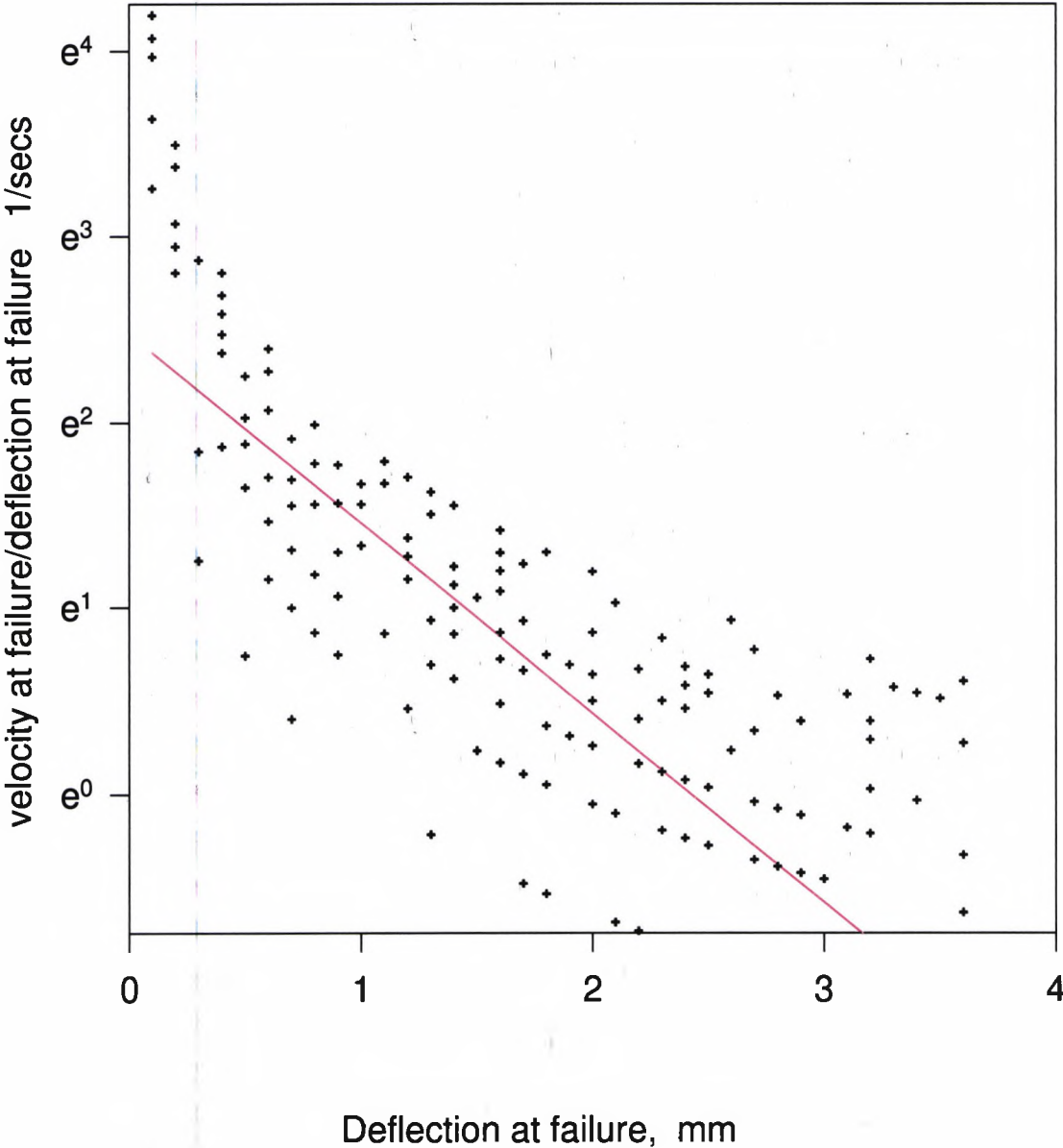


Deflection at failure v. velocity at failure/deflection at failure Figure 35

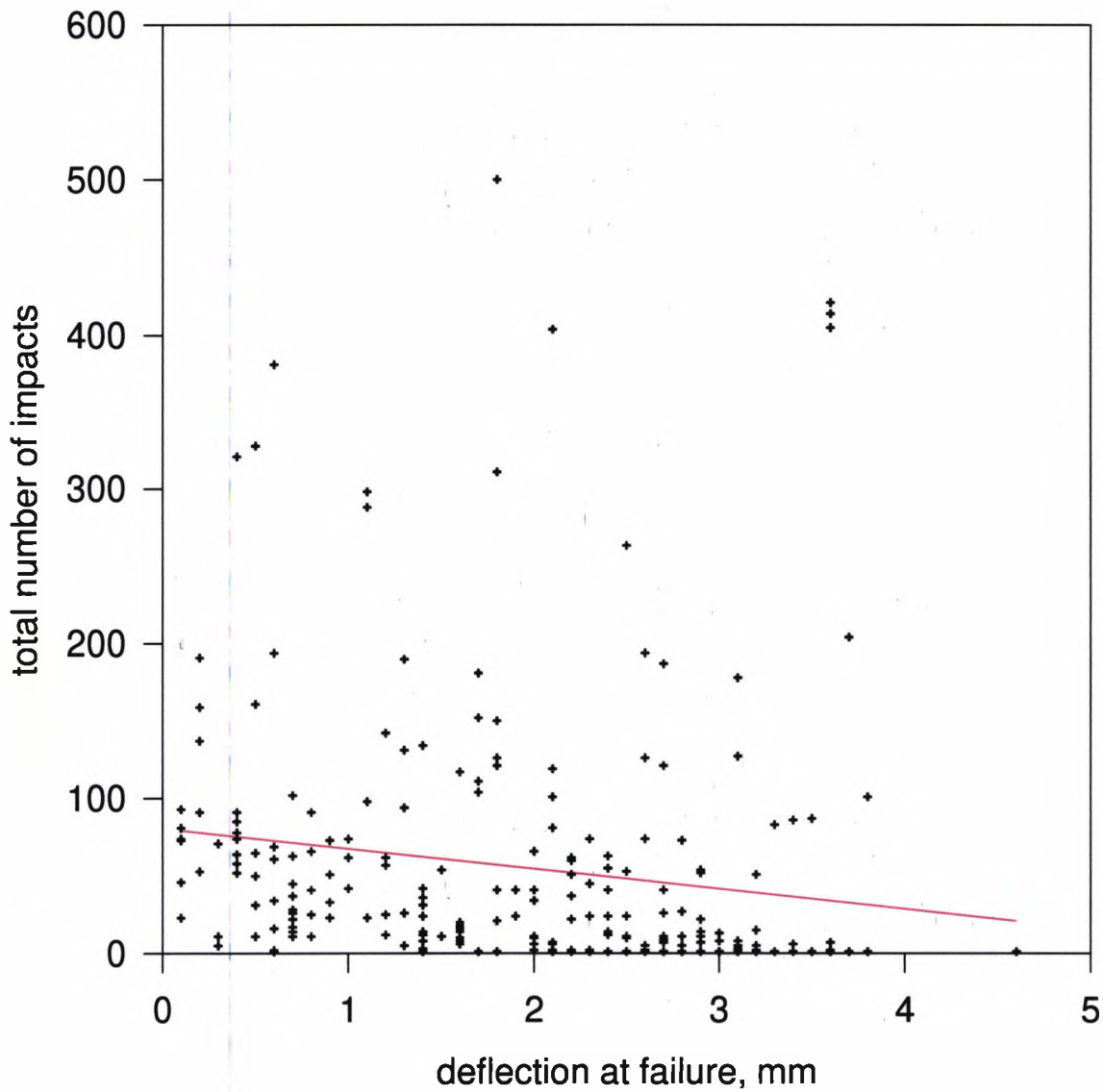


Deflection at failure v. velocity at failure/deflection at failure

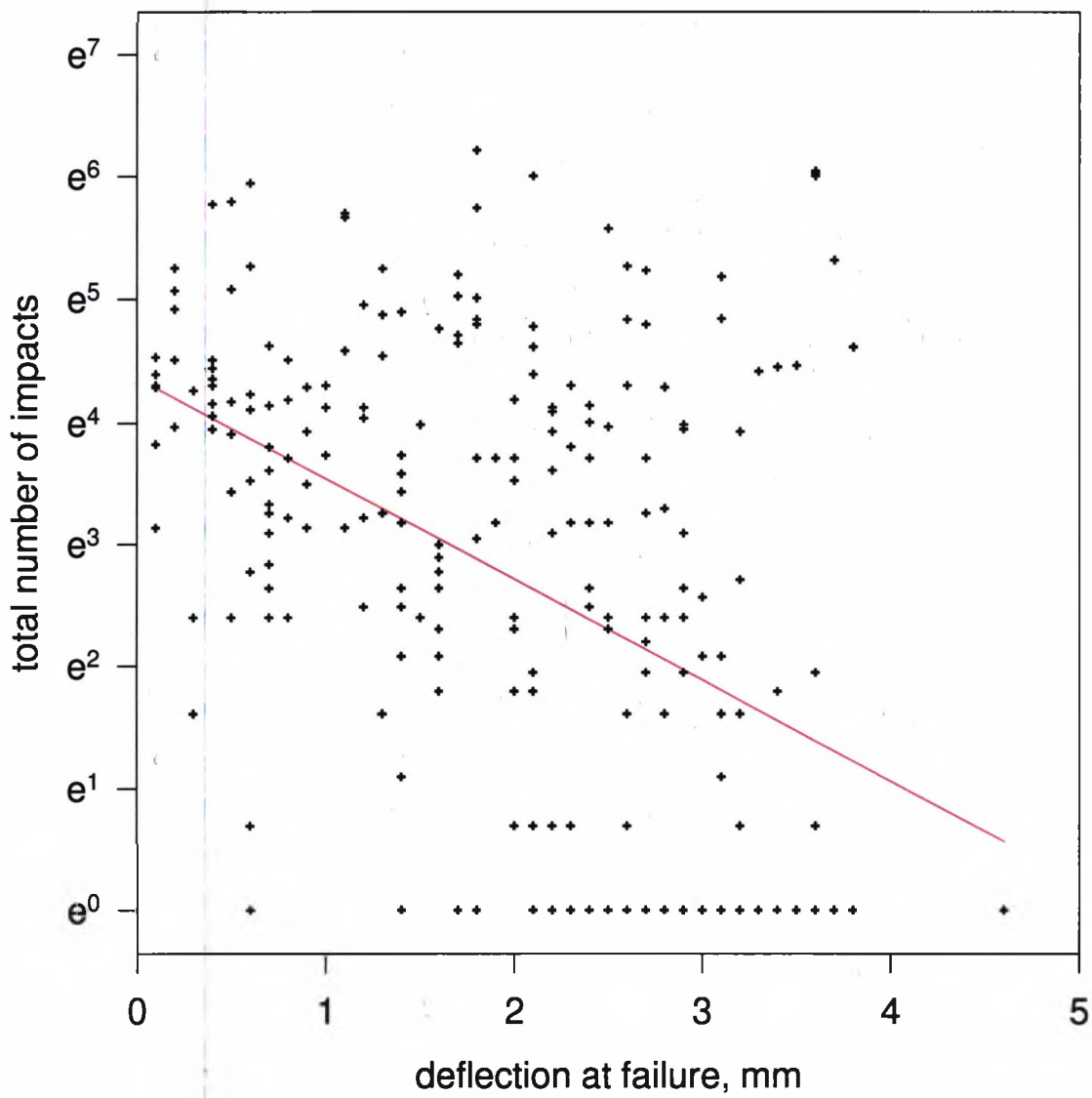
Figure 36



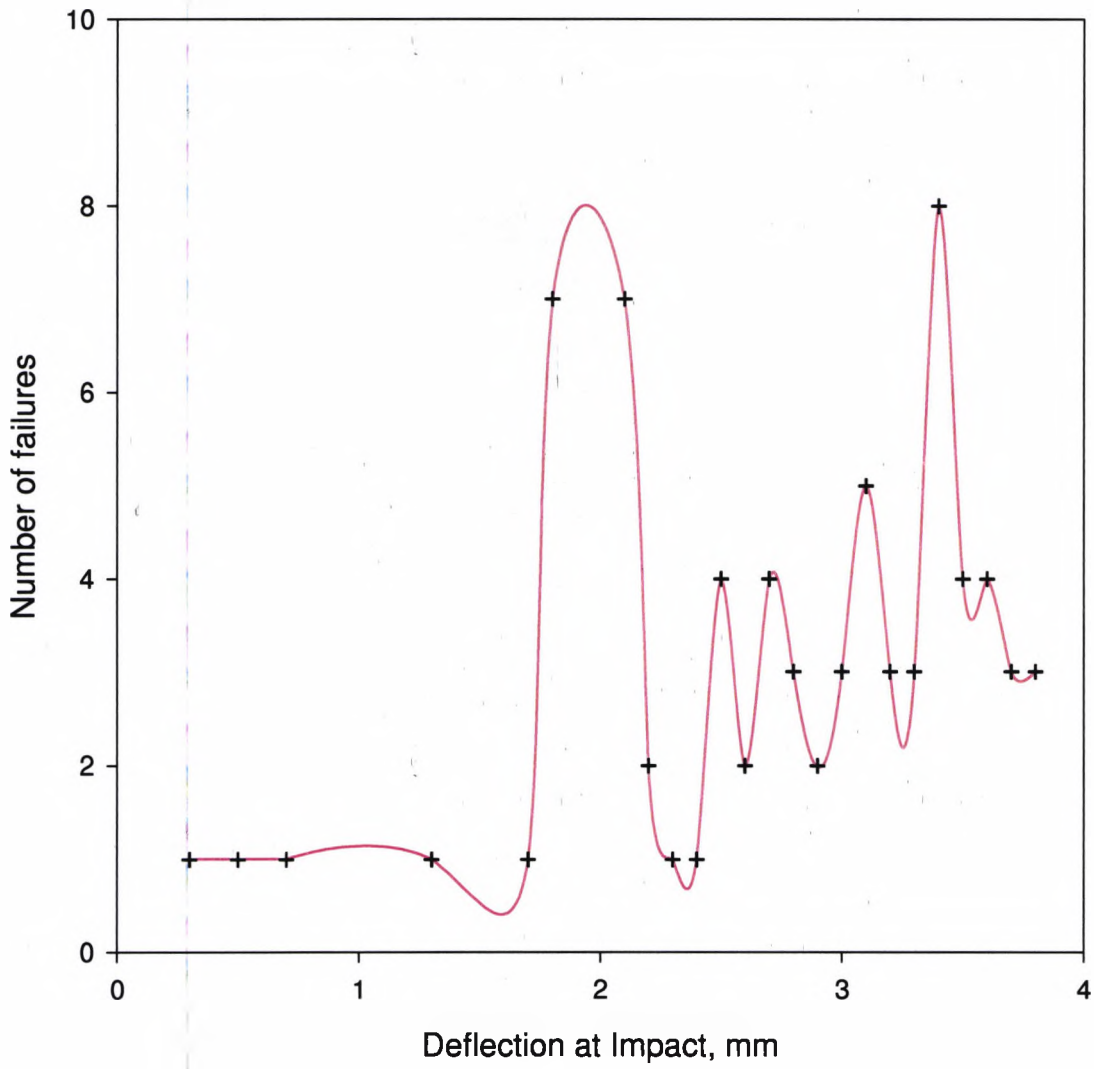
Deflection at failure v. total number of impacts
Figure 37



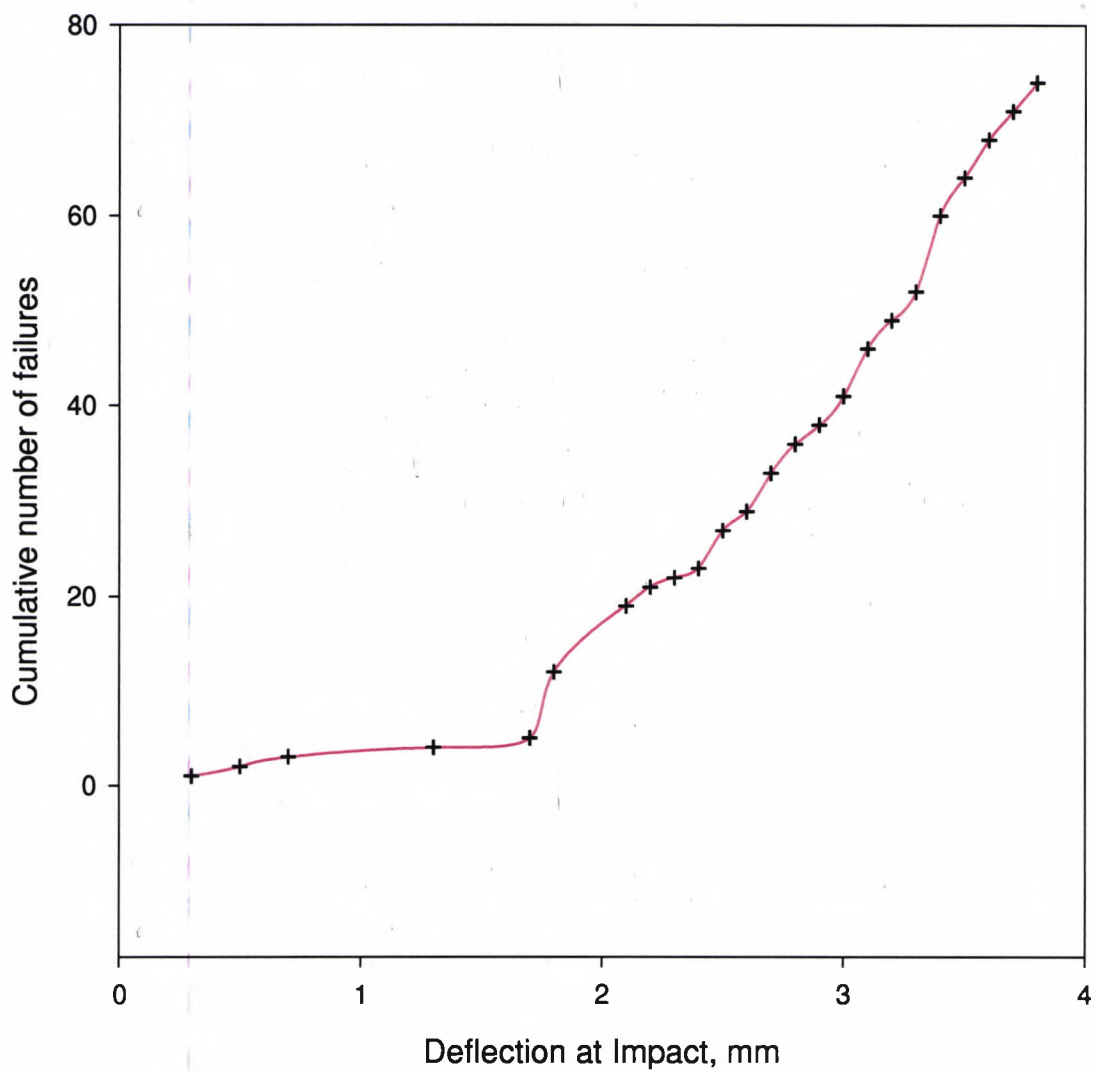
Deflection at failure v. total number of impacts
Figure 38



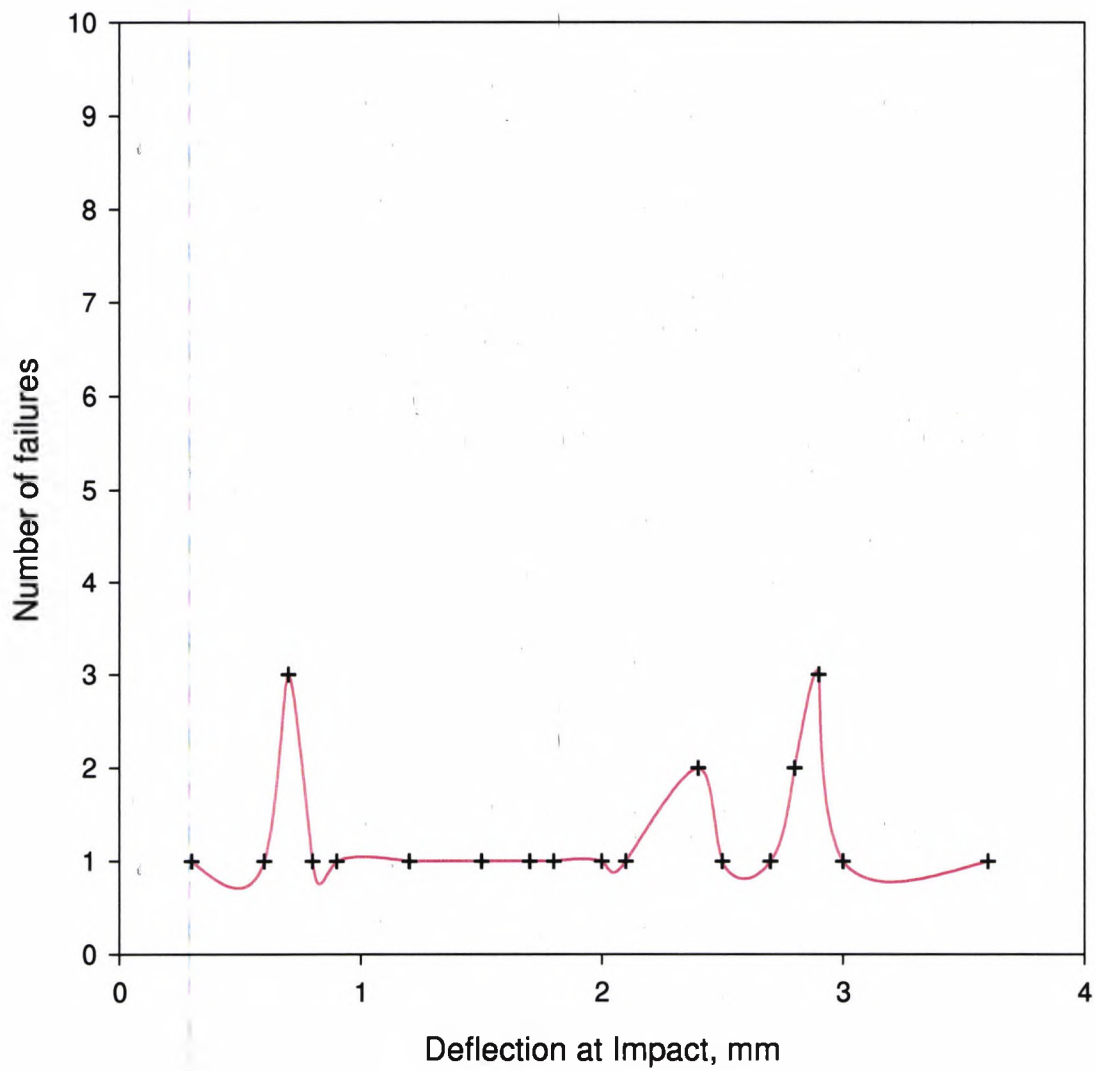
Deflection at Impact v. Number of failures for an impact velocity of 1.05 m/s
Figure 39



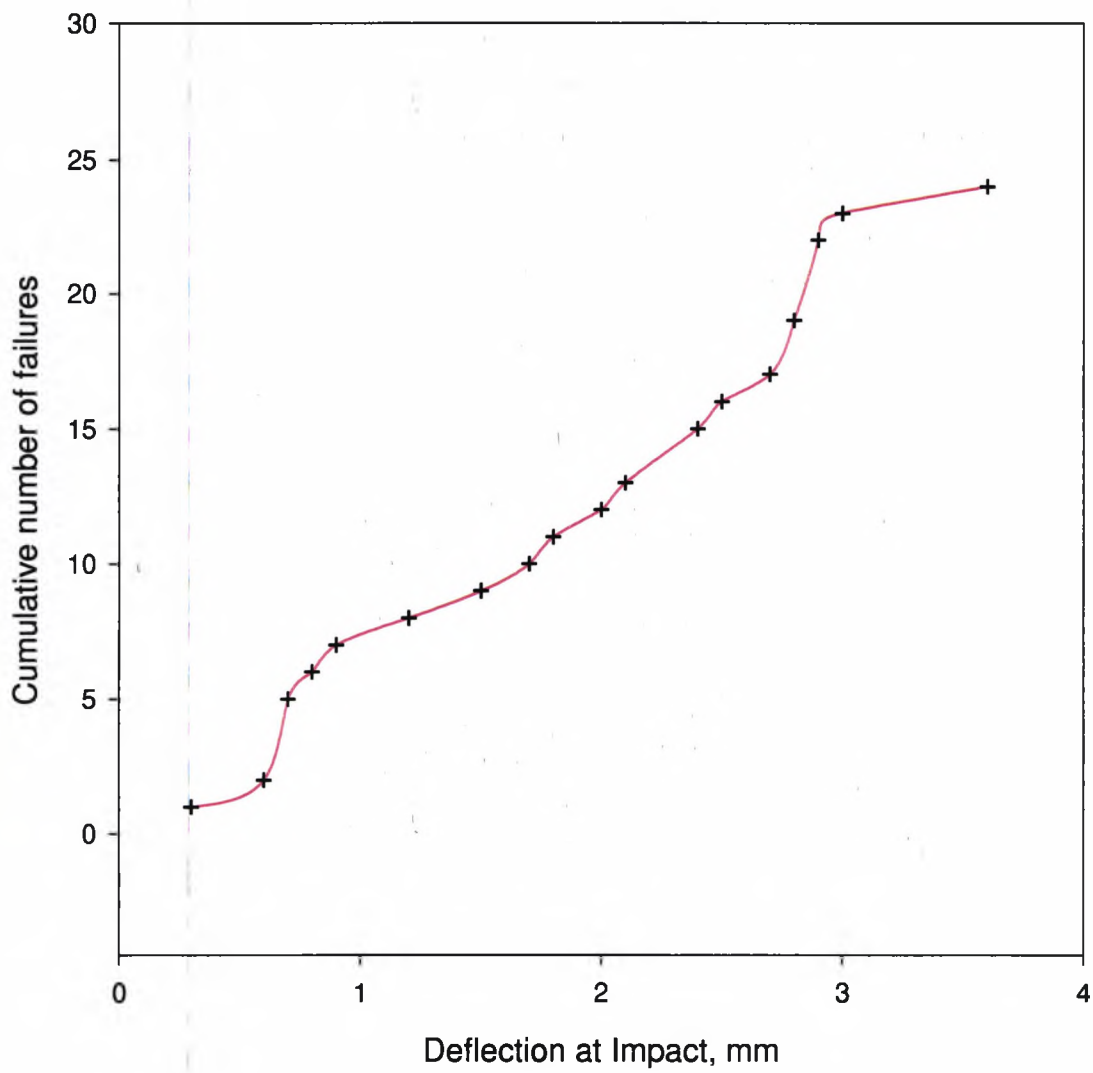
Deflection at Impact v. Cumulative number of failures
for an impact velocity of 1.05 m/s
Figure 40



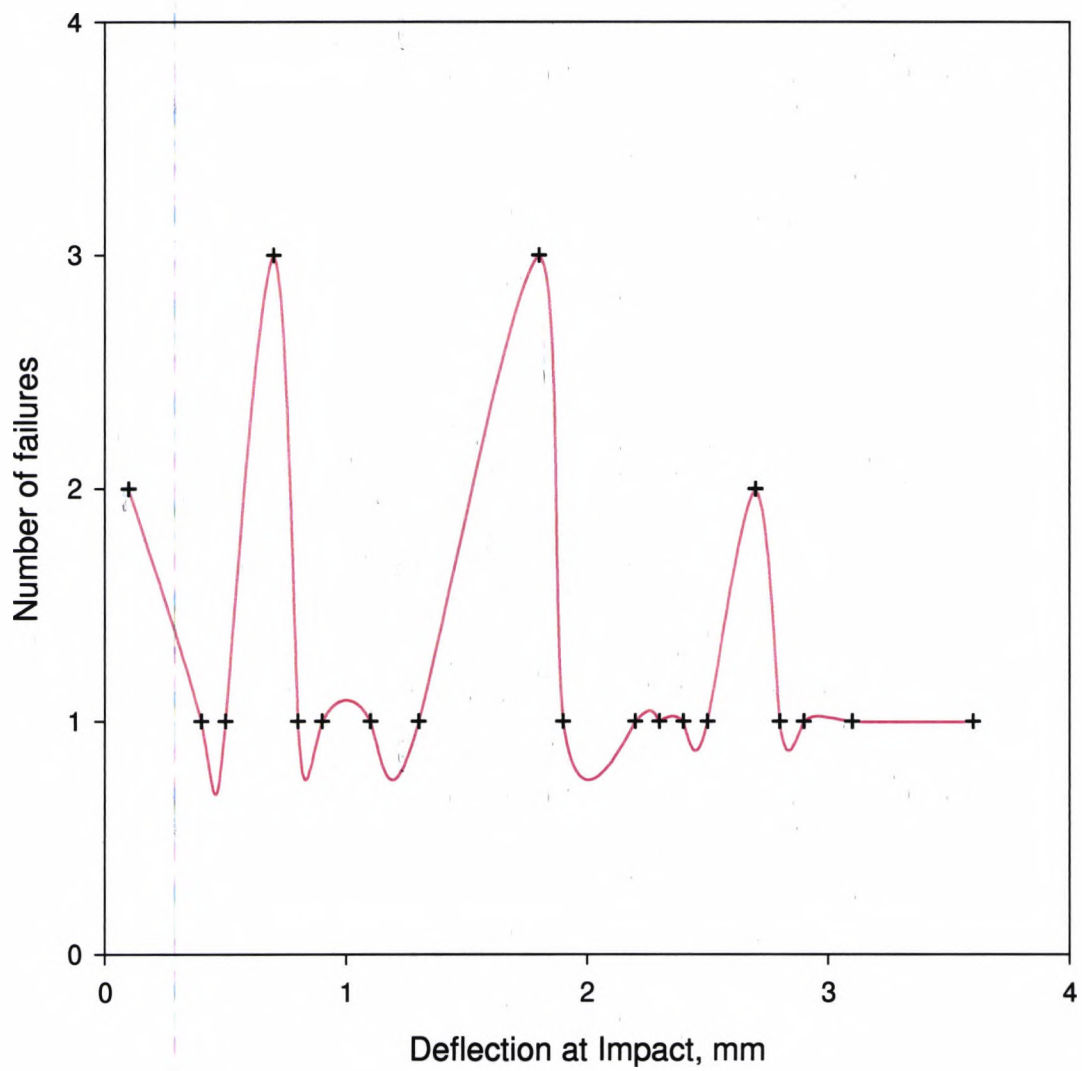
Deflection at Impact v. Number of failures for an impact velocity of 1.9 m/s
Figure 41



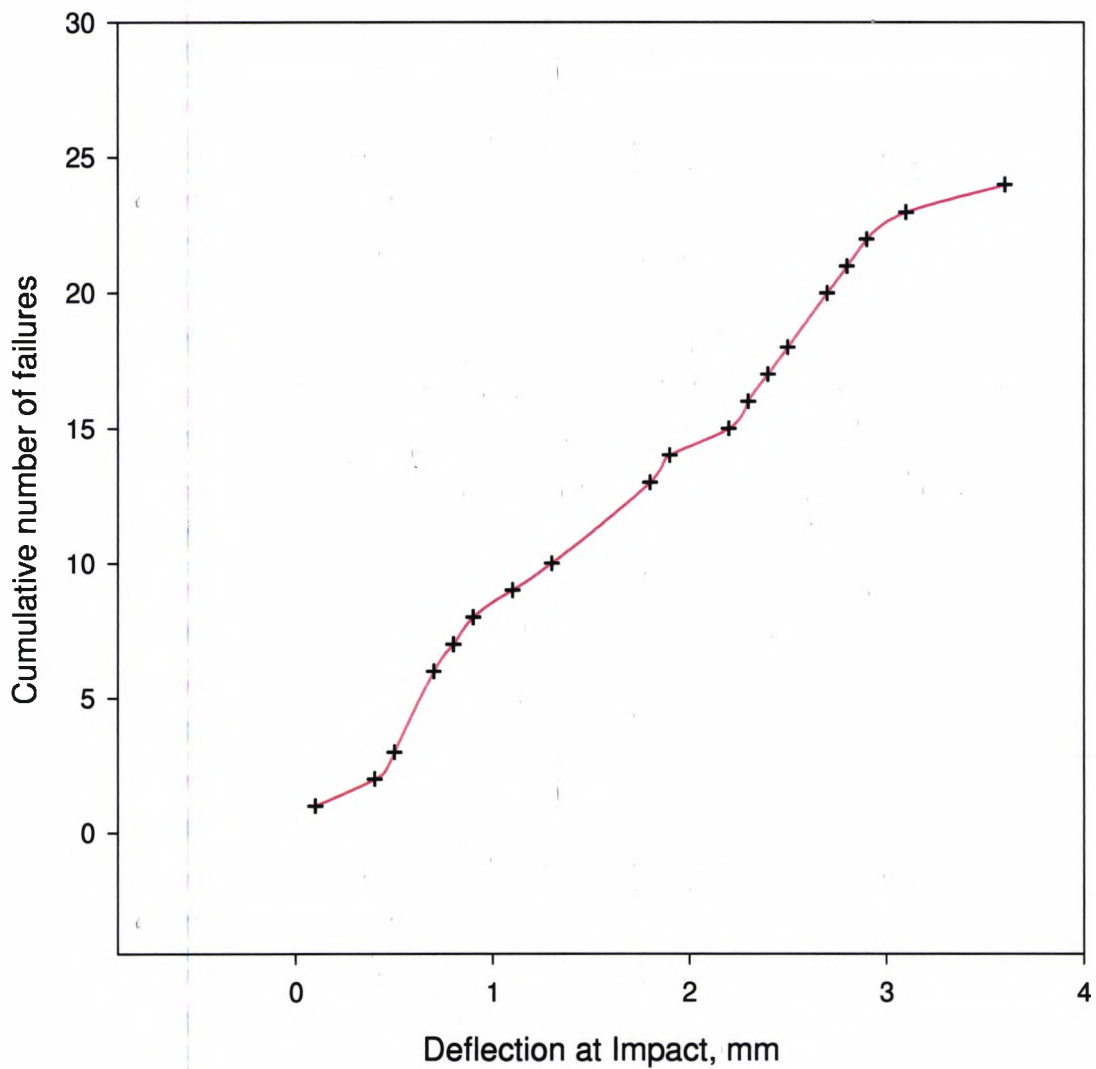
Deflection at Impact v. Cumulative number of failures
for an impact velocity of 1.9m/s
Figure 42



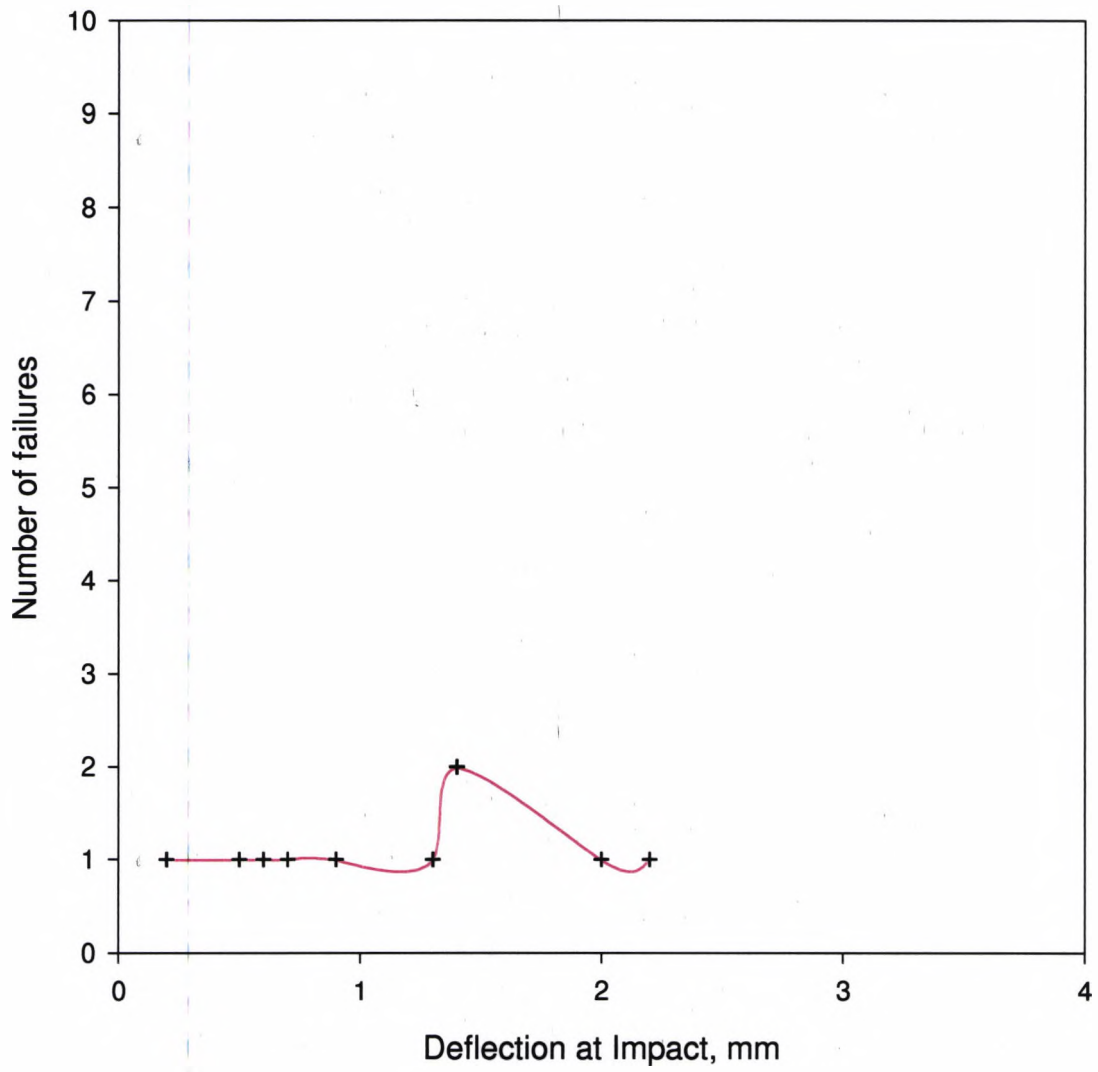
Deflection at Impact v. Number of failures
for an impact velocity of 2.6m/s
Figure 43



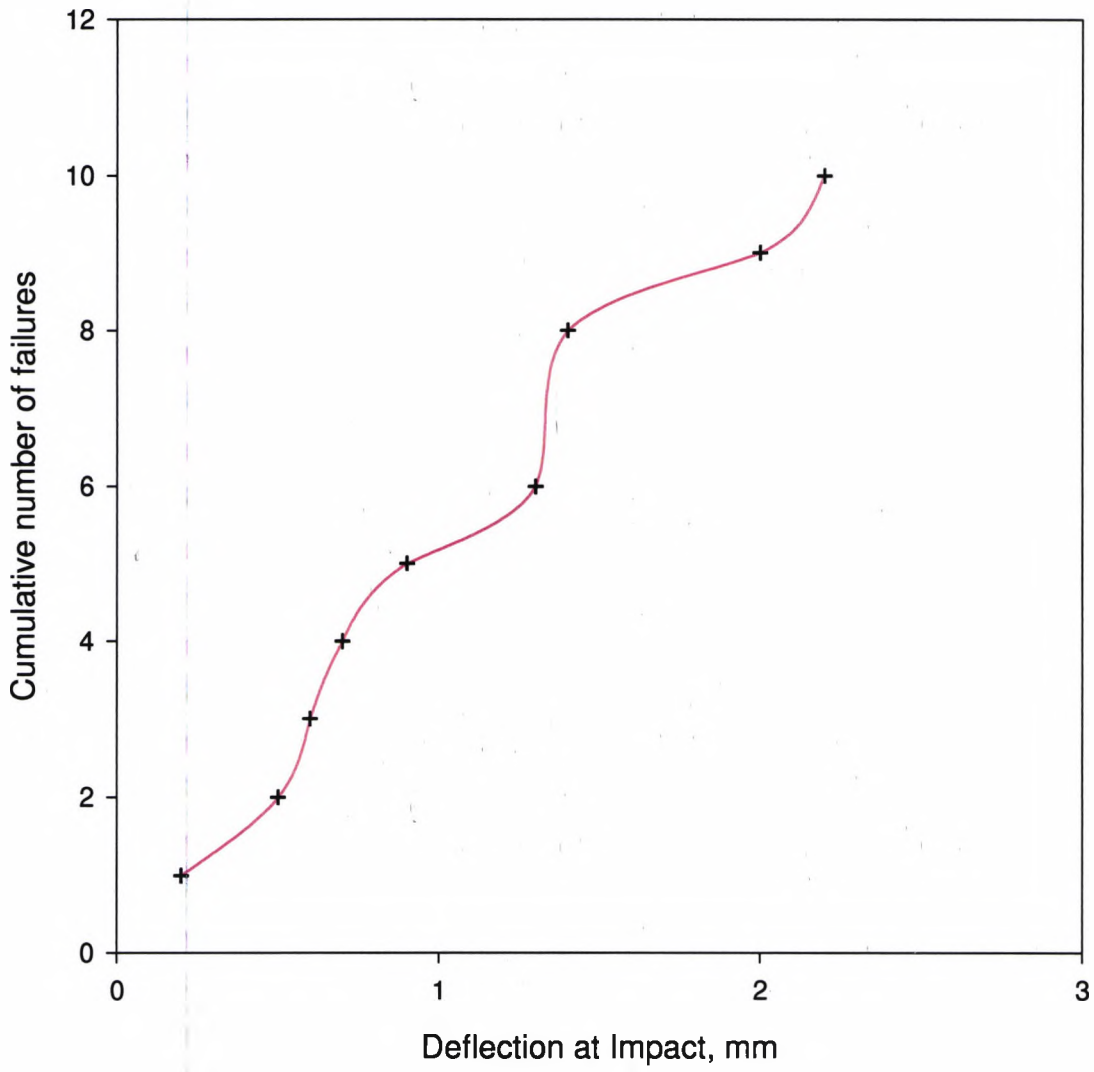
Deflection at Impact v. Cumulative number of failures
for an impact velocity of 2.6m/s
Figure 44



Deflection at Impact v. Number of failures for an impact velocity of 3.3 m/s
Figure 45

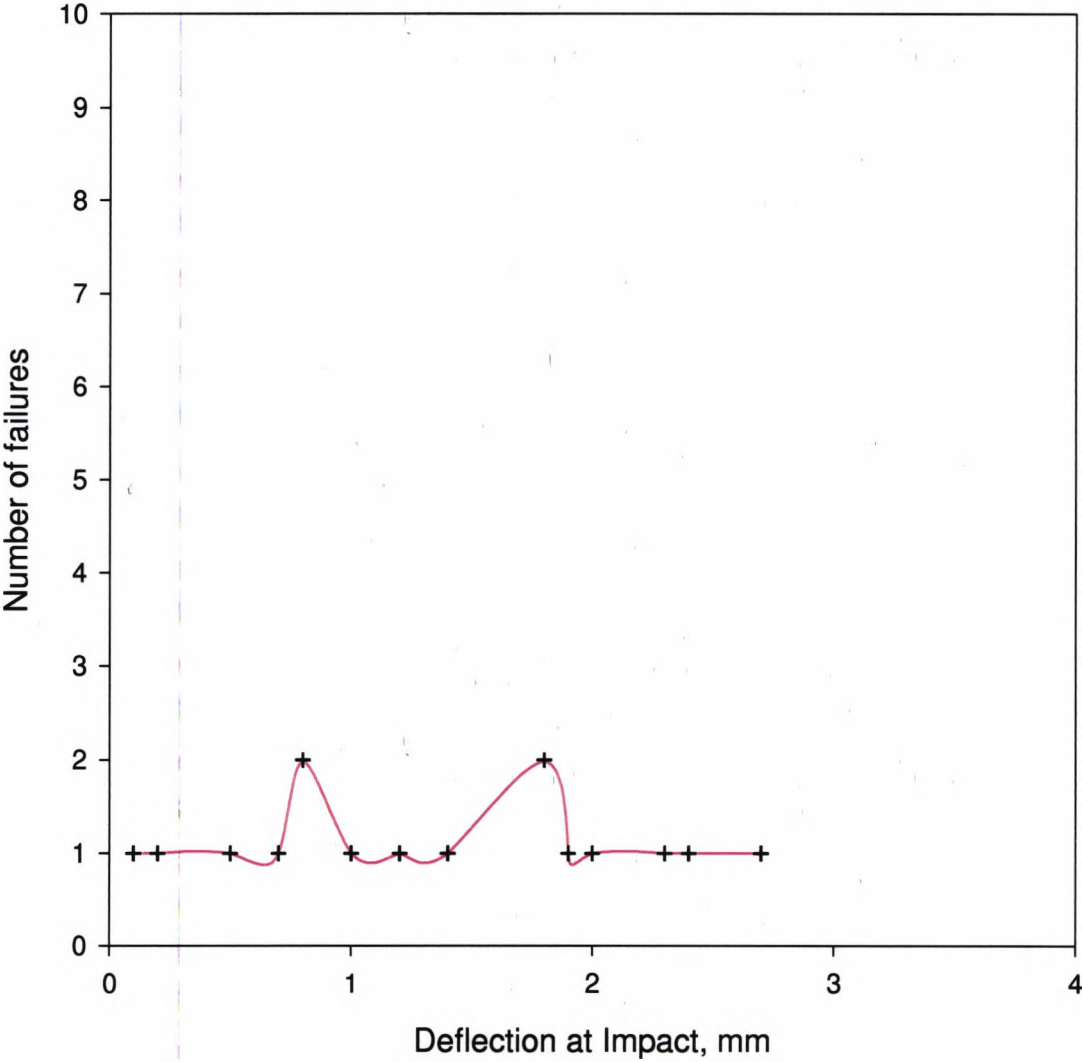


Deflection at Impact v. Cumulative number of failures
for an impact velocity of 3.3m/s
Figure 46

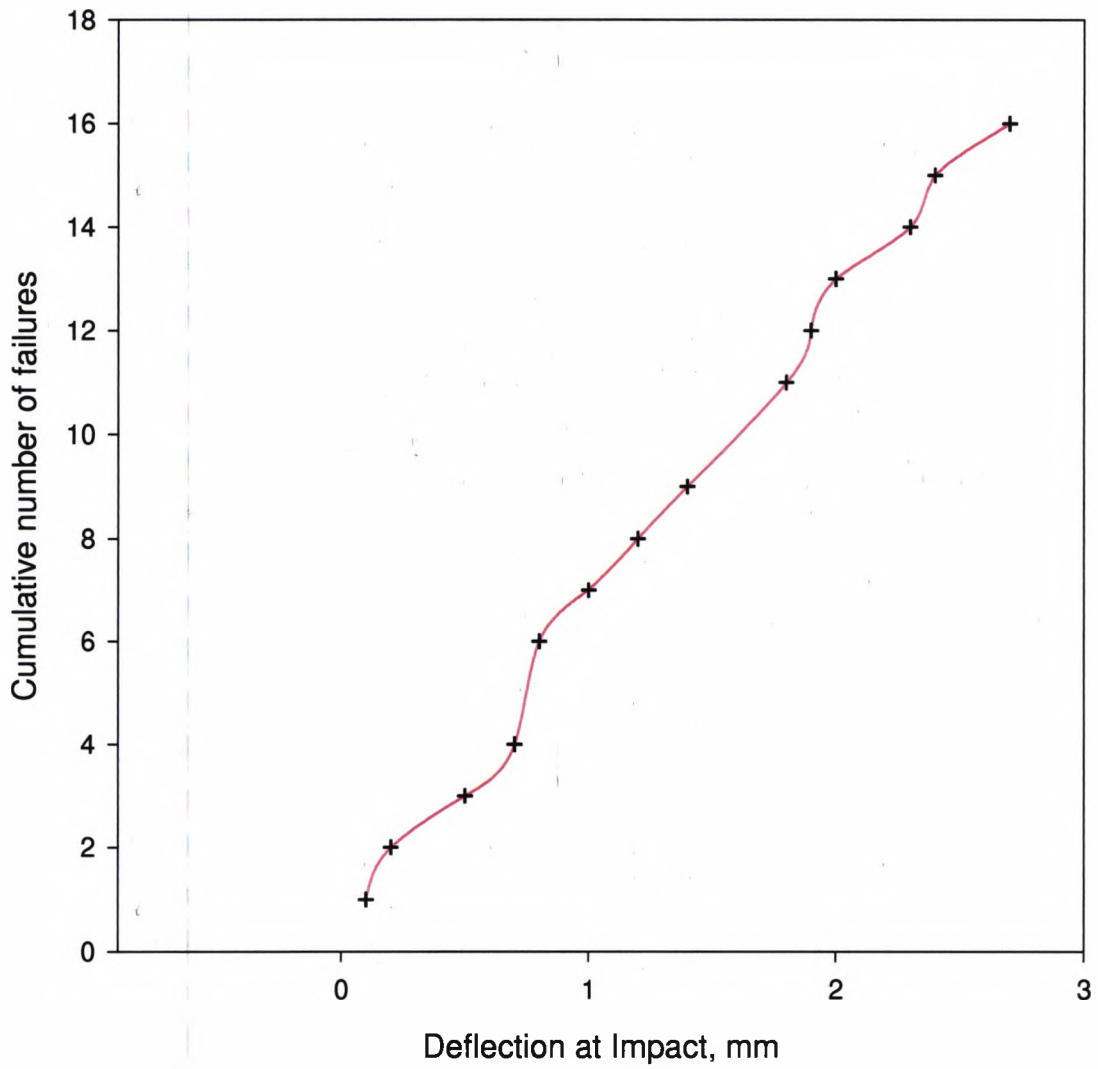


Deflection at Impact v. Number of failures for an impact velocity of 3.8 m/s

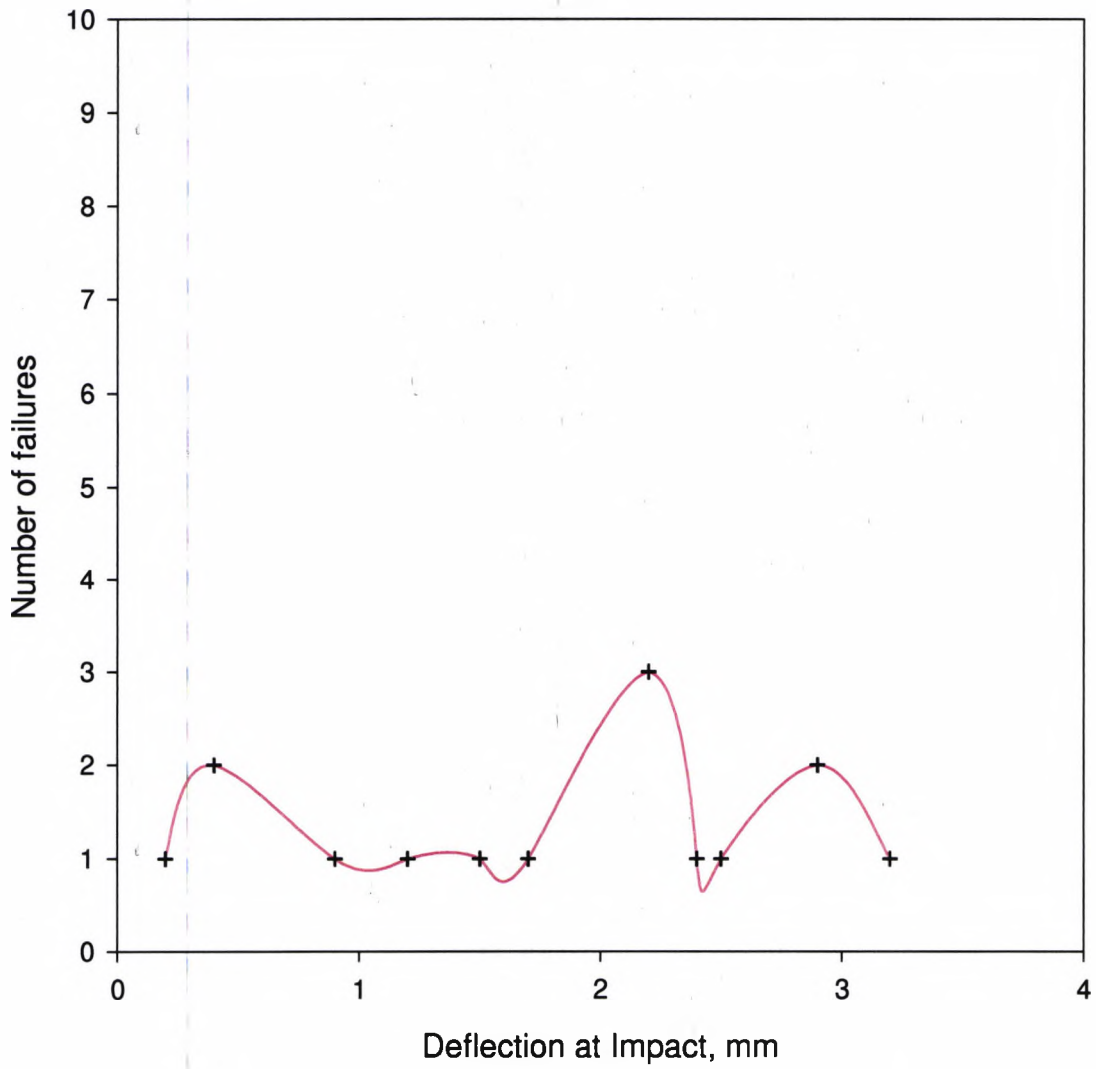
Figure 47



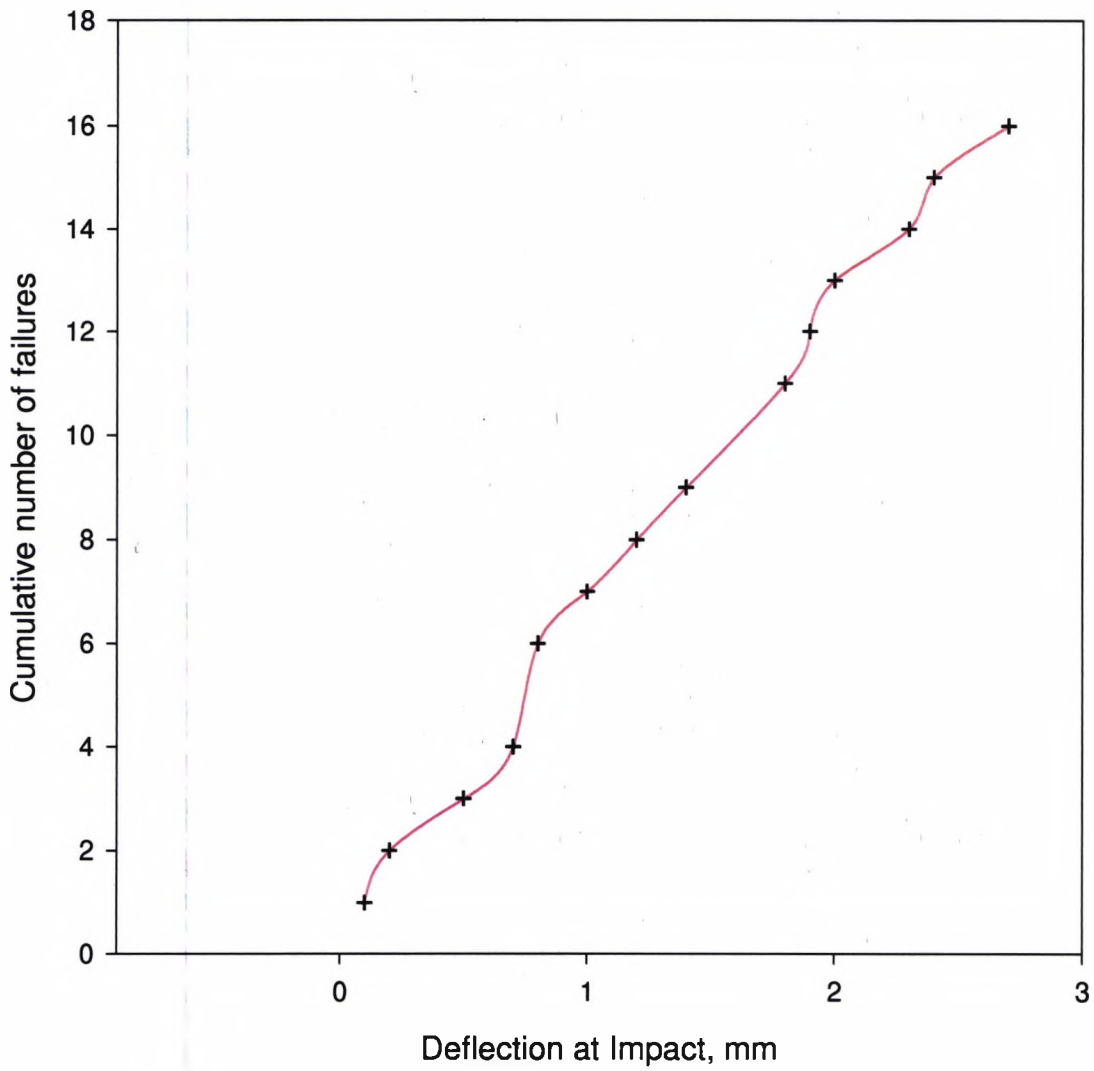
Deflection at Impact v. Cumulative number of failures
for an impact velocity of 3.8 m/s
Figure 48



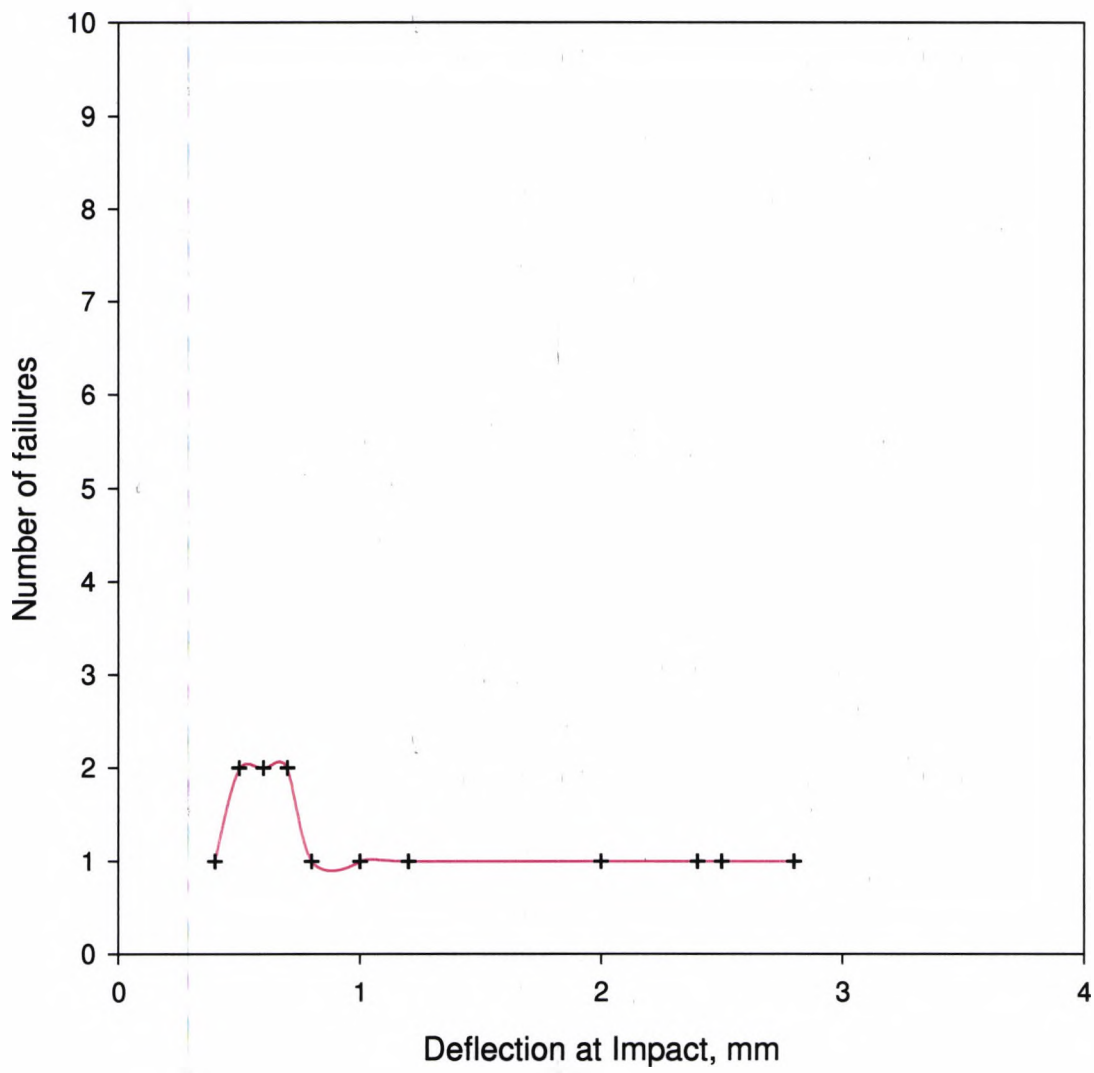
Deflection at Impact v. Number of failures for an impact velocity of 4.3 m/s
Figure 49



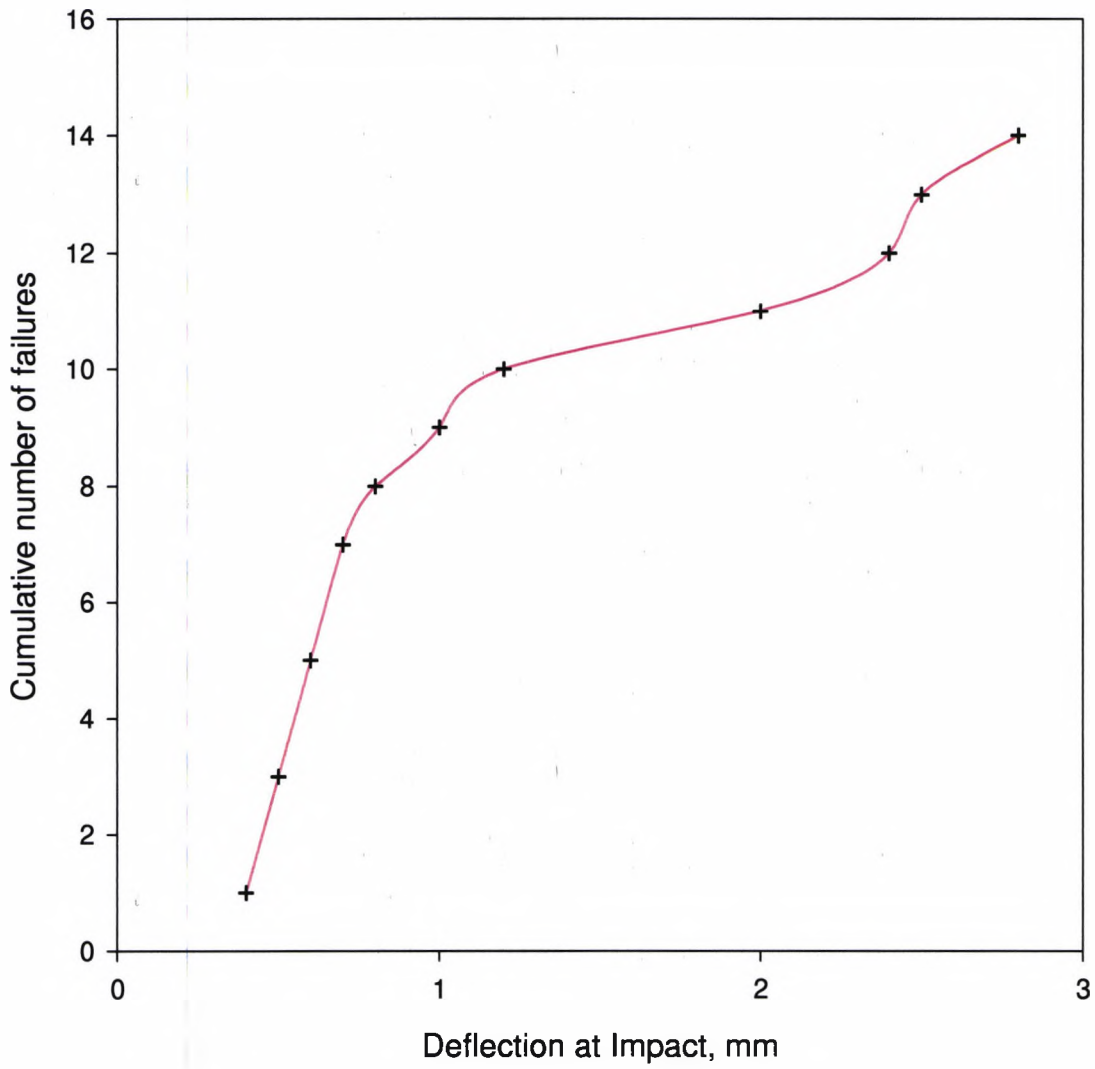
Deflection at Impact v. Cumulative number of failures
for an impact velocity of 4.3 m/s
Figure 50



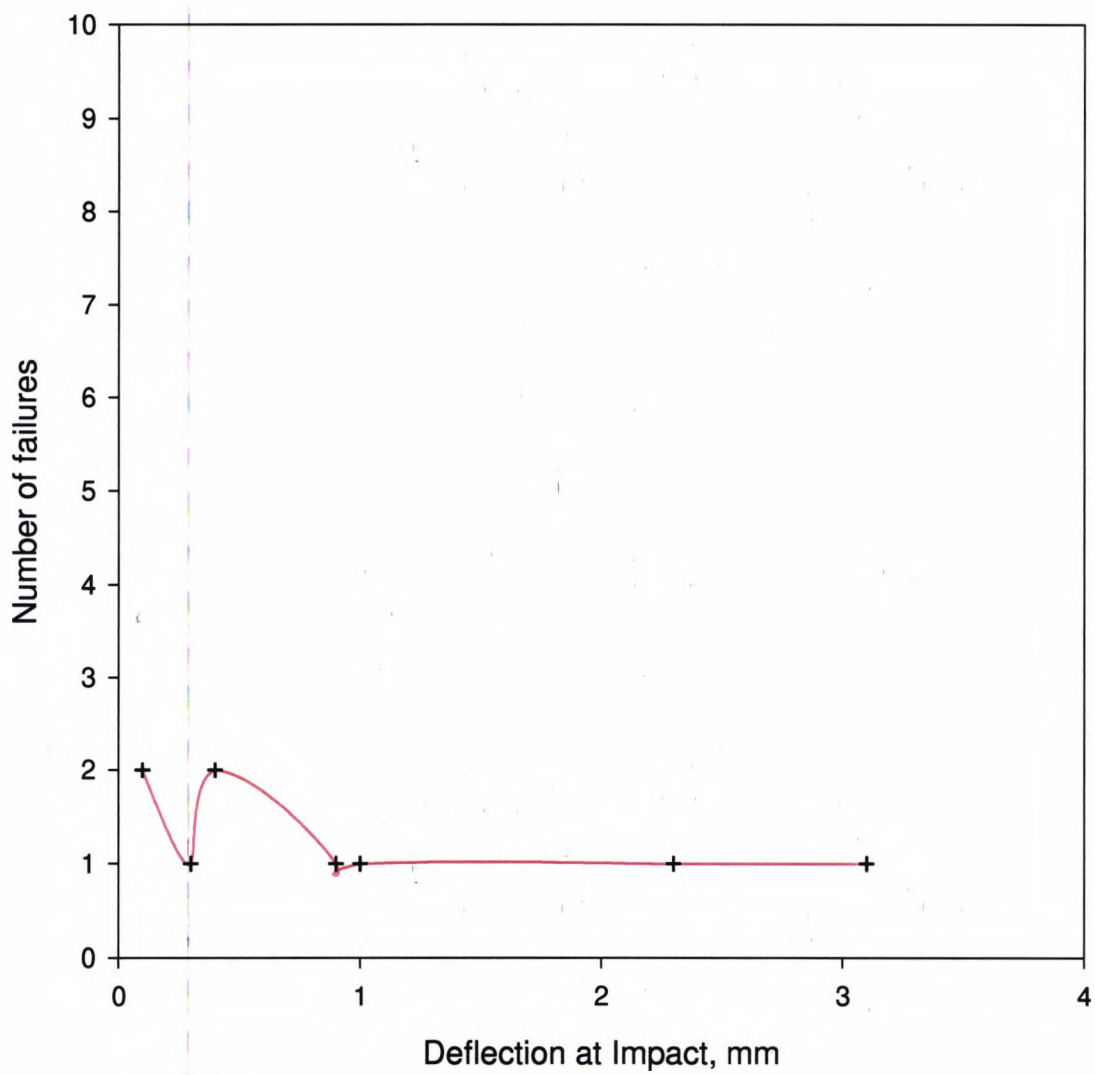
Deflection at Impact v. Number of failures for an impact velocity of 4.75 m/s
Figure 51



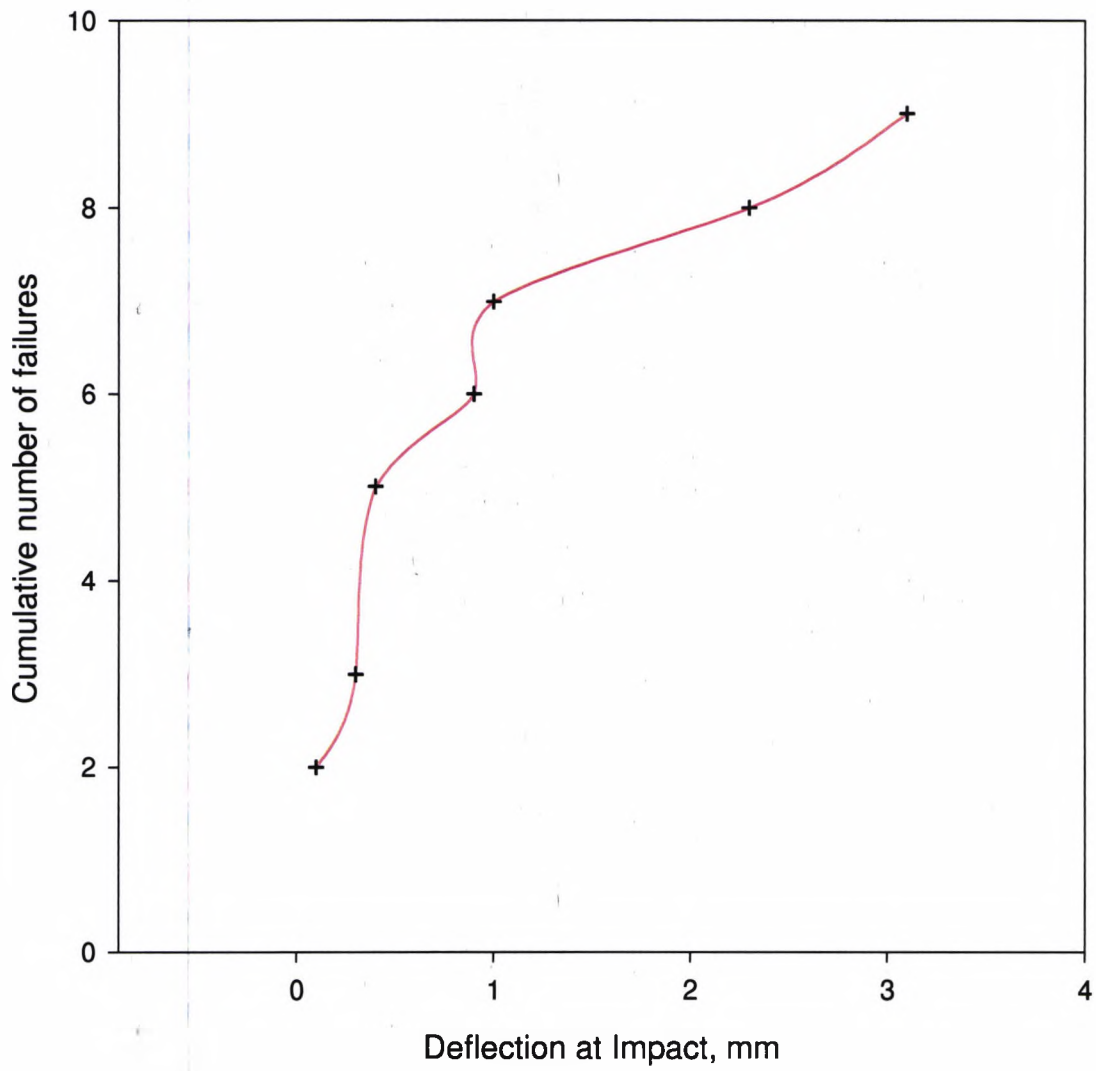
Deflection at Impact v. Cumulative number of failures
for an impact velocity of 4.75 m/s
Figure 52



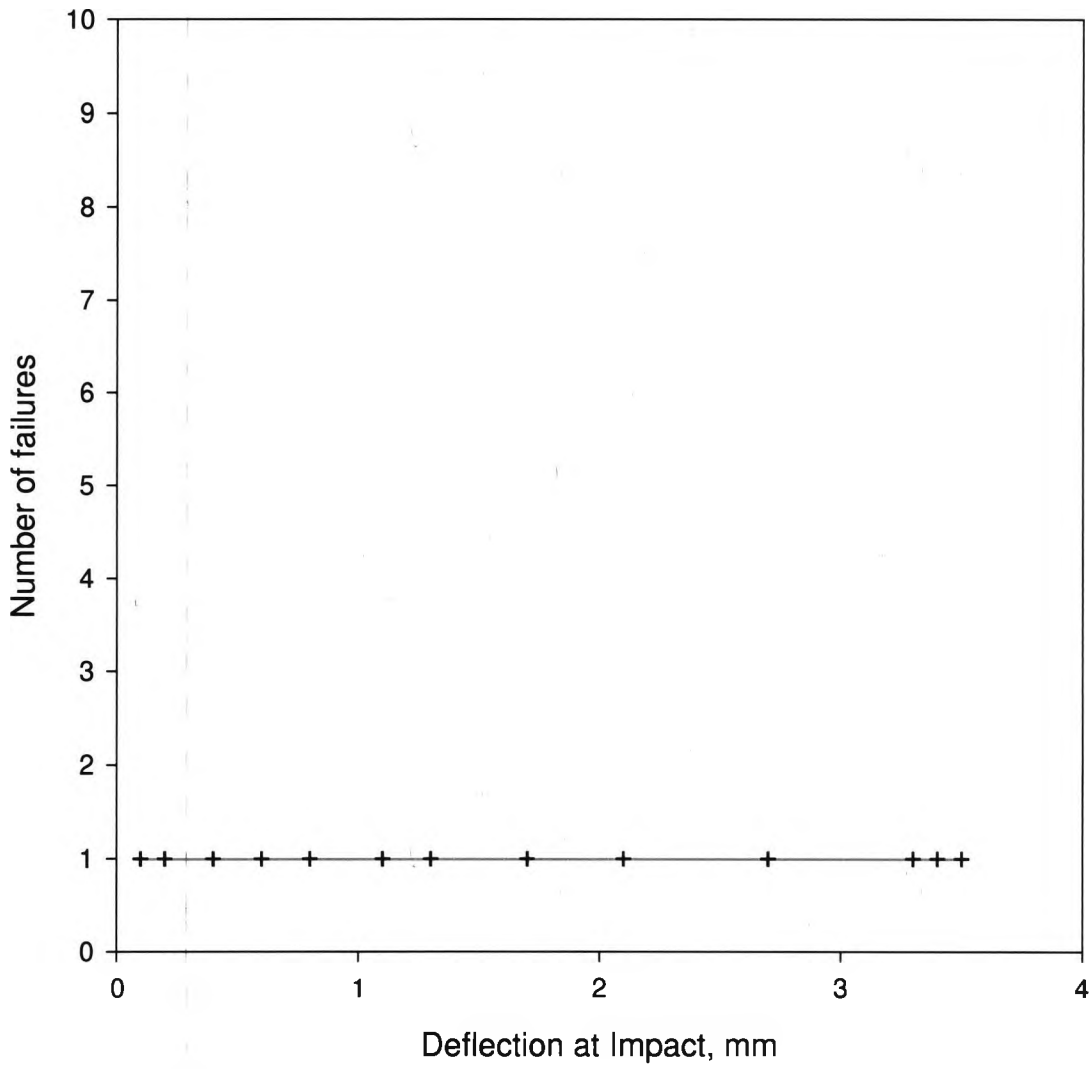
Deflection at Impact v. Number of failures for an impact velocity of 5.3 m/s
Figure 53



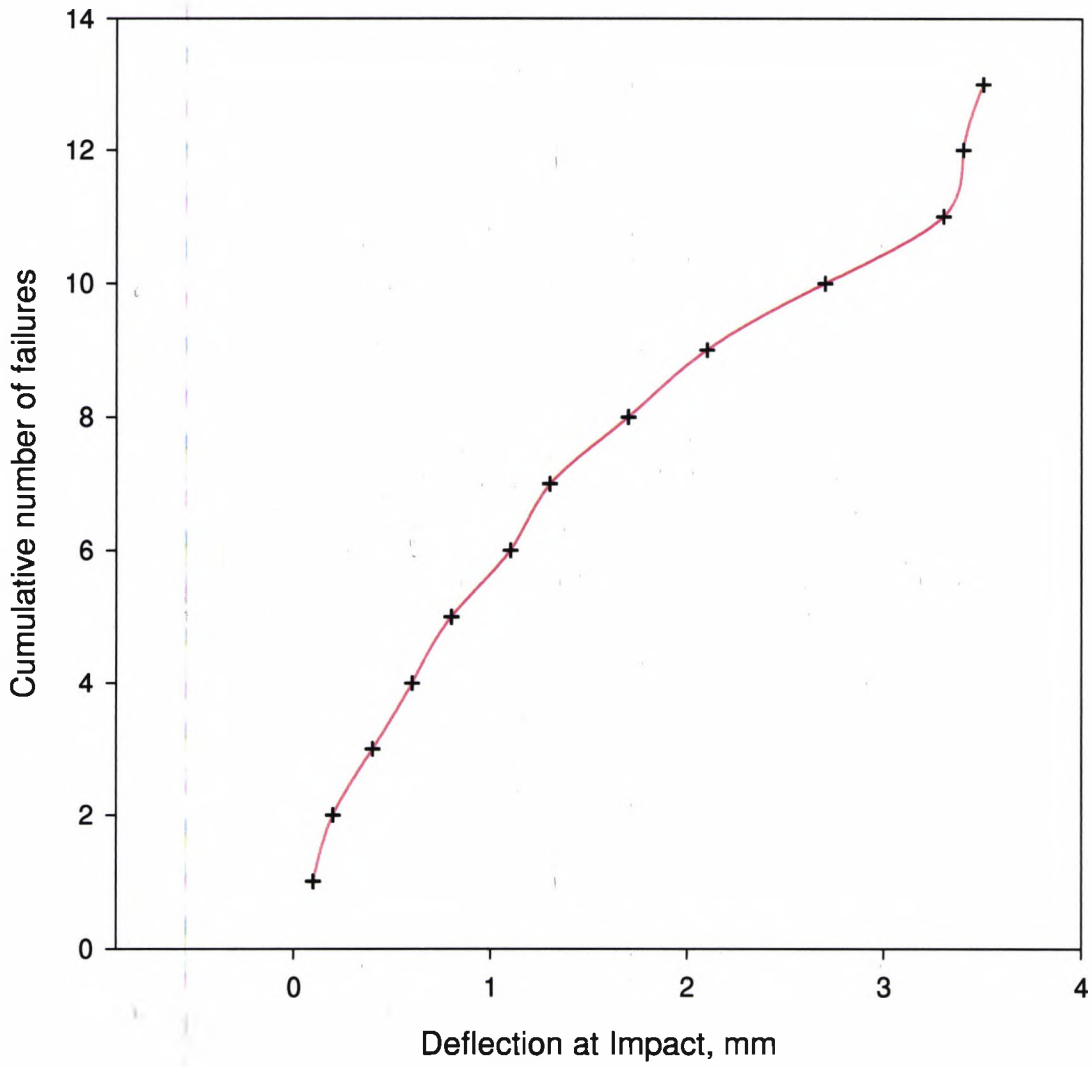
Deflection at Impact v. Cumulative number of failures
for an impact velocity of 5.3 m/s
Figure 54



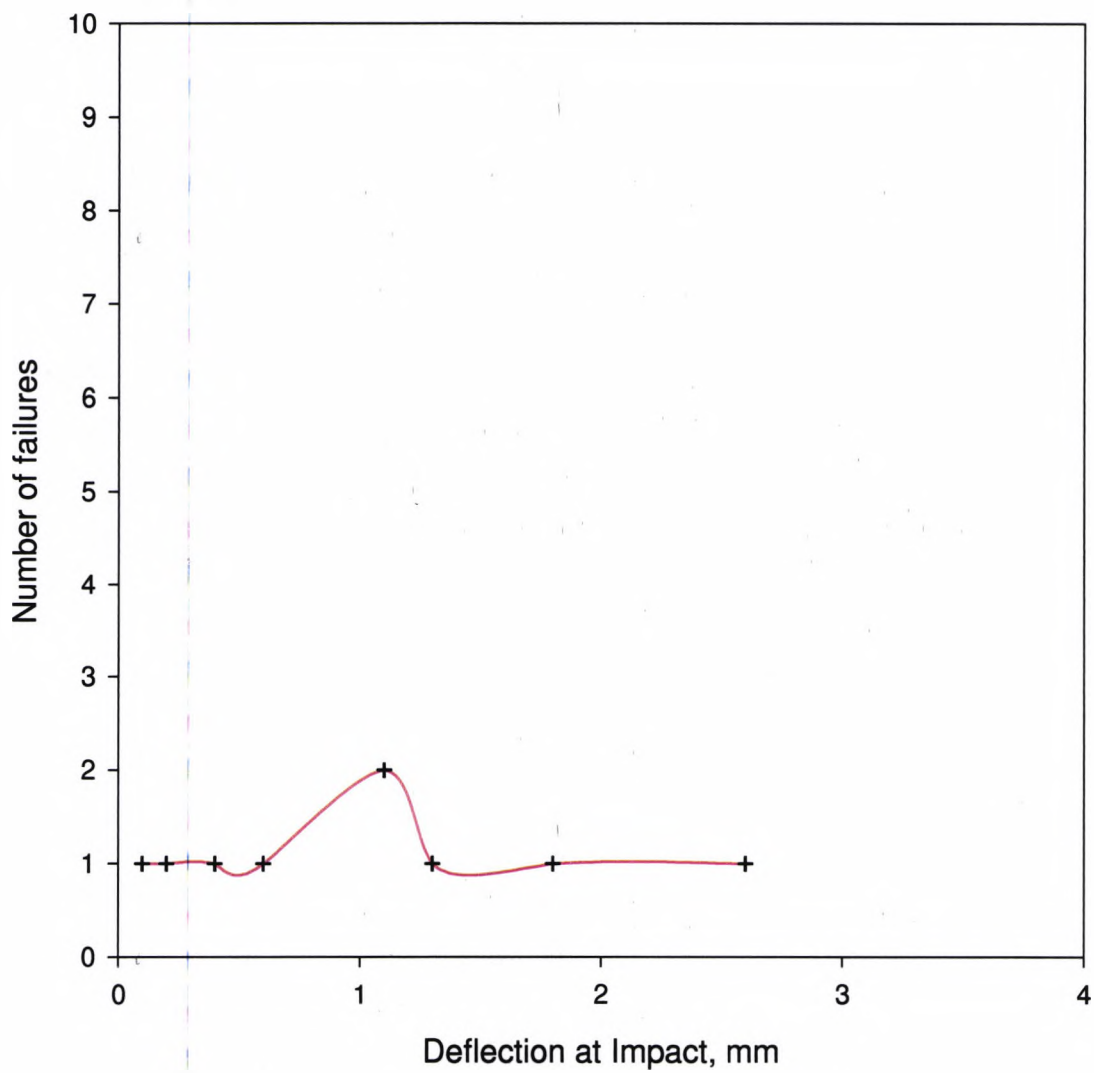
Deflection at Impact v. Number of failures for an impact velocity of 5.85 m/s
Figure 55



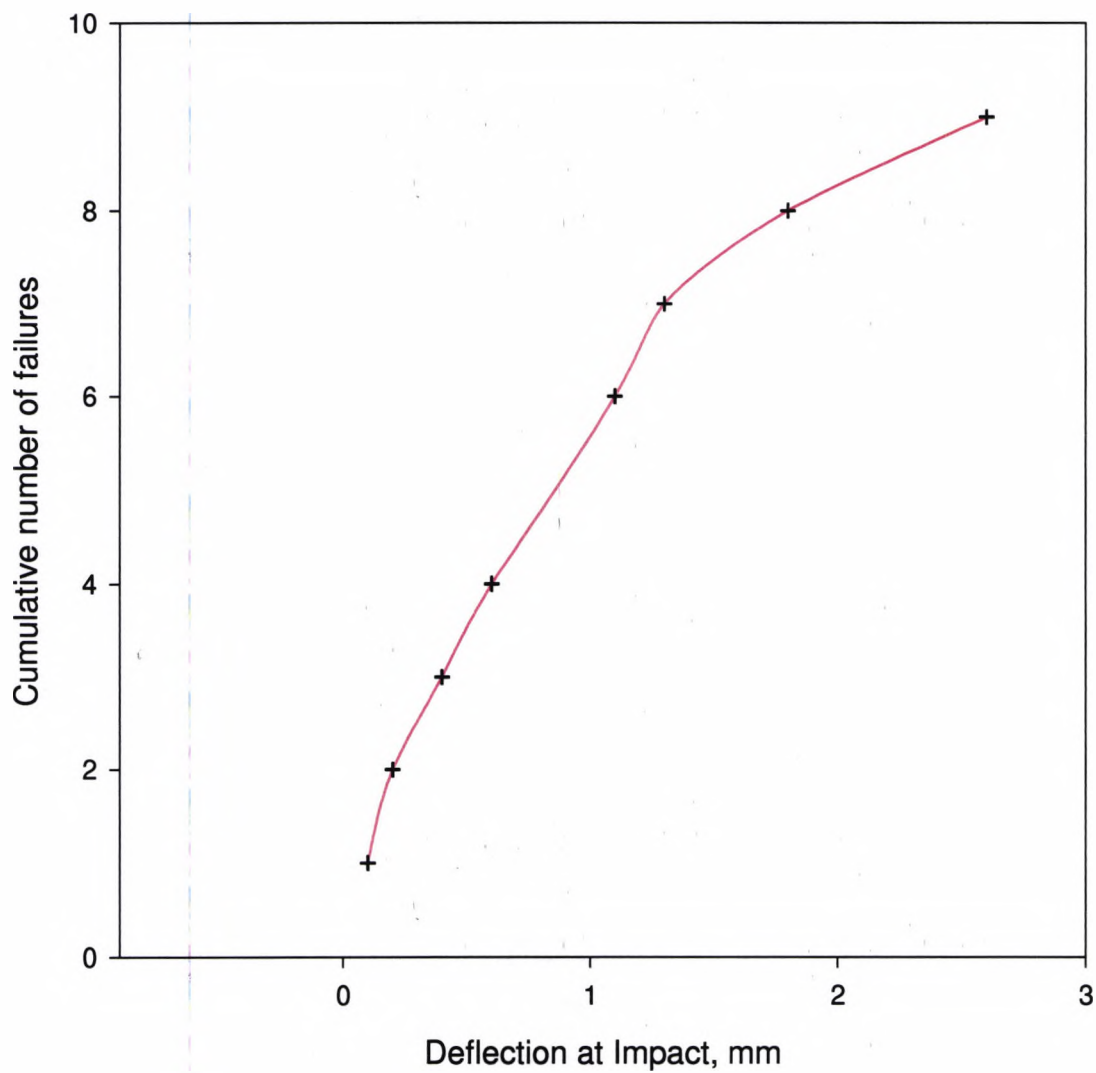
Deflection at Impact v. Cumulative number of failures
for an impact velocity of 5.85 m/s
Figure 56



Deflection at Impact v. Number of failures for an impact velocity of 6.6 m/s
Figure 57

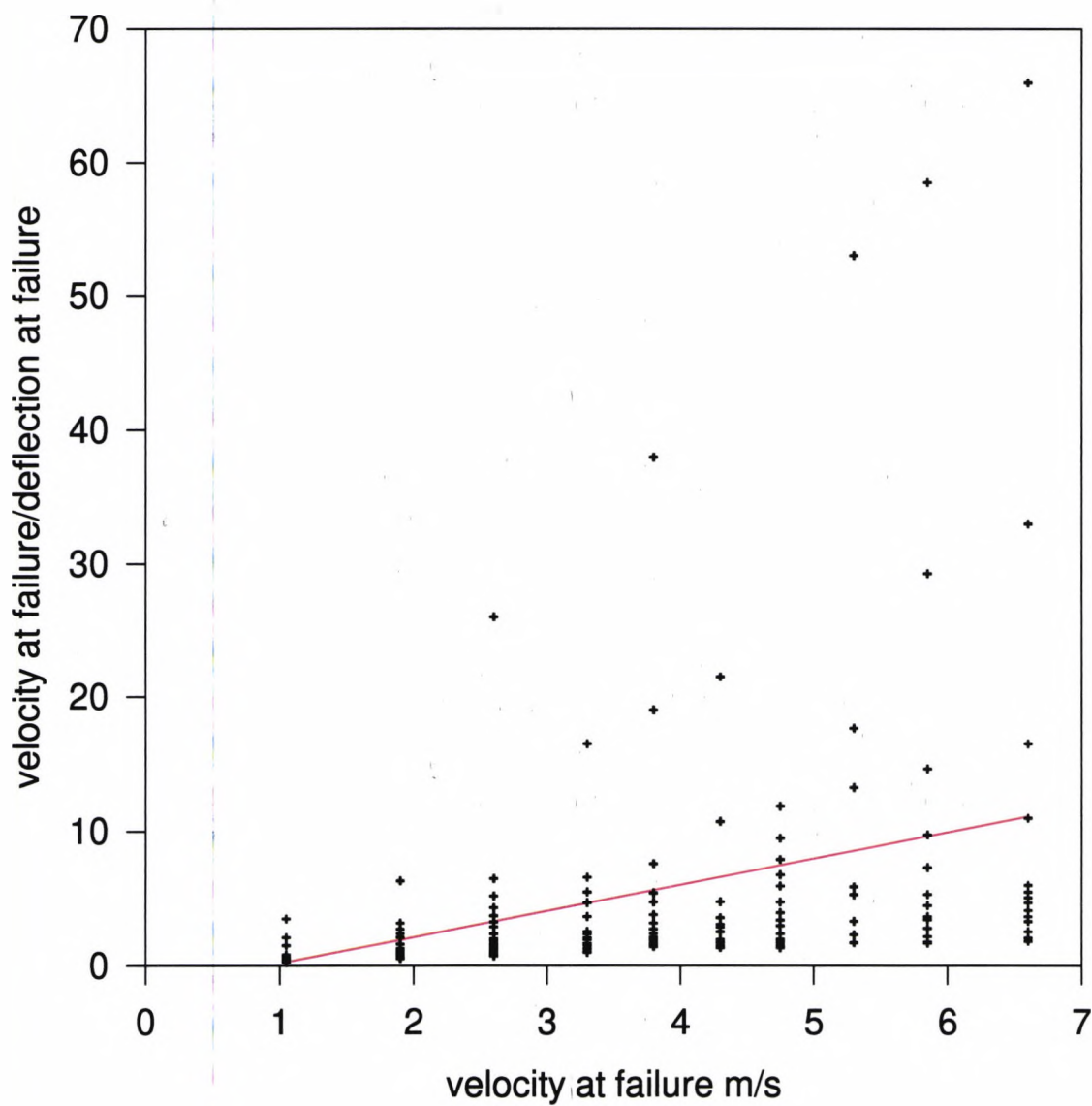


Deflection at Impact v. Cumulative number of failures
for an impact velocity of 6.6 m/s
Figure 58



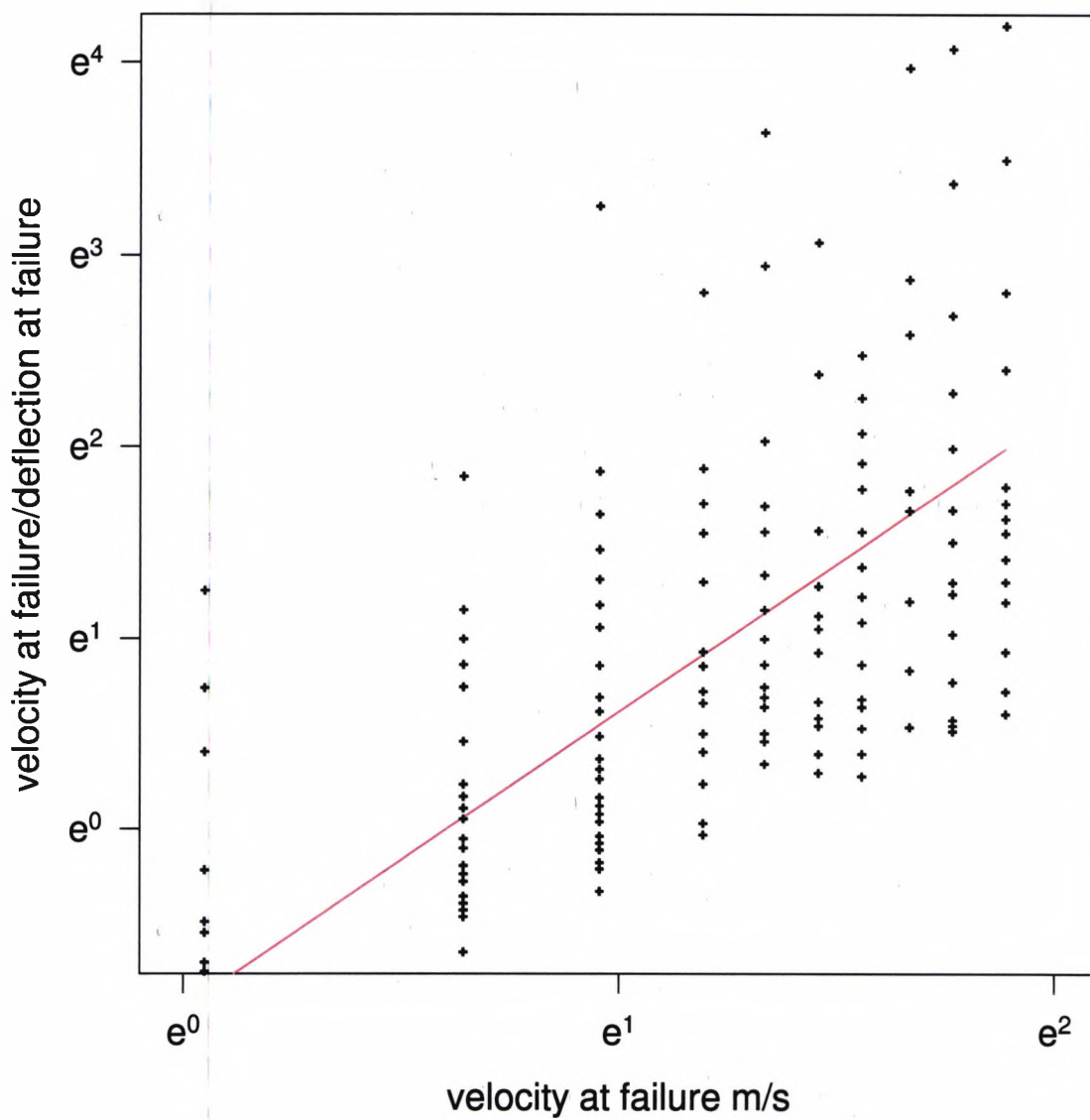
Velocity at failure v. Velocity at failure/Deflection at failure

Figure 59

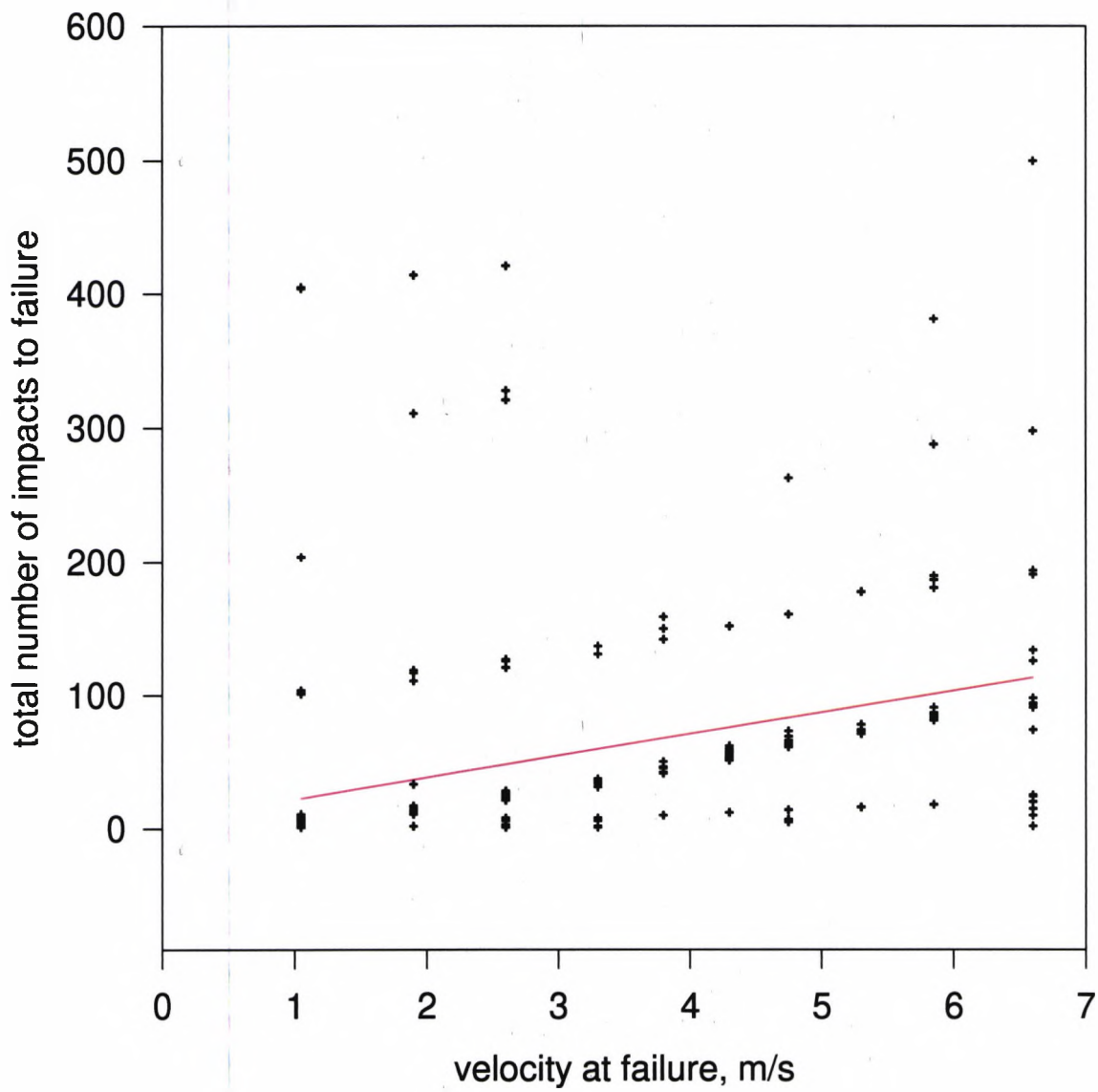


Velocity at failure v. Velocity at failure/Deflection at failure

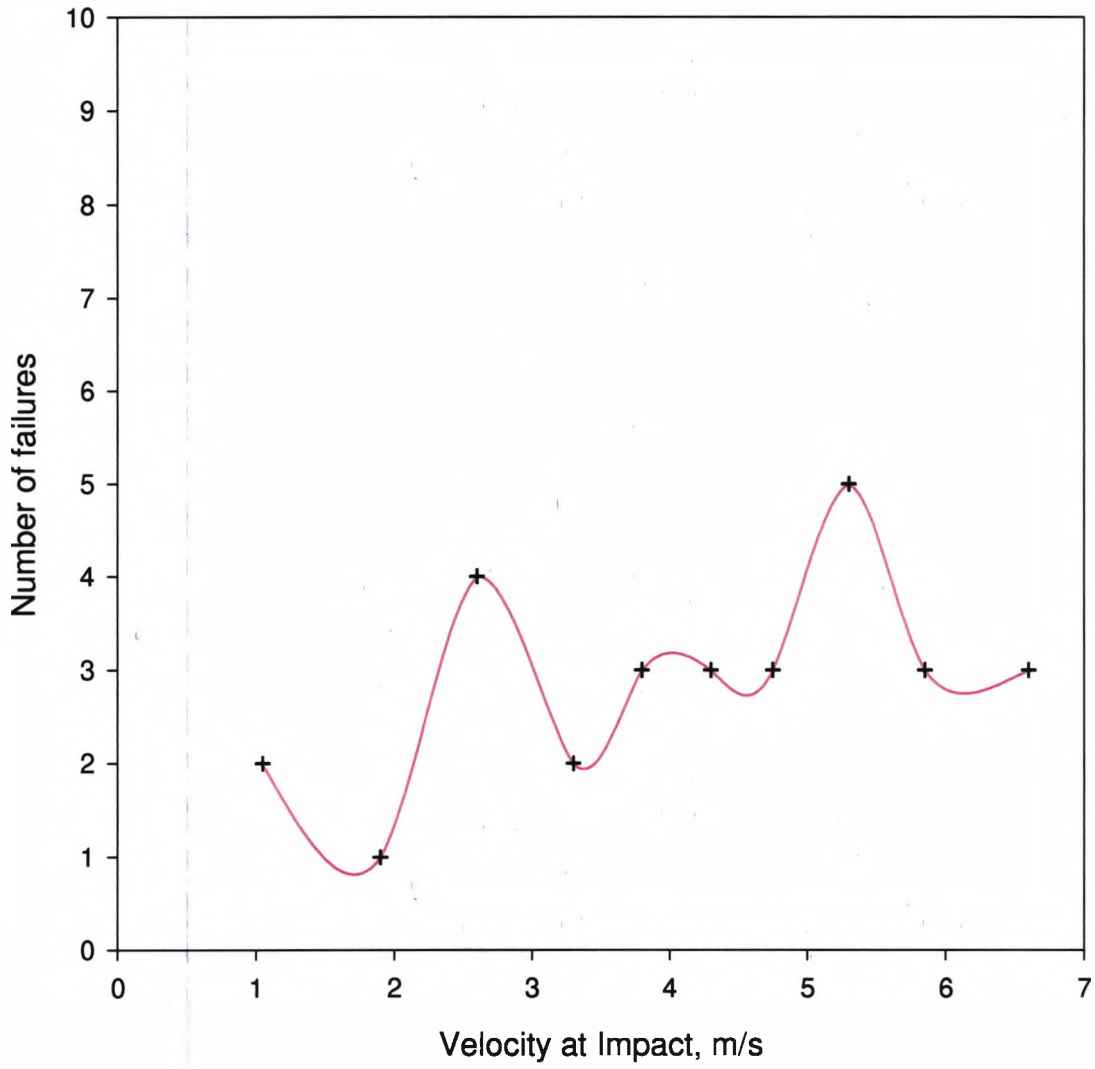
Figure 60



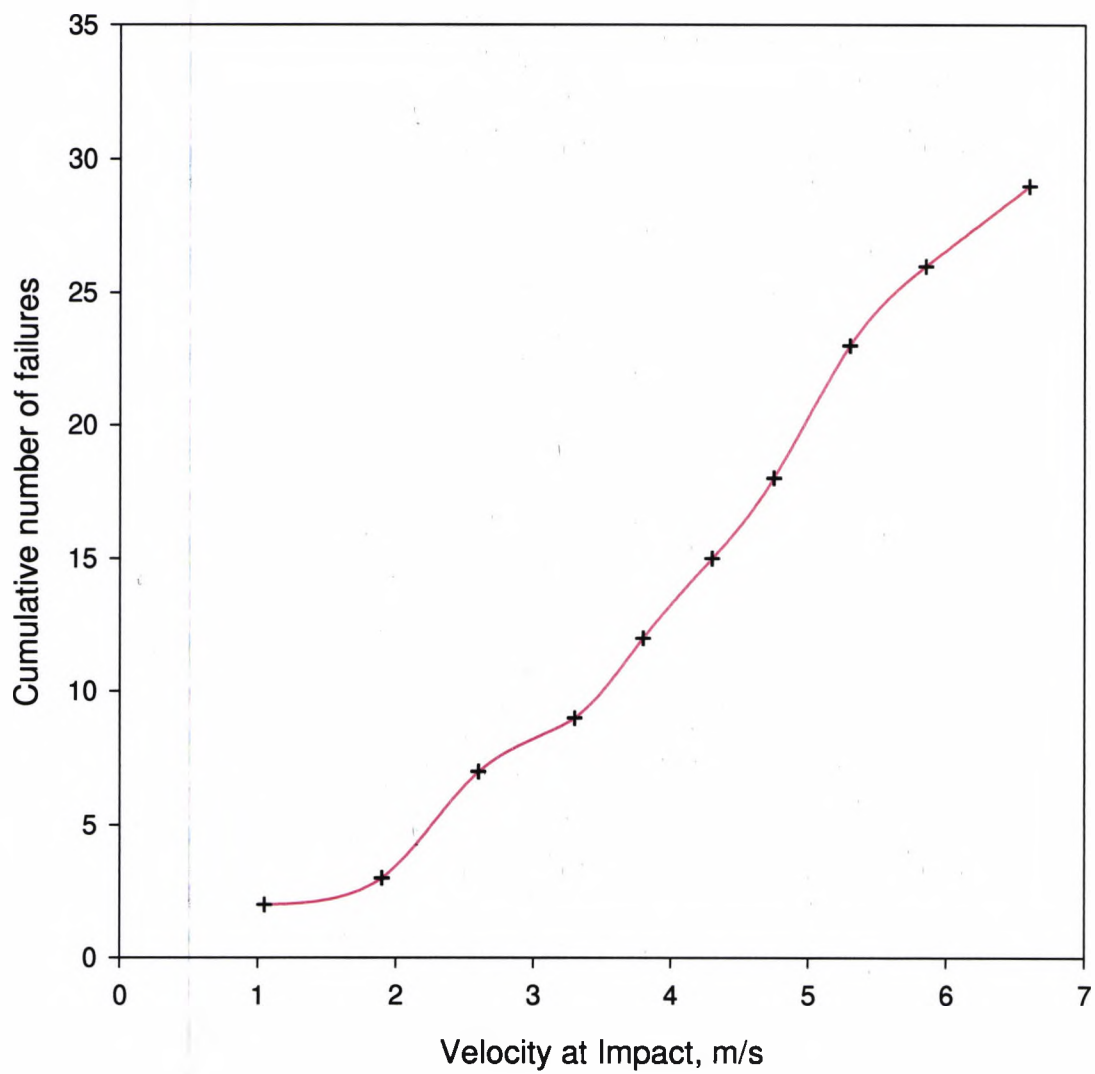
Velocity at failure v. Total number of impacts
Figure 61



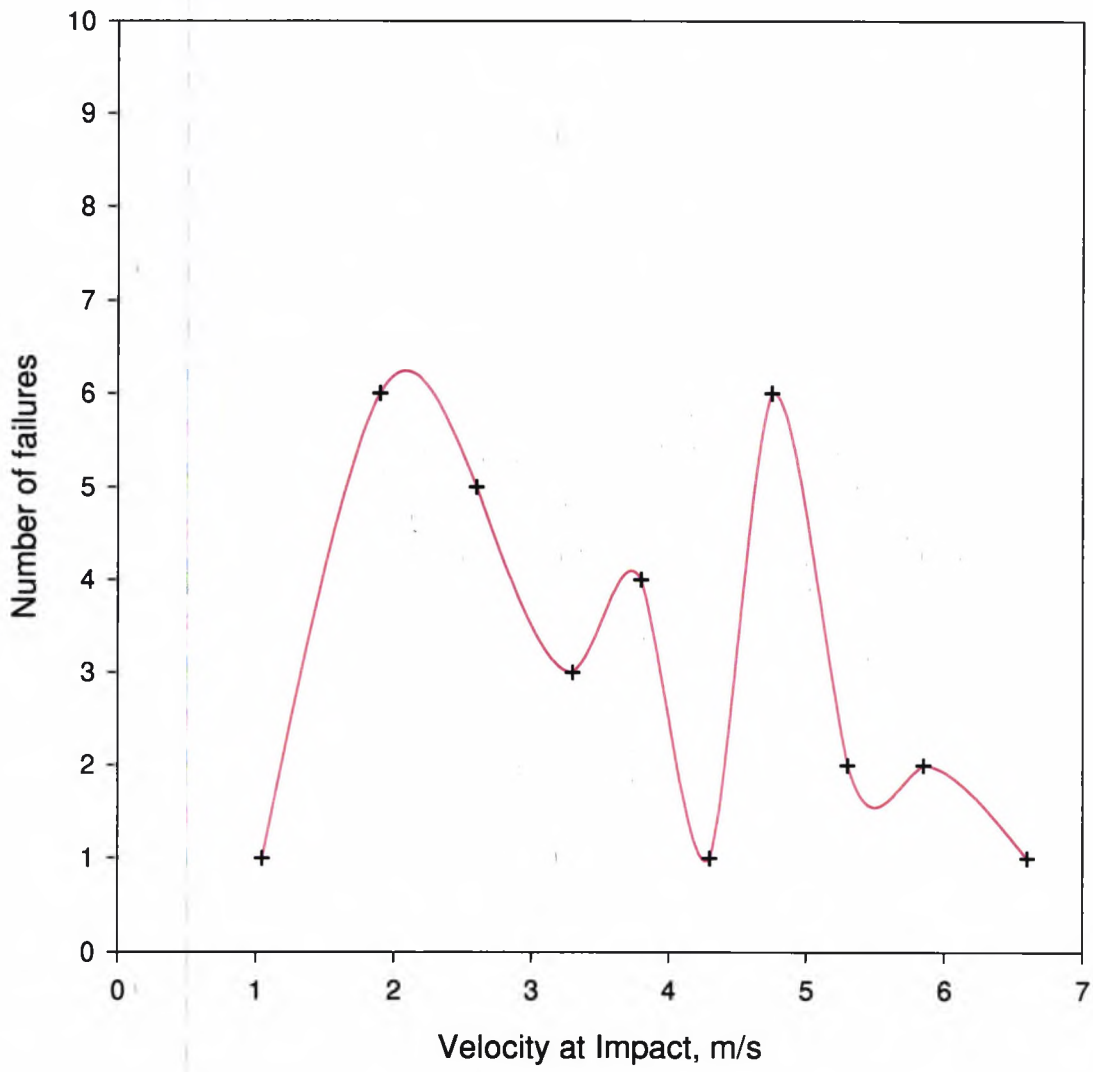
Velocity at Impact v. Number of failures for a deflection of 0 to 0.5 mm
Figure 62



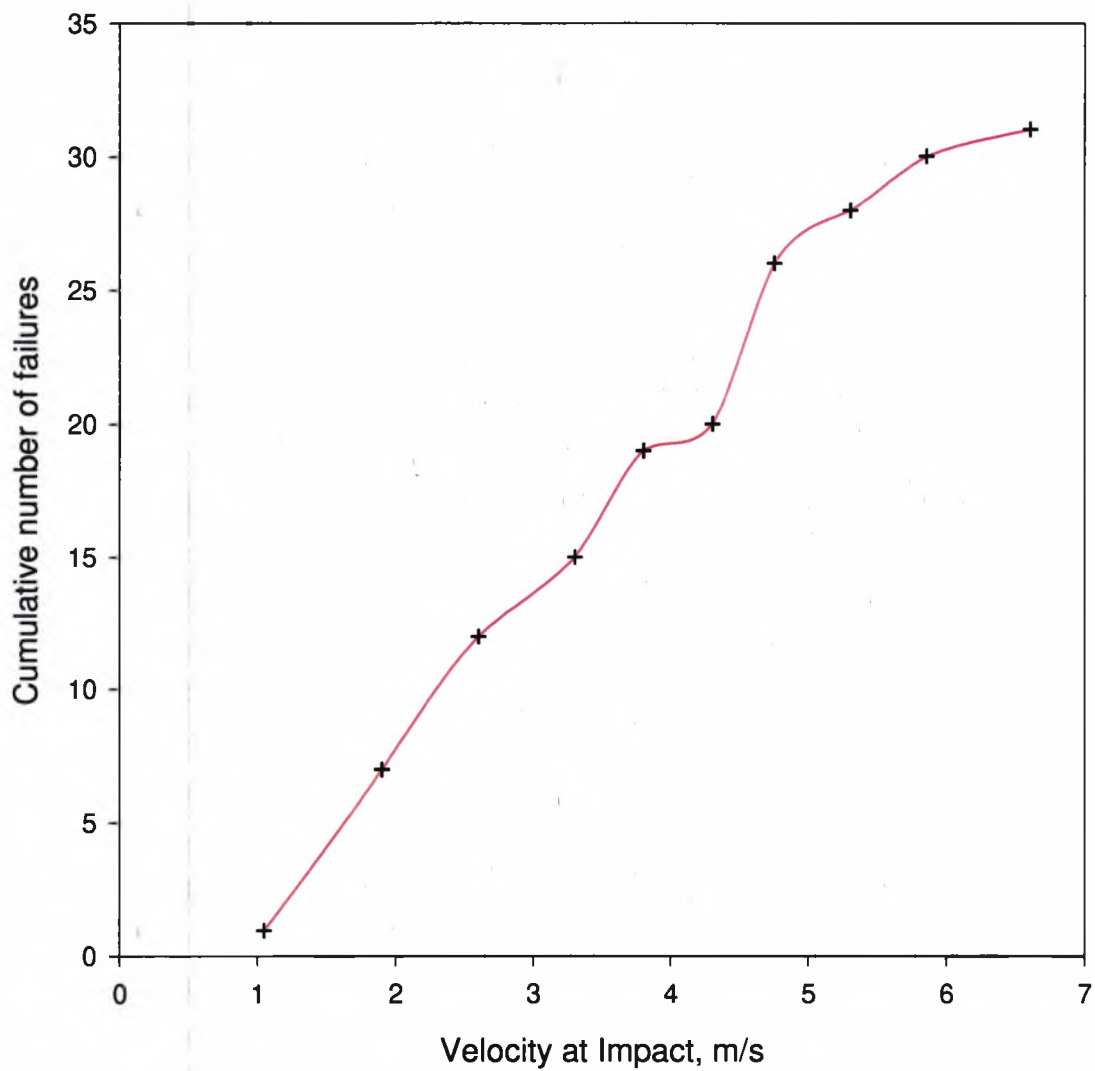
Velocity at Impact v. Cumulative Number of failures for a deflection of 0 to 0.5 mm
Figure 63



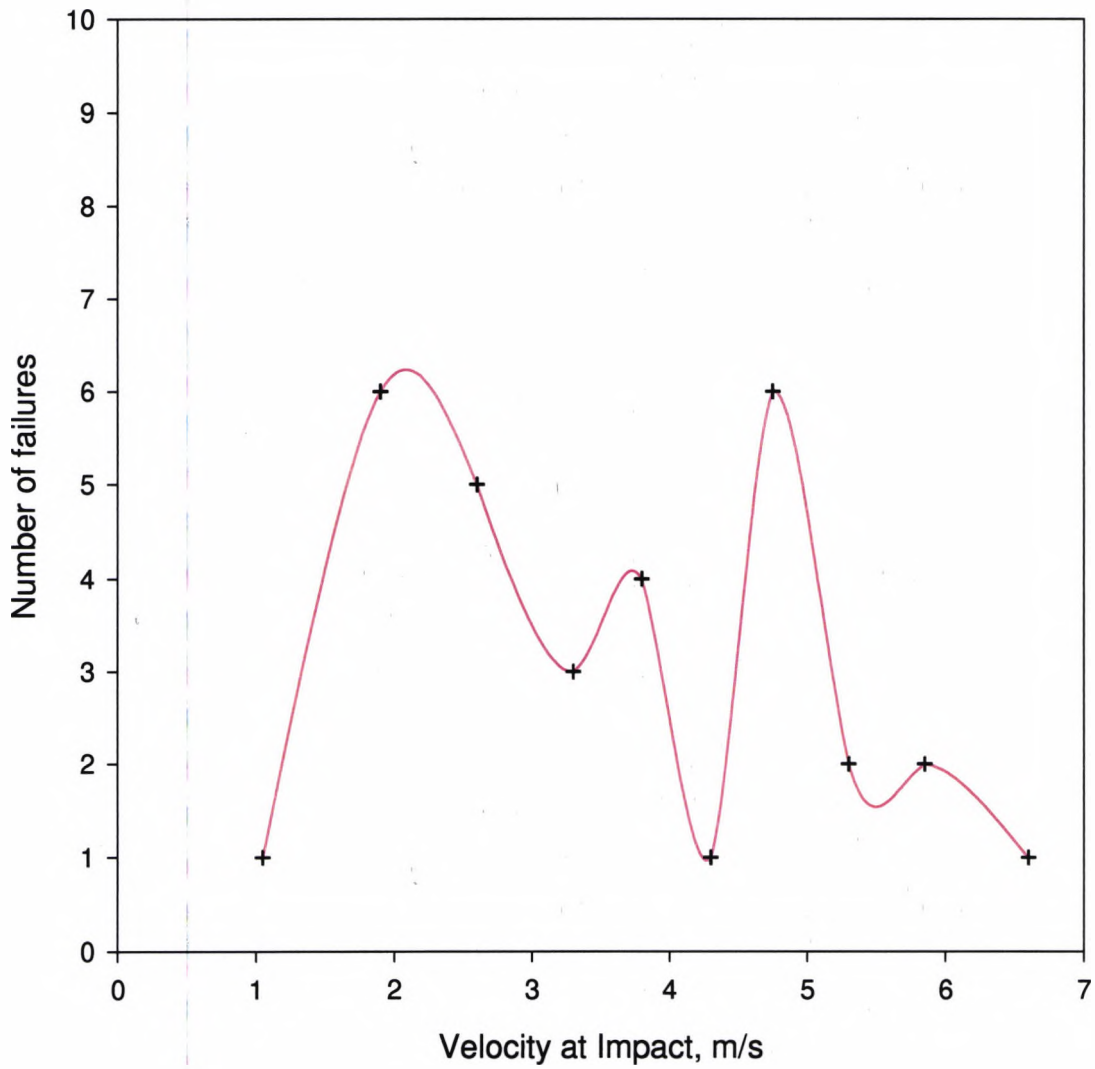
Velocity at Impact v. Number of failures for a deflection of 0.6 to 1.0 mm
Figure 64



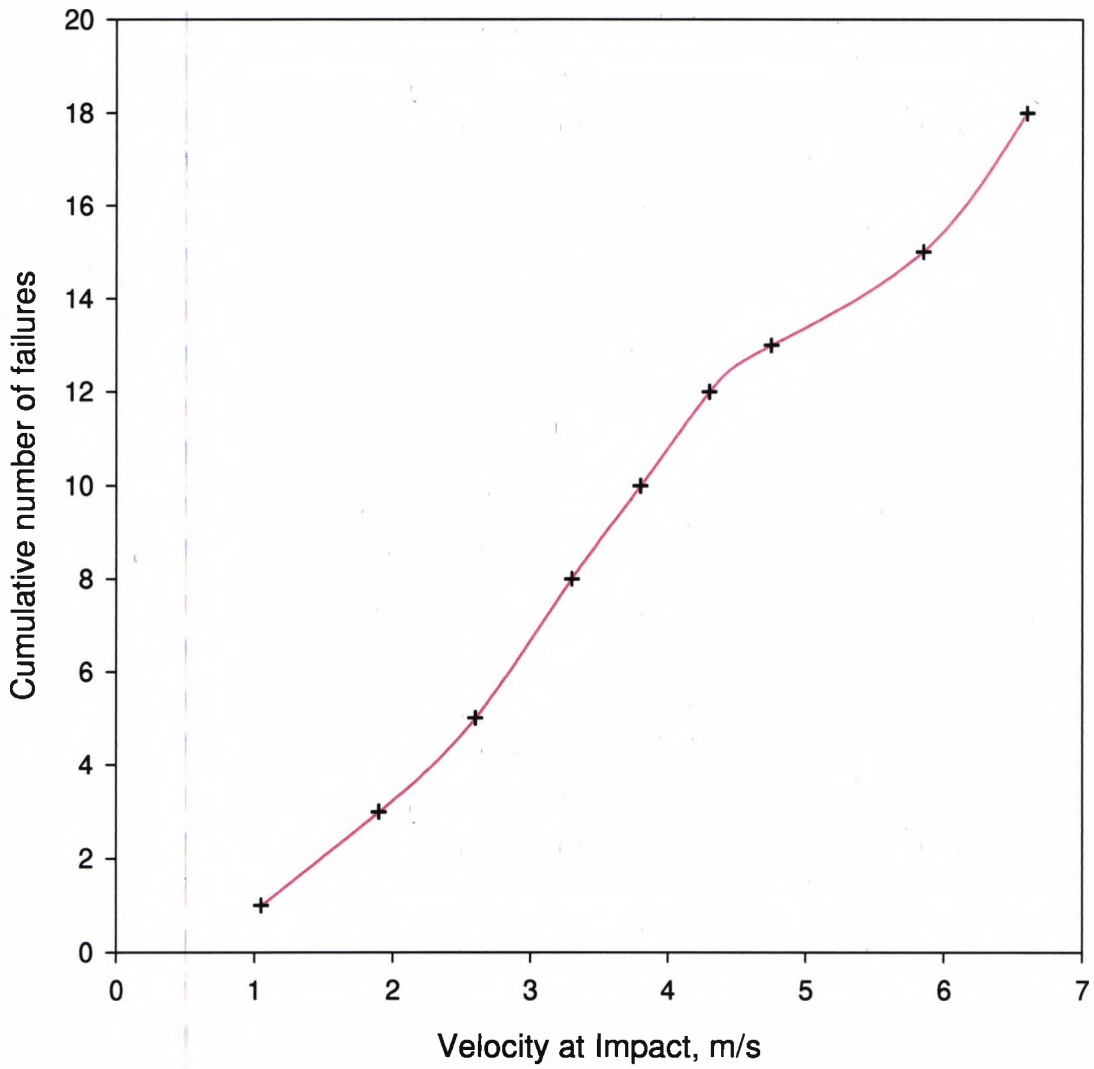
Velocity at Impact v. Cumulative Number of failures for a deflection of 0.6 to 1.0 mm
Figure 65



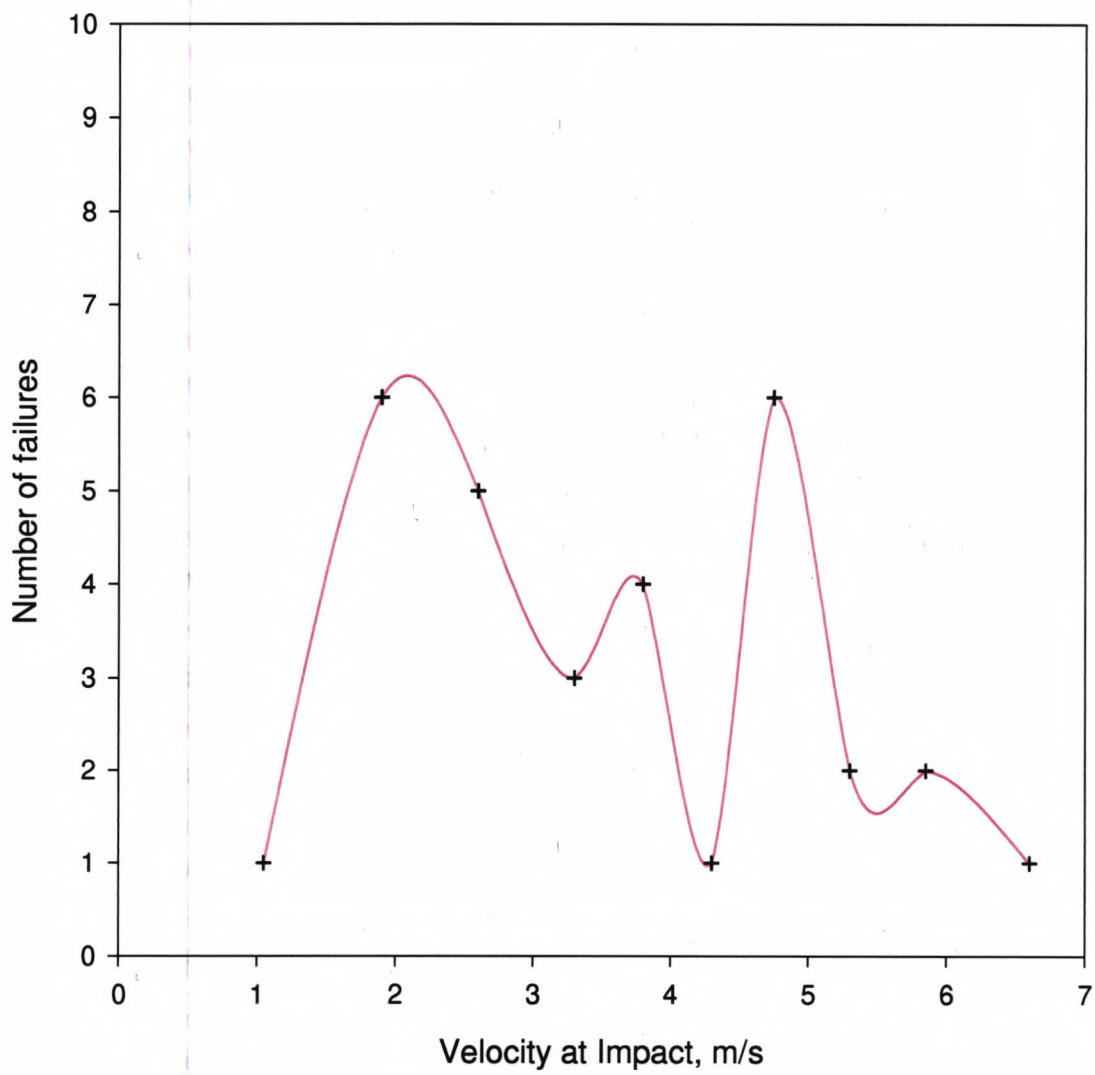
Velocity at Impact v. Number of failures for a deflection of 1.1 to 1.5 mm
Figure 66



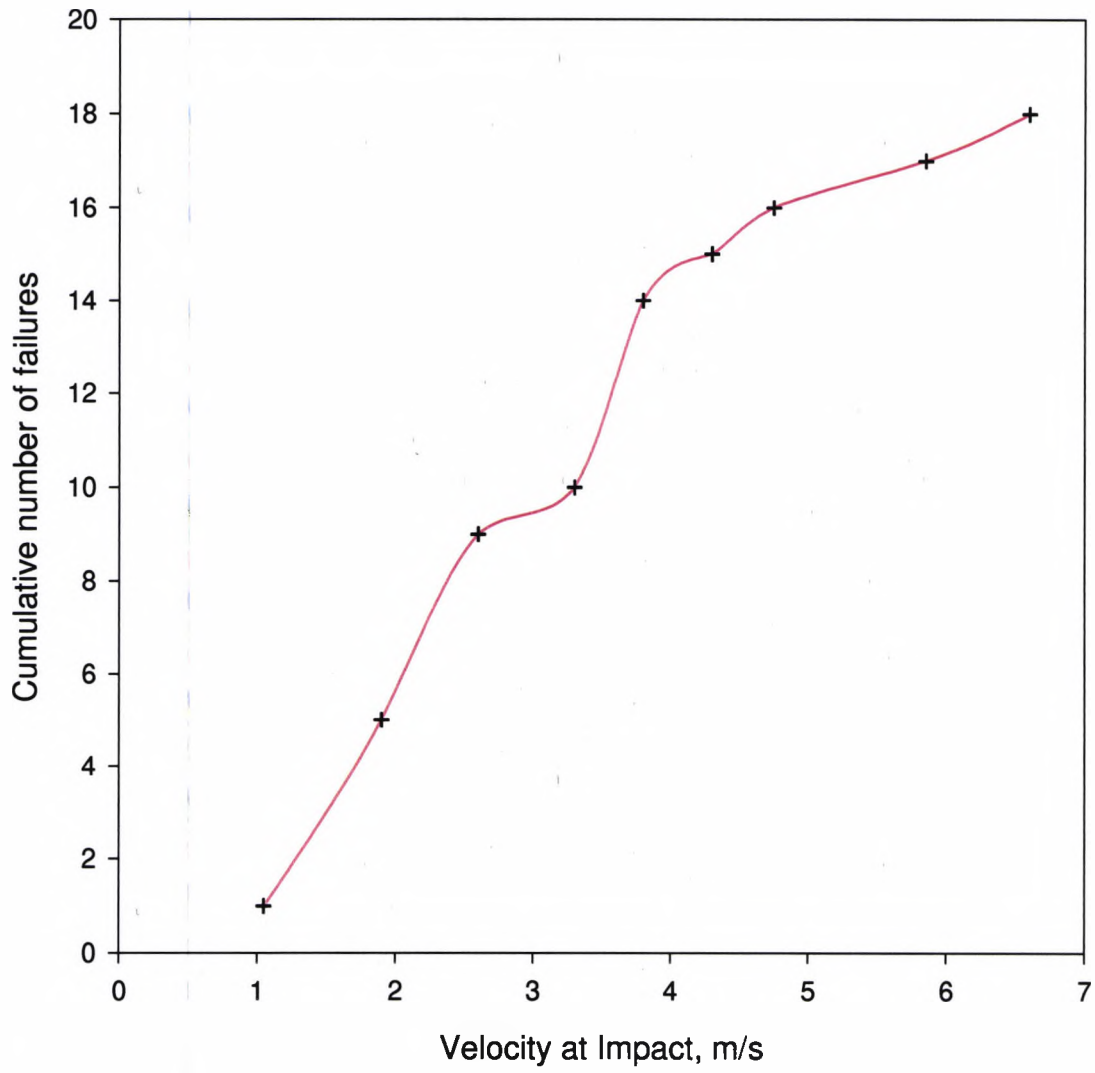
Velocity at Impact v. Cumulative Number of failures for a deflection of 1.1 to 1.5 mm
Figure 67



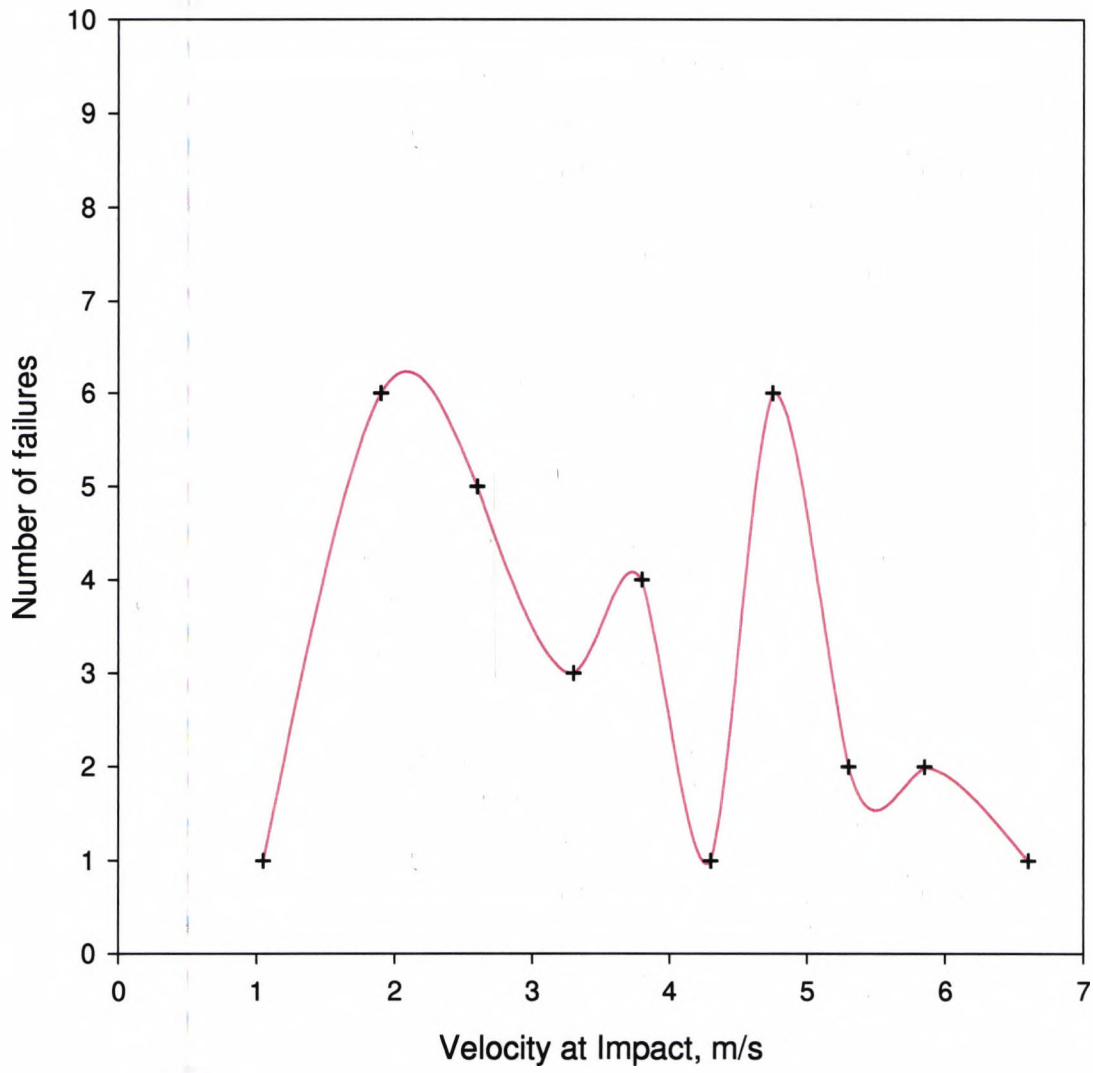
Velocity at Impact v. Number of failures for a deflection of 1.6 to 2.0 mm
Figure 68



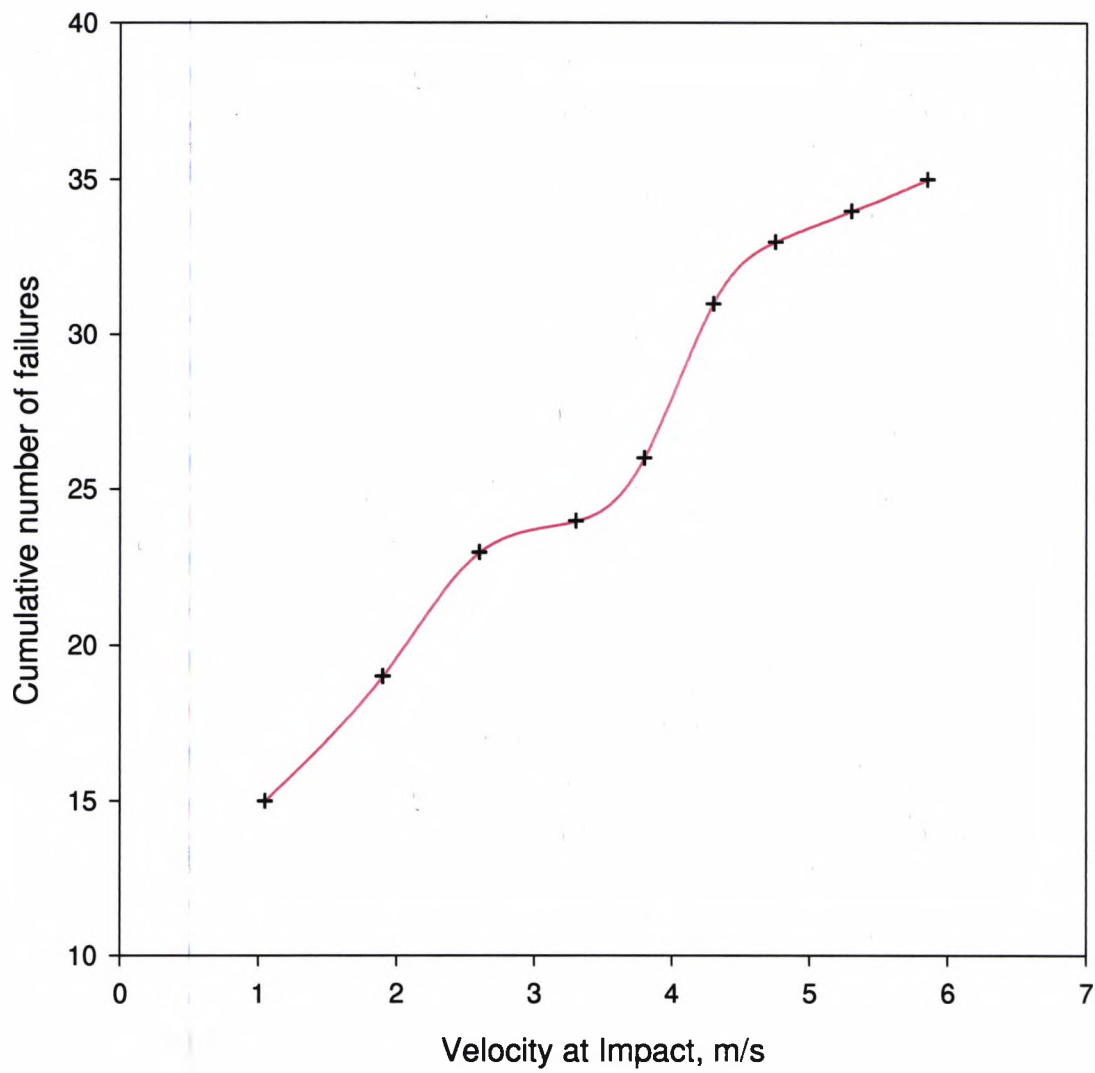
Velocity at Impact v. Cumulative Number of failures for a deflection of 1.6 to 2.0 mm
Figure 69



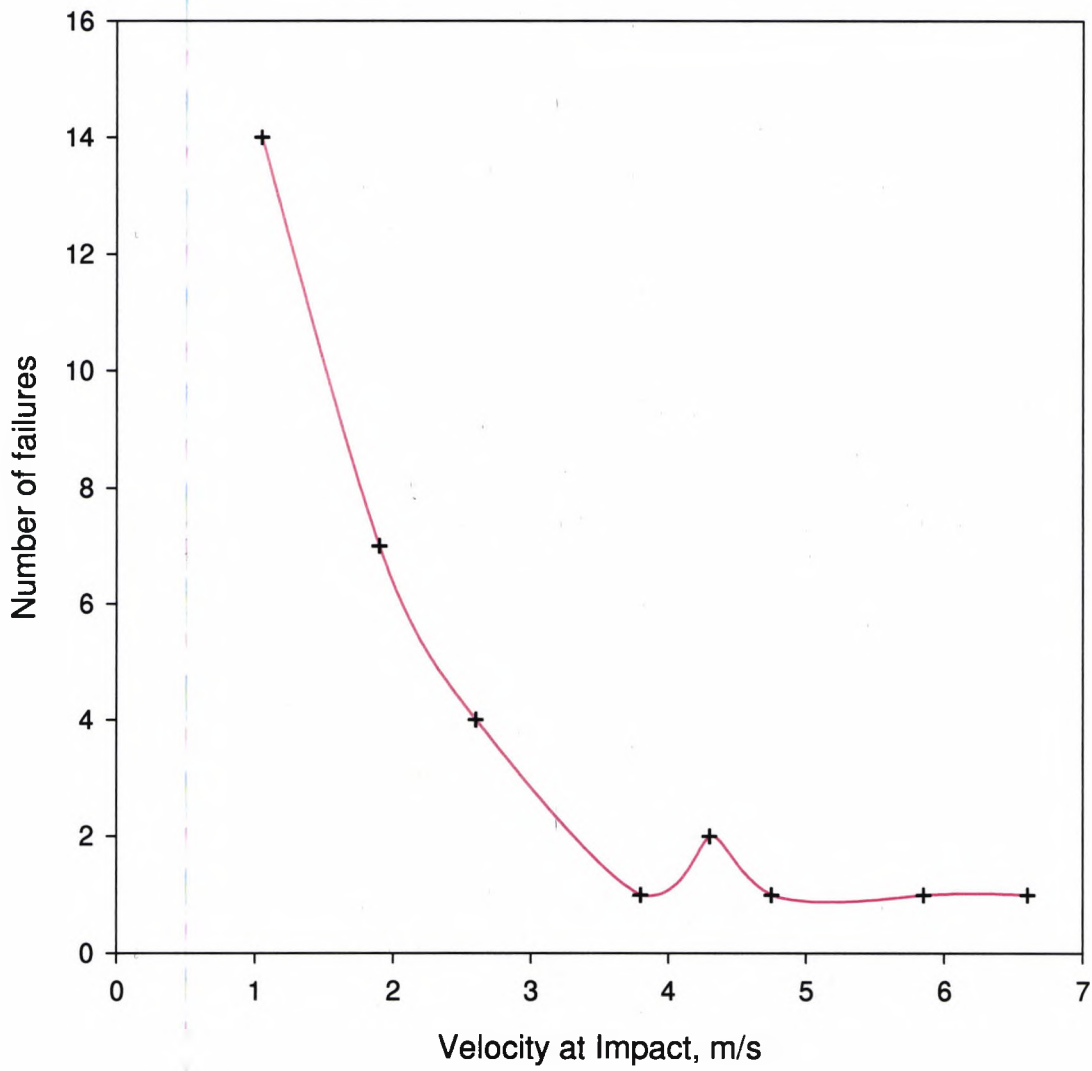
Velocity at Impact v. Number of failures for a deflection of 2.1 to 2.5 mm
Figure 70



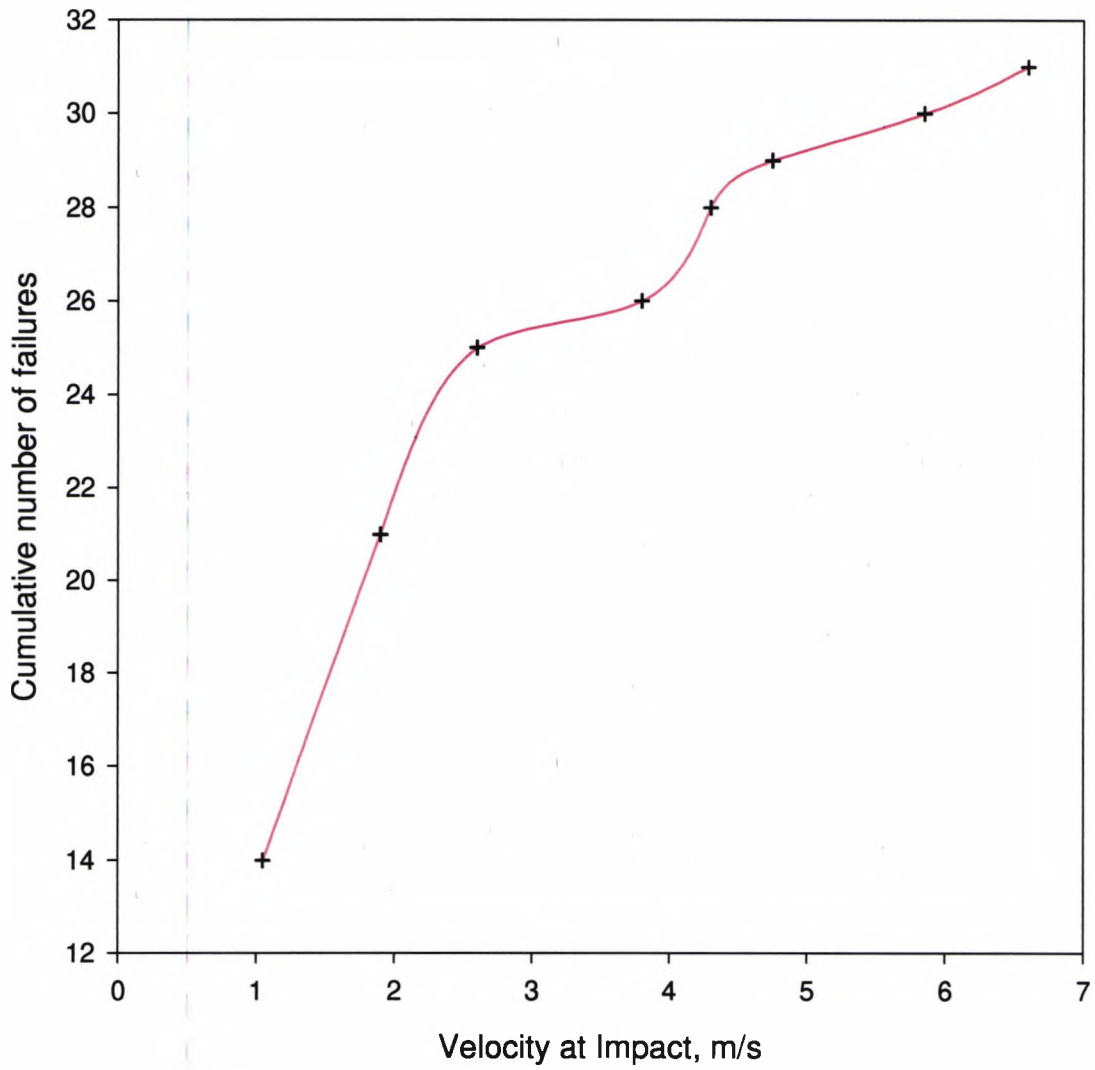
Velocity at Impact v. Cumulative Number of failures for a deflection of 2.0 to 2.5 mm
Figure 71



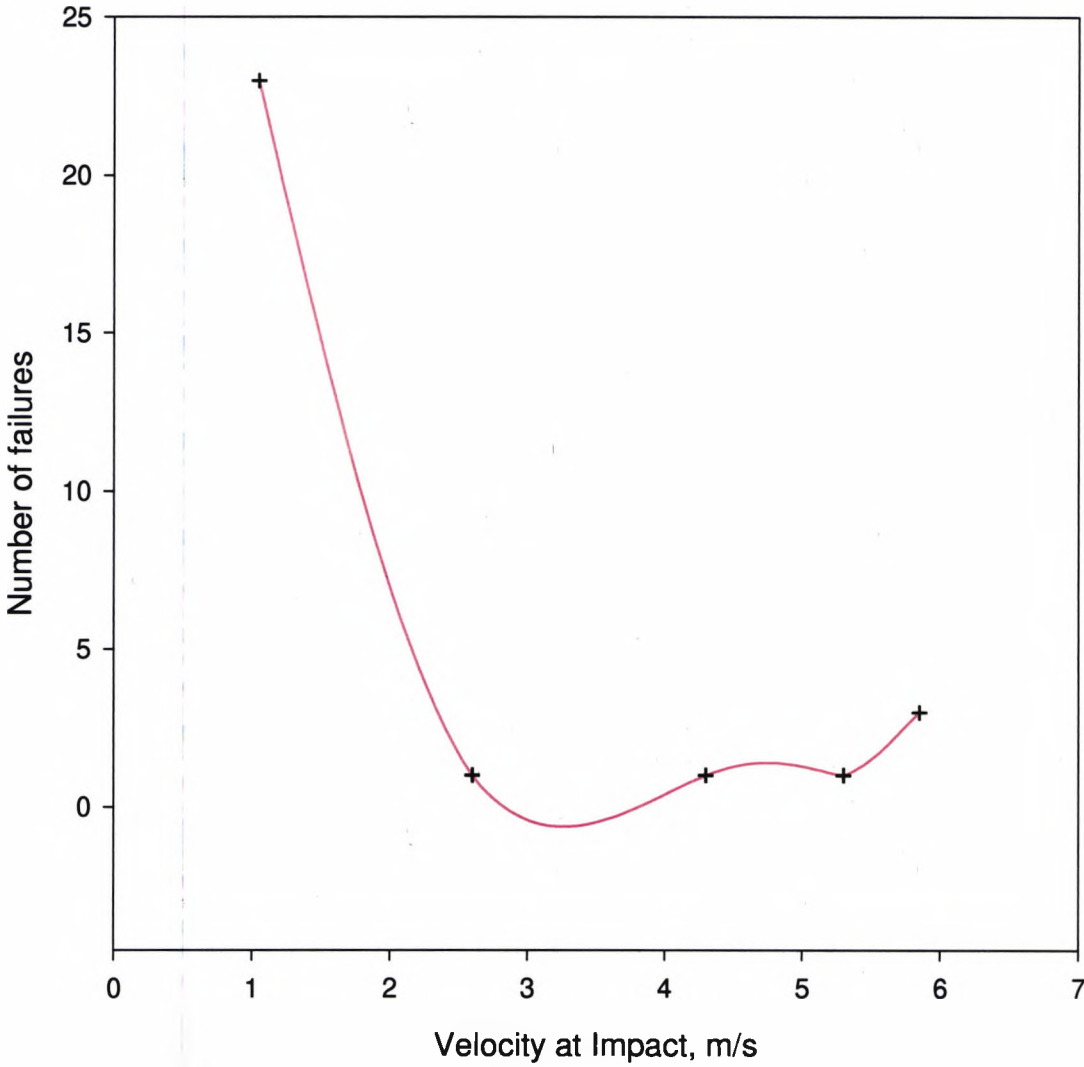
Velocity at Impact v. Number of failures for a deflection of 2.6 to 3.0 mm
Figure 72



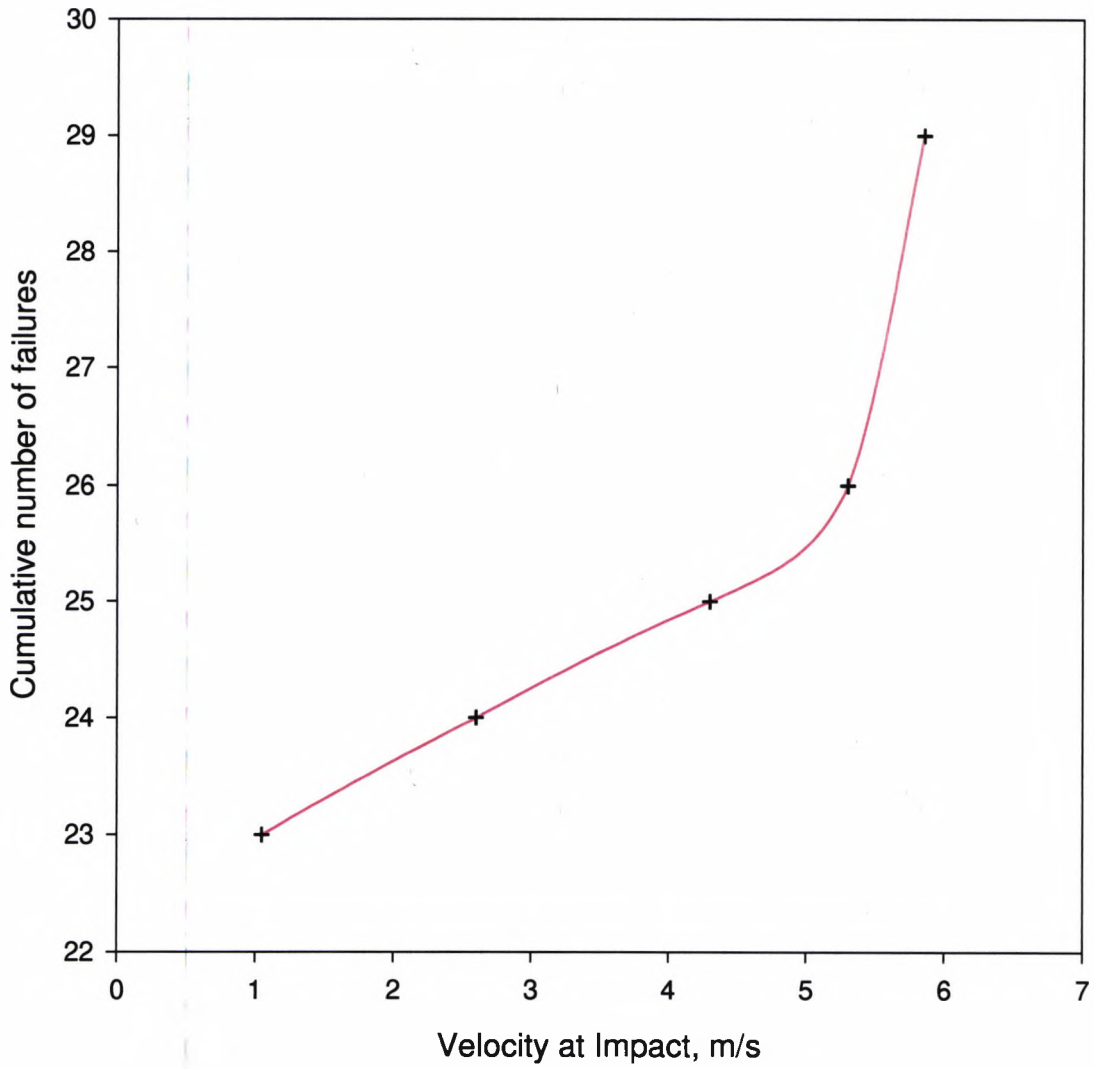
Velocity at Impact v. Cumulative Number of failures for a deflection of 2.6 to 3.0 mm
Figure 73



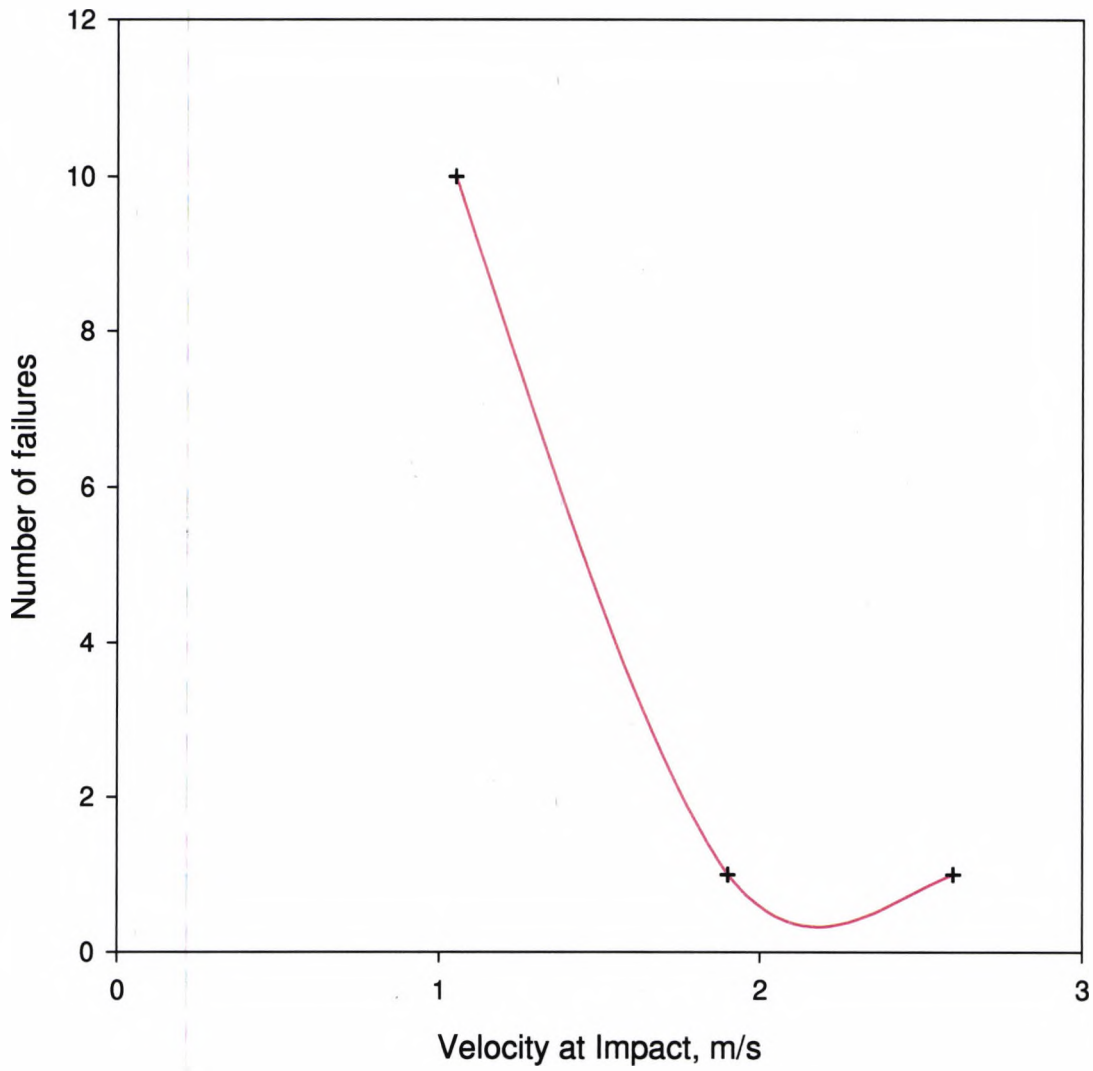
Velocity at Impact v. Number of failures for a deflection of 3.1 to 3.5 mm
Figure 74



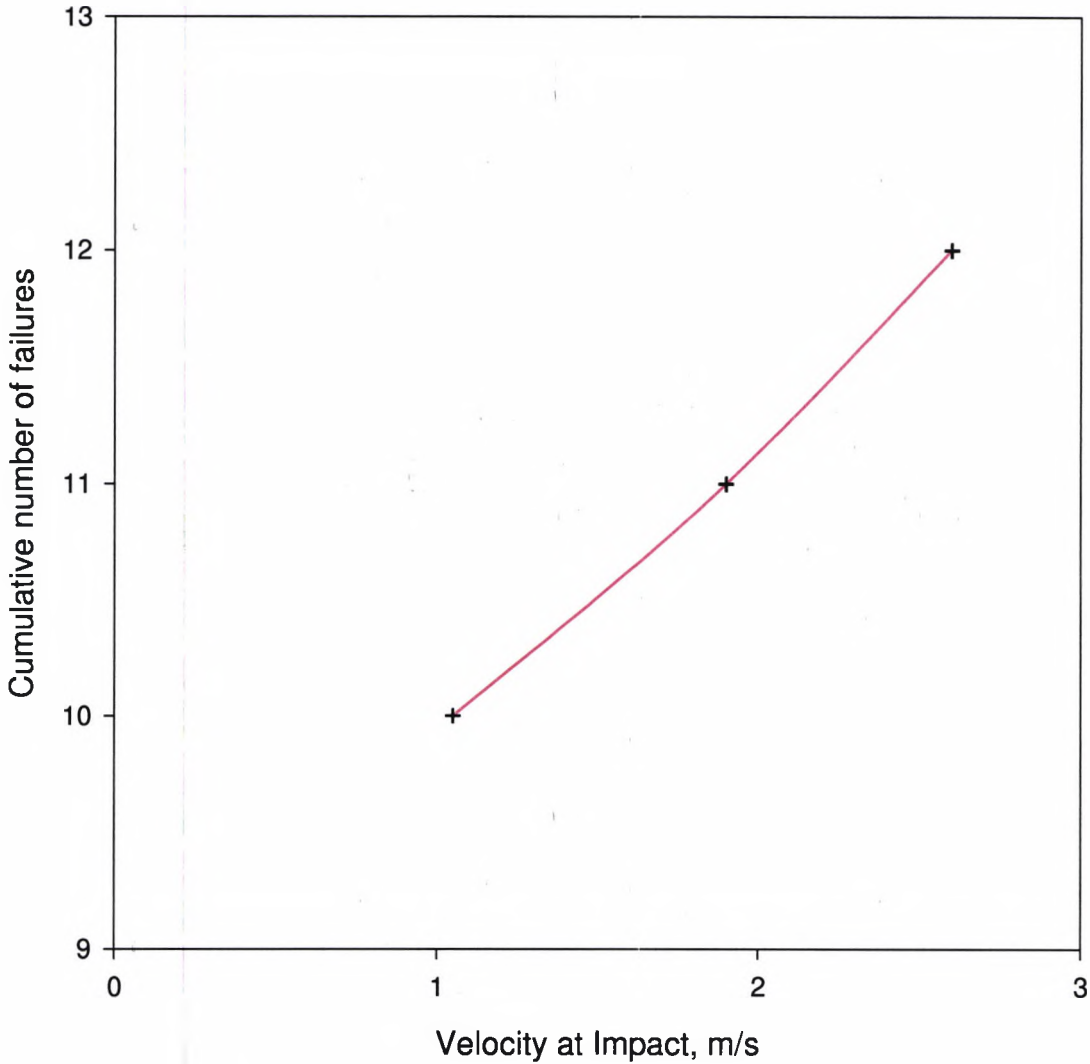
Velocity at Impact v. Cumulative Number of failures for a deflection of 3.1 to 3.5 mm
Figure 75



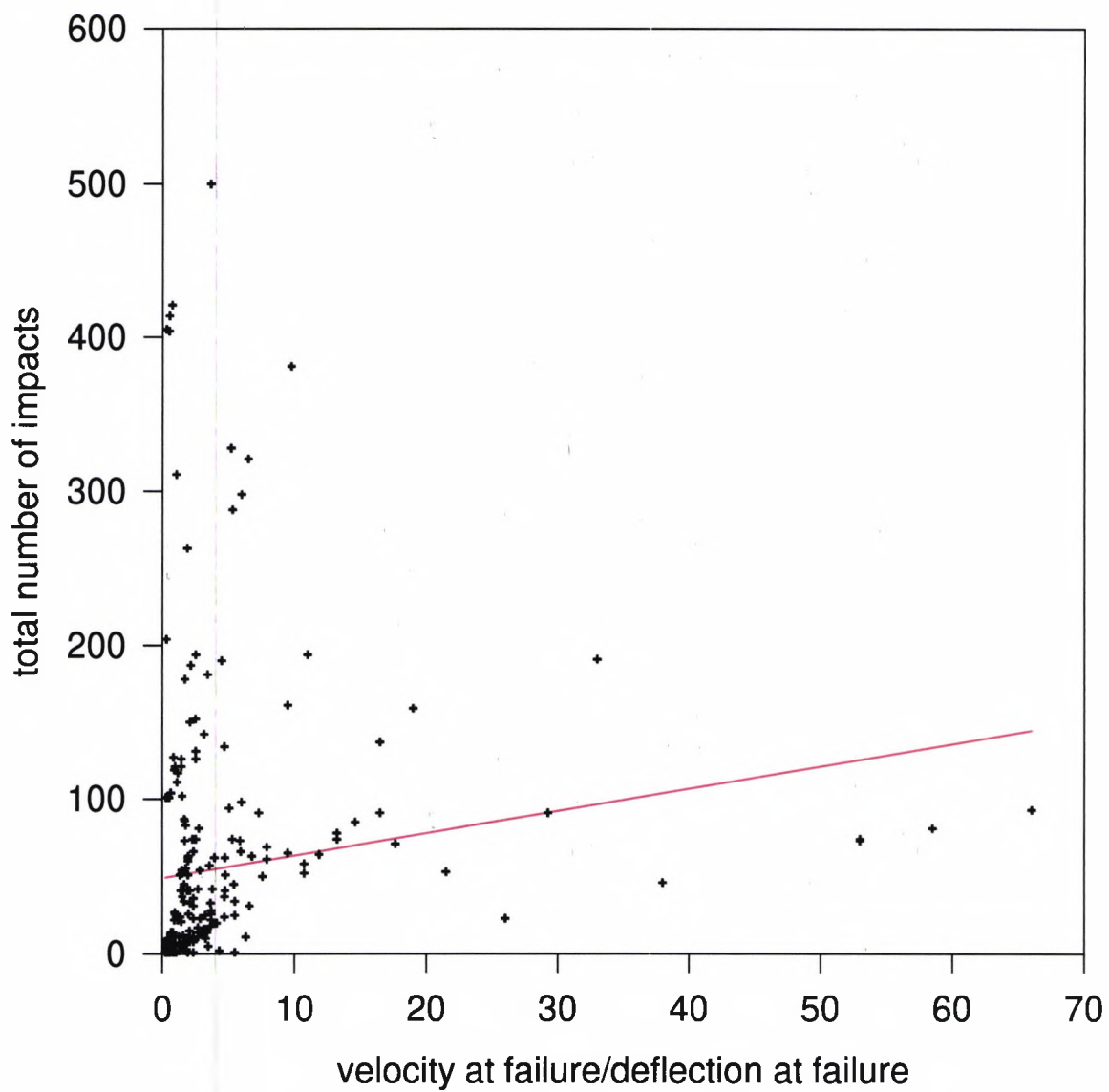
Velocity at Impact v. Number of failures for a deflection of 3.6 to 3.8 mm
Figure 76



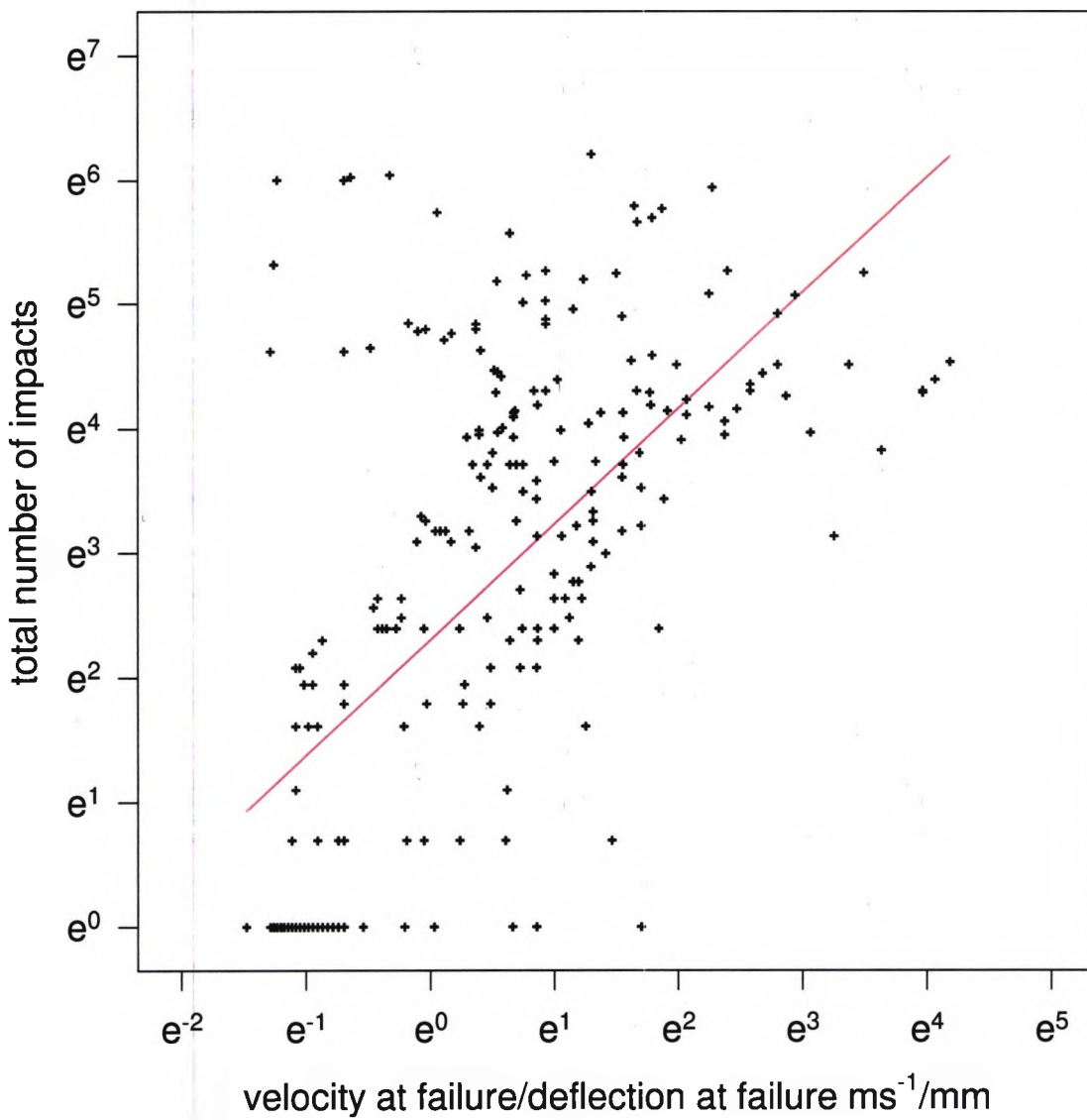
Velocity at Impact v. Cumulative Number of failures for a deflection of 3.6 to 3.8 mm
Figure 77



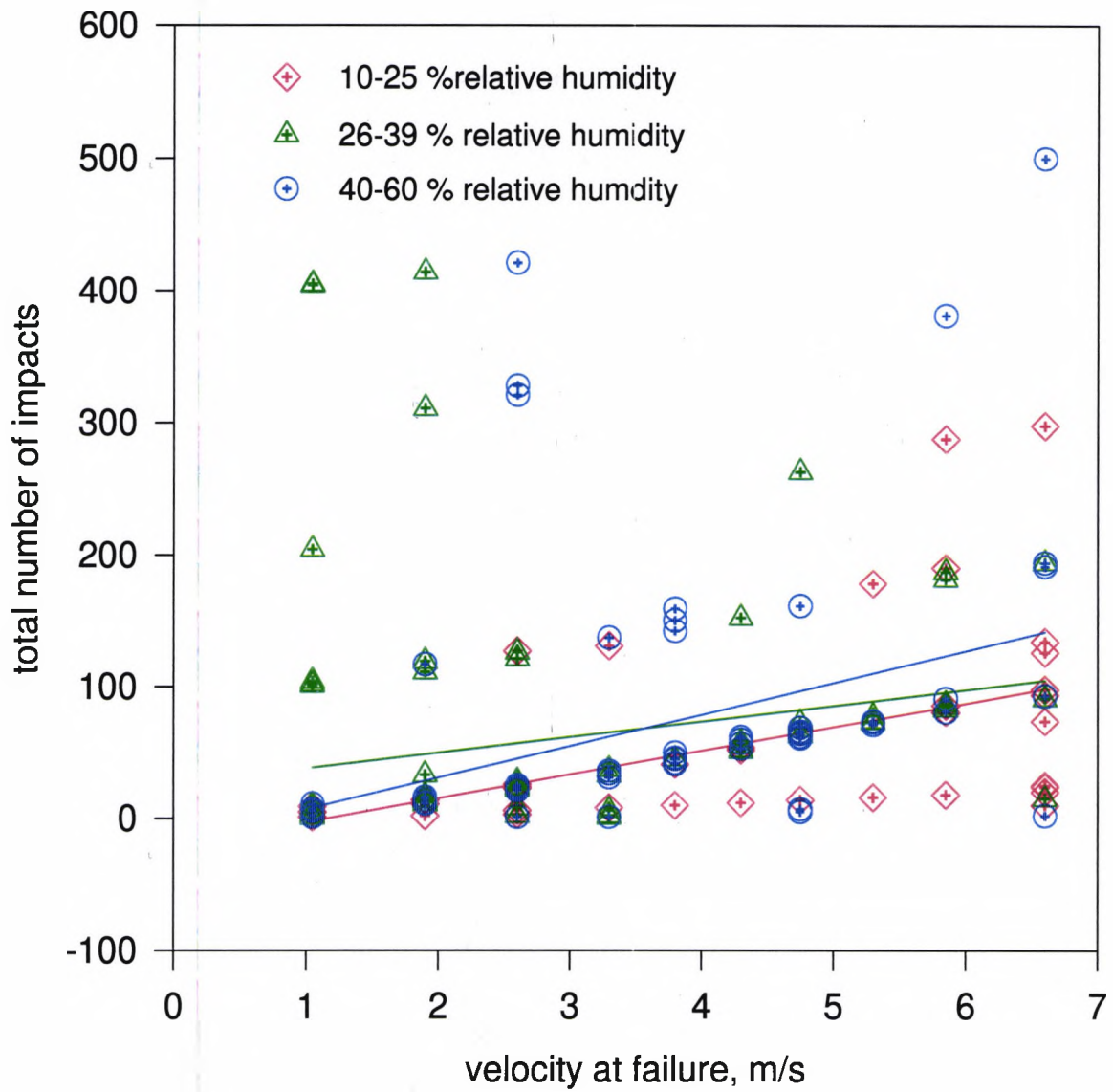
Velocity at failure/Deflection at failure v. Total number of impacts to failure
Figure 78



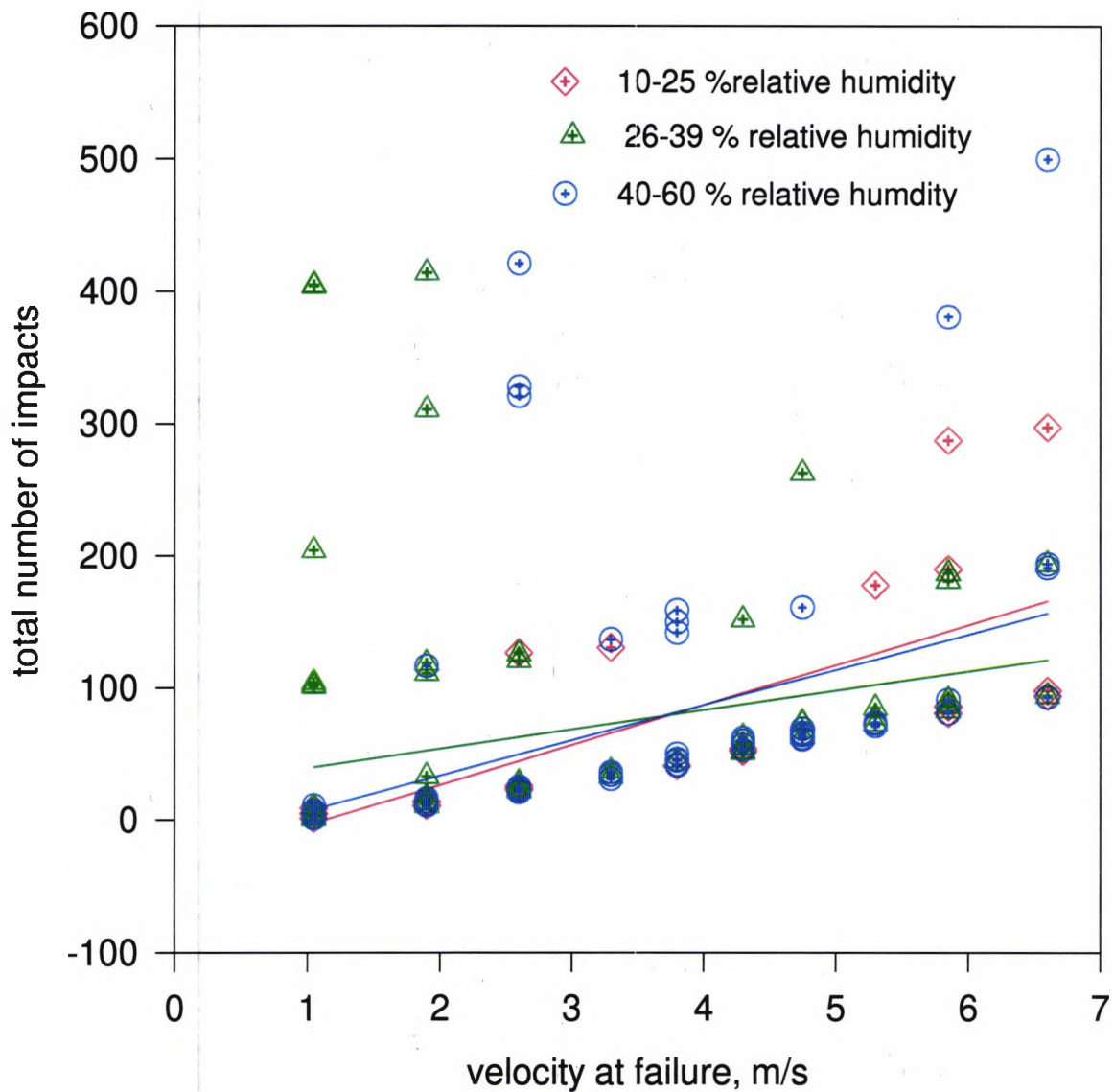
Velocity at failure/Deflection at failure v. Total number of impacts to failure
Figure 79



Velocity at failure v. total number of impacts
Figure 80

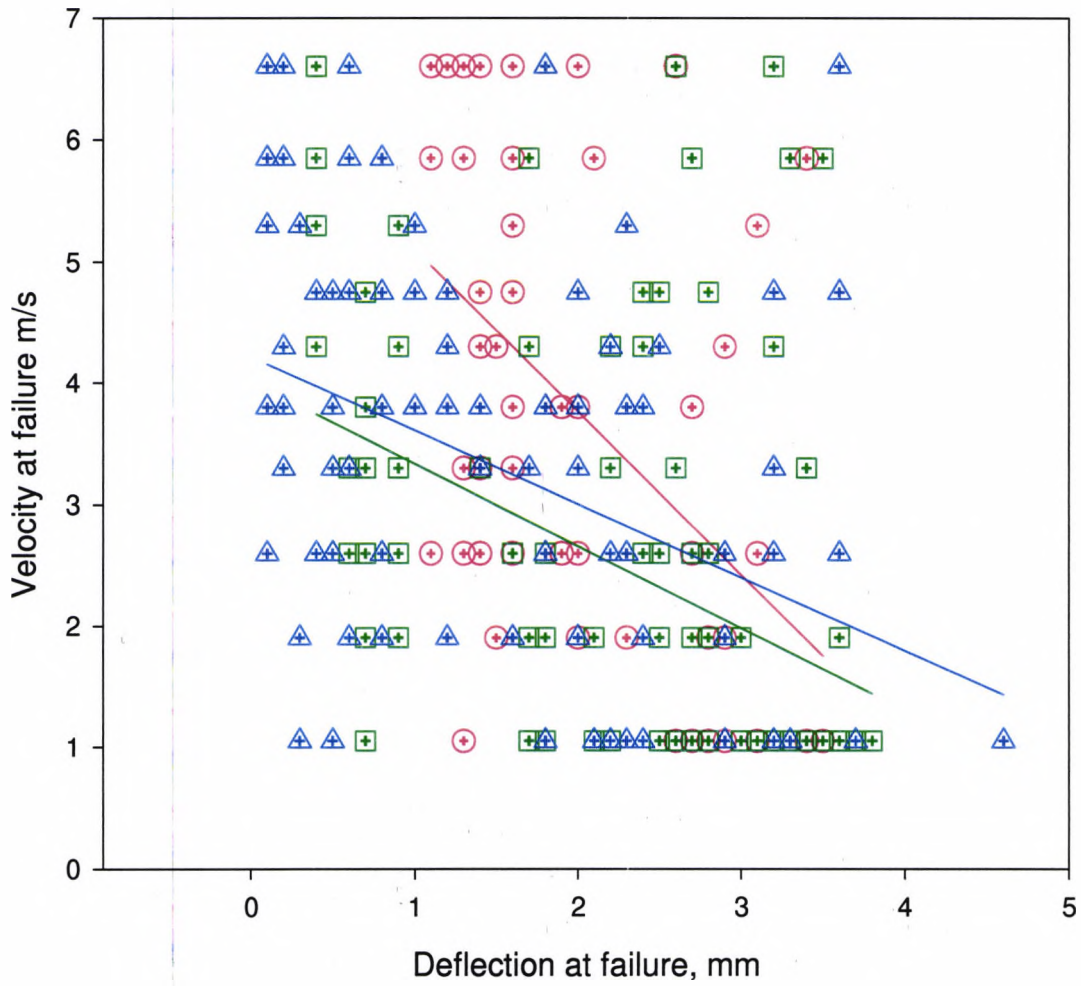


Velocity at failure v. total number of impacts Figure 81



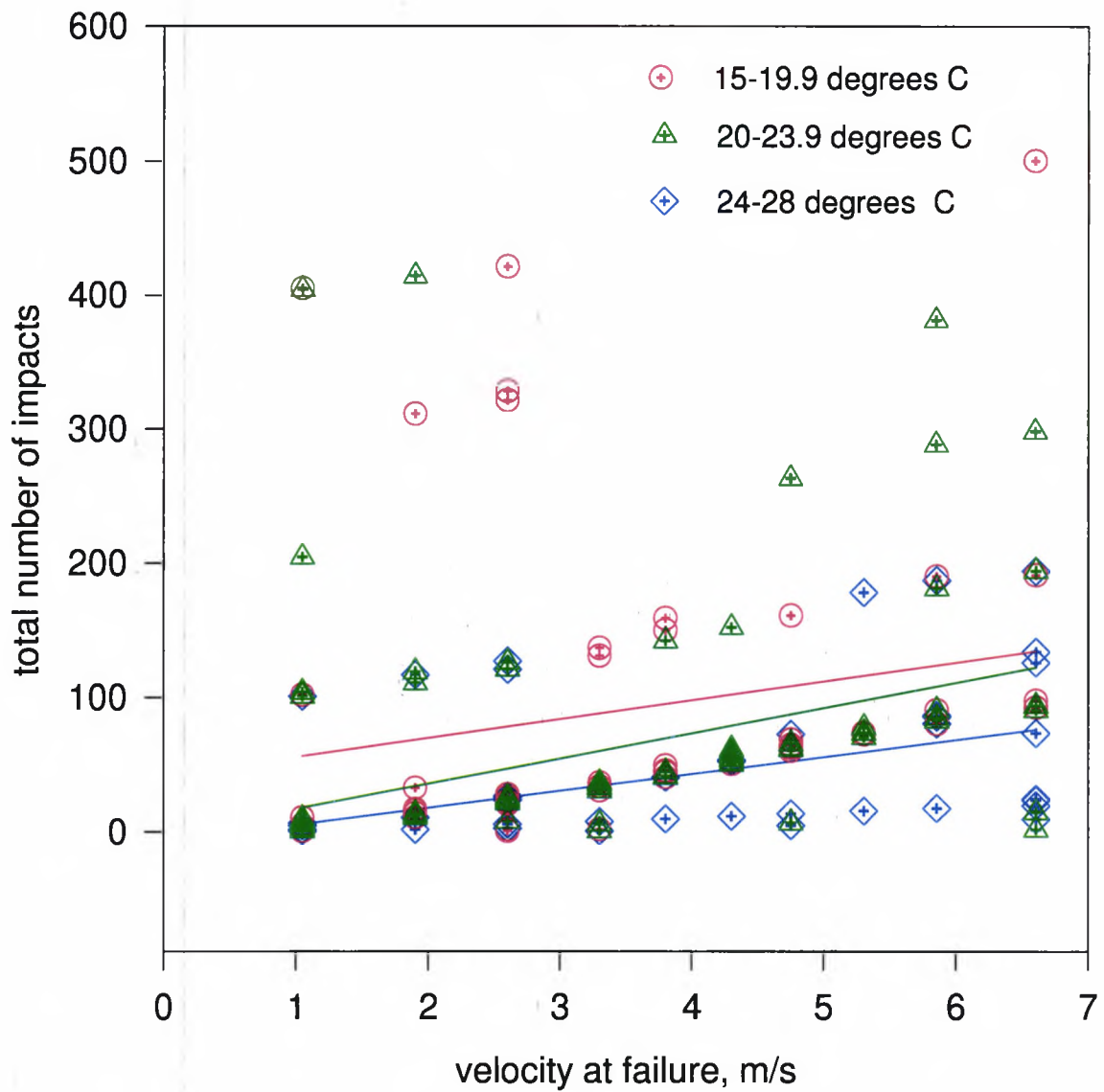
Reduced Data Set

Deflection at failure v. Velocity at failure
Figure 82

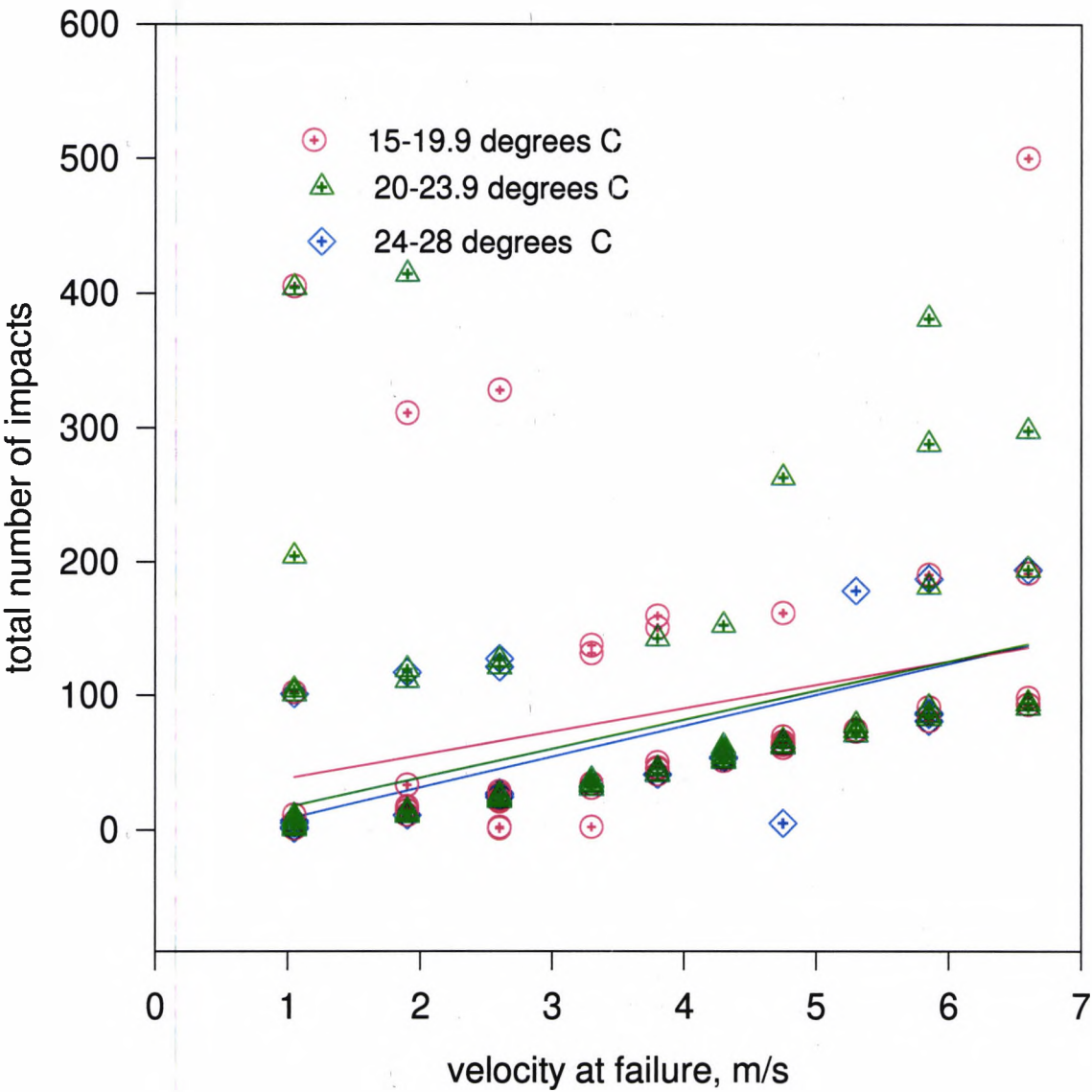


- ⊕ 10-25 rh def vs 10-25 rh vel
- Plot 1 Regr
- ⊕ 26-39rh def vs 26-39 rh vel
- Plot 2 Regr
- △ 40-60 rh def vs 40-60 rh vel
- Plot 3 Regr

Velocity at failure v total number of impacts
Figure 83

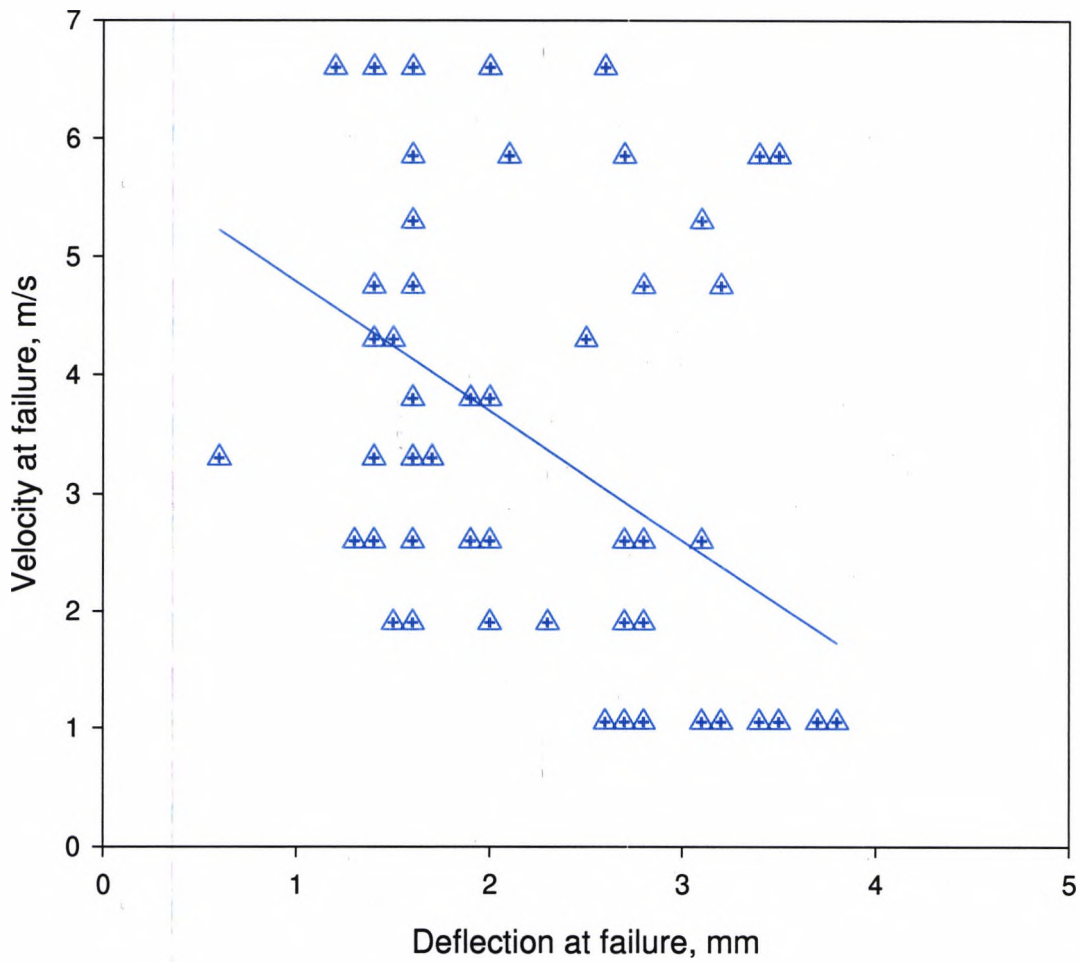


Velocity at failure v total number of impacts
Figure 84



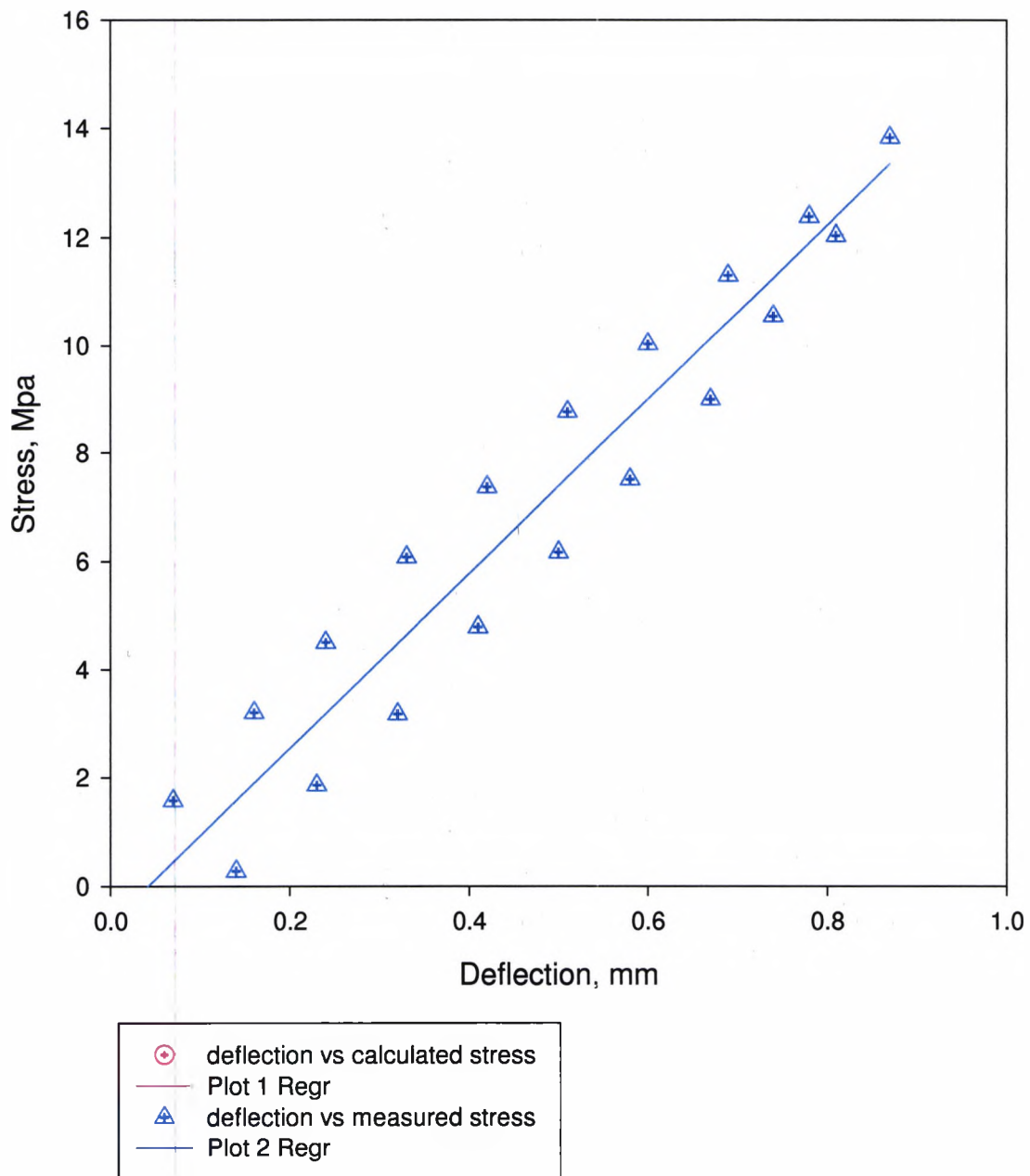
Reduced Data Set

Deflection at failure v. Velocity at failure
Figure 85

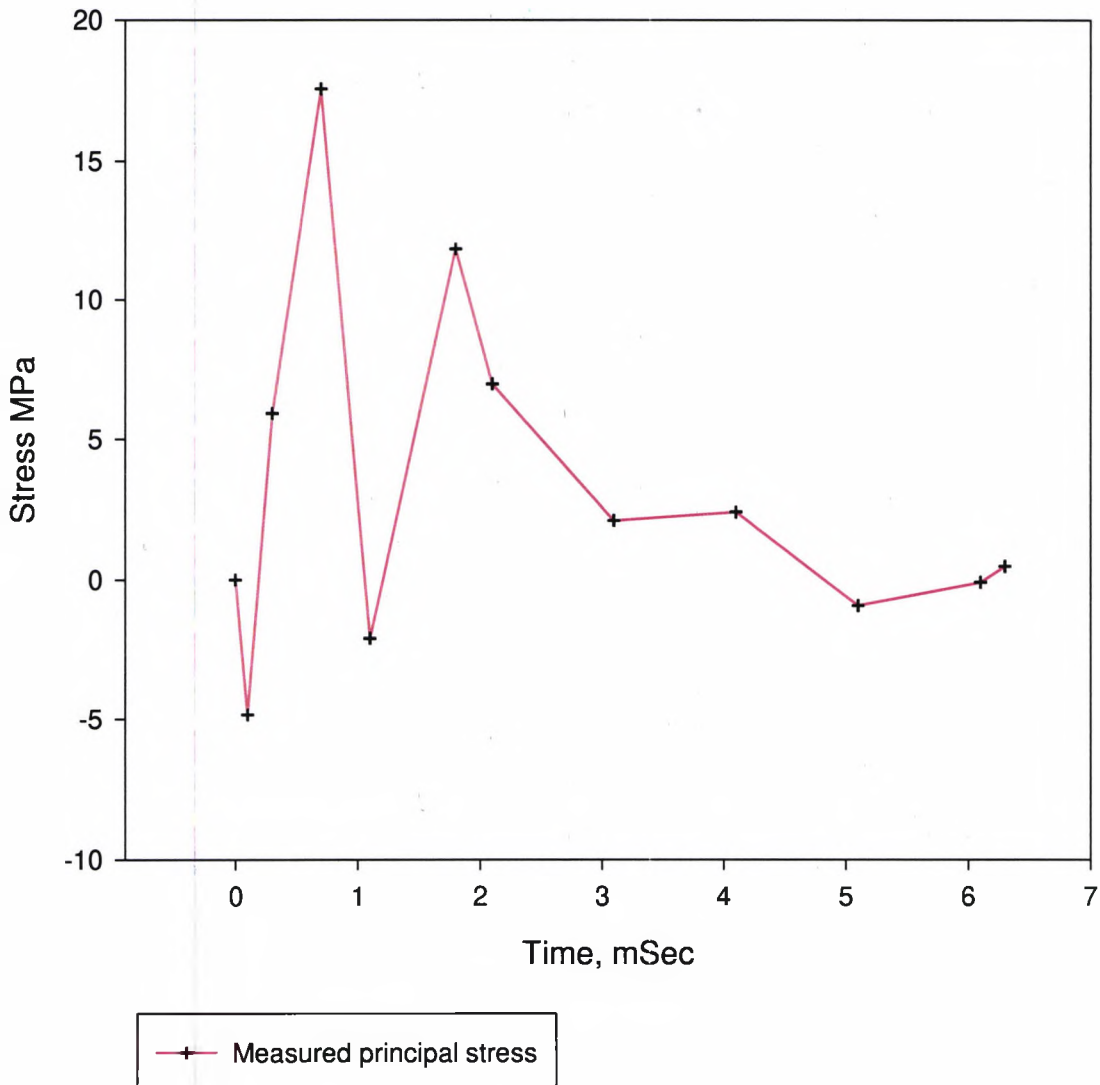


-  15-19.9 temp defl vs 15-19.9 temp vel
-  Plot 1 Regr
-  20-23.9 temp defl vs 20-23.9 temp vel
-  Plot 2 Regr
-  24+ temp defl vs 24+ temp vel
-  Plot 3 Regr

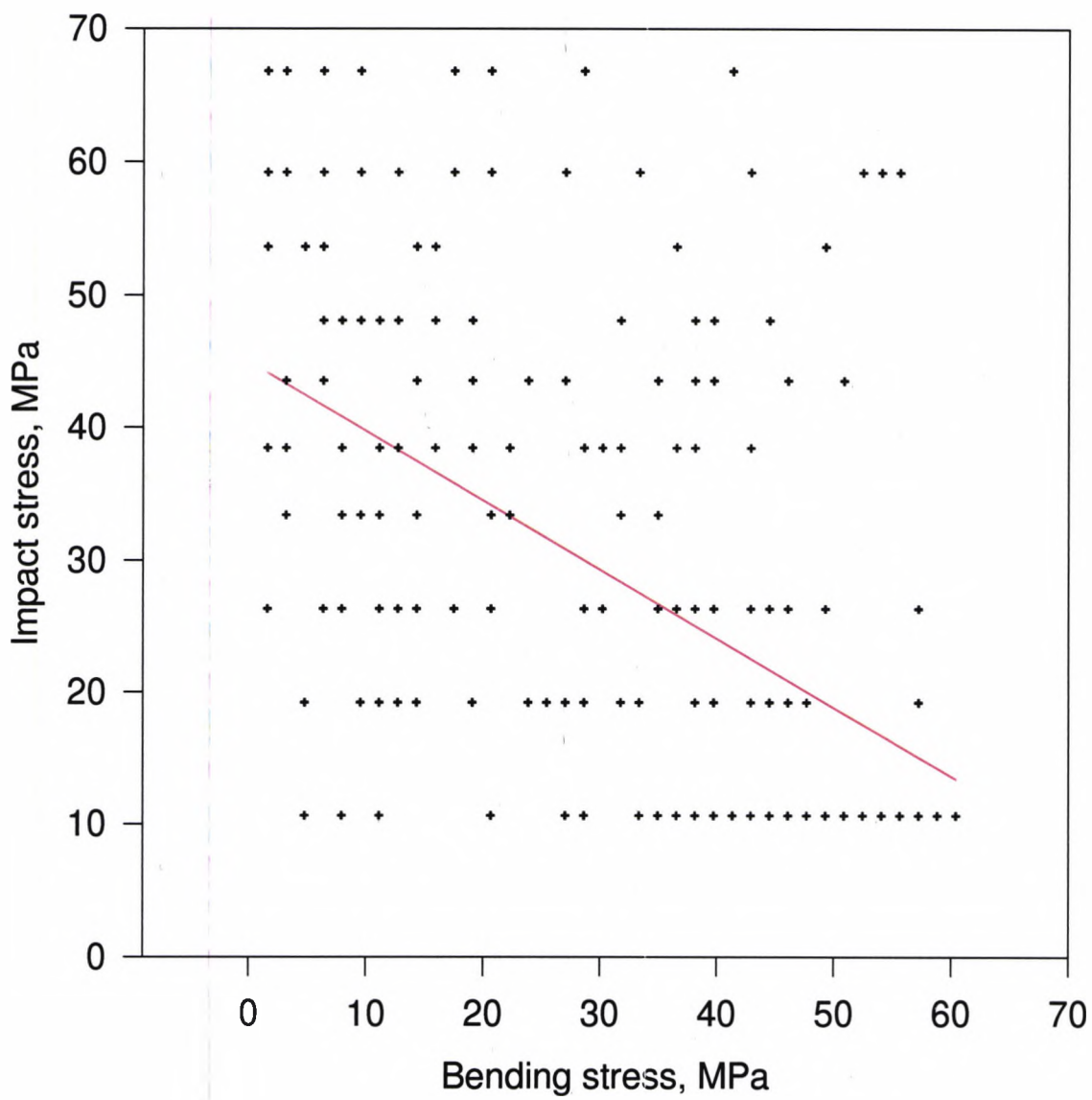
Comparison between measured and calculated stress on sample loaded centrally.
Figure 86



Measured principal stress history at an impact velocity of 2.6m/s
Figure 87

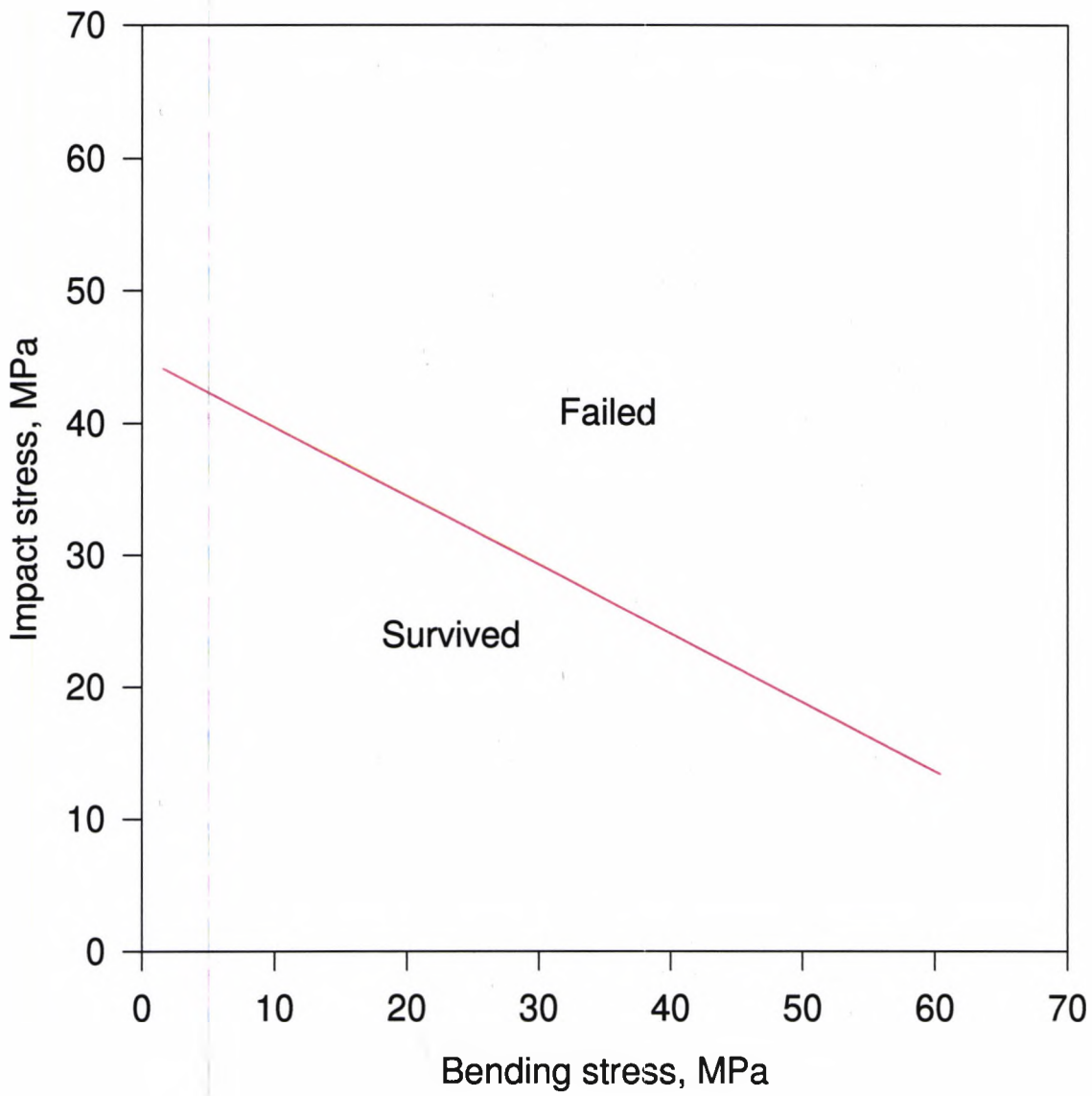


bending stress at failure v. impact stress at failure
Figure 88



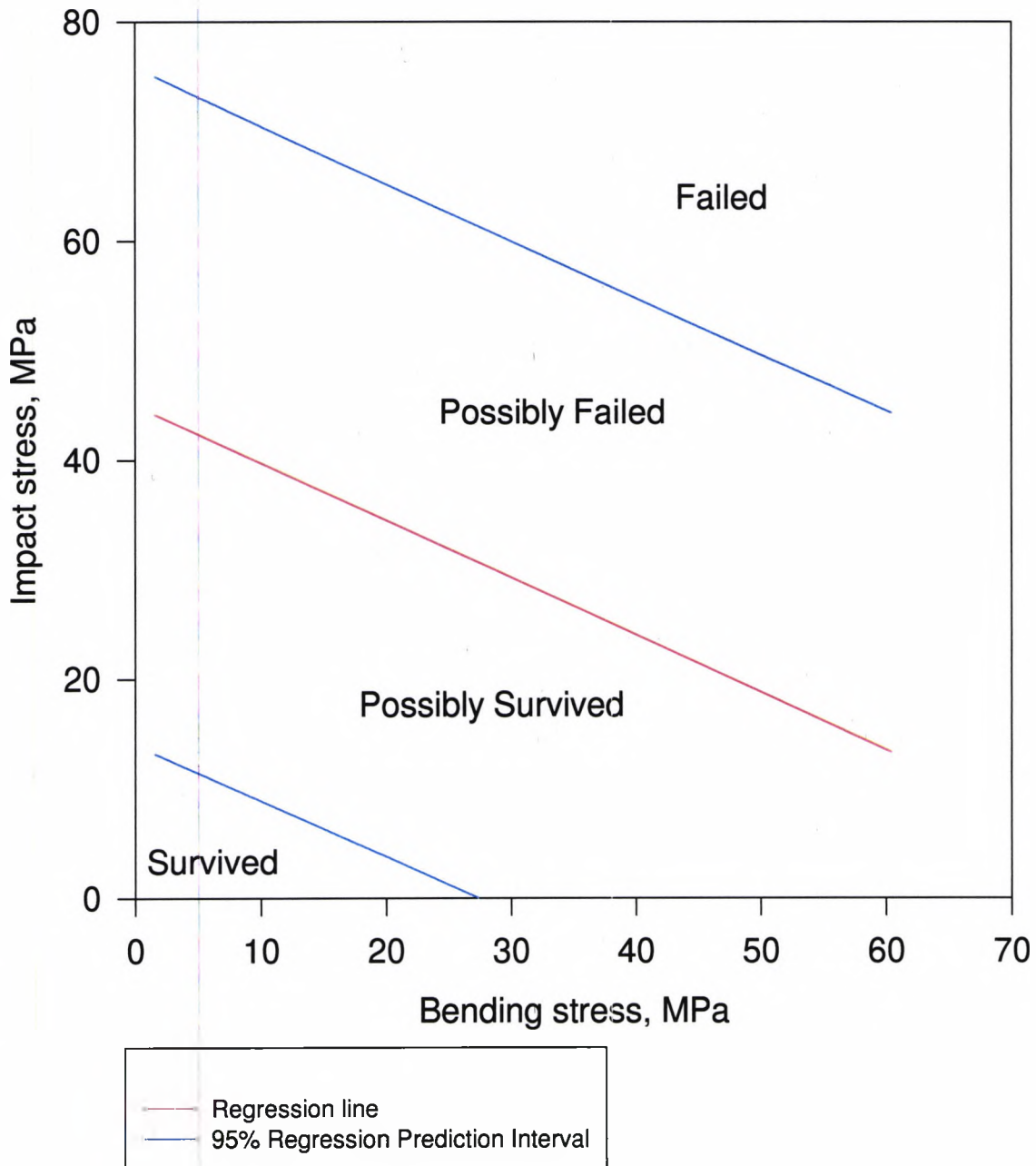
Bending stress at failure v. Impact stress at failure

Figure 89

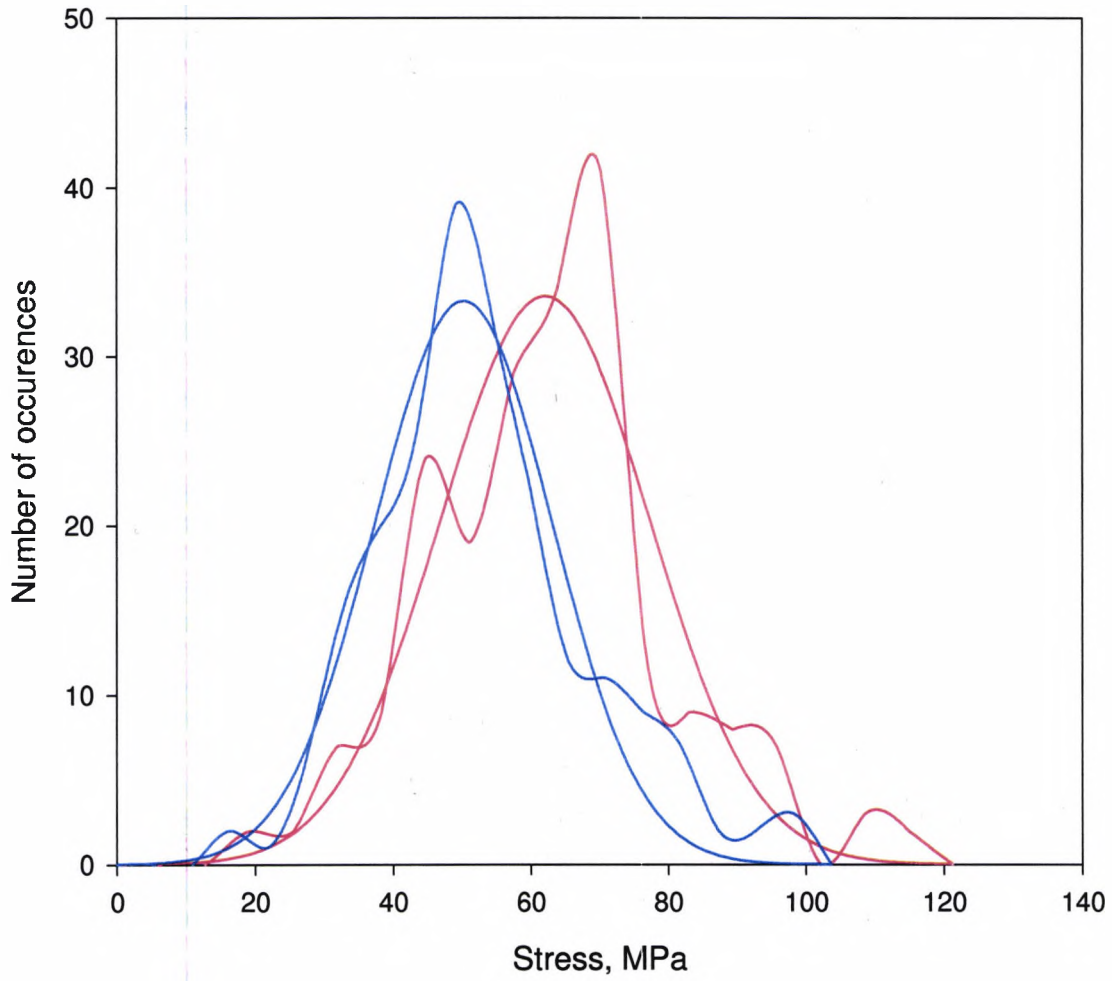


Bending stress at failure v. Impact stress at failure

Figure 90

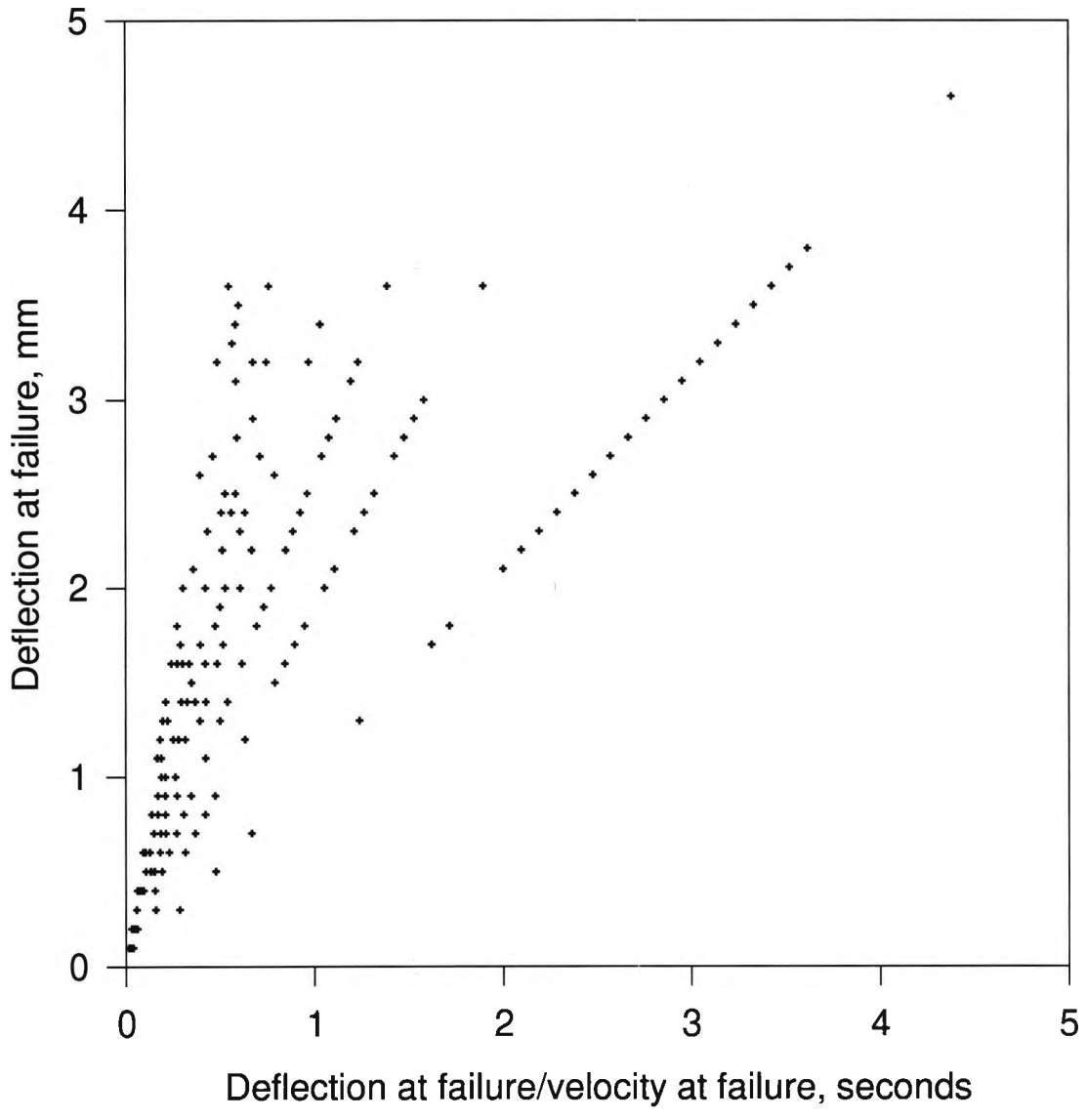


Distribution graph for stress levels at failure
Figure 91

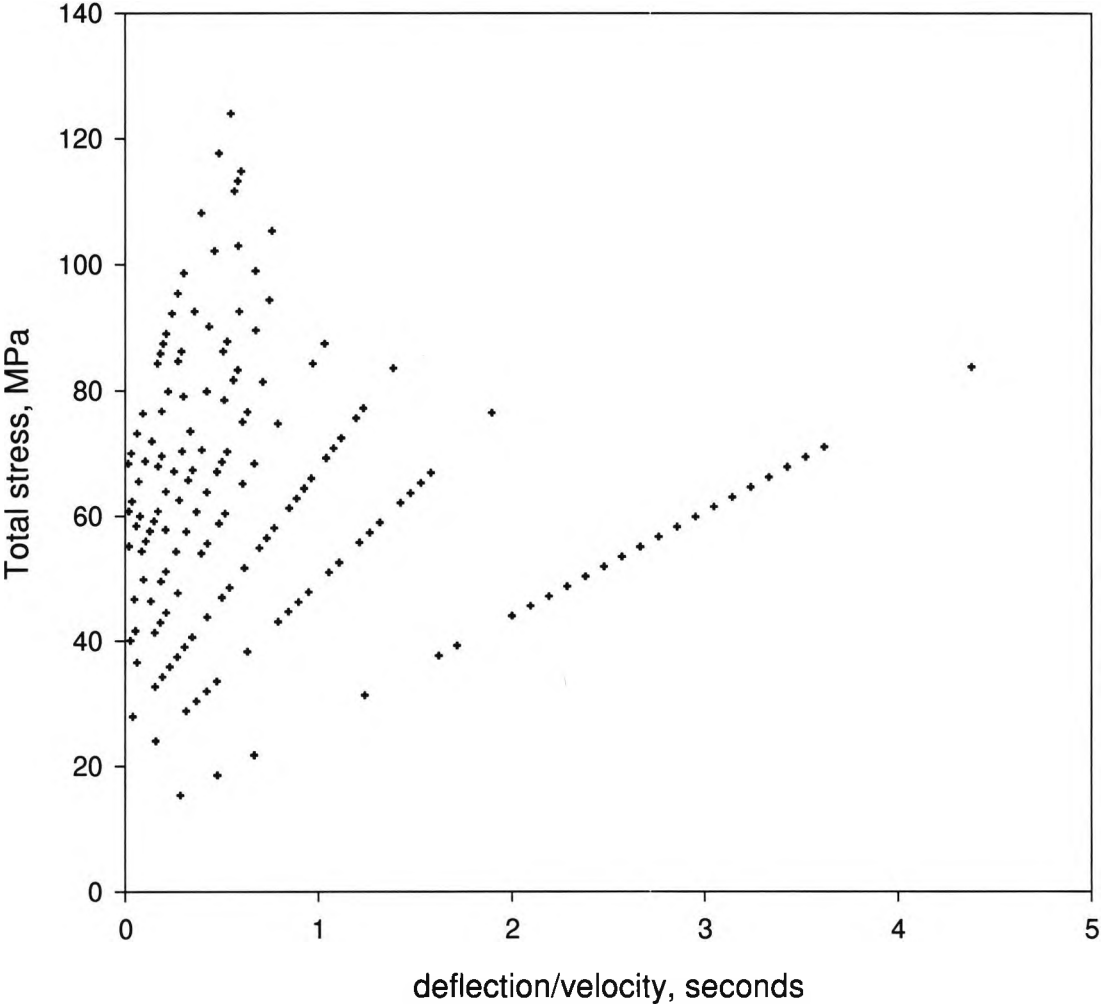


- Stress levels v. Occurrence , $f = 1.0$
- Gaussian curve fit
- Stress levels v. Occurrence, $f = 0.7$
- Gaussian curve fit

Deflection at failure/velocity at failure v. deflection at failure
Figure 92

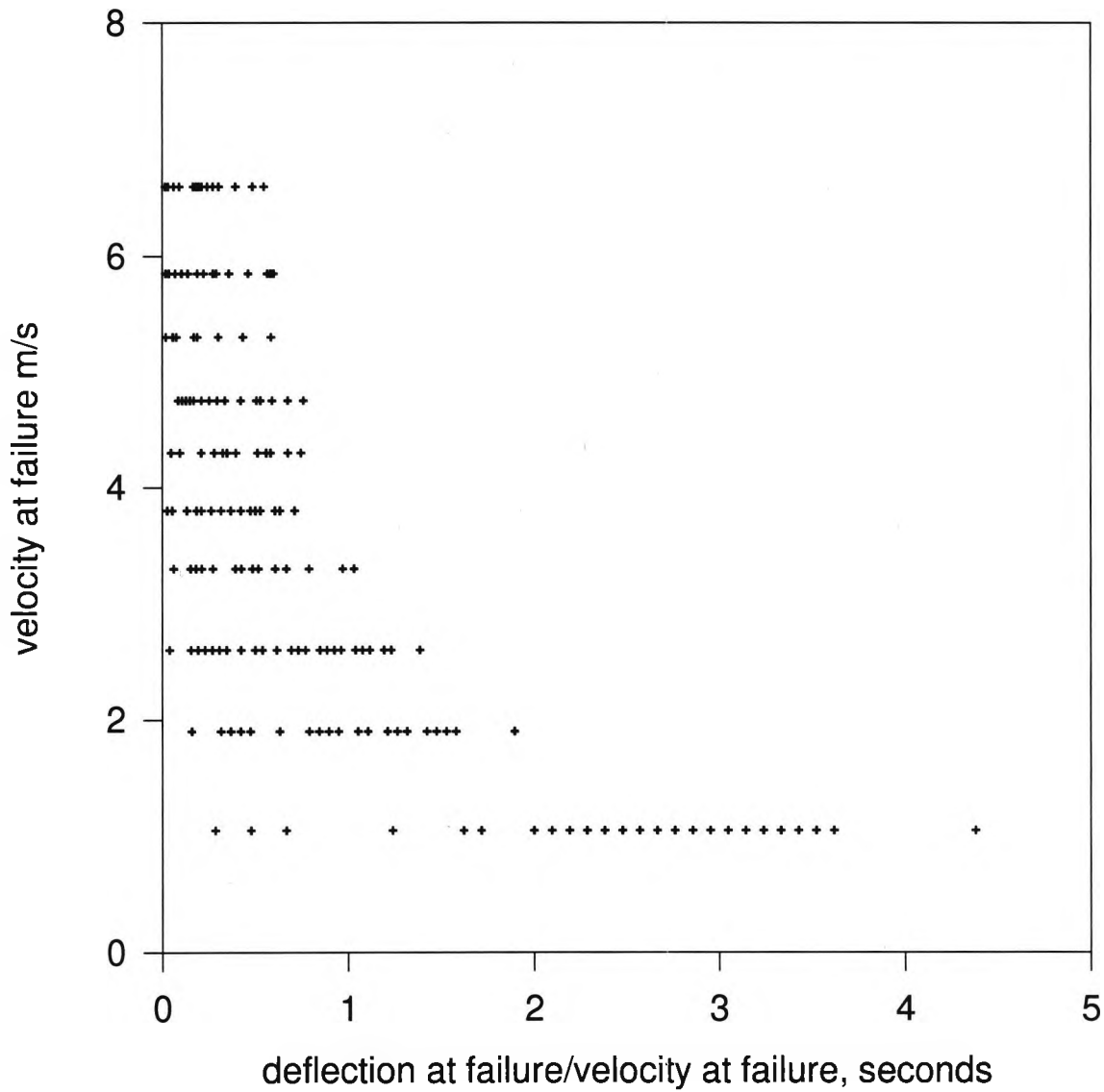


Deflection/velocity v. Total stress
Figure 93

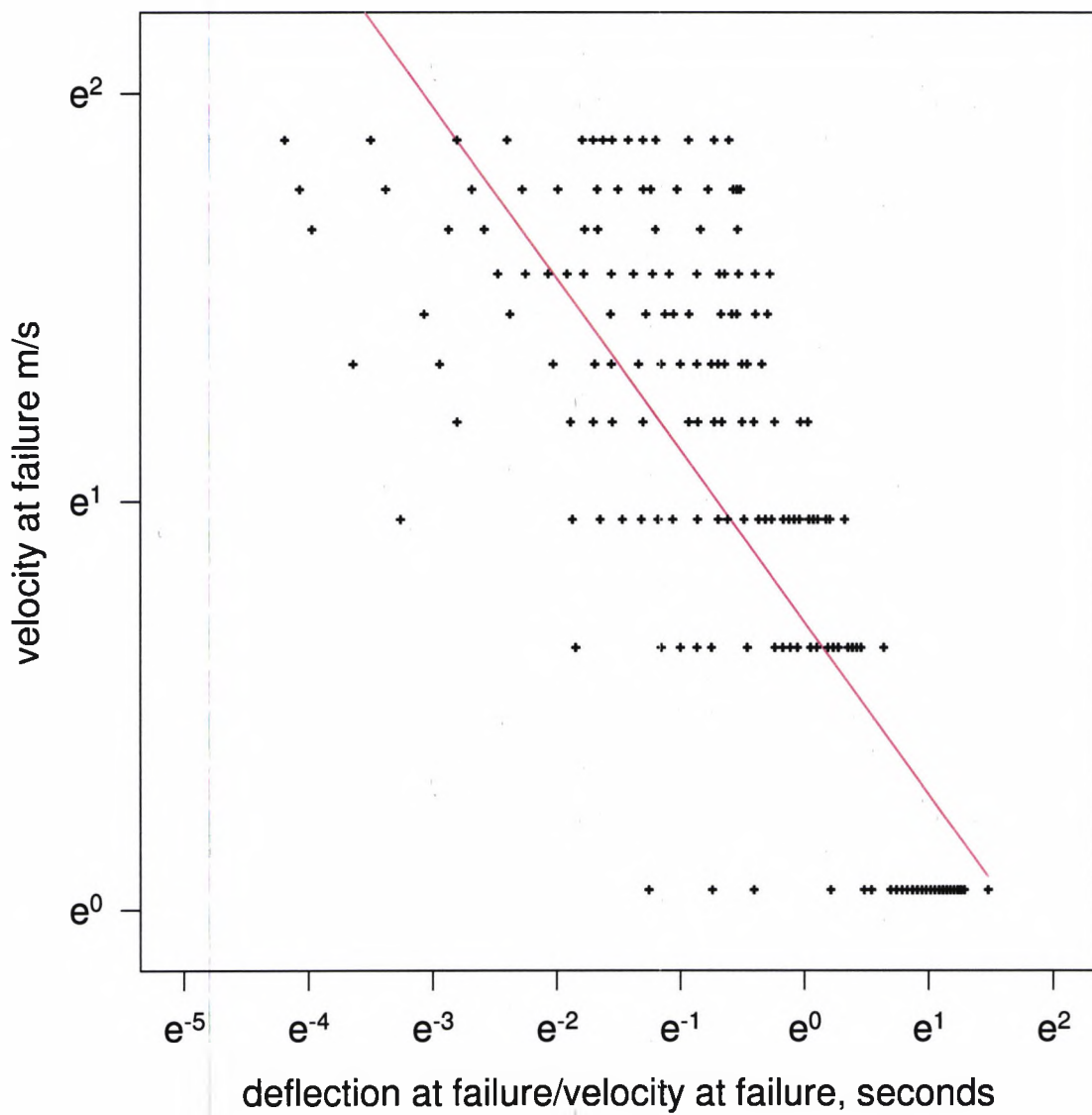


• defl/vel vs total stress

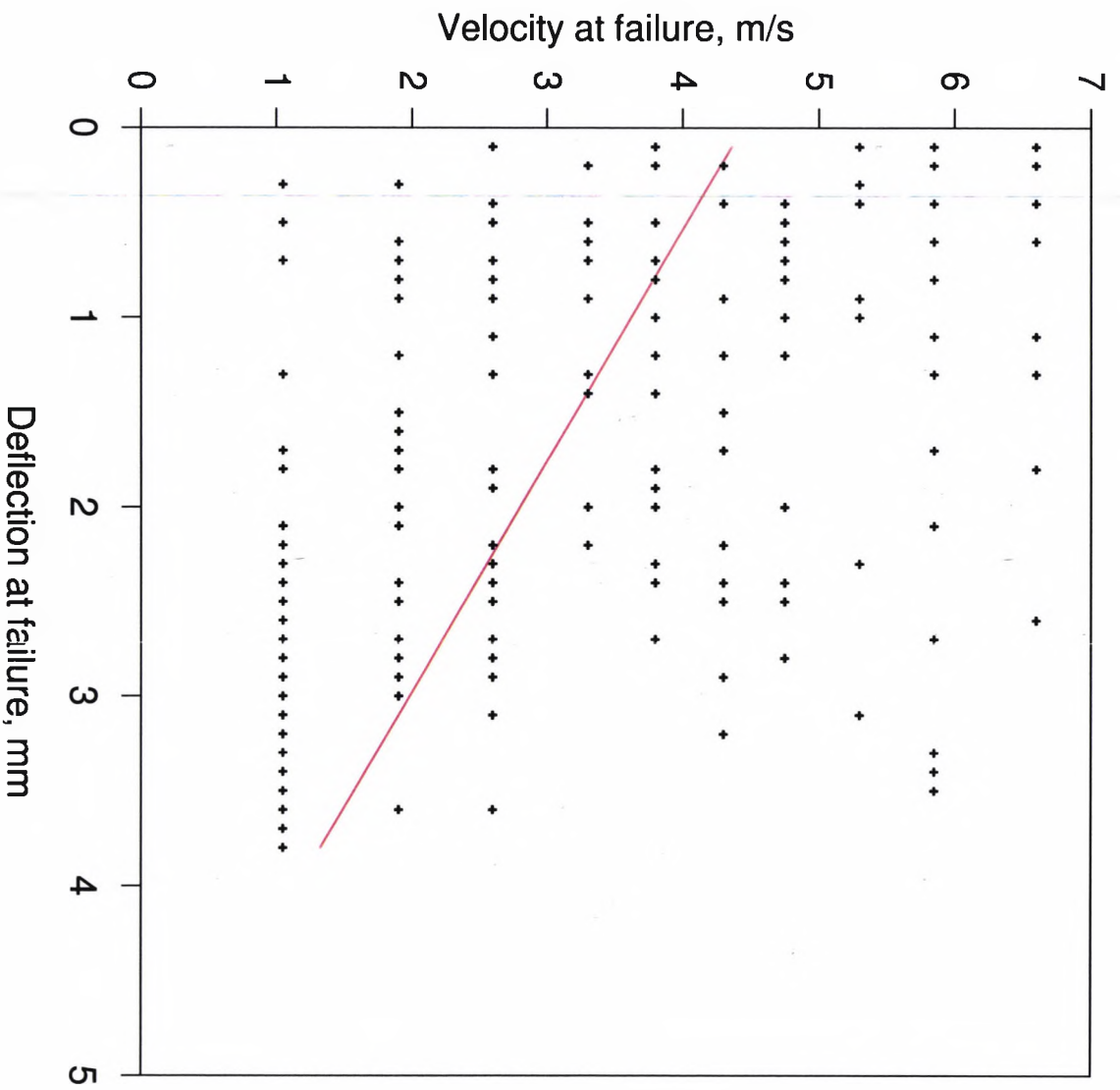
Deflection at failure/velocity at failure v. velocity at failure Figure 94



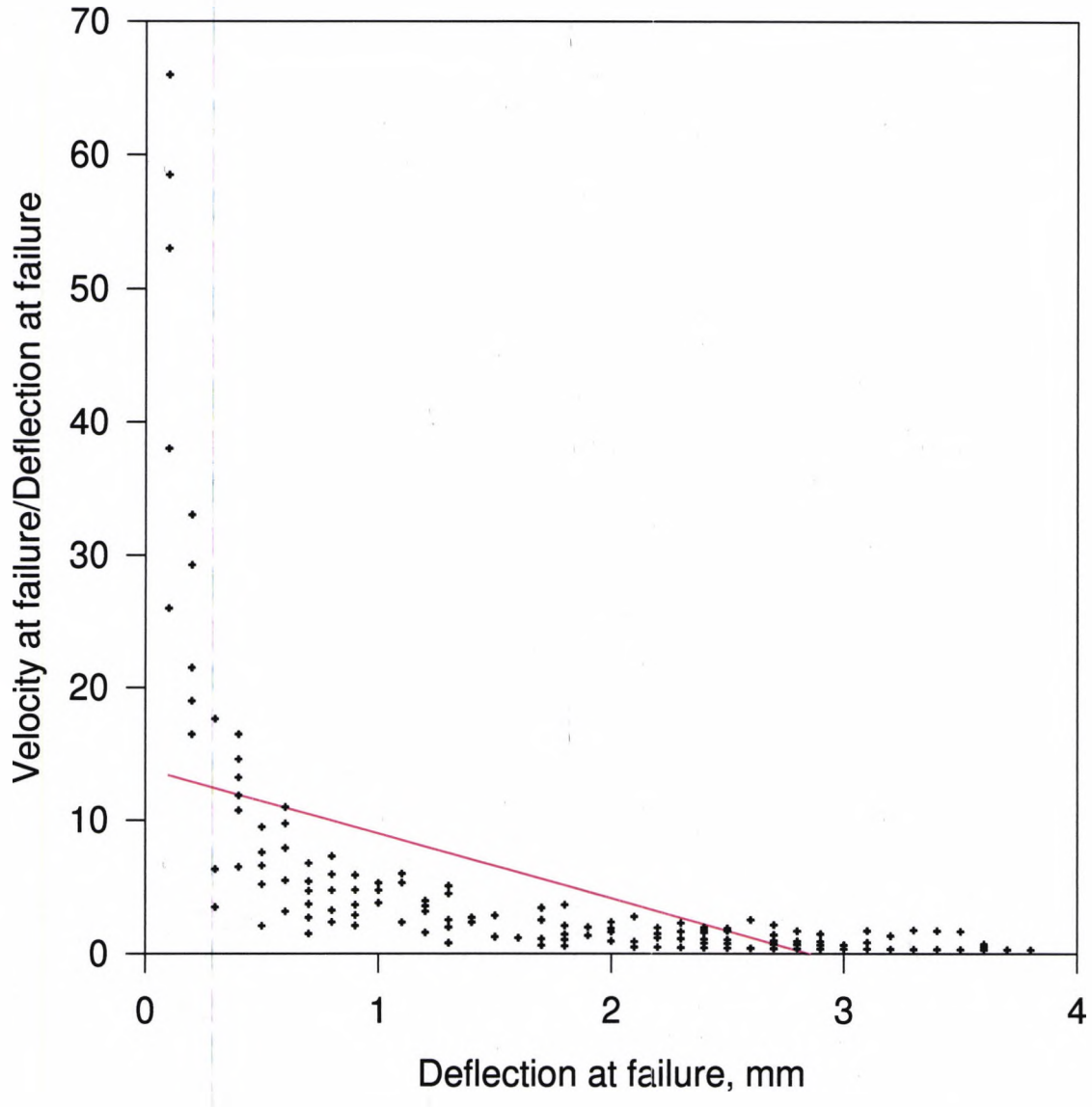
Deflection at failure/velocity at failure v. velocity at failure Figure 95



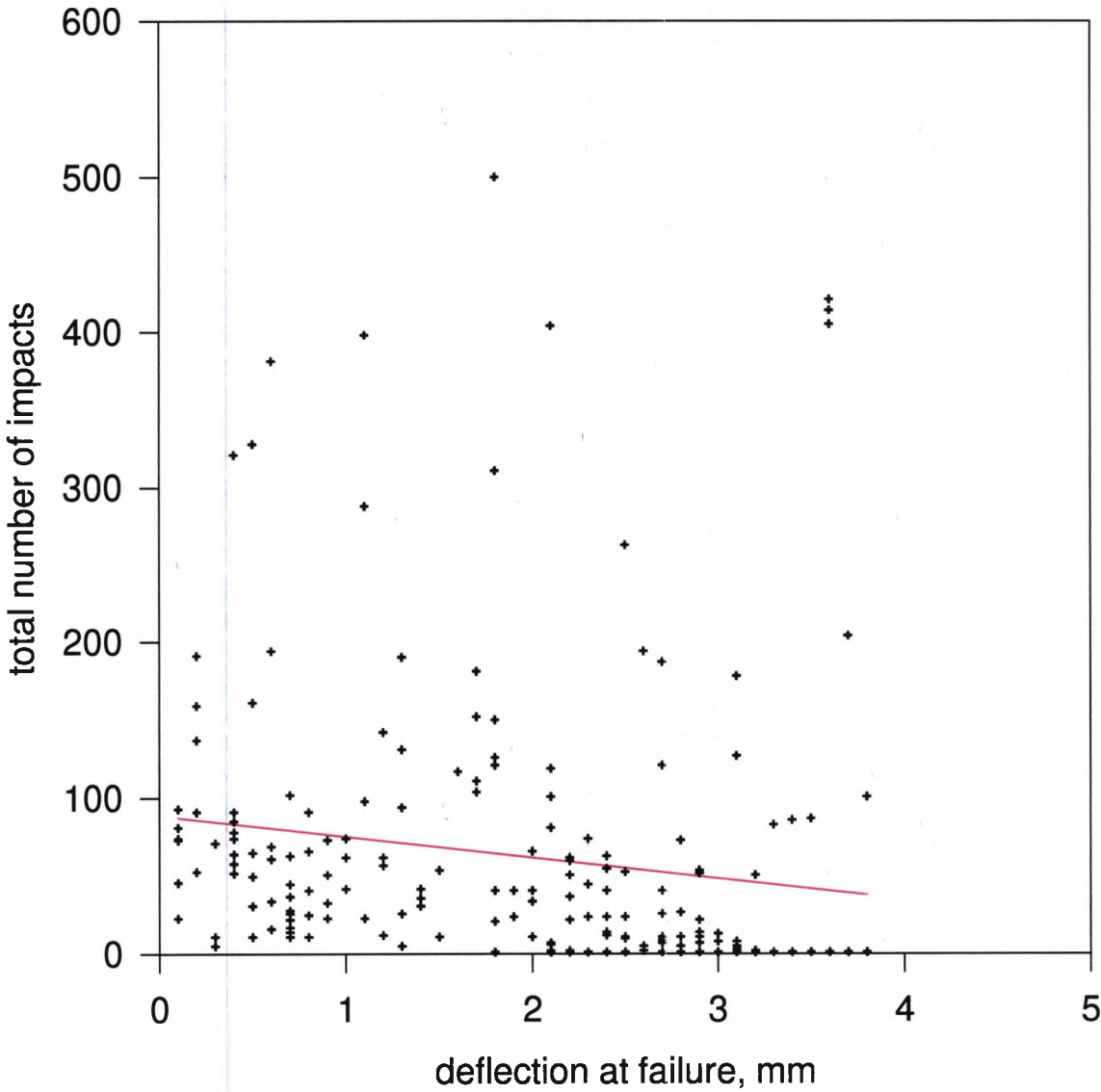
Deflection at failure v. velocity at failure
Figure 96



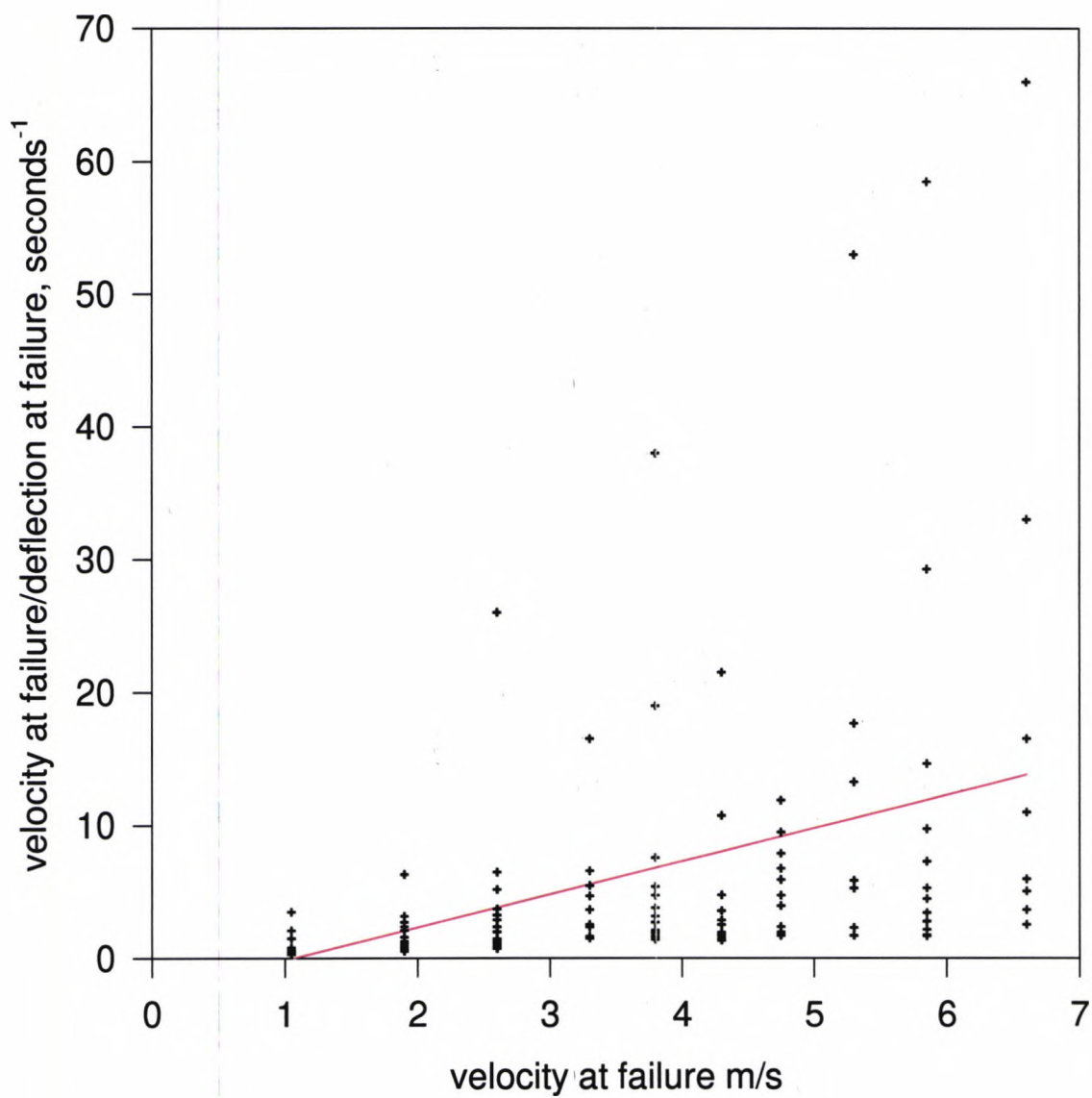
Deflection at failure v. velocity at failure/deflection at failure
Figure 97



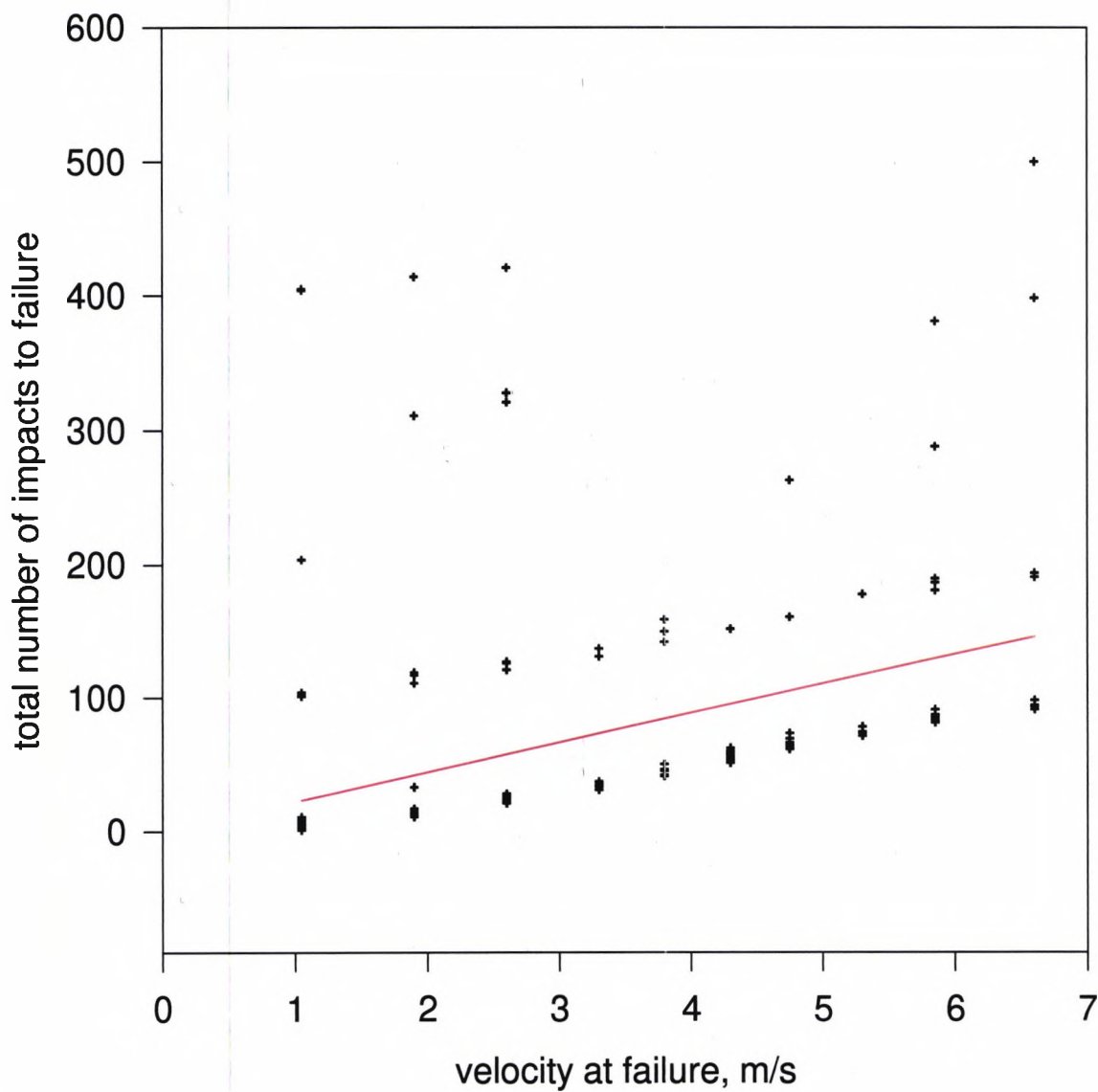
deflection at failure v. total number of impacts
Figure 98



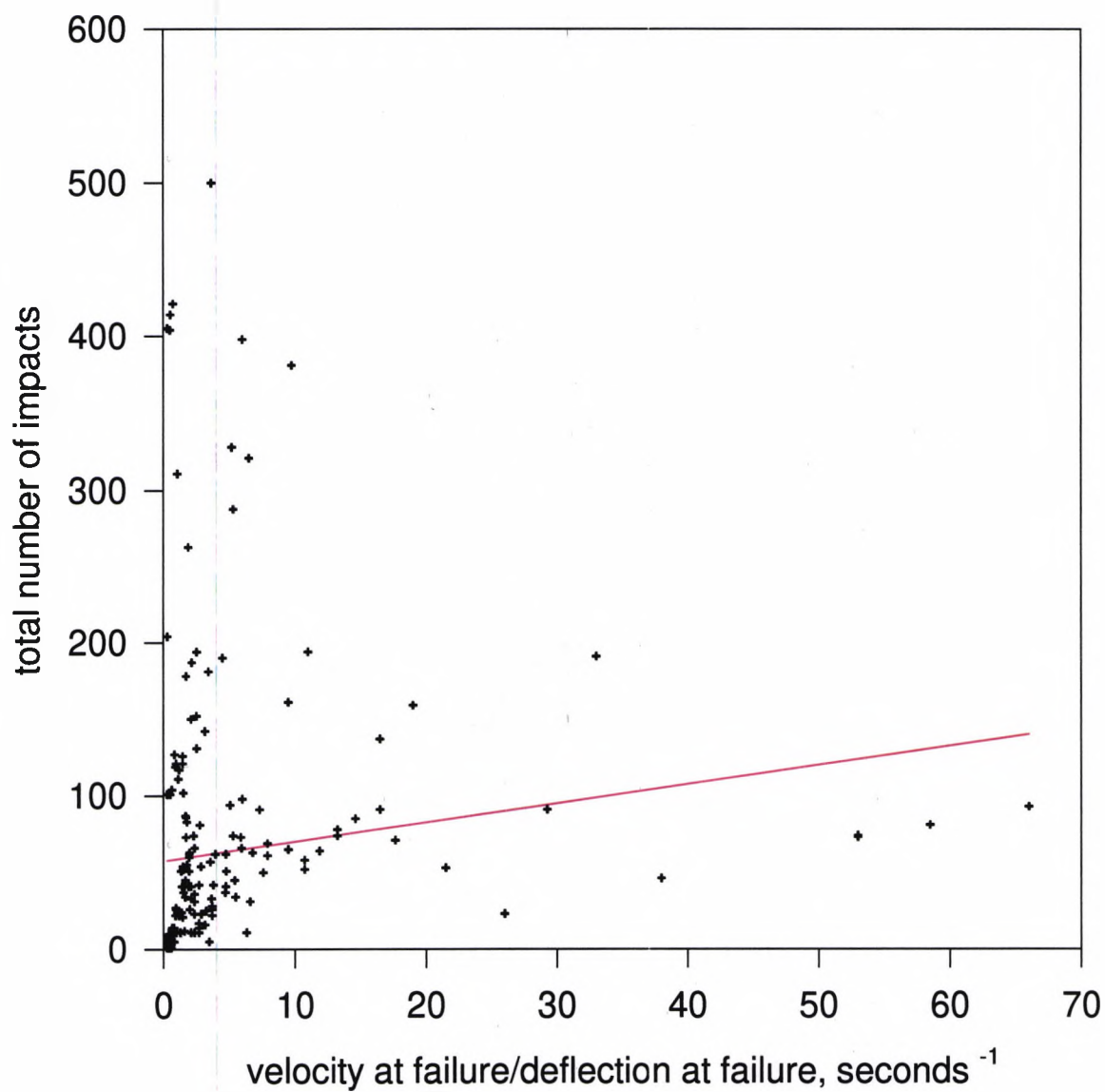
velocity at failure v. velocity at failure/deflection at failure Figure 99



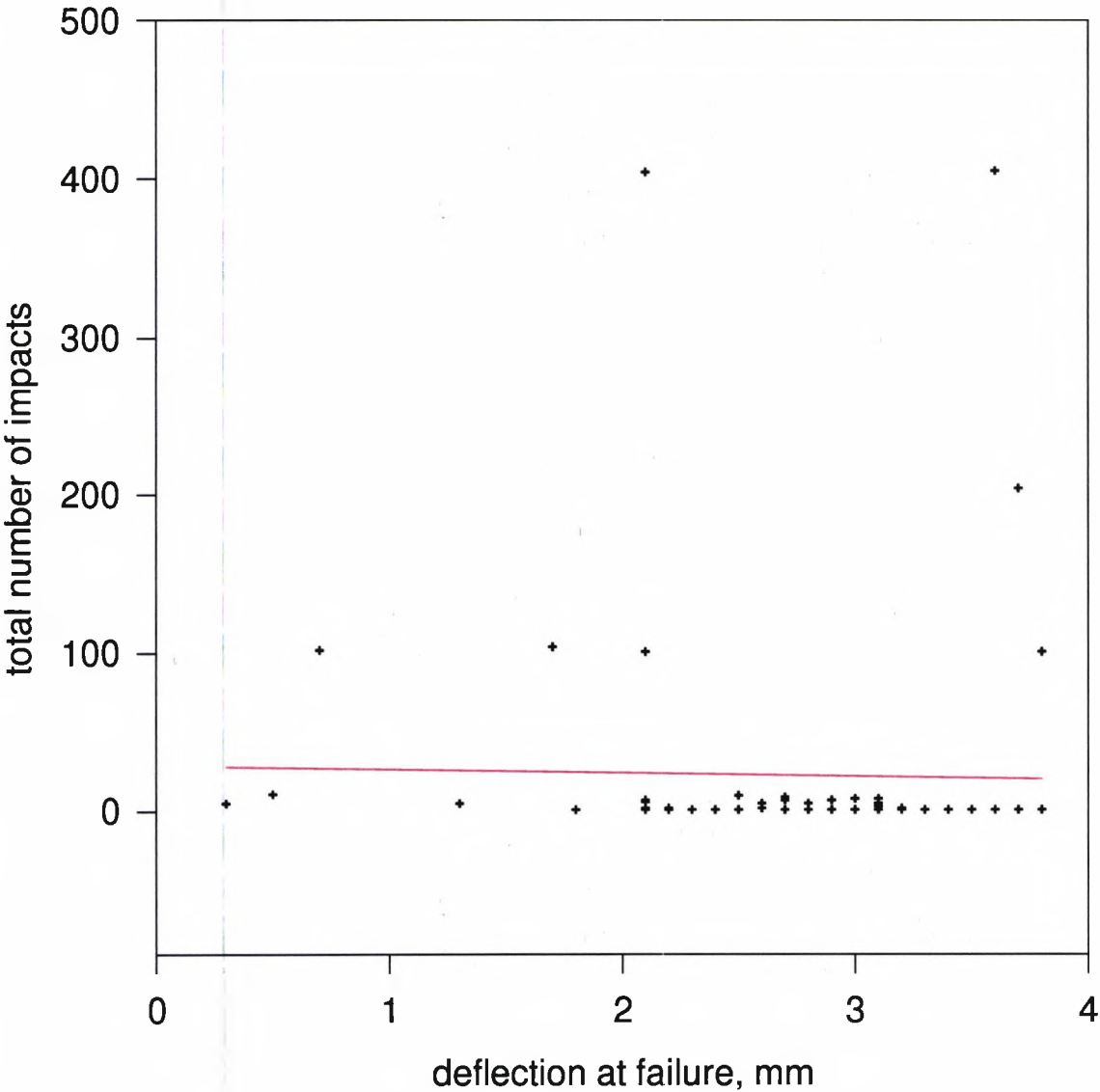
velocity at failure v. total number of impacts
Figure 100



Velocity at failure/deflection at failure v. Total number of impacts
Figure 101

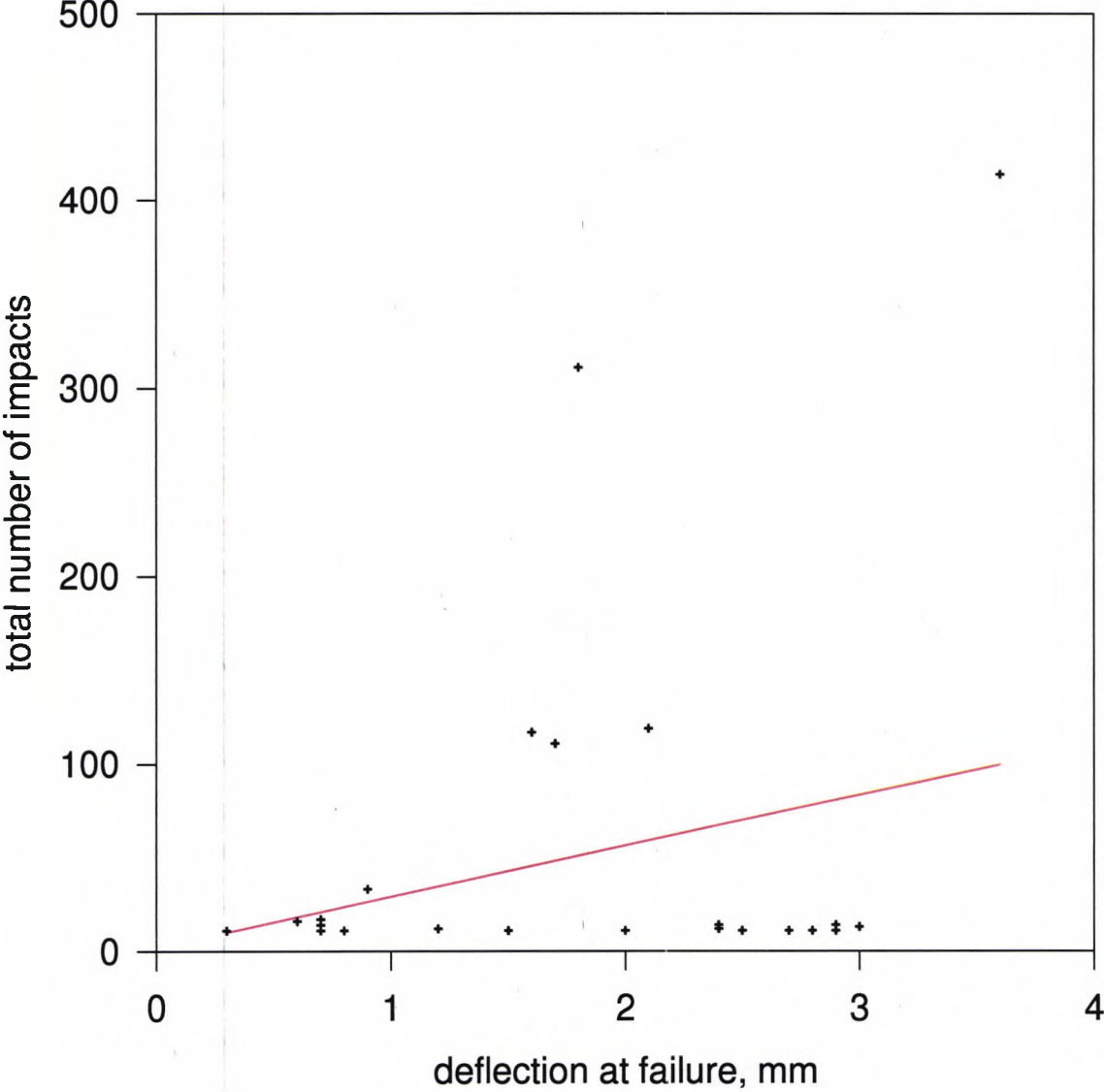


deflection at failure v. total number of impacts
Figure 102



Constant Velocity, 1.05 m/s

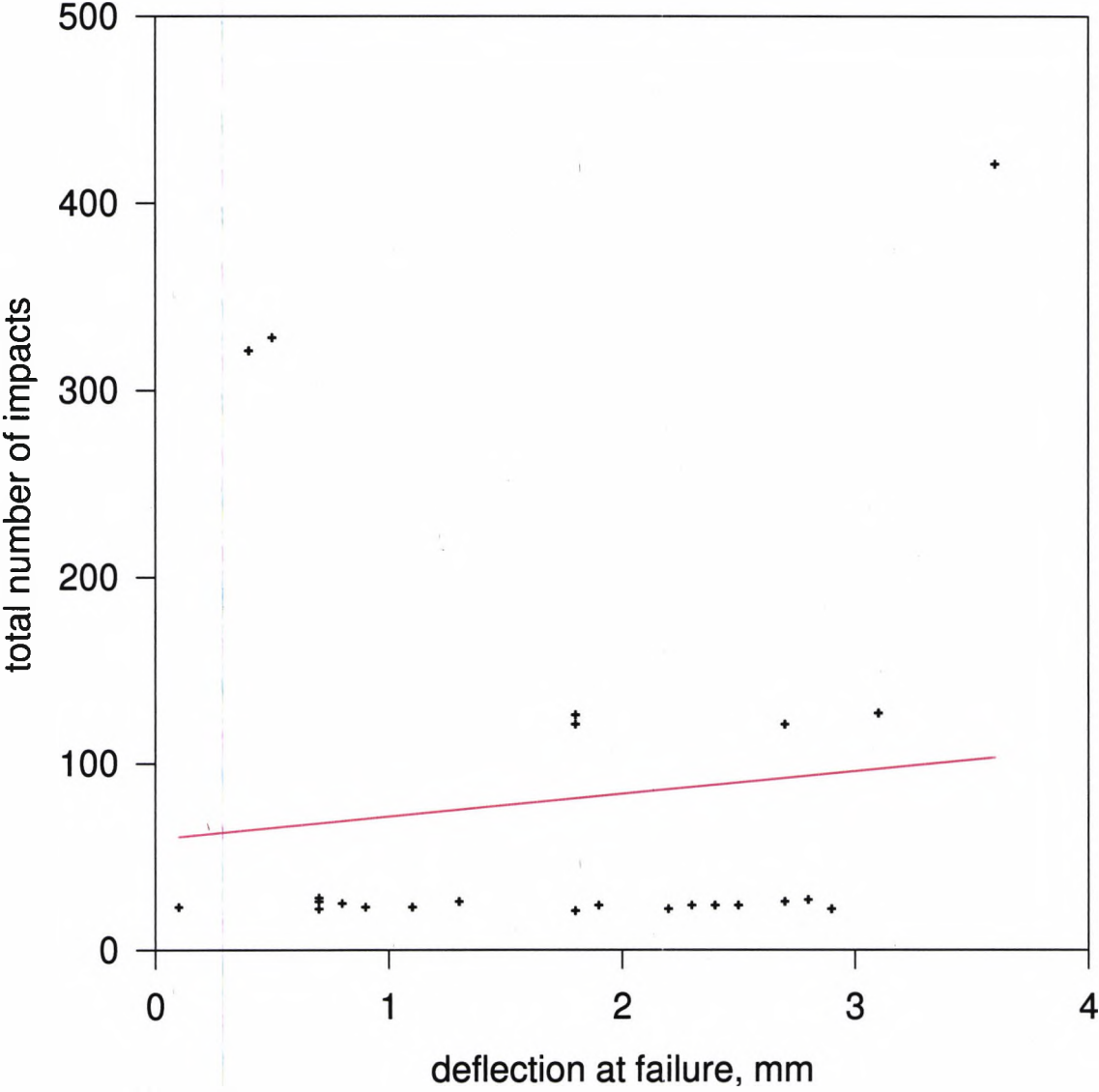
deflection at failure v. total number of impacts
Figure 103



Constant Velocity, 1.9 m/s

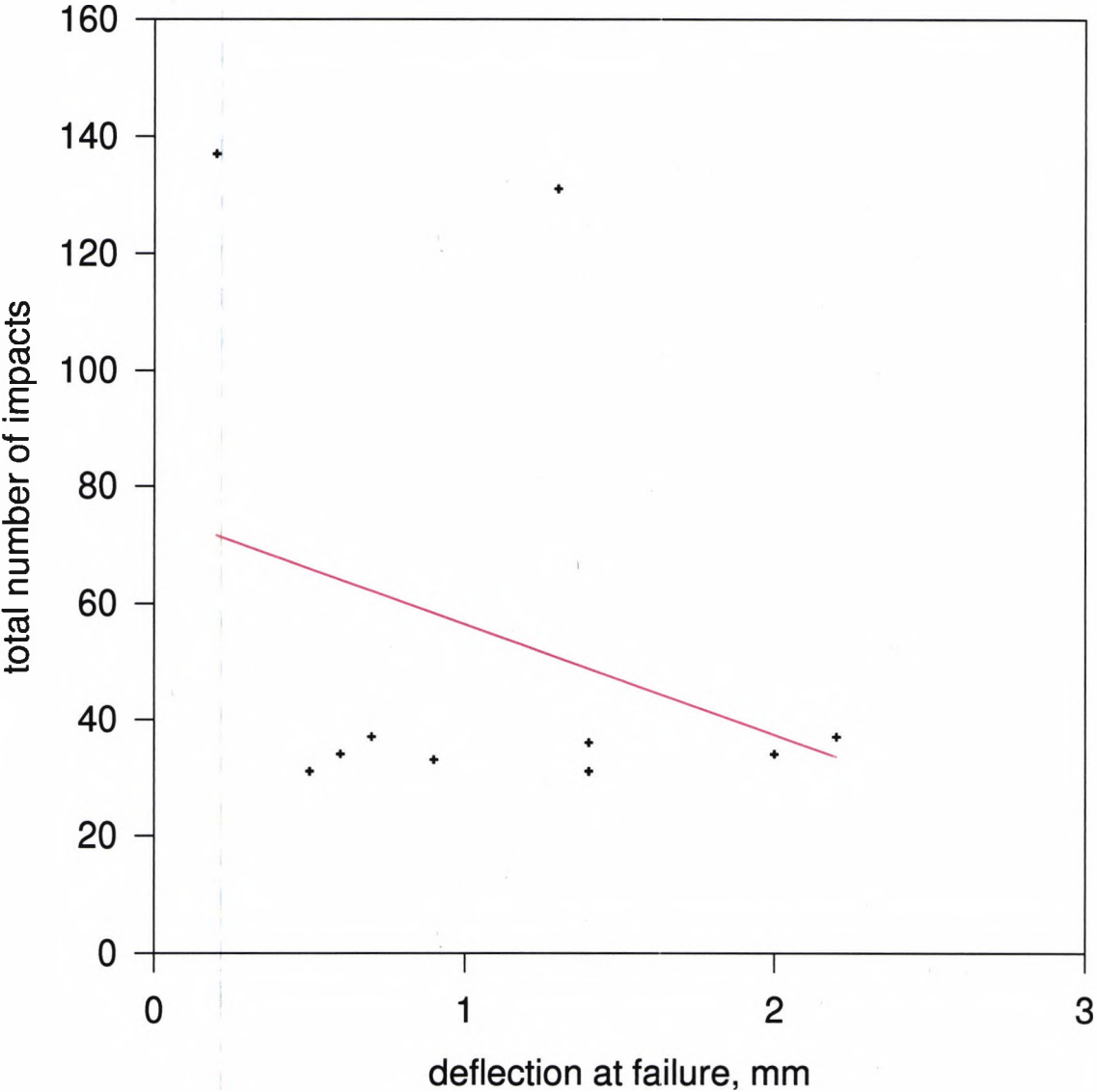
deflection at failure v. total number of impacts

Figure 104



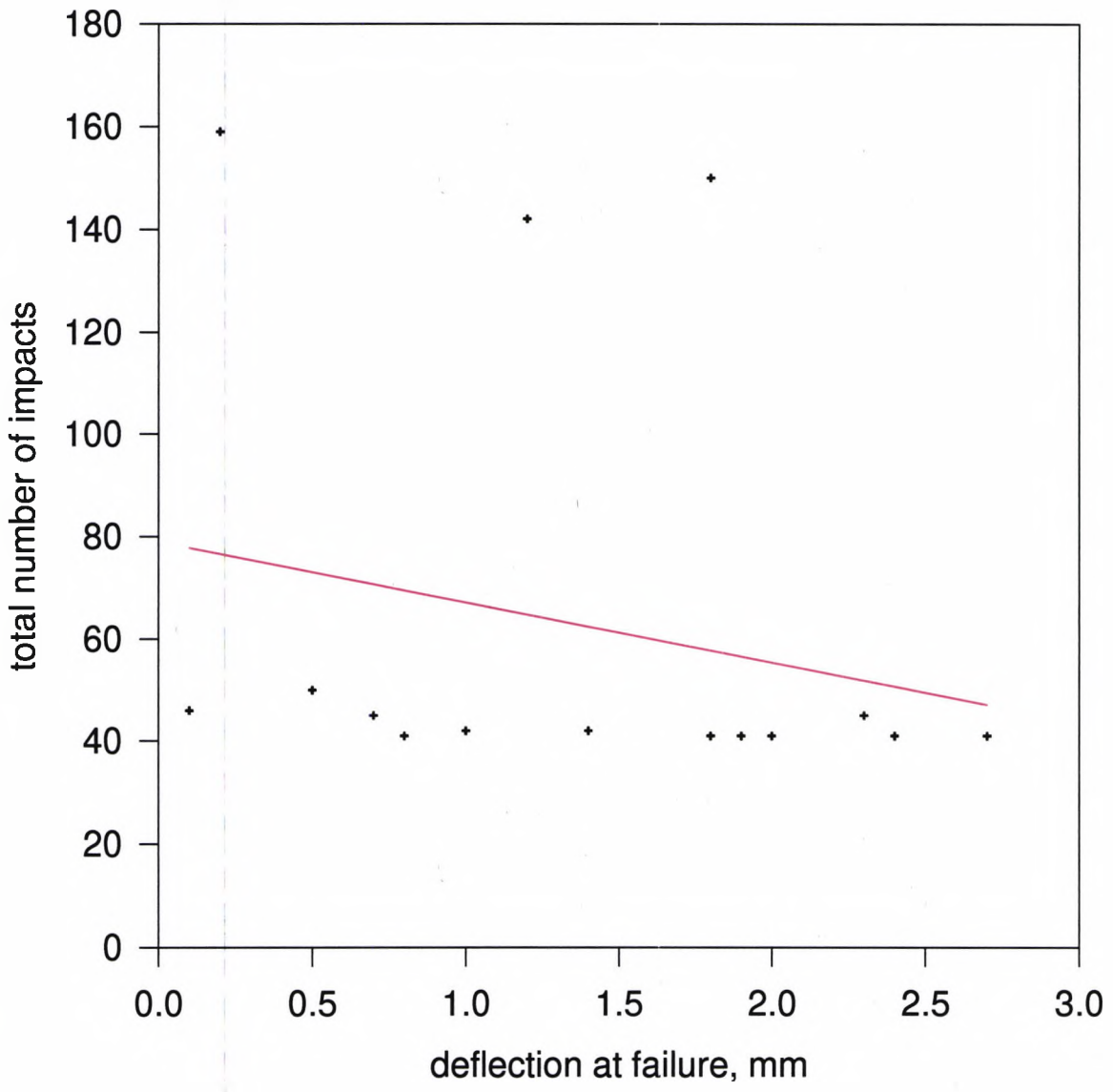
Constant Velocity, 2.6 m/s

deflection at failure v. total number of impacts
Figure 105



Constant Velocity, 3.3 m/s

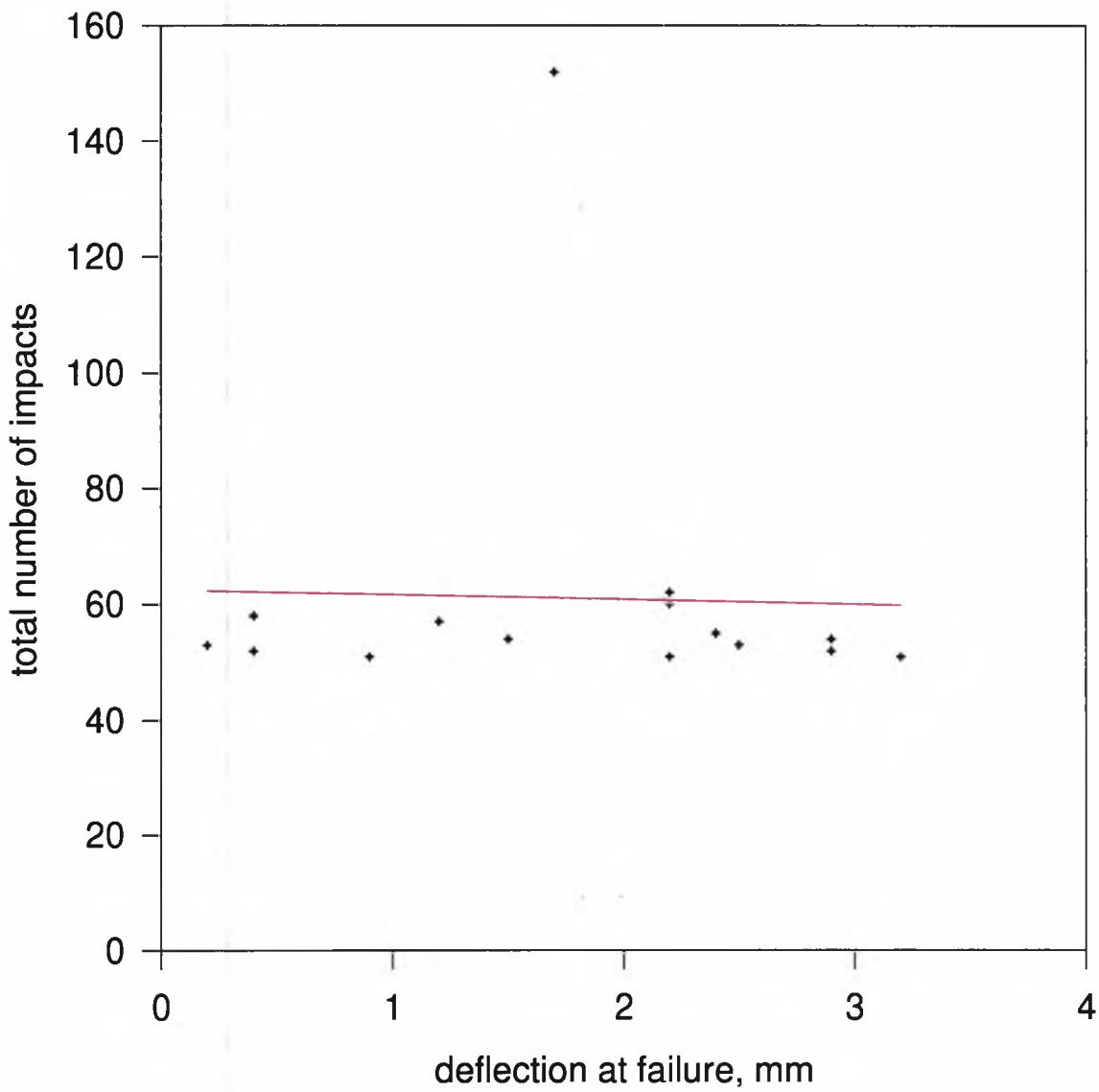
deflection at failure v. total number of impacts
Figure 106



Constant Velocity, 3.8 m/s

deflection at failure v. total number of impacts

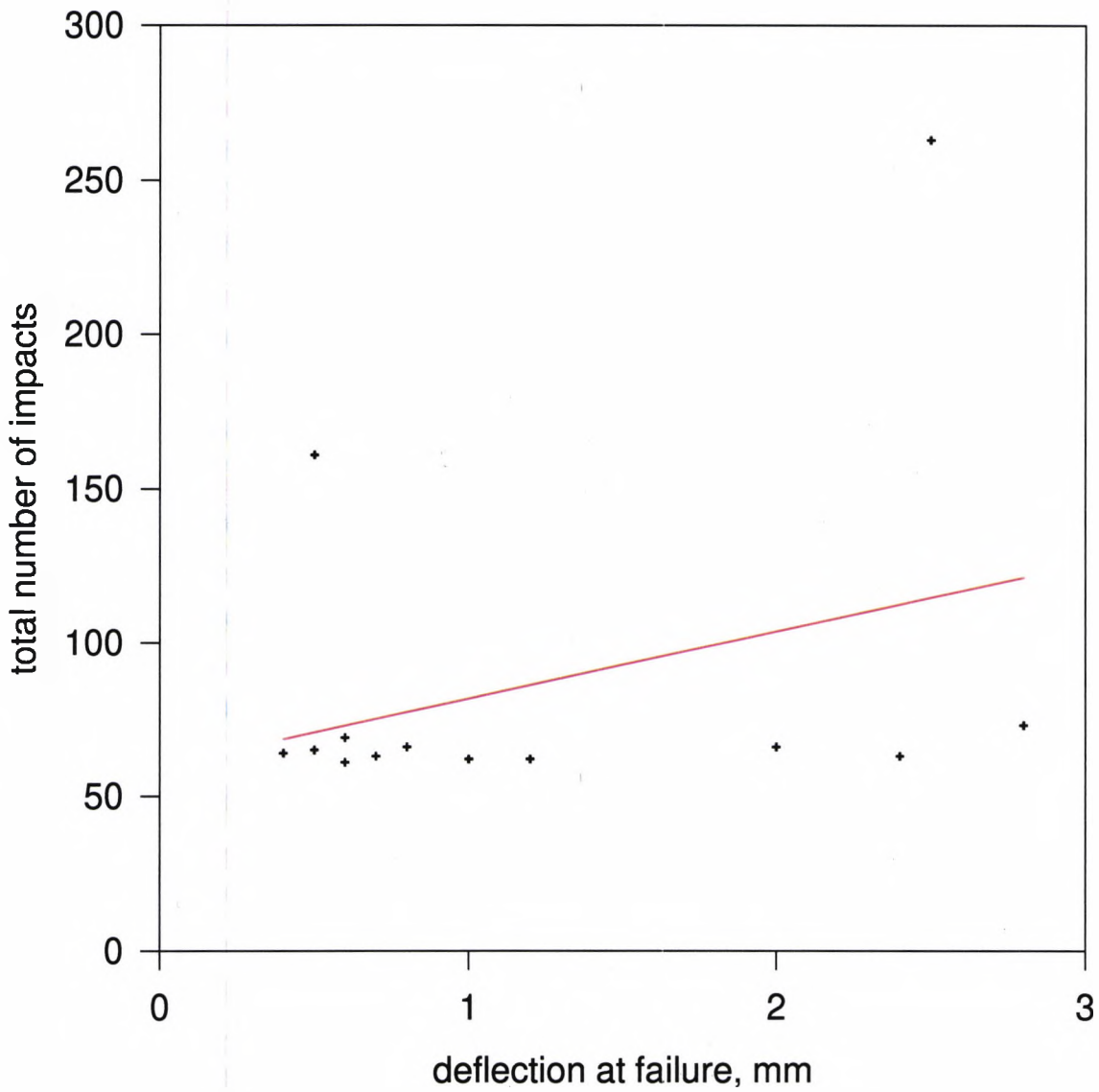
Figure 107



Constant Velocity, 4.3 m/s

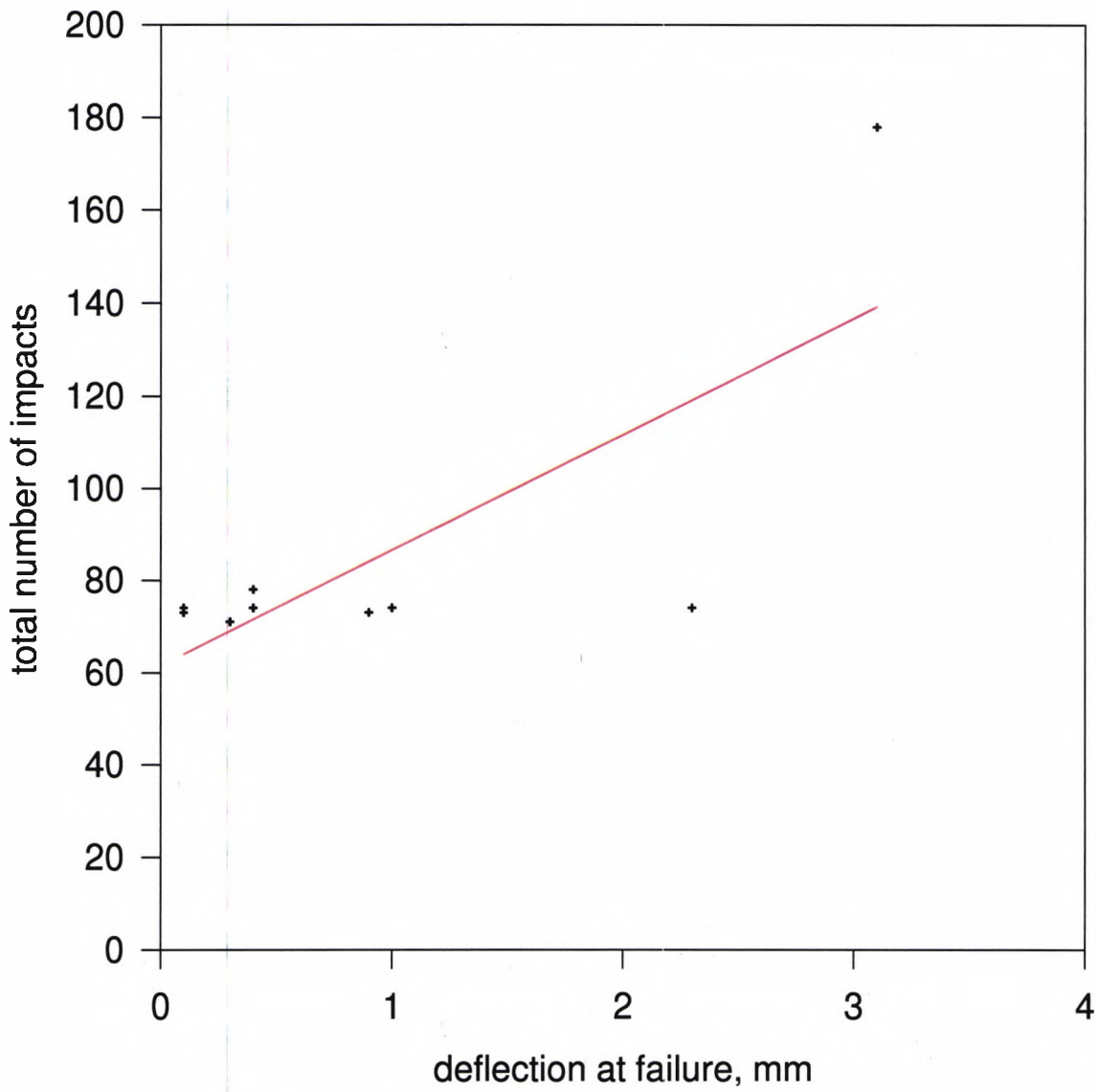
deflection at failure v. total number of impacts

Figure 108



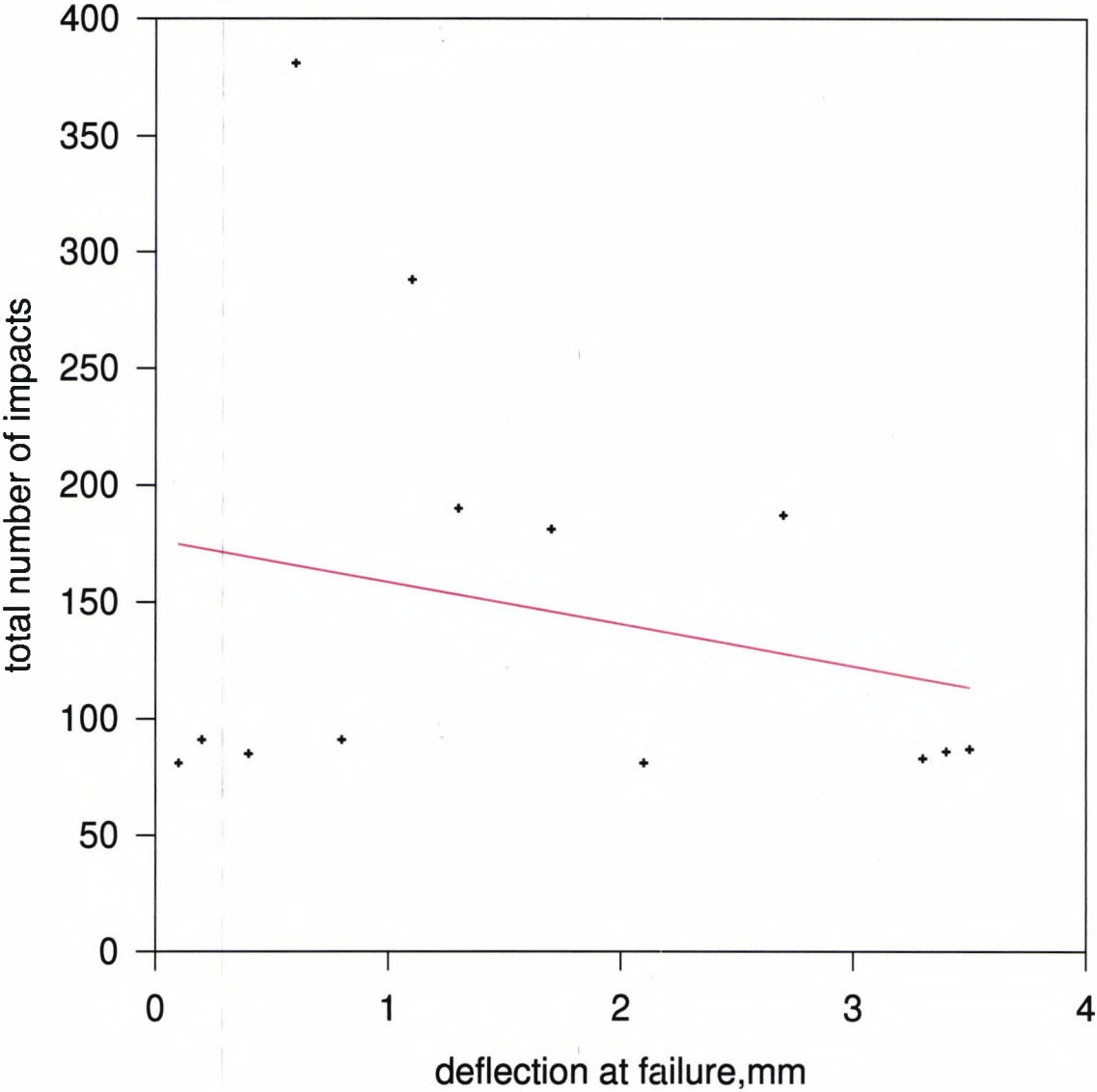
Constant Velocity, 4.75 m/s

deflection at failure v. total number of impacts Figure 109



Constant Velocity, 5.3 m/s

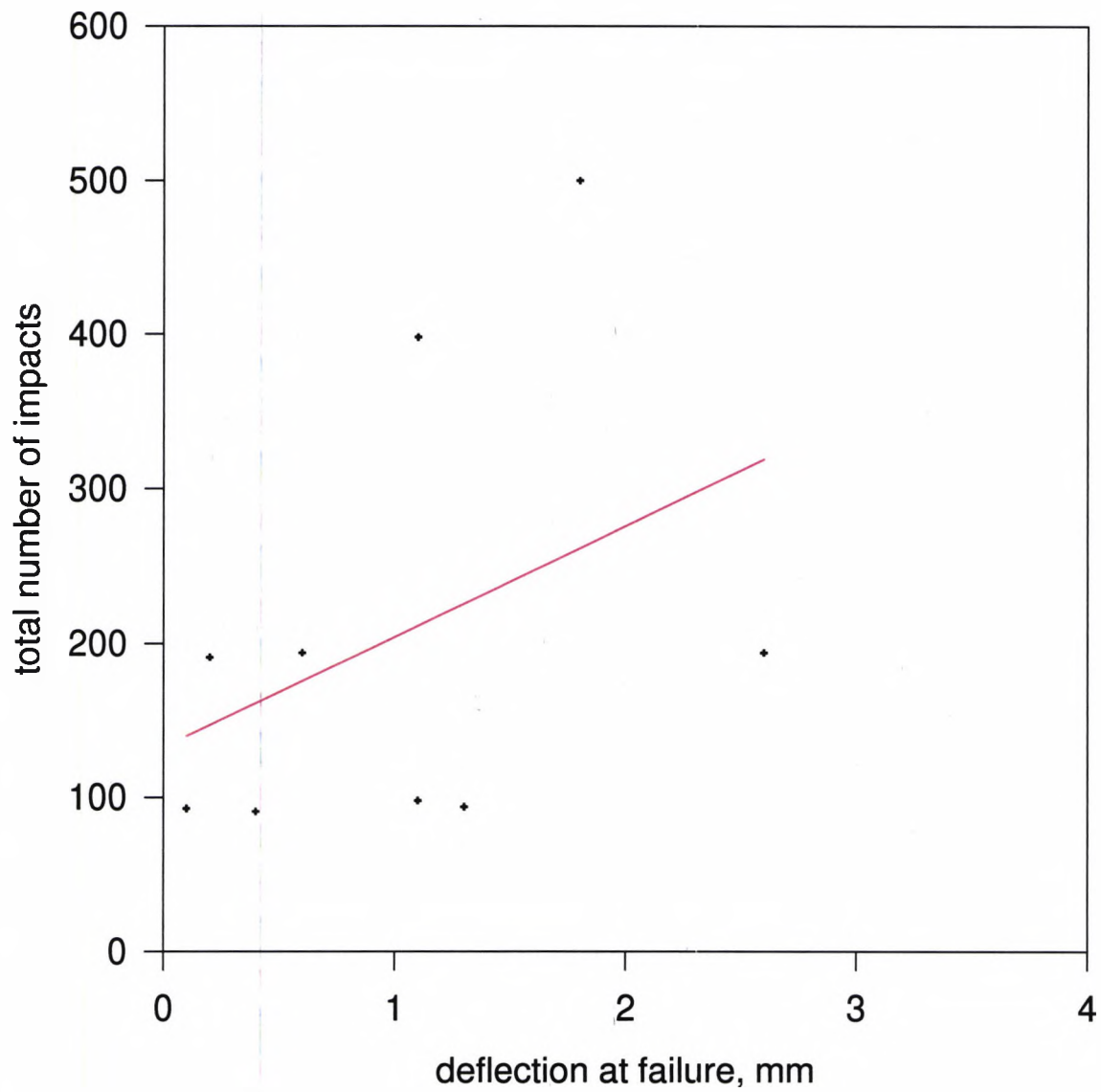
deflection at failure v. total number of impacts
Figure 110



Constant Velocity, 5.85 m/s

deflection at failure v. total number of impacts

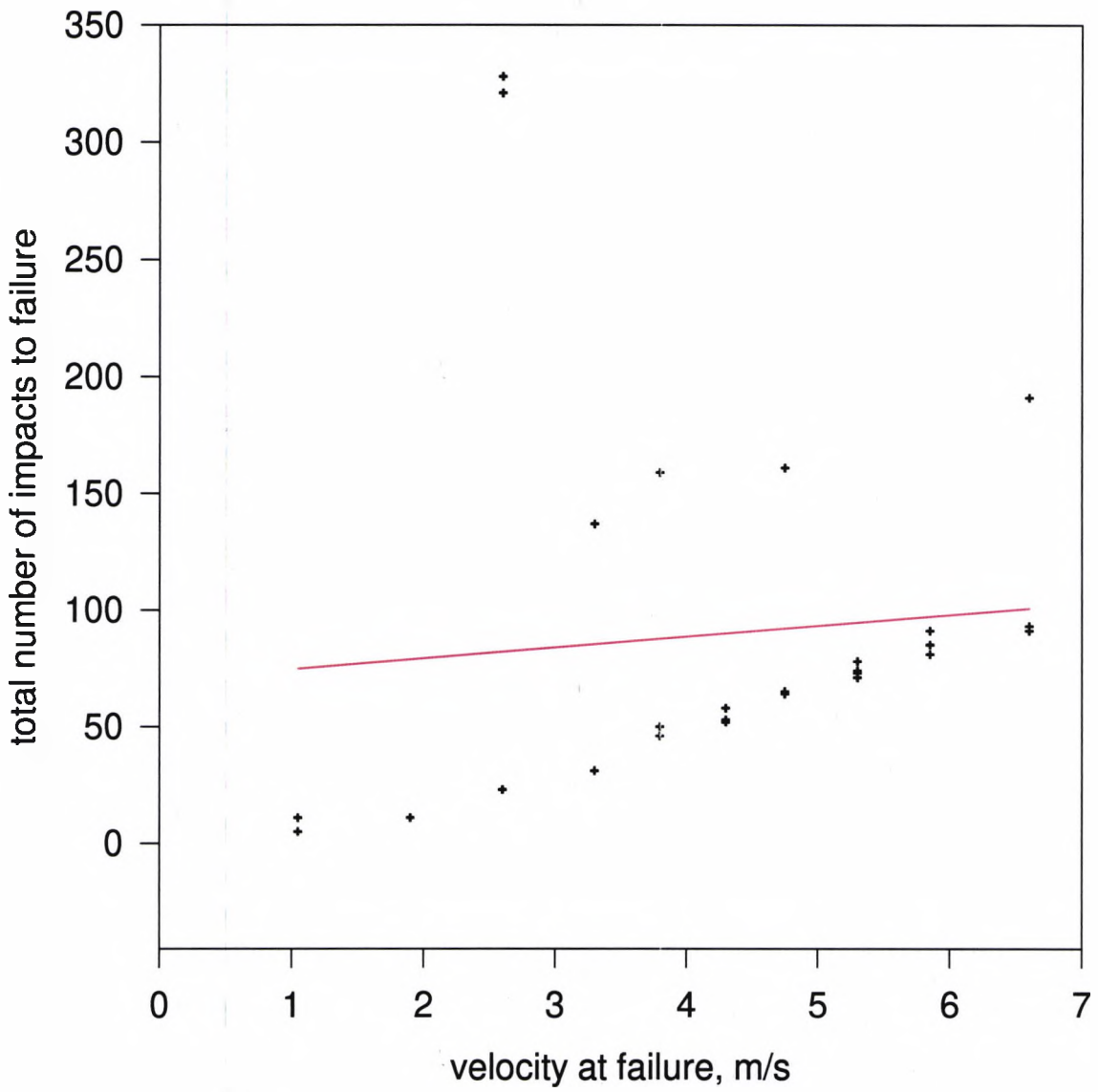
Figure 111



Constant Velocity, 6.6 m/s

velocity at failure v. total number of impacts

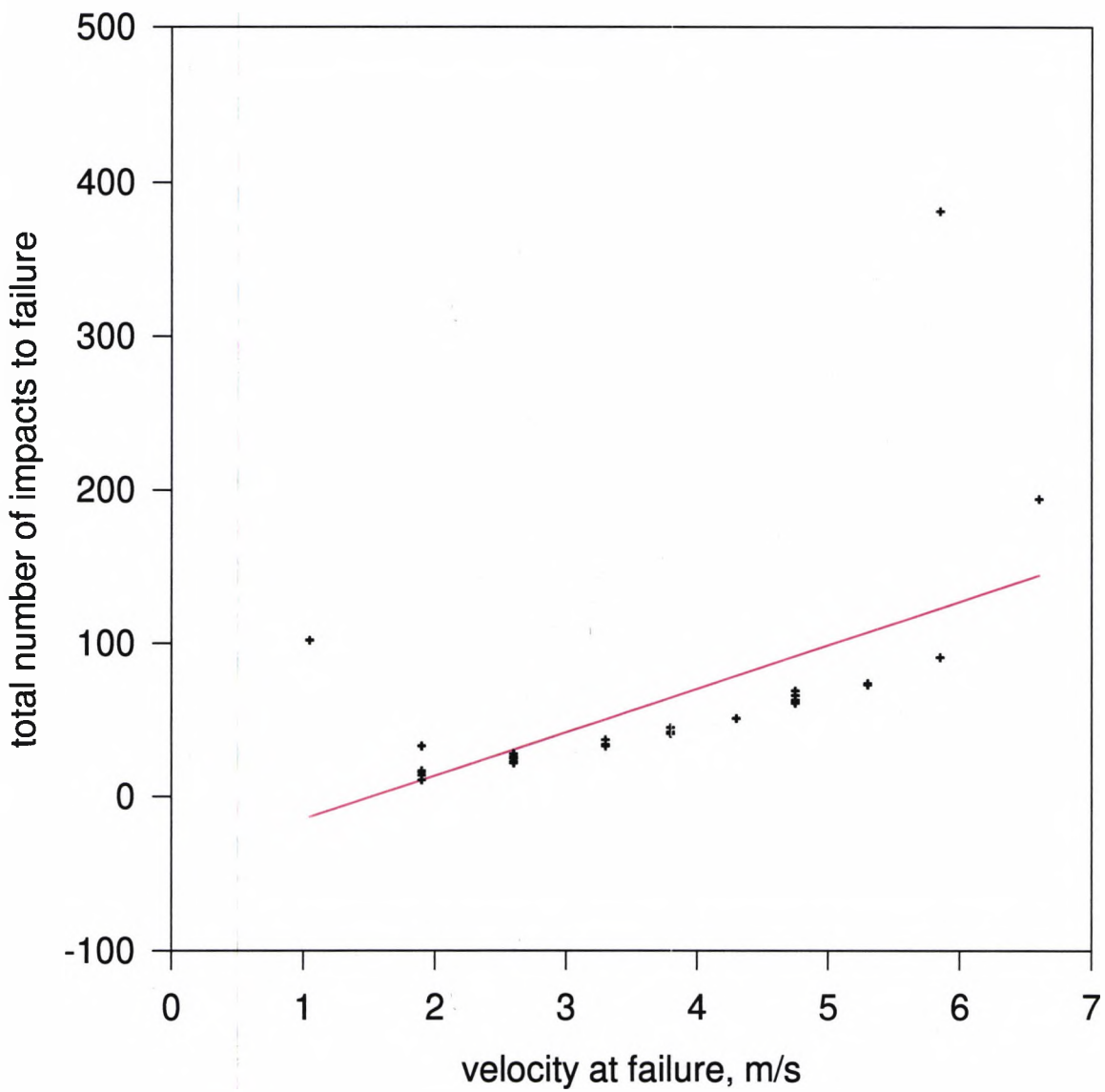
Figure 112



Constant deflection between 0 and 0.5

velocity at failure v. total number of impacts

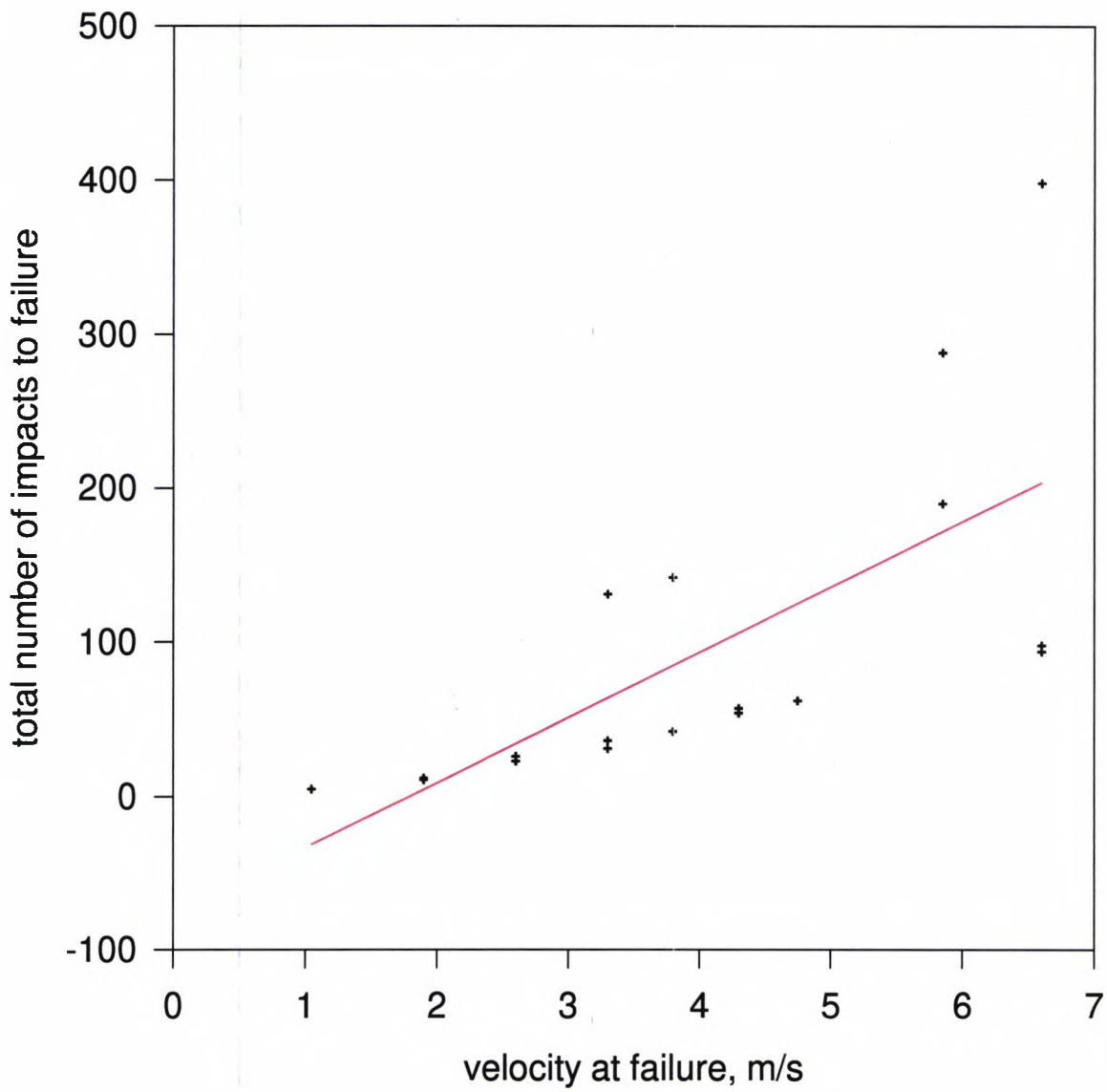
Figure 113



Constant deflection between 0.6 and 1.0

velocity at failure v. total number of impacts

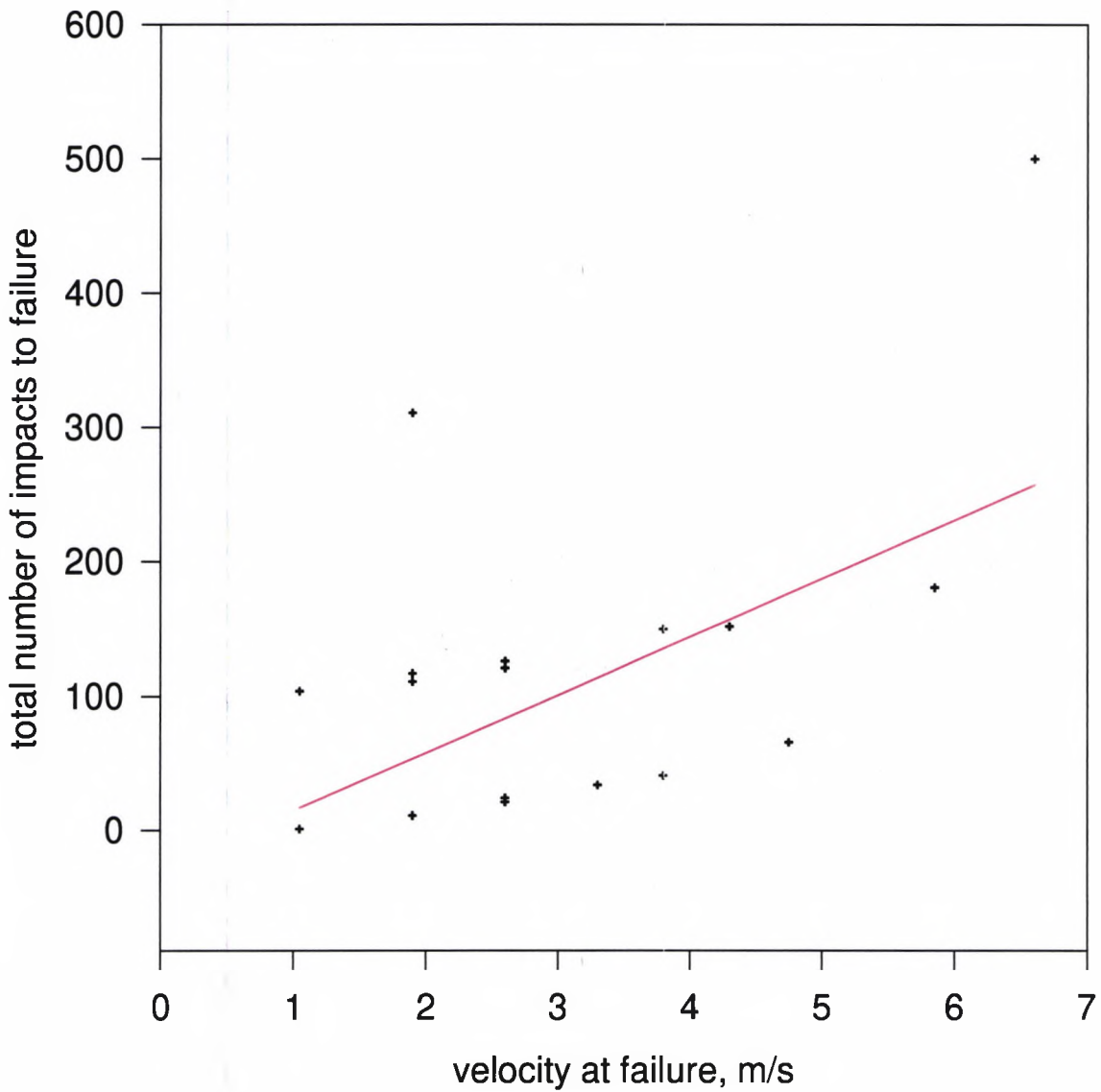
Figure 114



Constant deflection between 1.1 and 1.5

velocity at failure v. total number of impacts

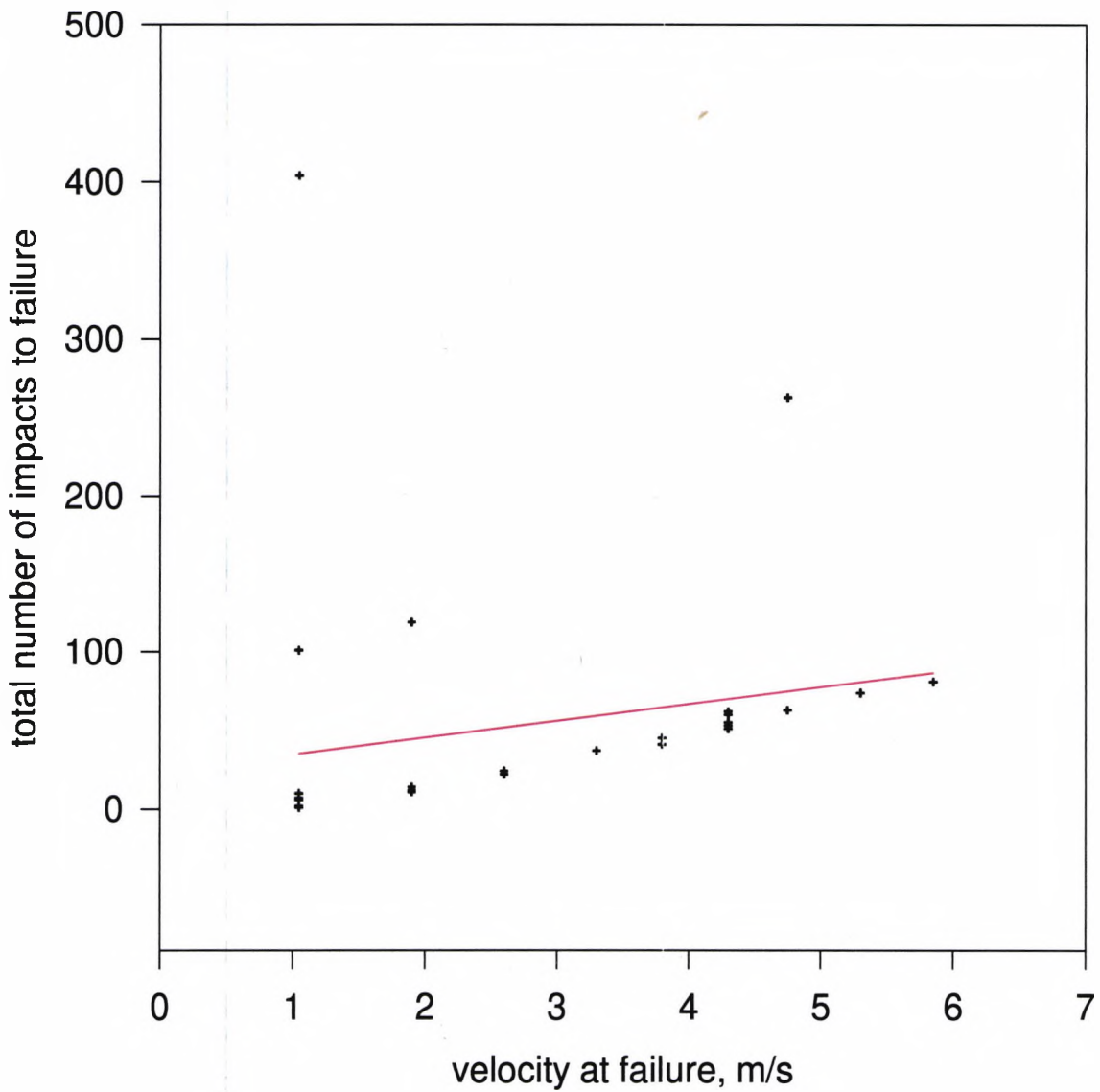
Figure 115



Constant deflection between 1.6 and 2.0

velocity at failure v. total number of impacts

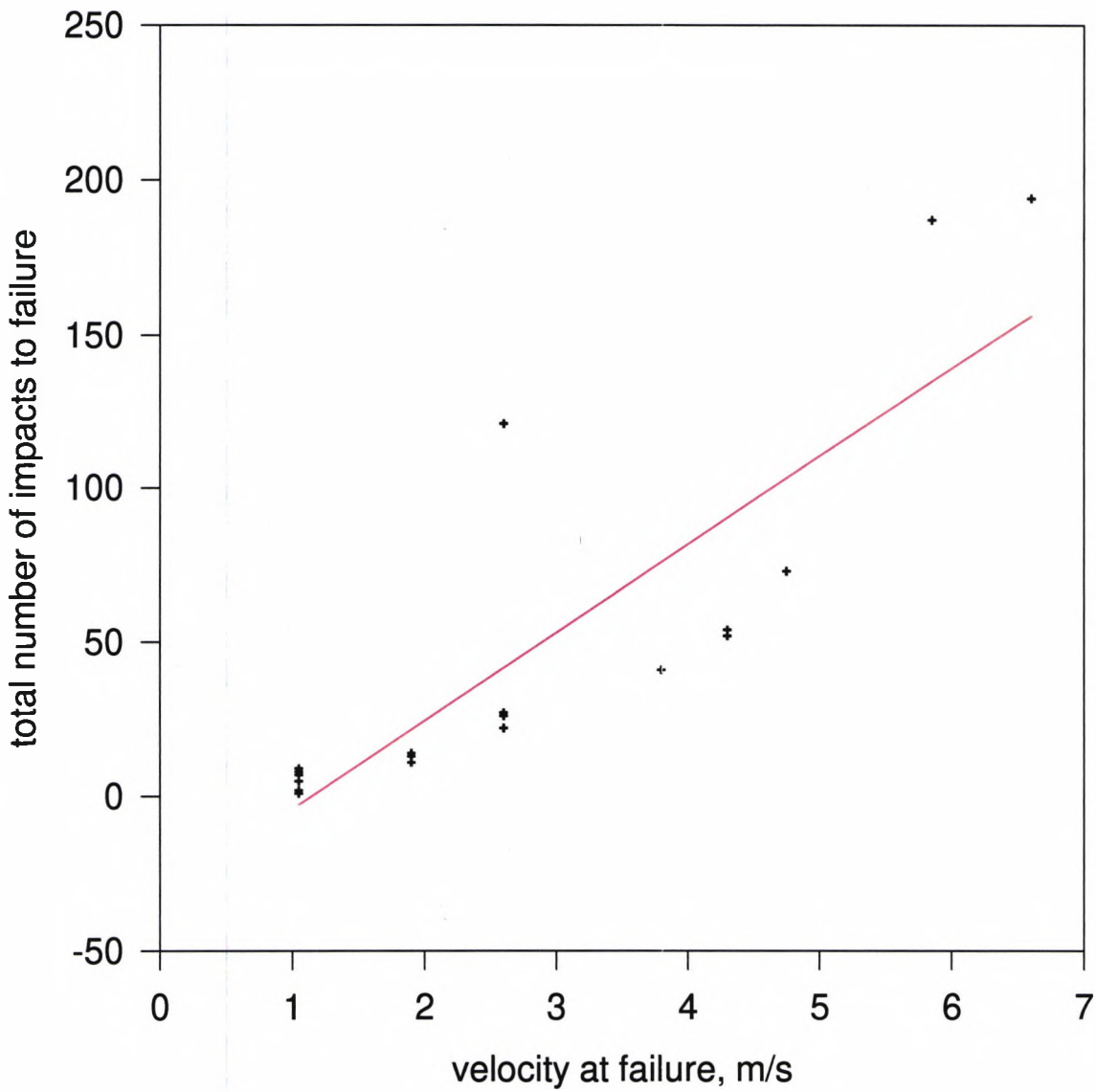
Figure 116



Constant deflection between 2.1 and 2.5

velocity at failure v. total number of impacts

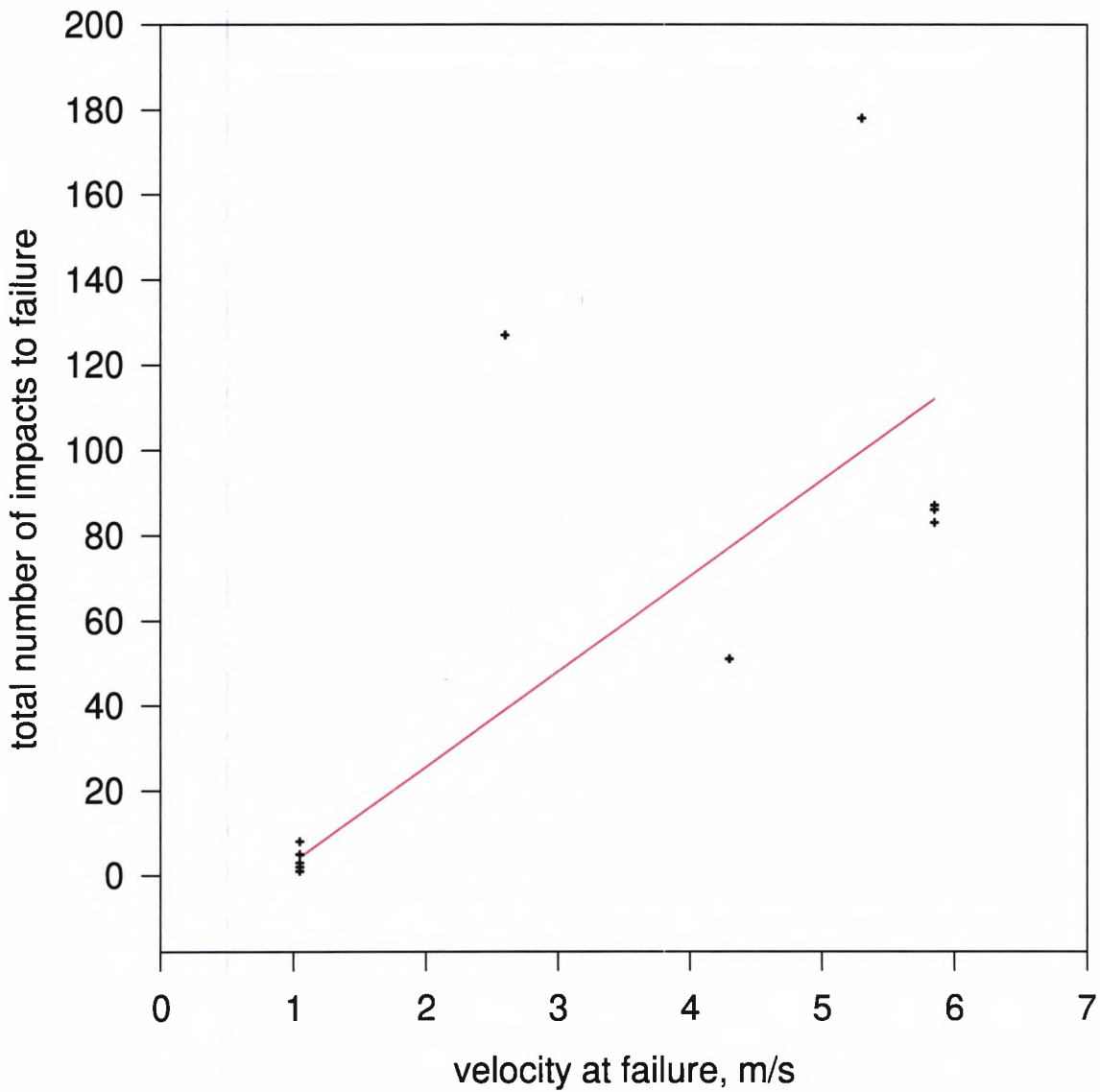
Figure 117



Constant deflection between 2.6 and 3.0

velocity at failure v. total number of impacts

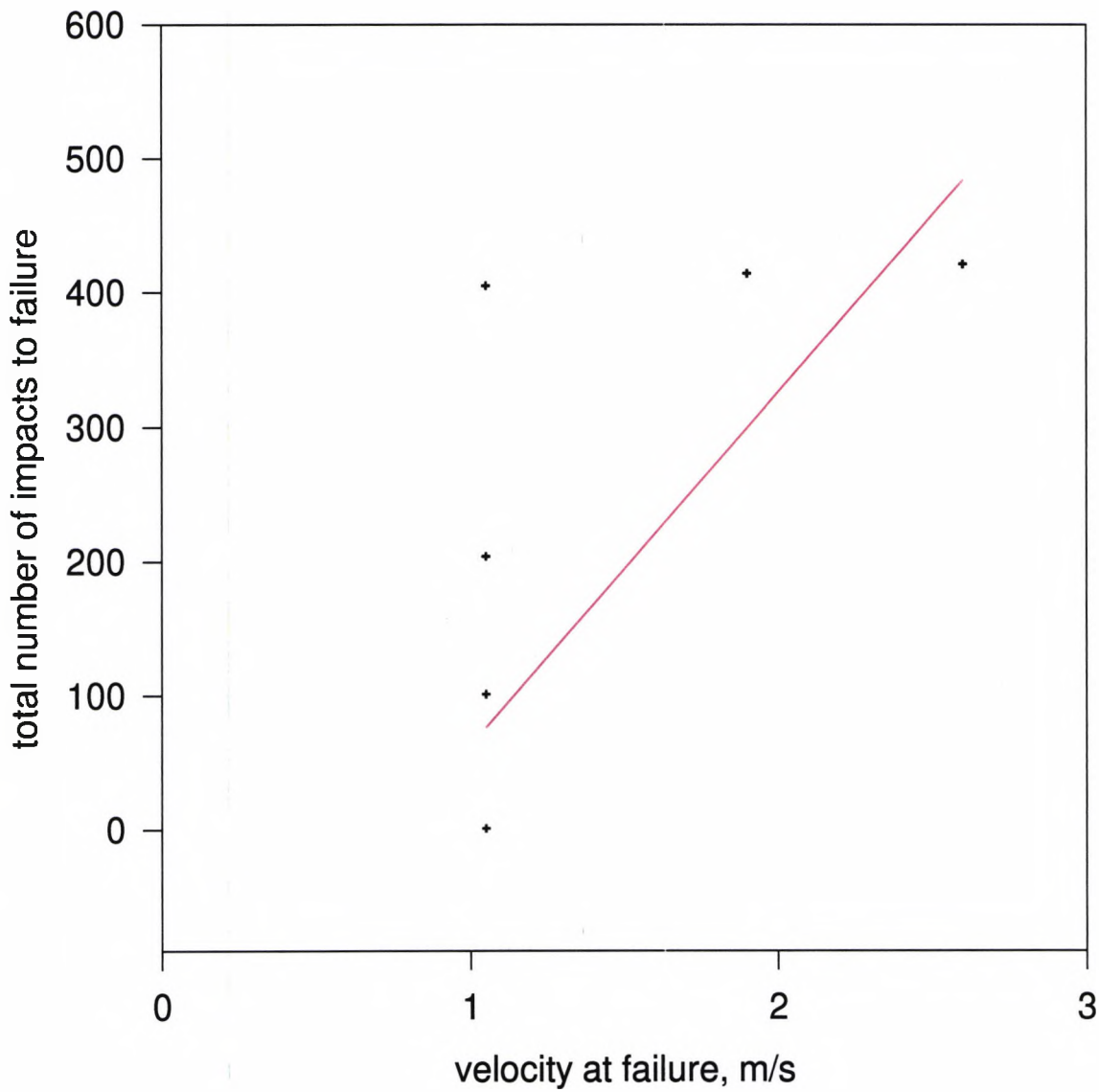
Figure 118



Constant deflection between 3.1 and 3.5

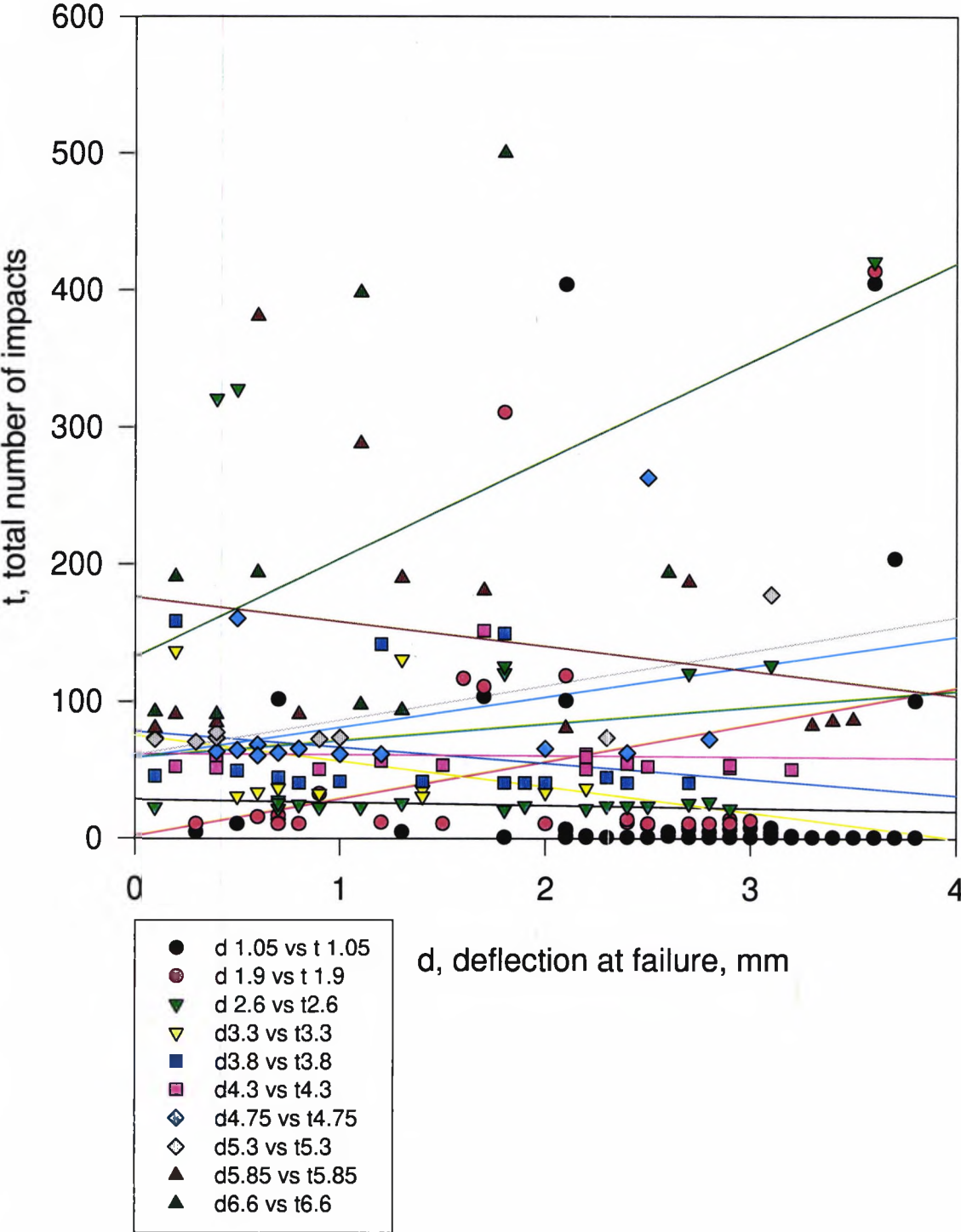
velocity at failure v. total number of impacts

Figure 119

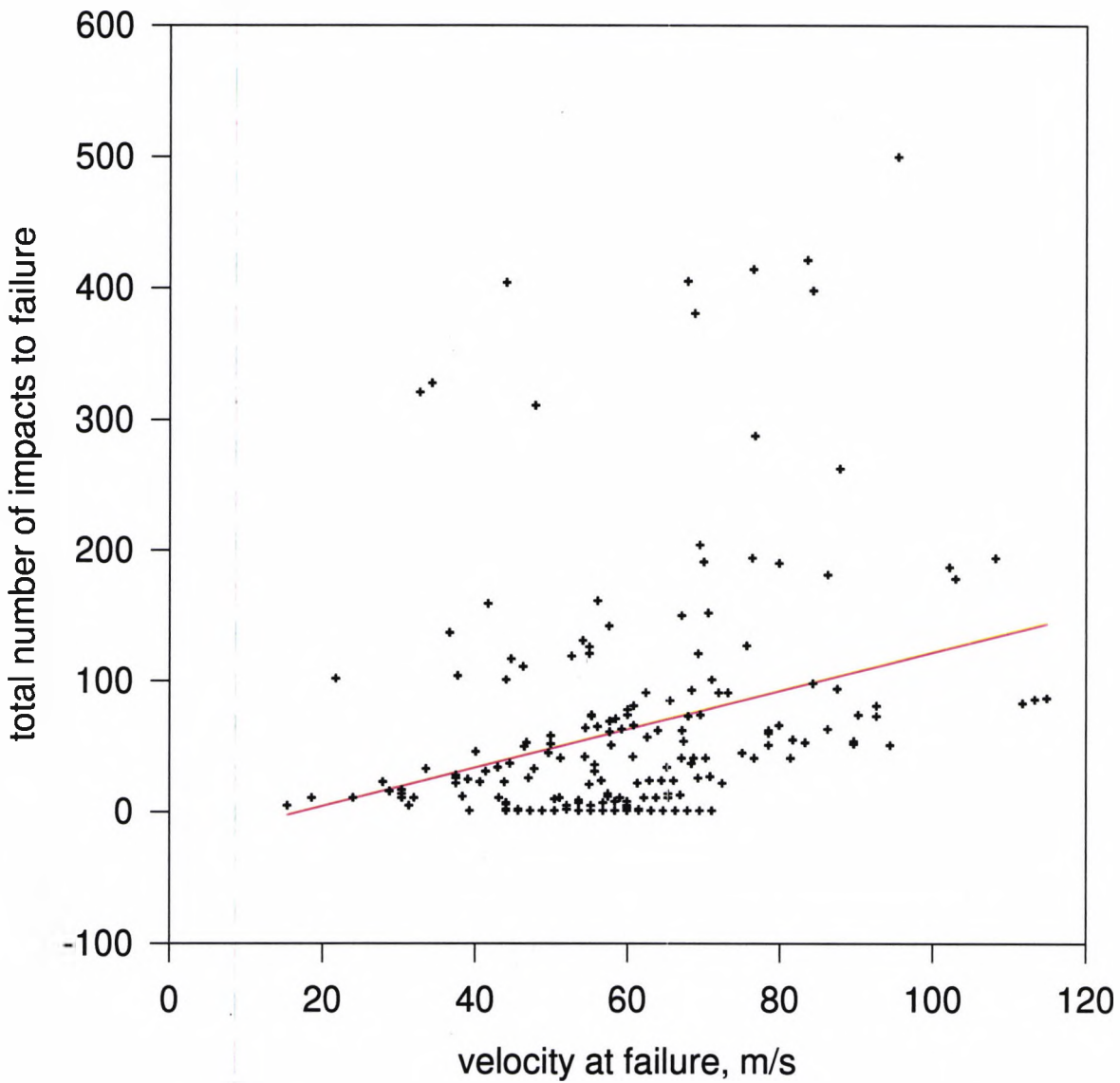


Constant deflection between 3.6 and 4.0

deflection at failure v. total number of impacts
Figure 120



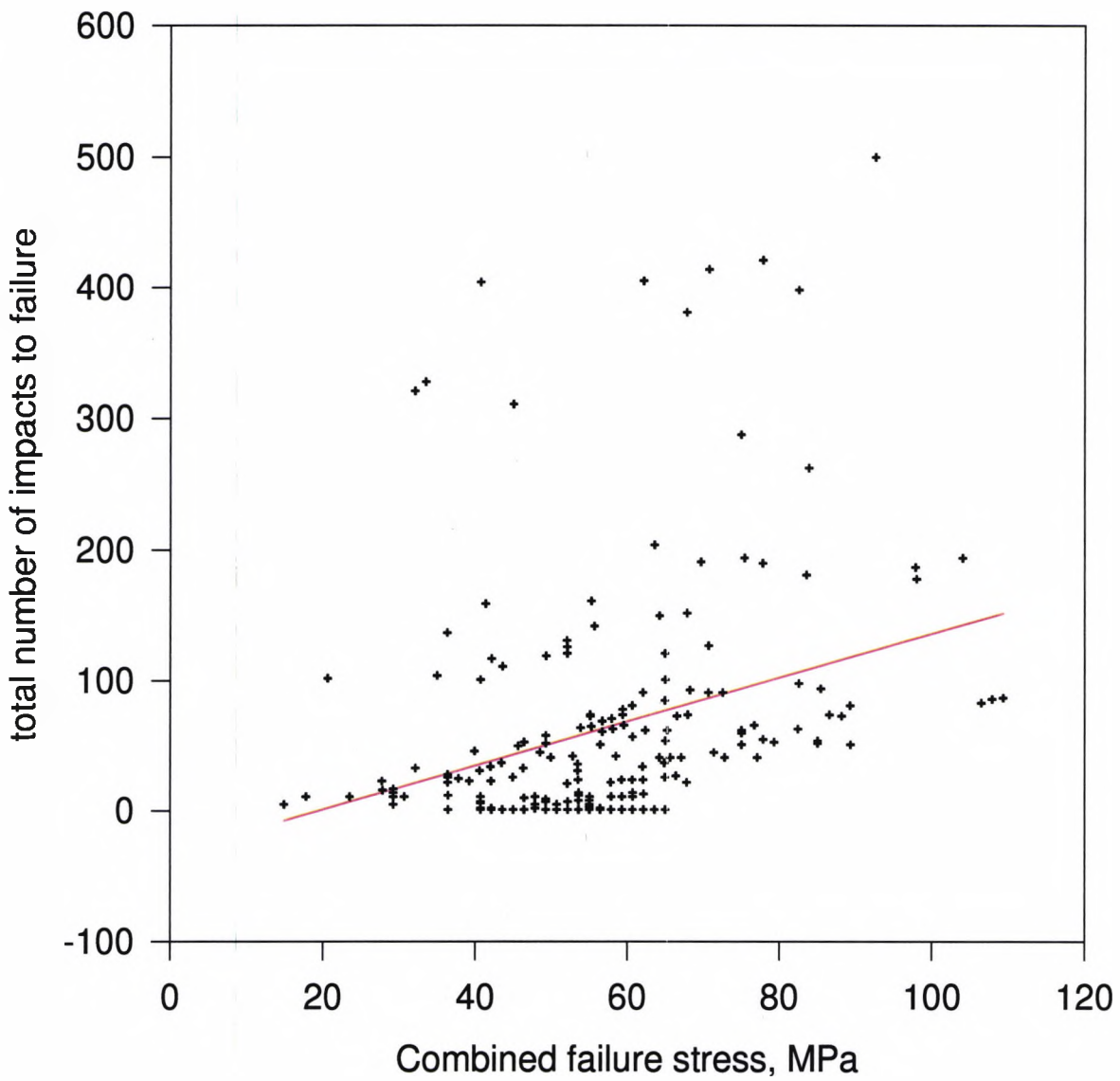
Total failure stress v. total number of impacts
Figure 121



Stress combination factor of 1.0

Total failure stress v. total number of impacts

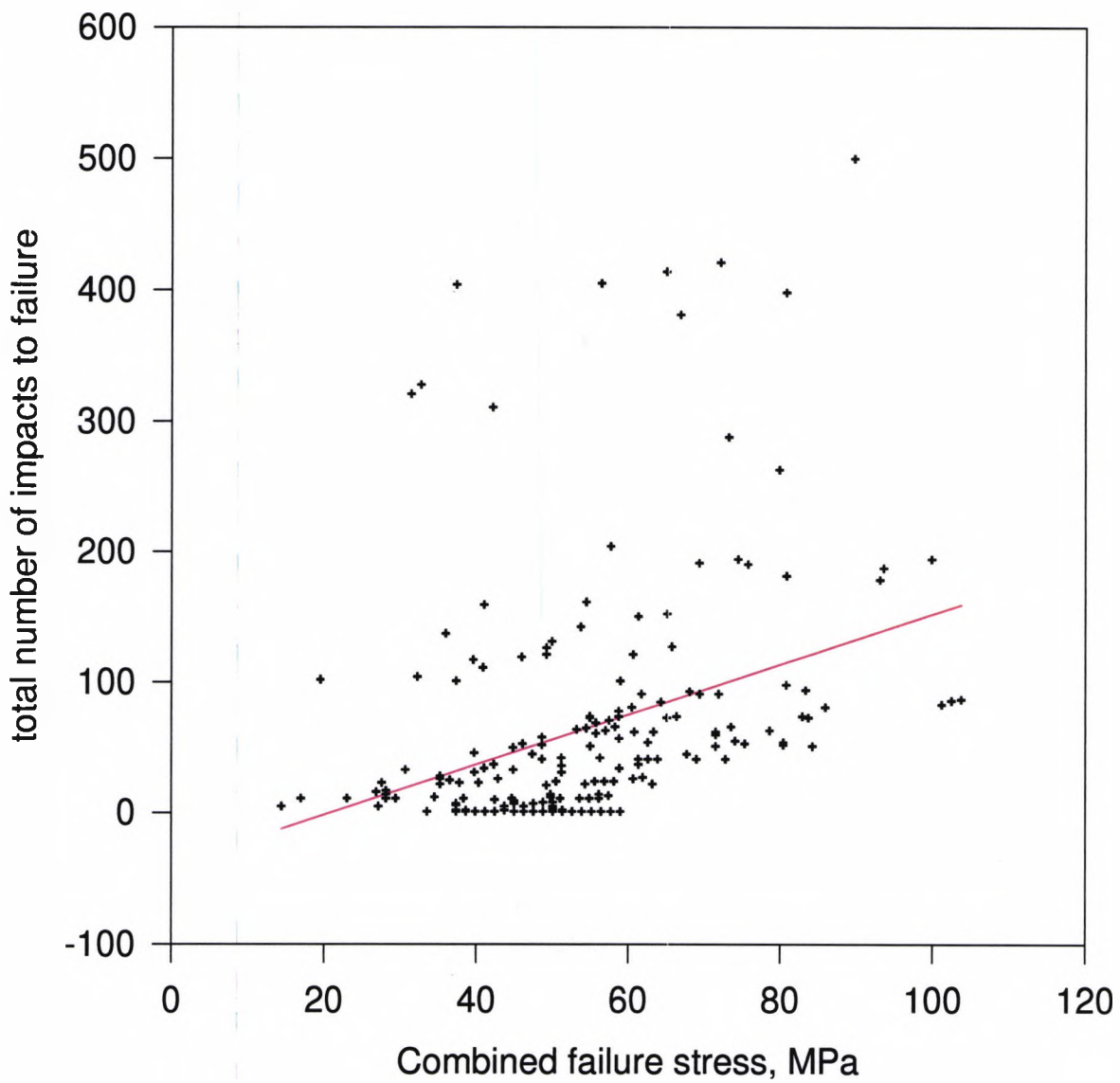
Figure 122



Stress combination factor of 0.9

Total failure stress v. total number of impacts

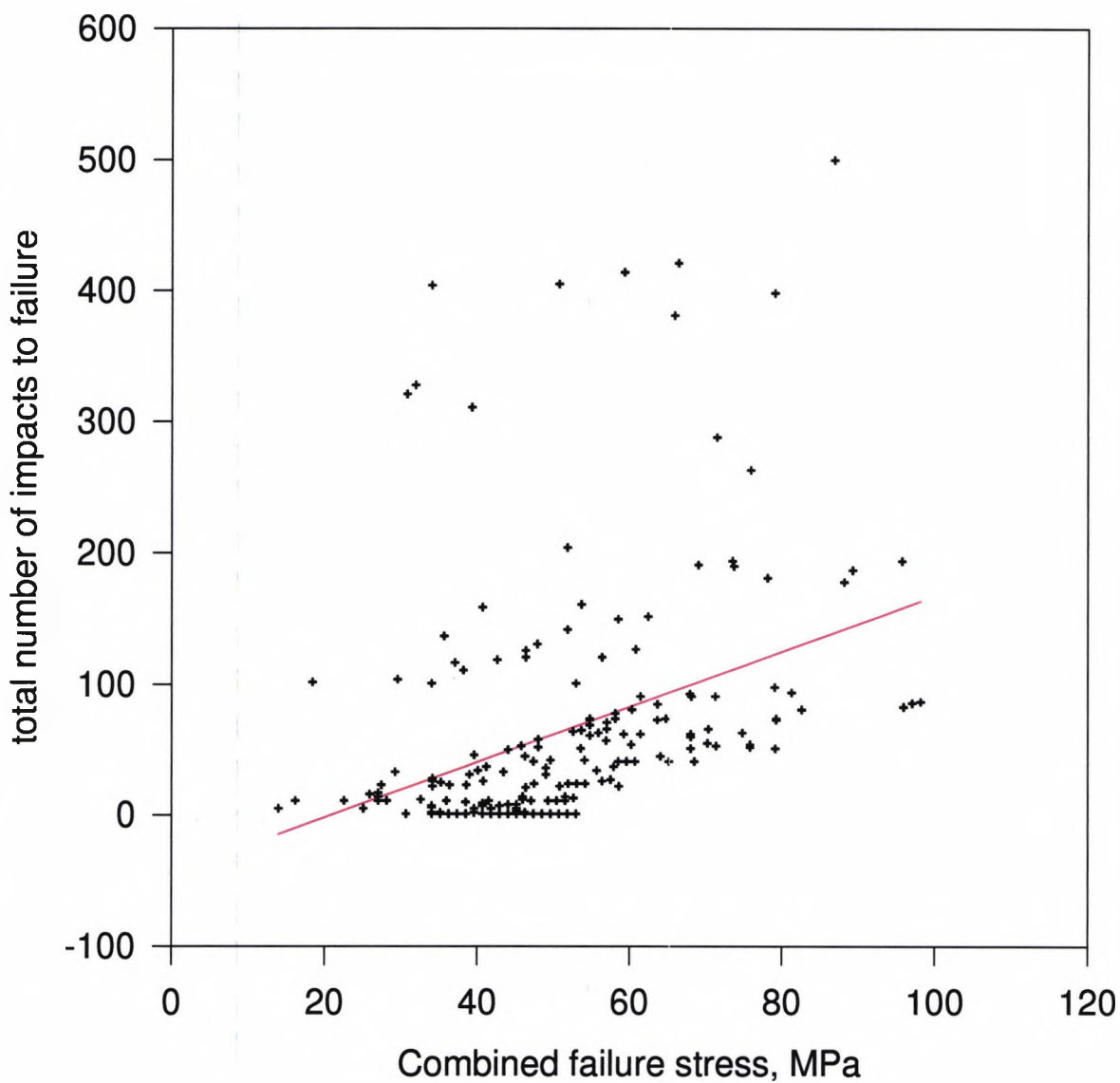
Figure 123



Stress combination factor of 0.8

Total failure stress v. total number of impacts

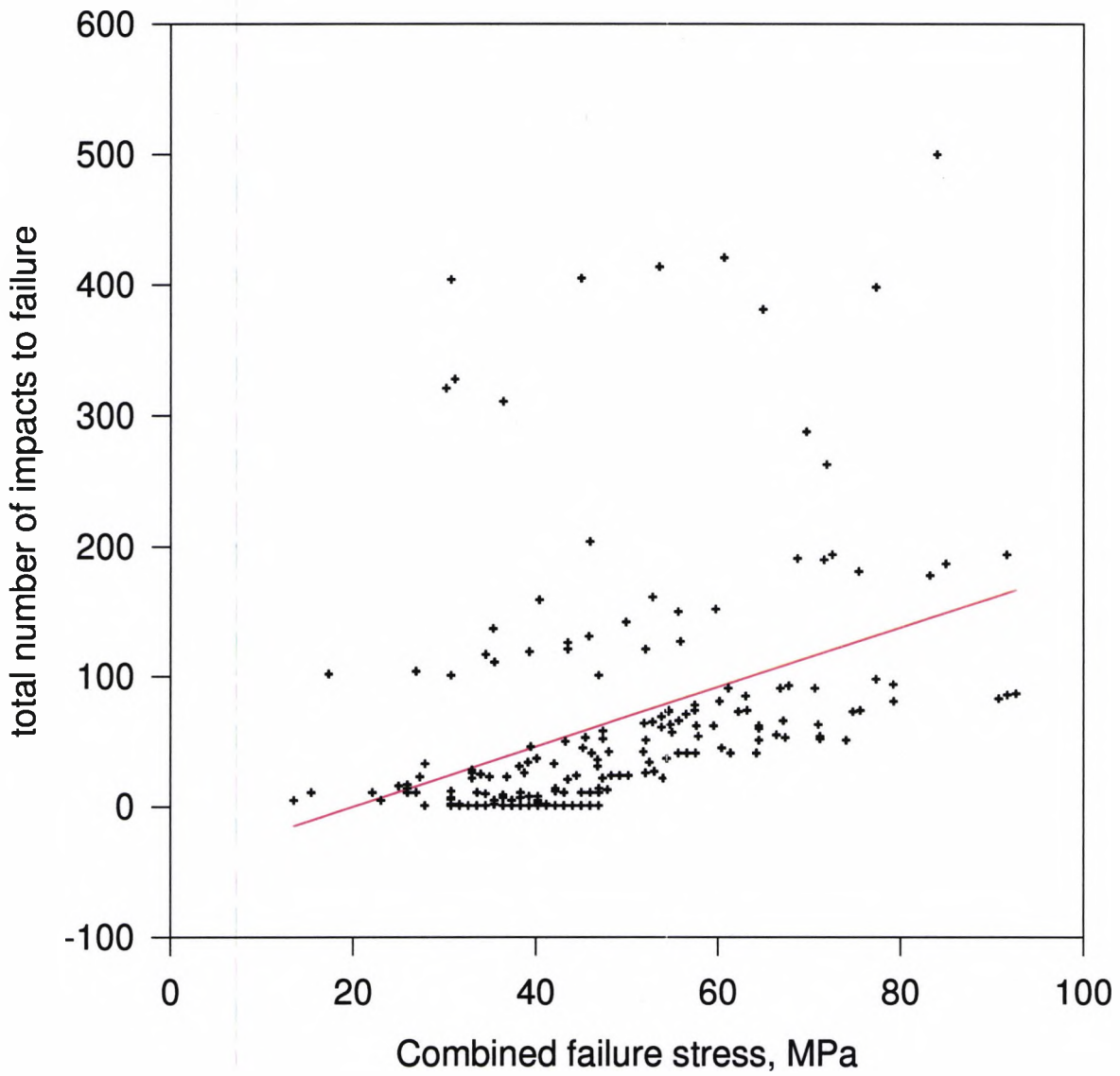
Figure 124



Stress combination factor of 0.7

Total failure stress v. total number of impacts

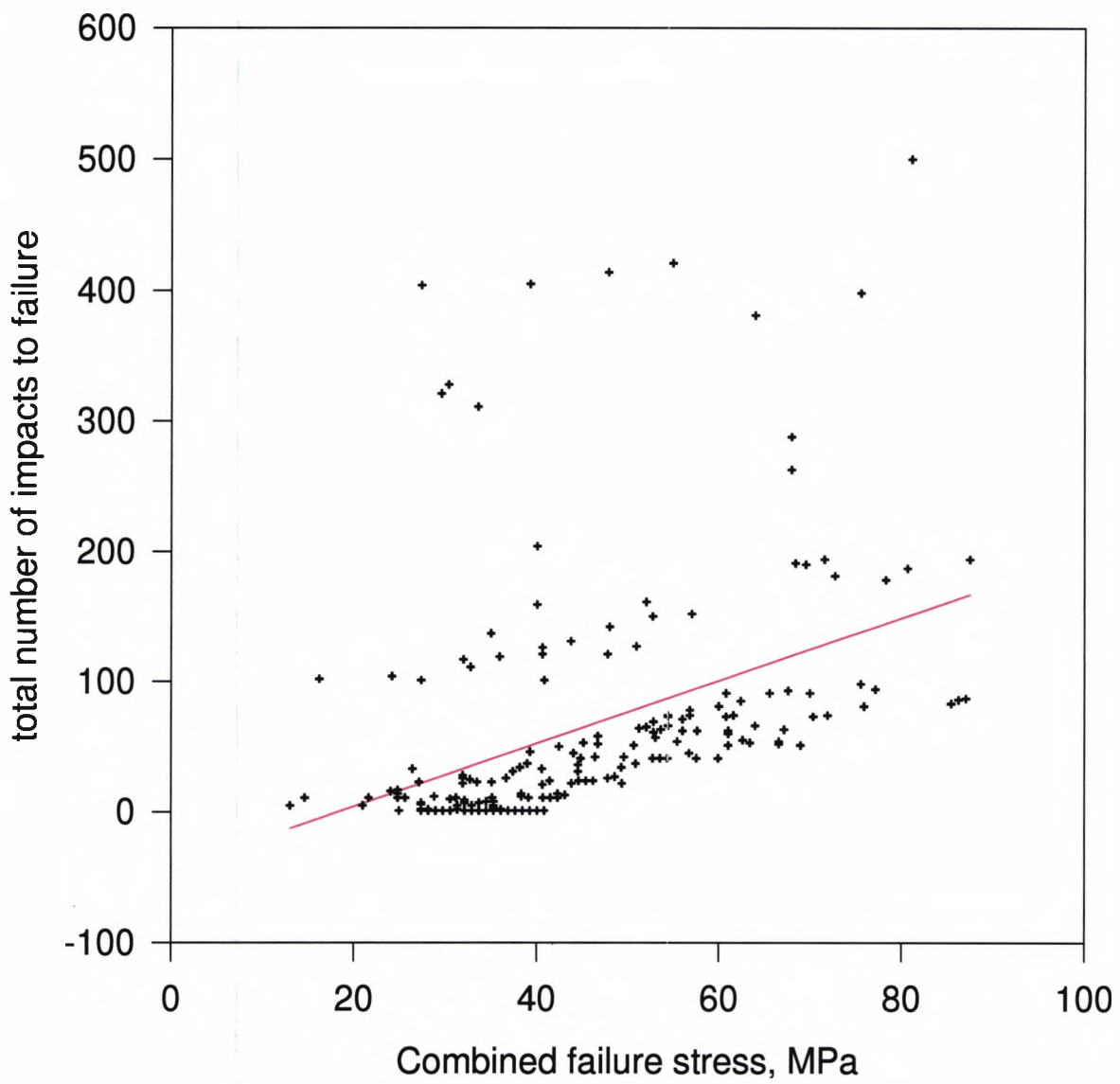
Figure 125



Stress combination factor of 0.6

Total failure stress v. total number of impacts

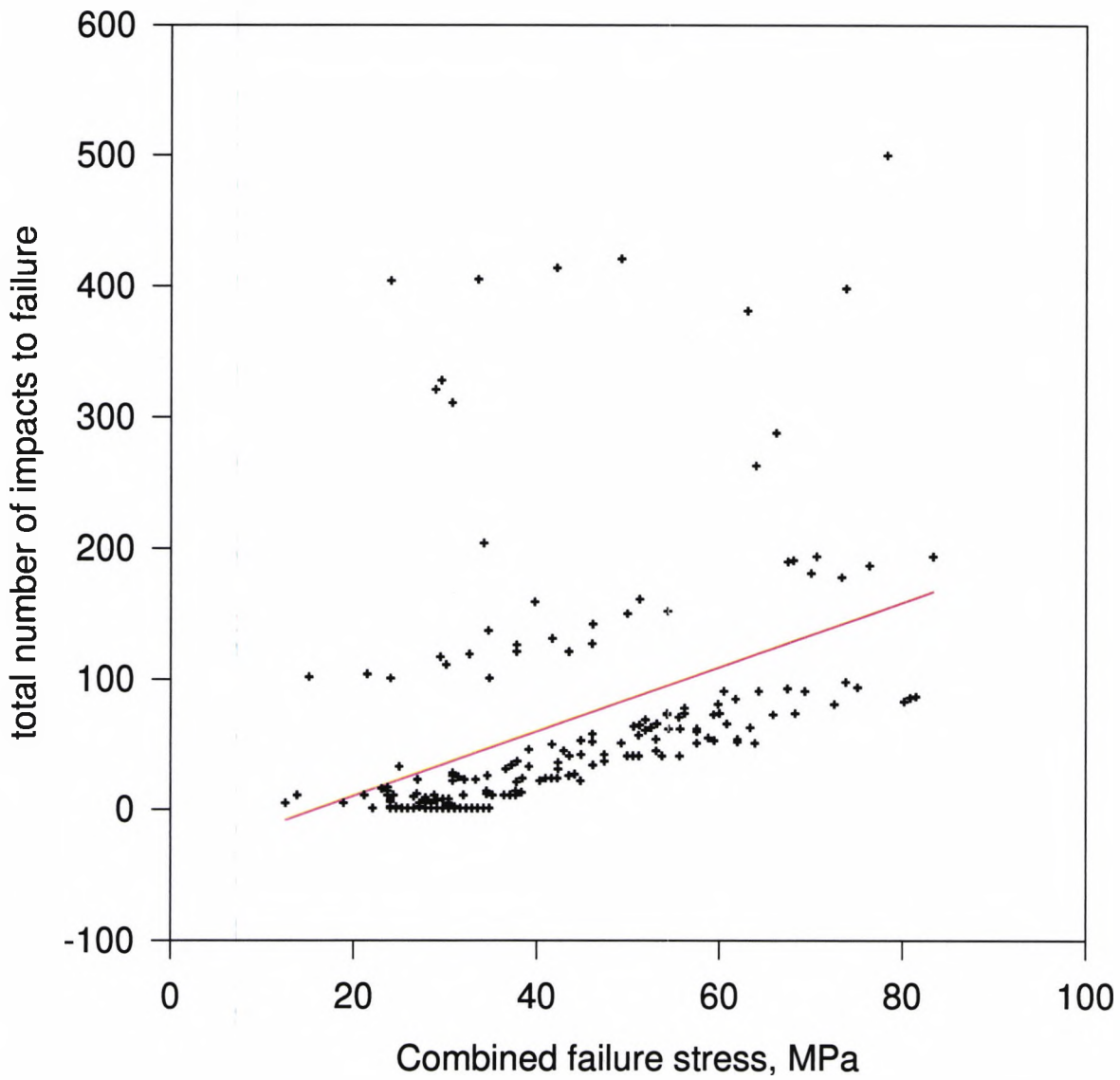
Figure 126



Stress combination factor of 0.5

Total failure stress v. total number of impacts

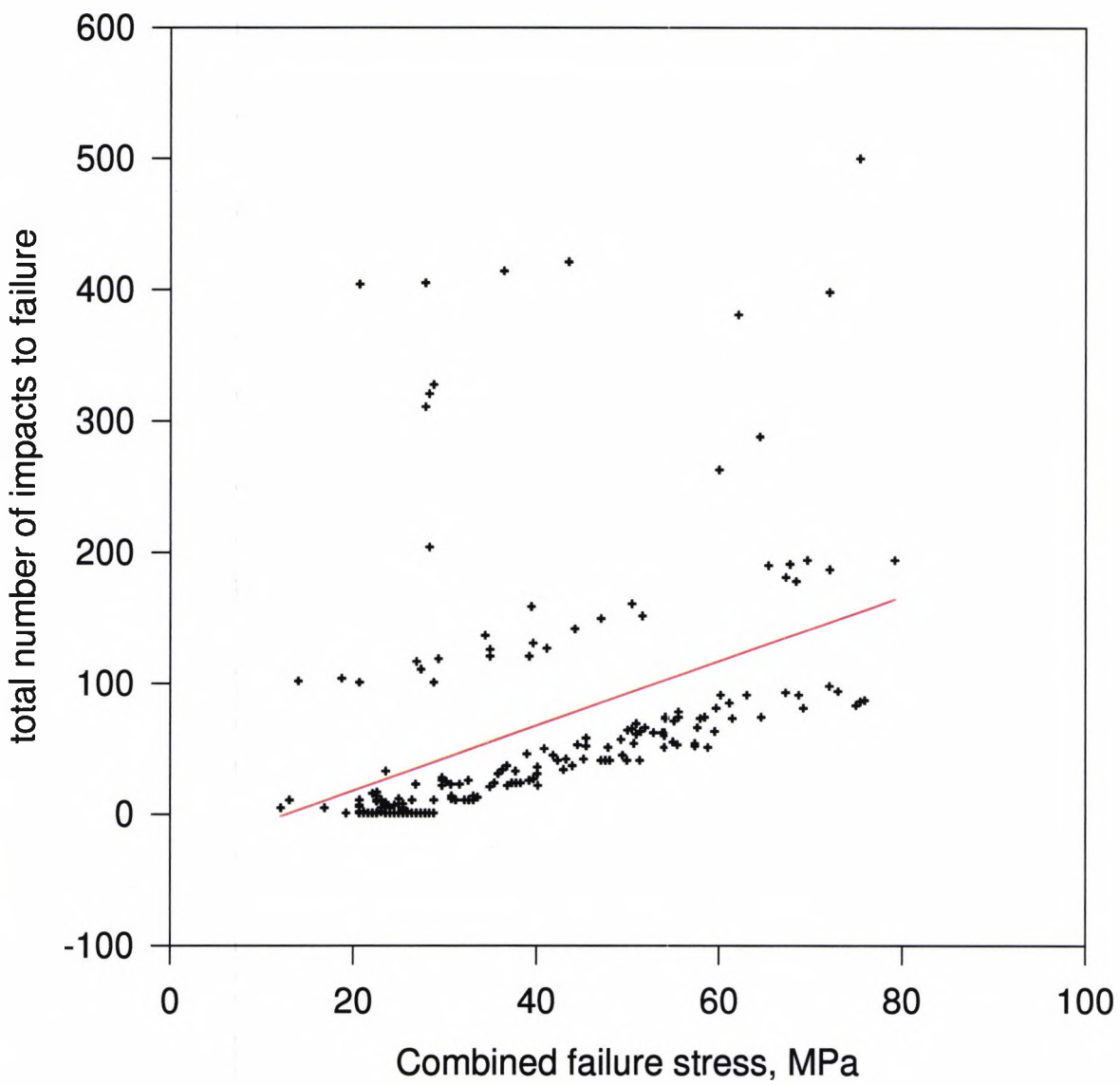
Figure 127



Stress combination factor of 0.4

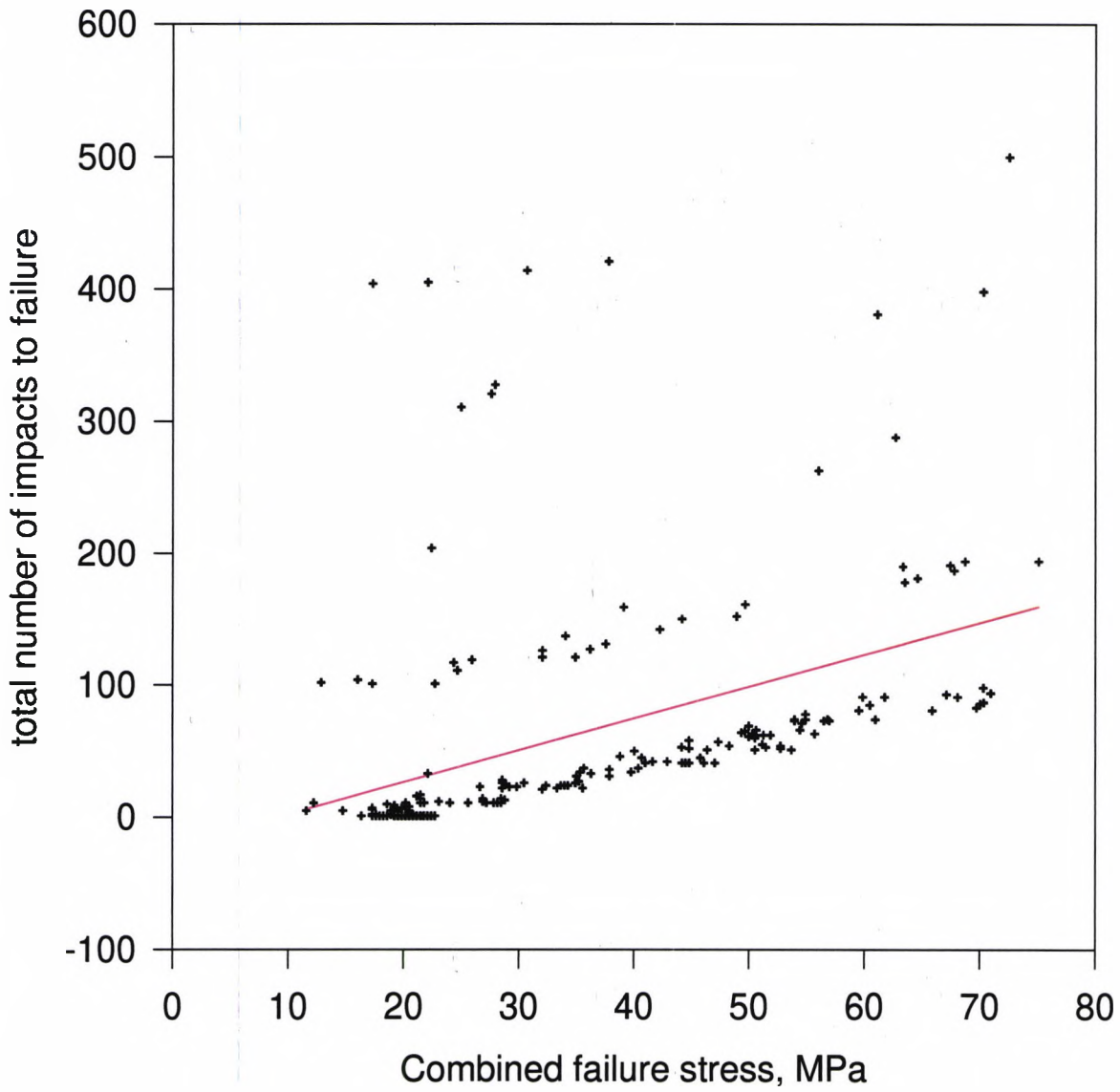
Total failure stress v. total number of impacts

Figure 128



Total failure stress v. total number of impacts

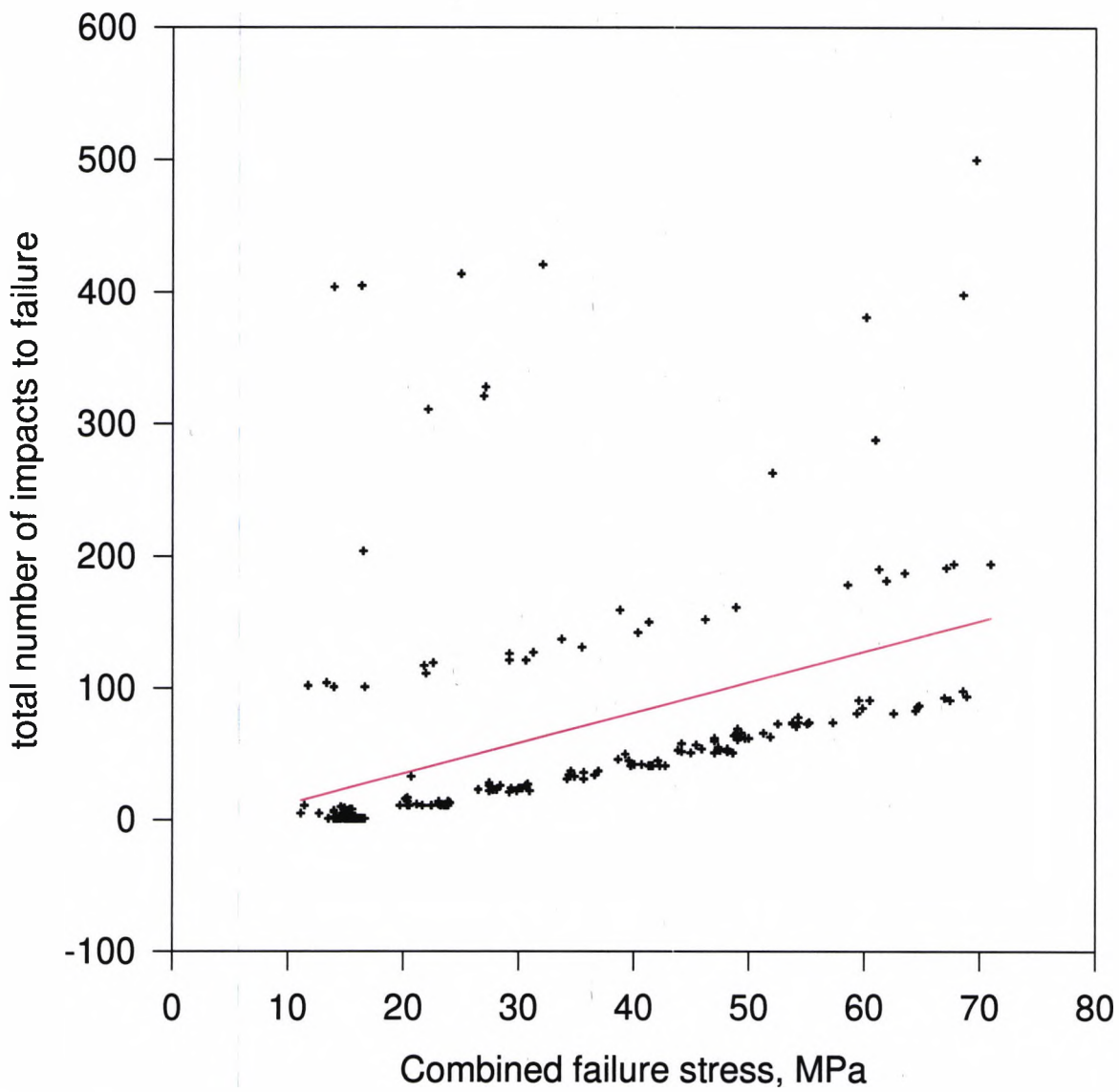
Figure 129



Stress combination factor of 0.2

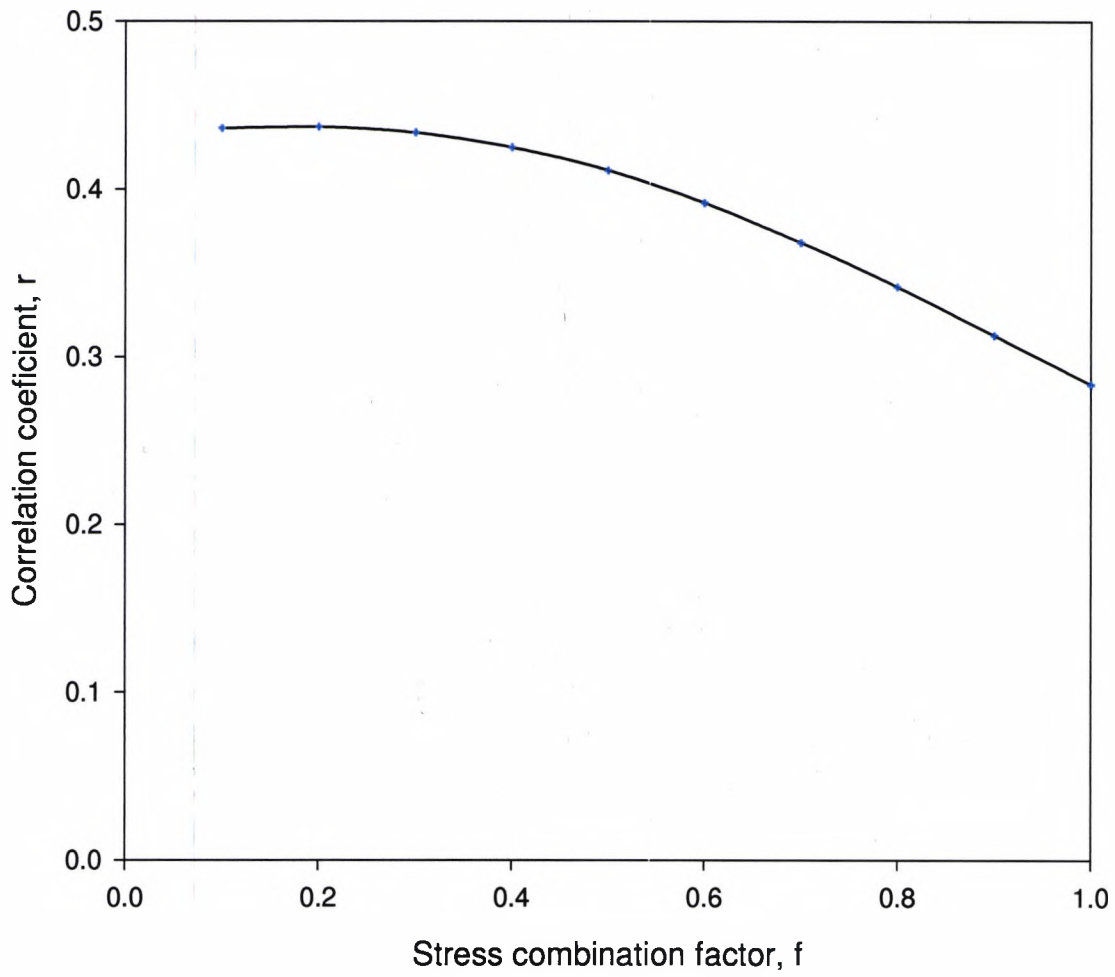
Total failure stress v. total number of impacts

Figure 130

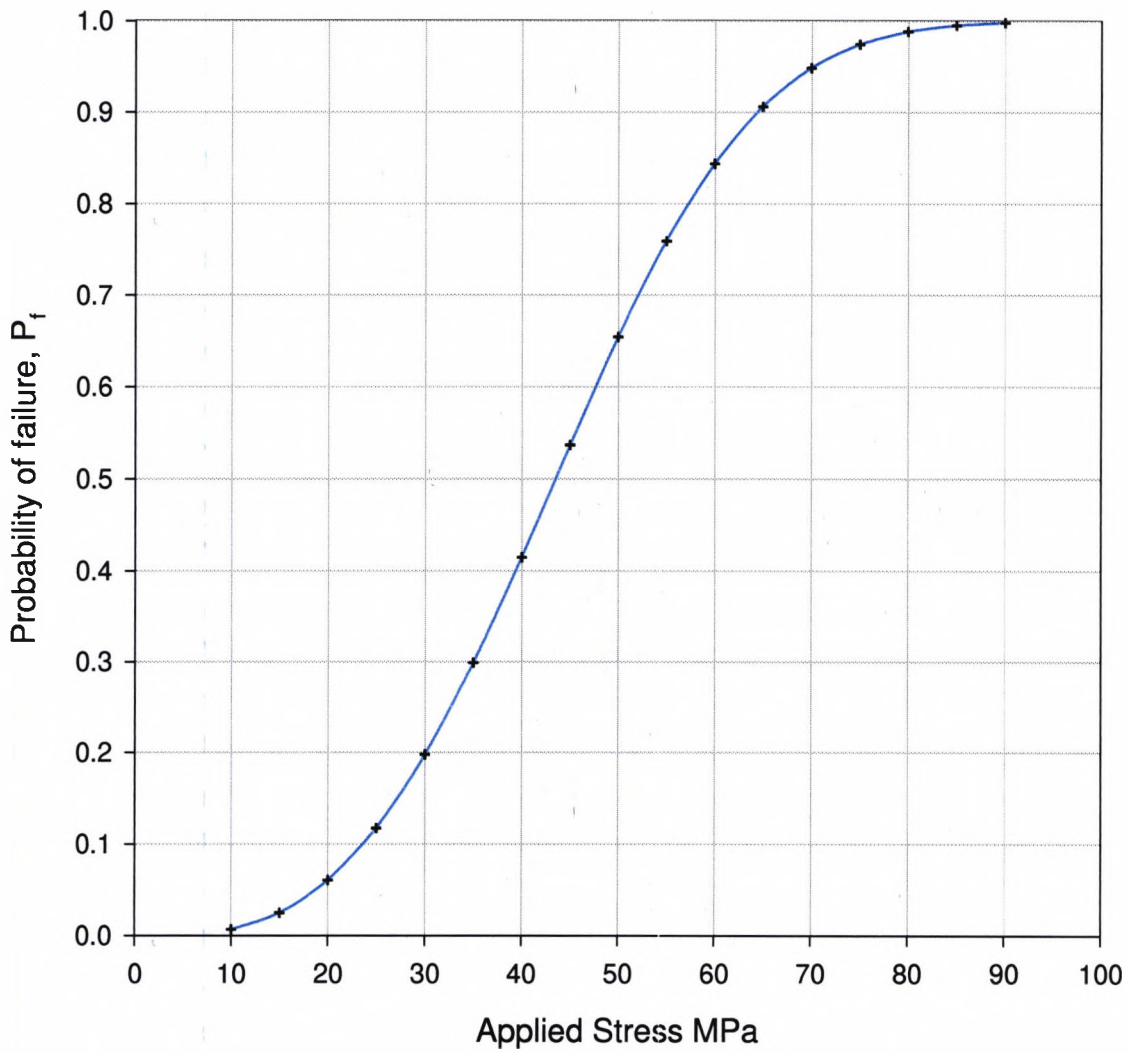


Stress combination factor of 0.1

Stress combination factor v. Correlation coefficient
Figure 131

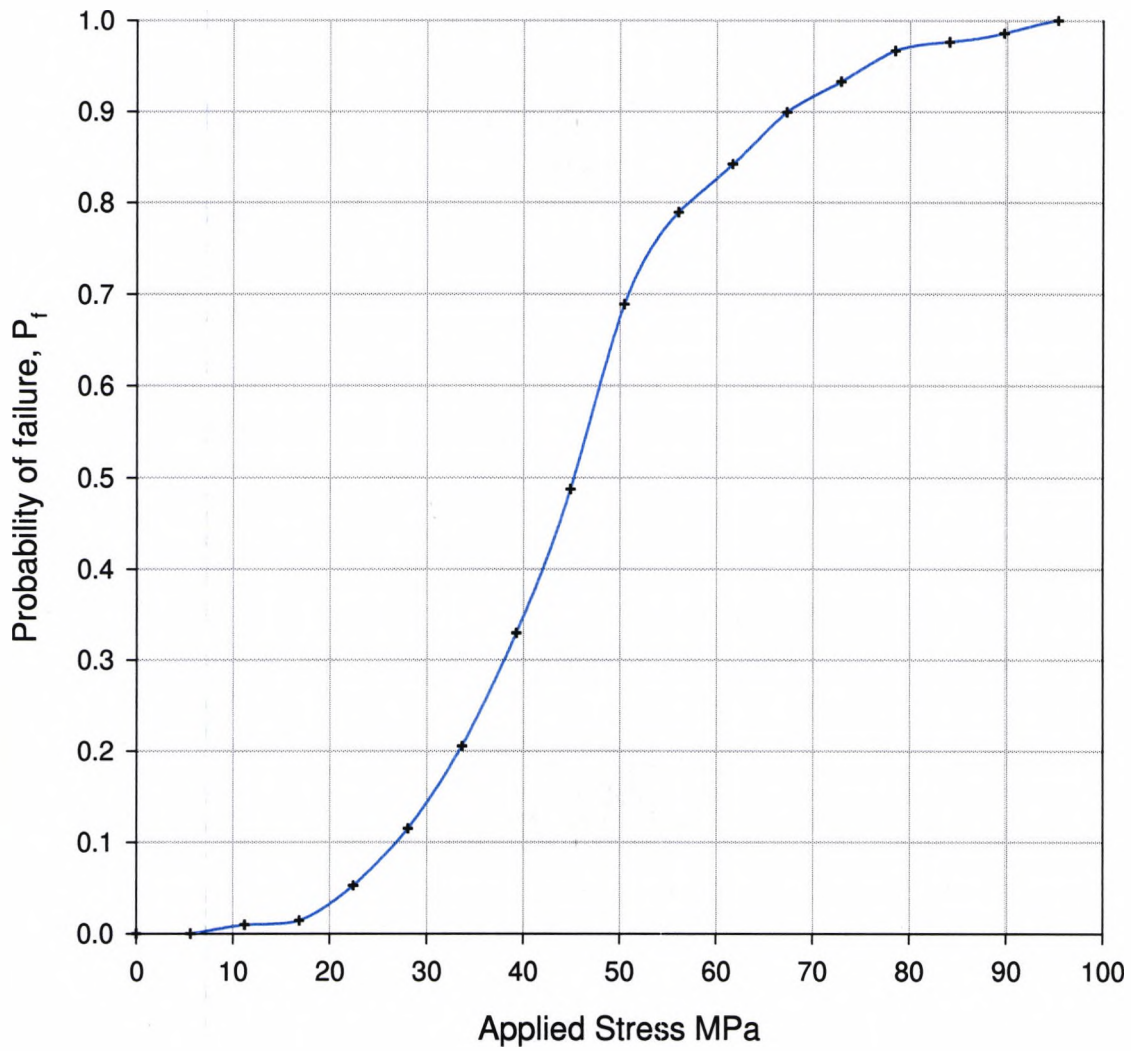


Weibull Distribution
Figure 132



Applied Stress vs Probability of failure

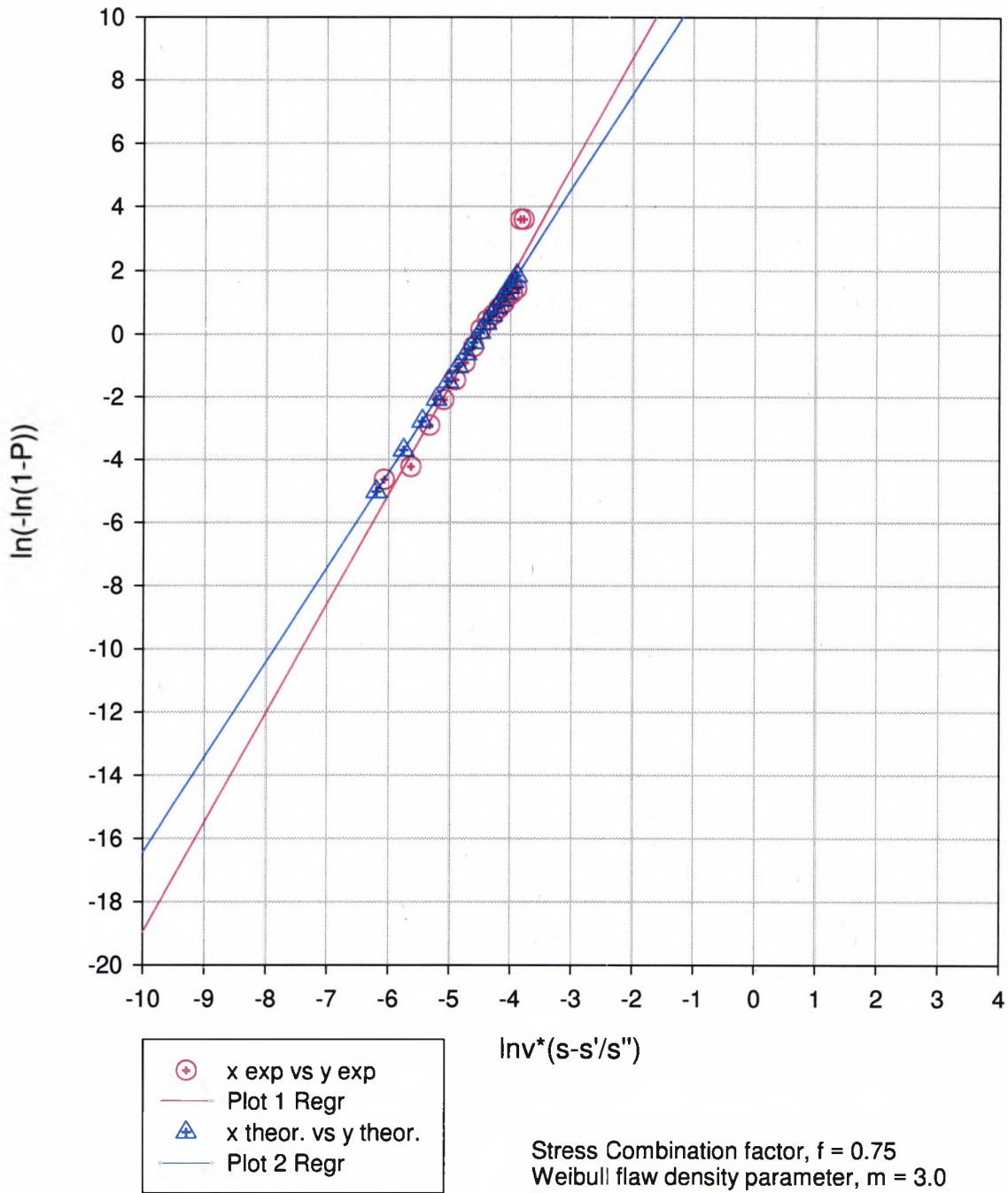
Weibull Distribution
Figure 133



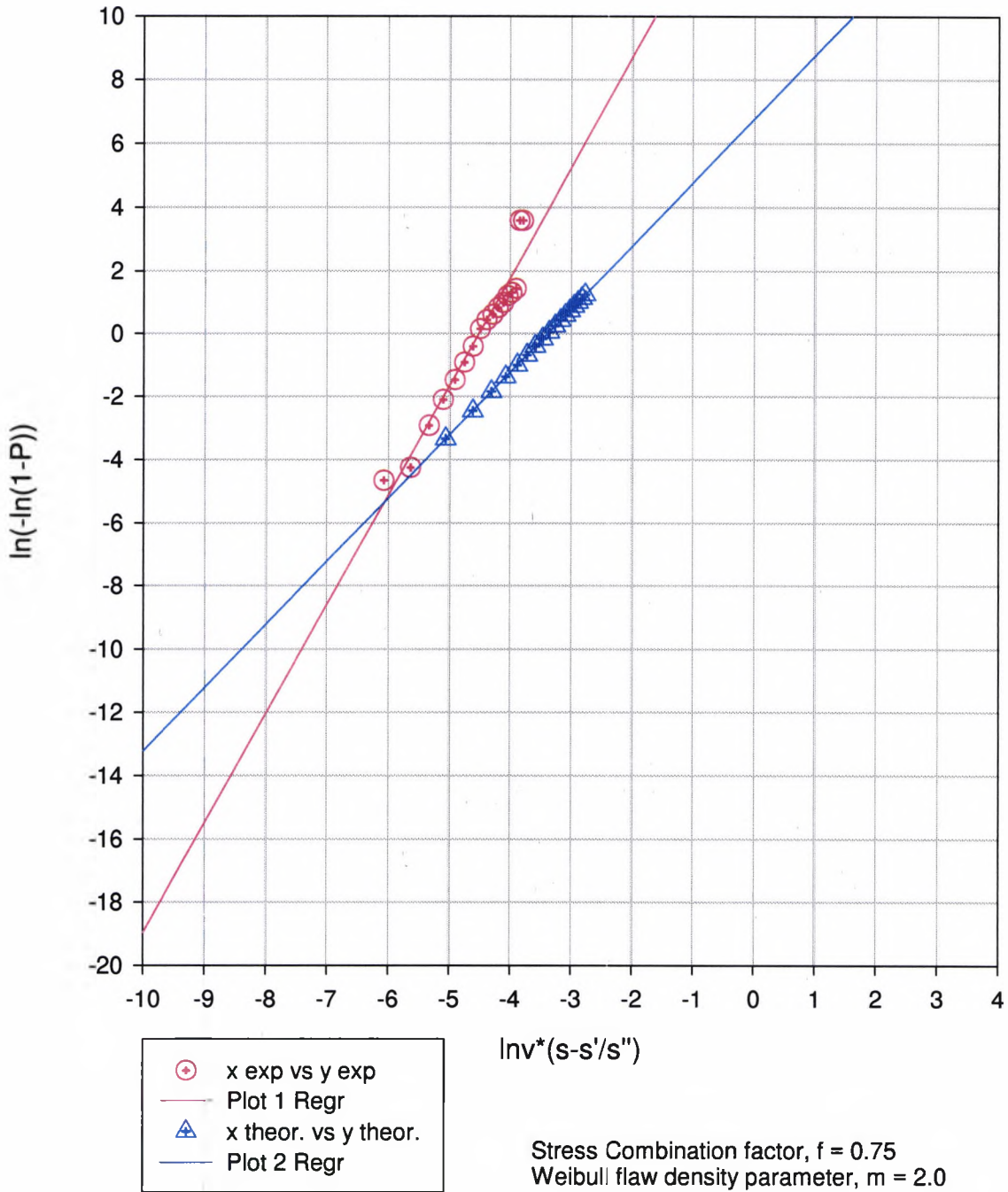
Applied Stress vs Probability of failure

Stress Combination factor, $f = 0.75$

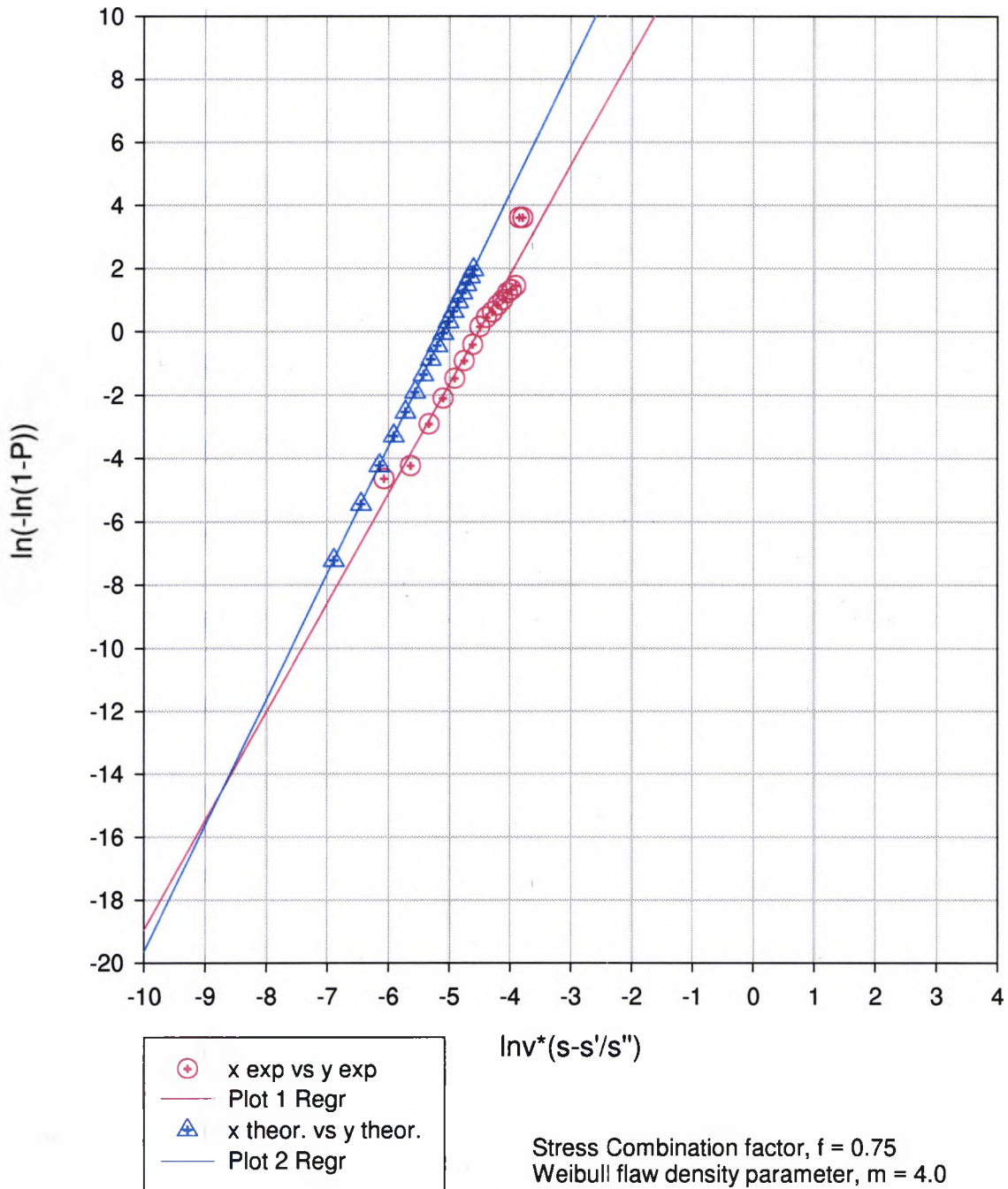
Comparison of Theoretical and Experimental
 Weibull Variables
 Figure 134



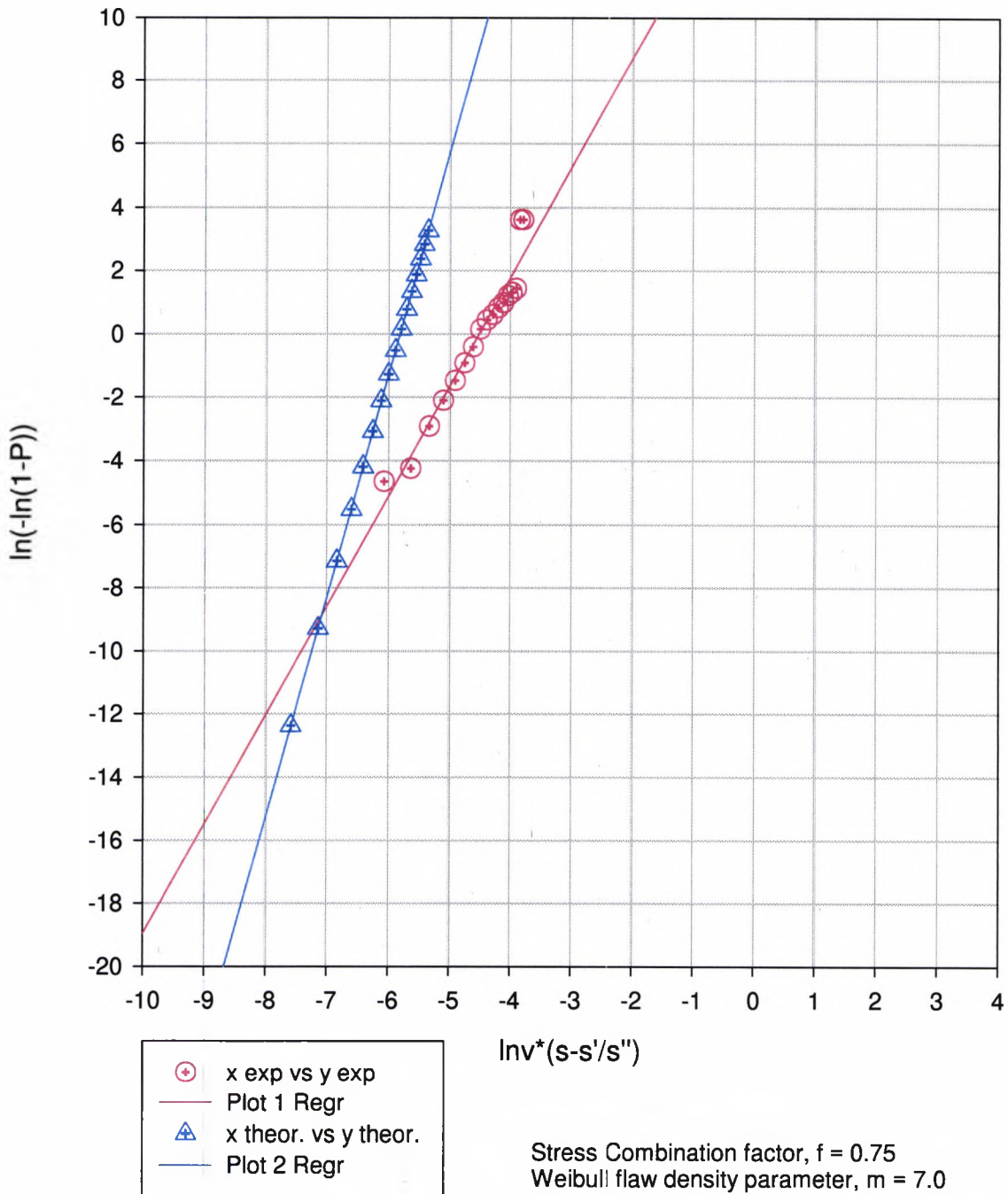
Comparison of Theoretical and Experimental
 Weibull Variables
 Figure 135



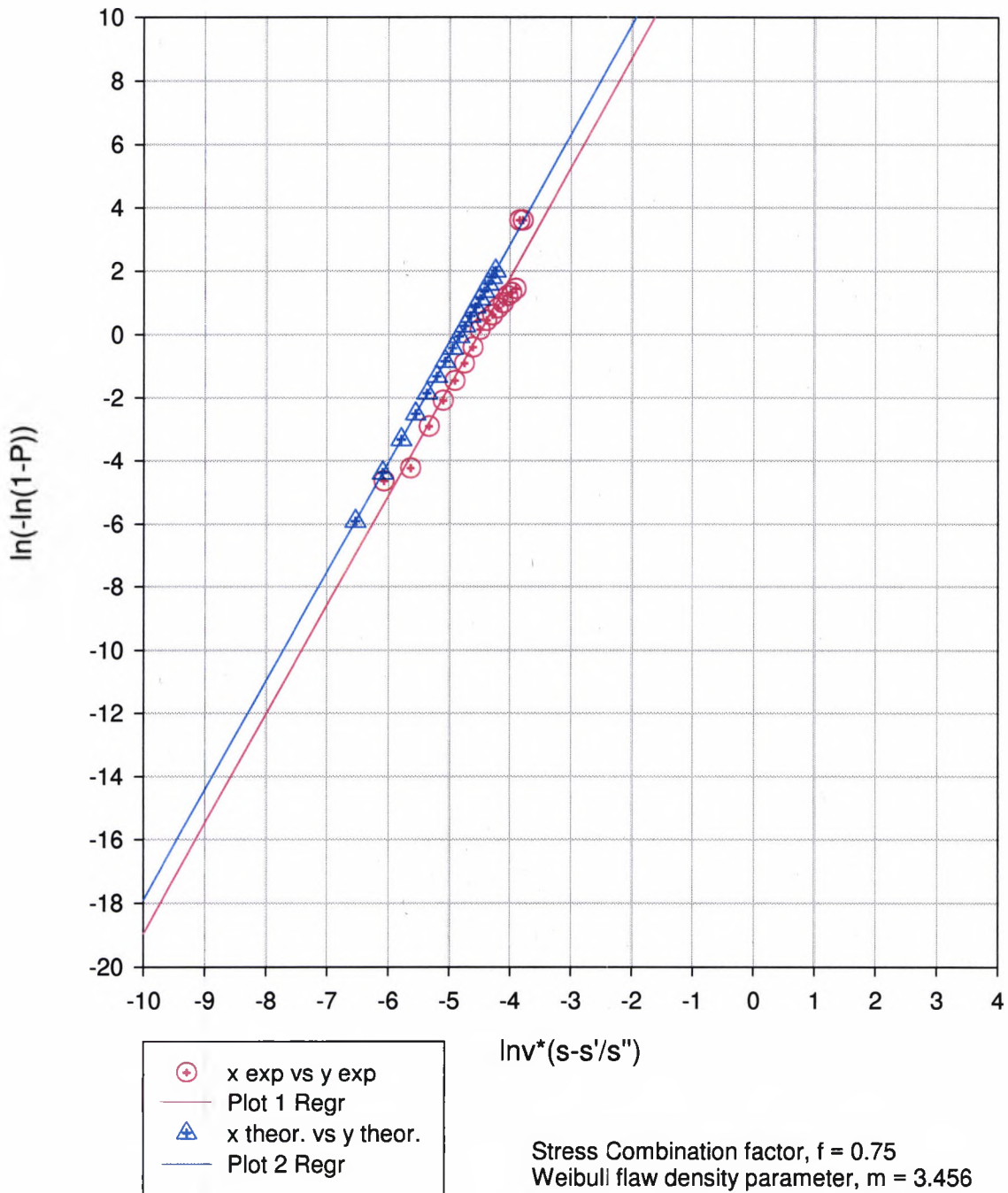
Comparison of Theoretical and Experimental
Weibull Variables
Figure 136



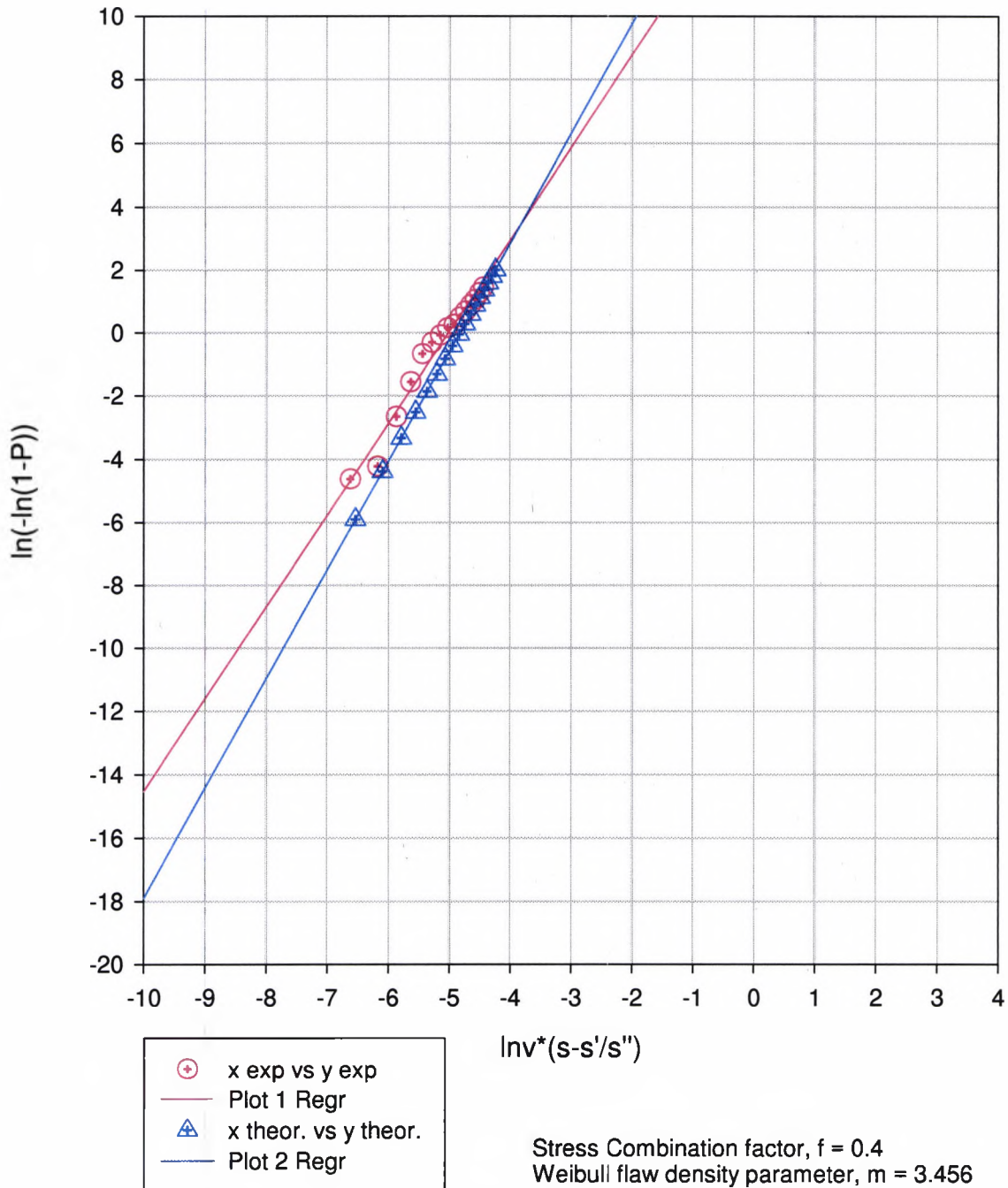
Comparison of Theoretical and Experimental
 Weibull Variables
 Figure 137



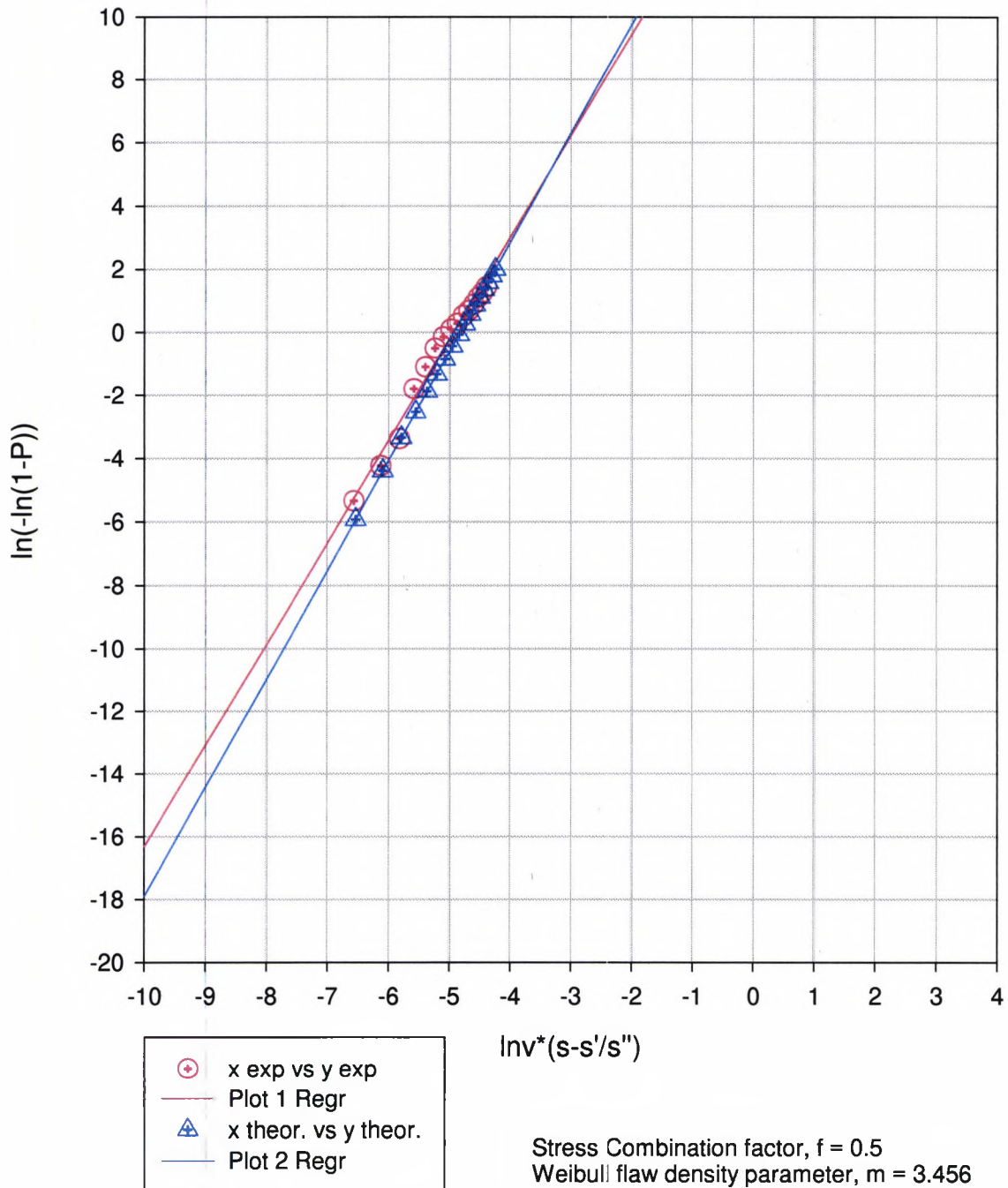
Comparison of Theoretical and Experimental
 Weibull Variables
 Figure 138



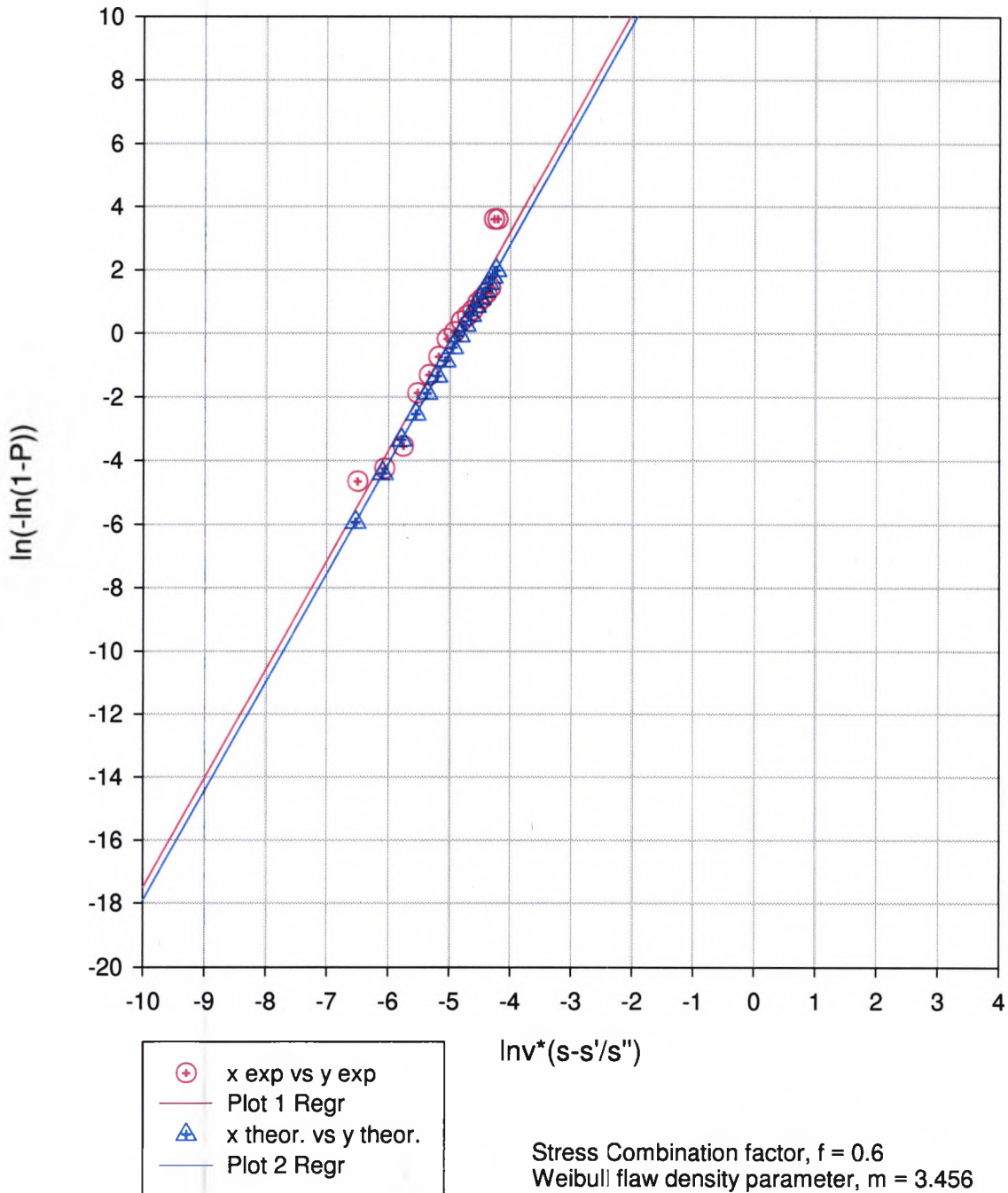
Comparison of Theoretical and Experimental
 Weibull Variables
 Figure 139



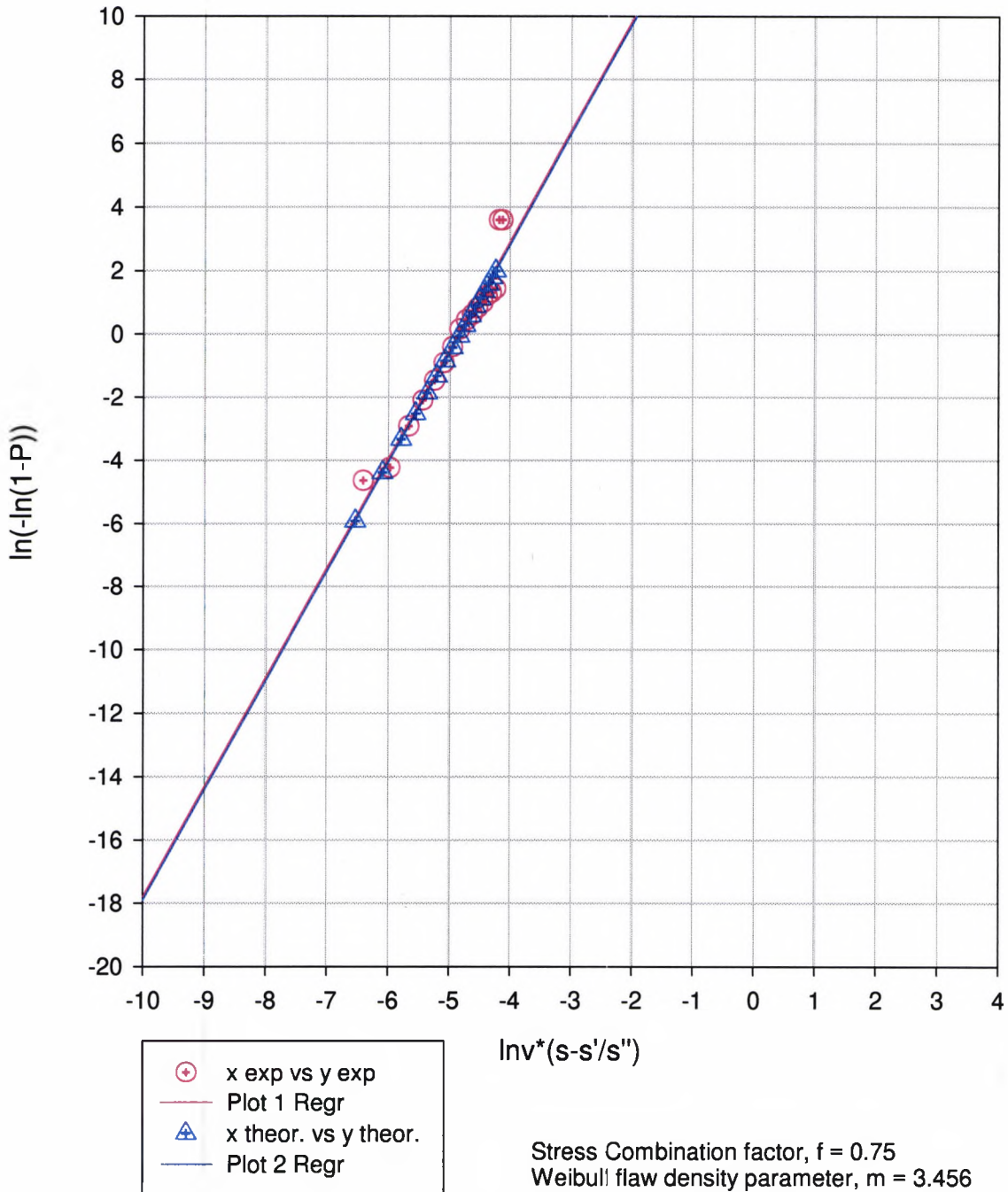
Comparison of Theoretical and Experimental
Weibull Variables
Figure 140



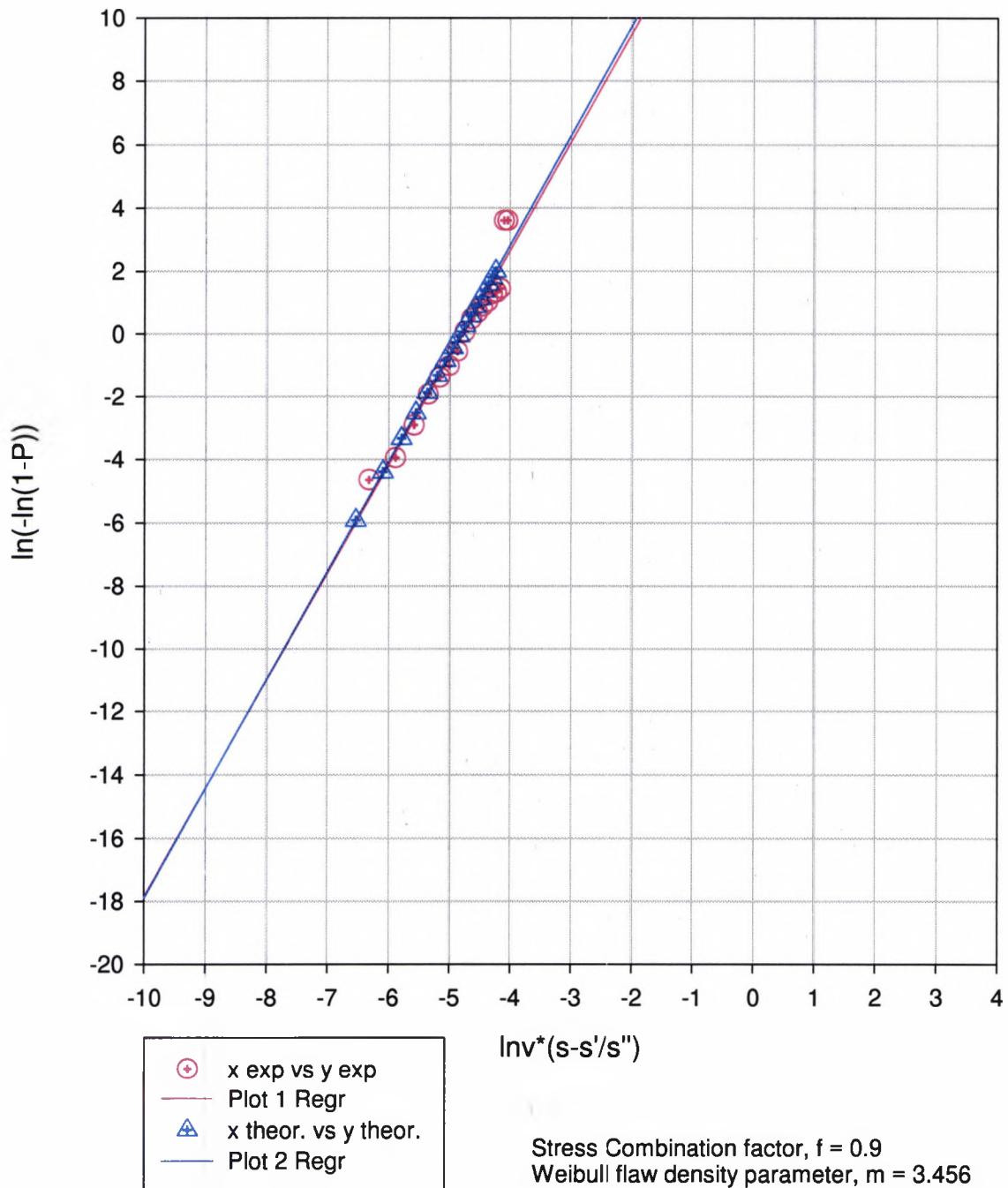
Comparison of Theoretical and Experimental
Weibull Variables
Figure 141



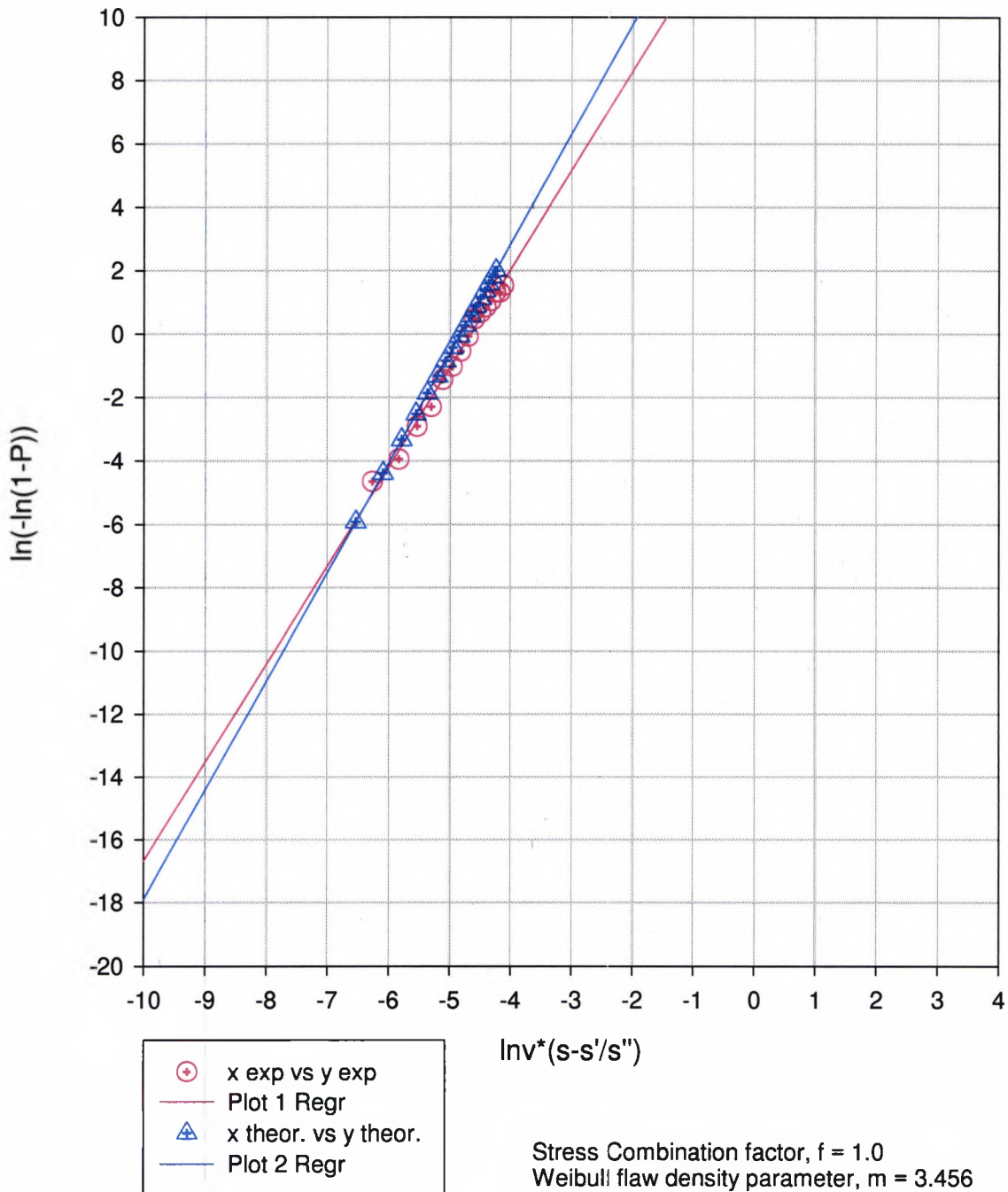
Comparison of Theoretical and Experimental
Weibull Variables
Figure 142



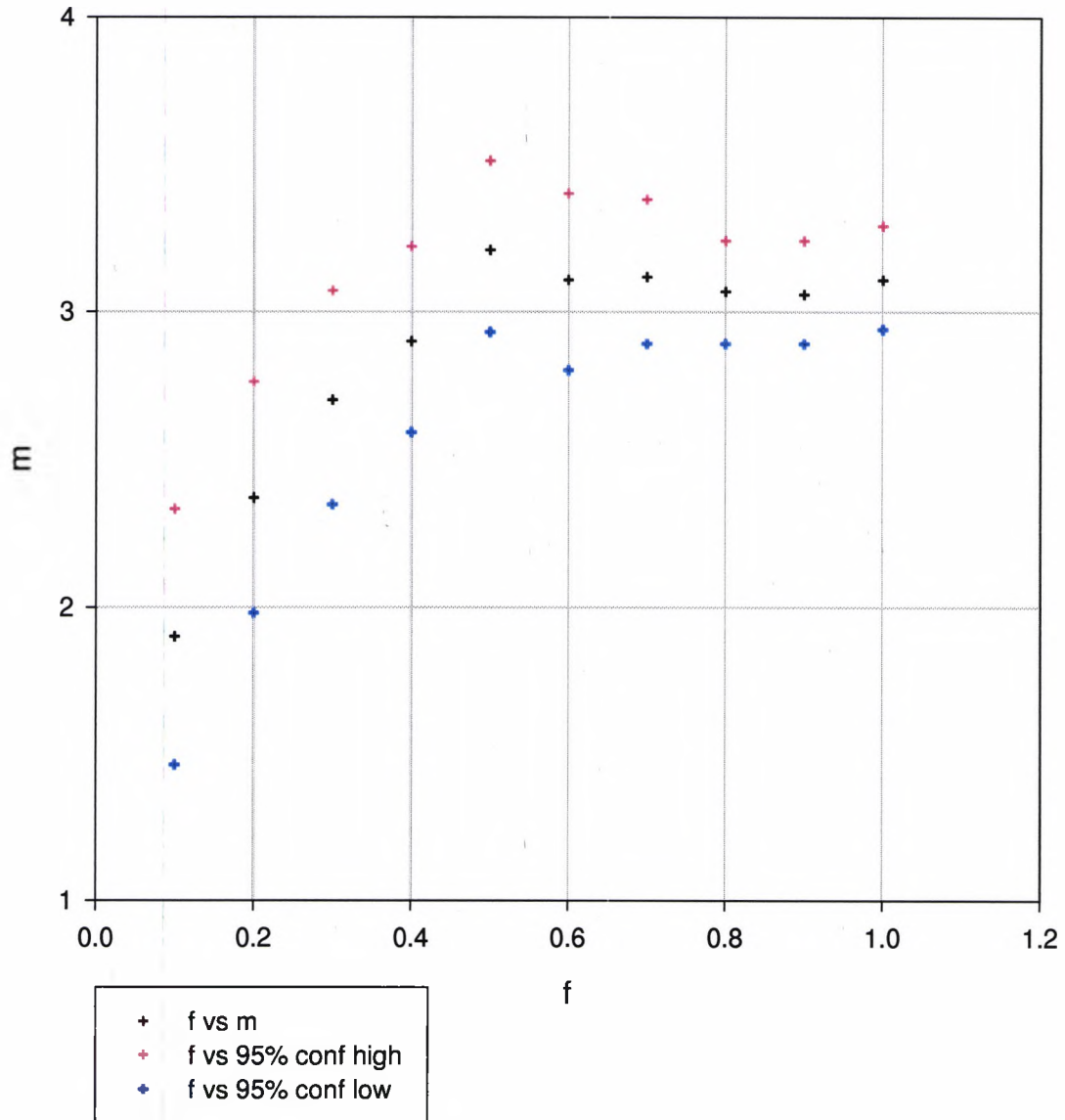
Comparison of Theoretical and Experimental
Weibull Variables
Figure 143



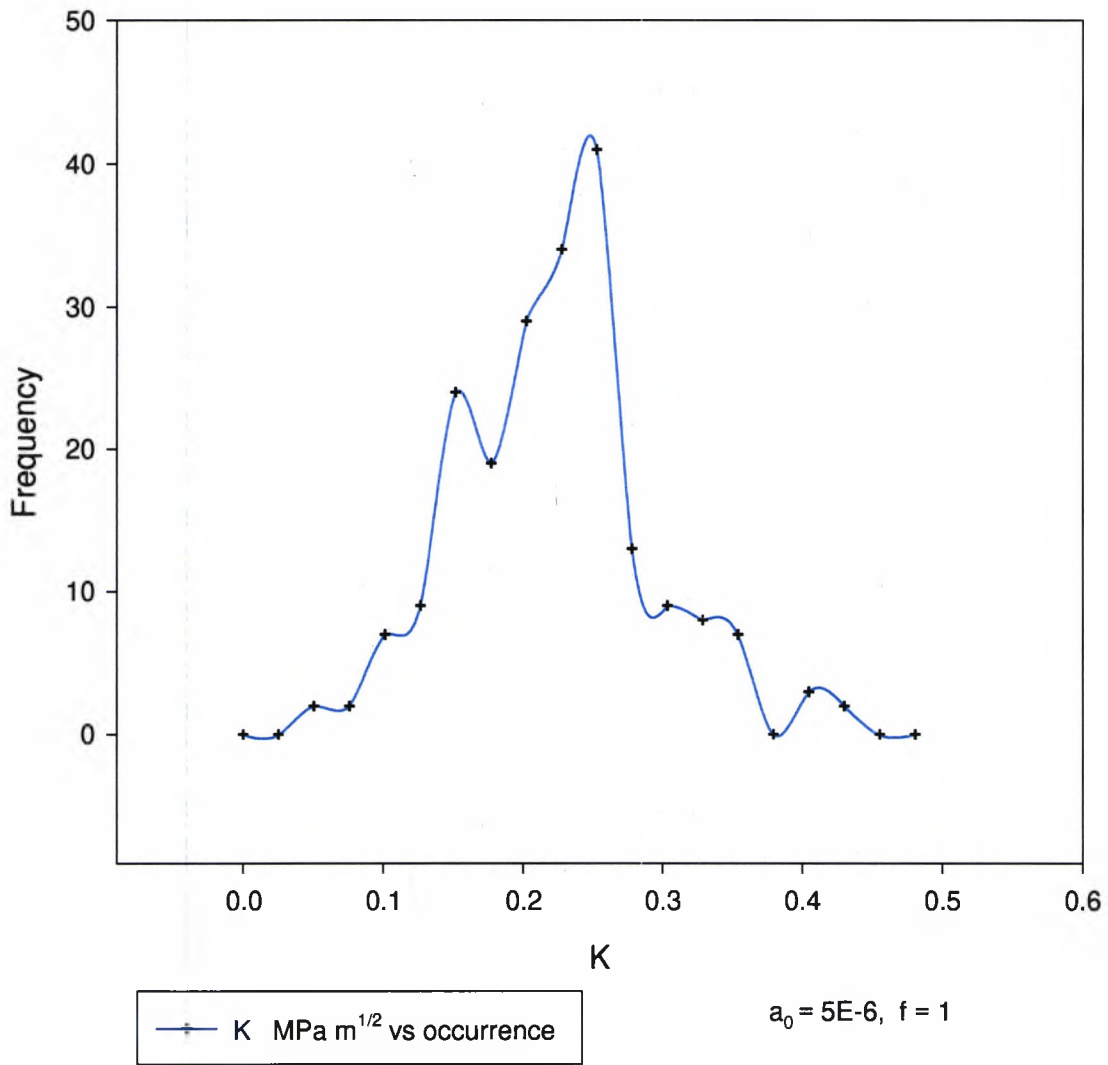
Comparison of Theoretical and Experimental
Weibull Variables
Figure 144



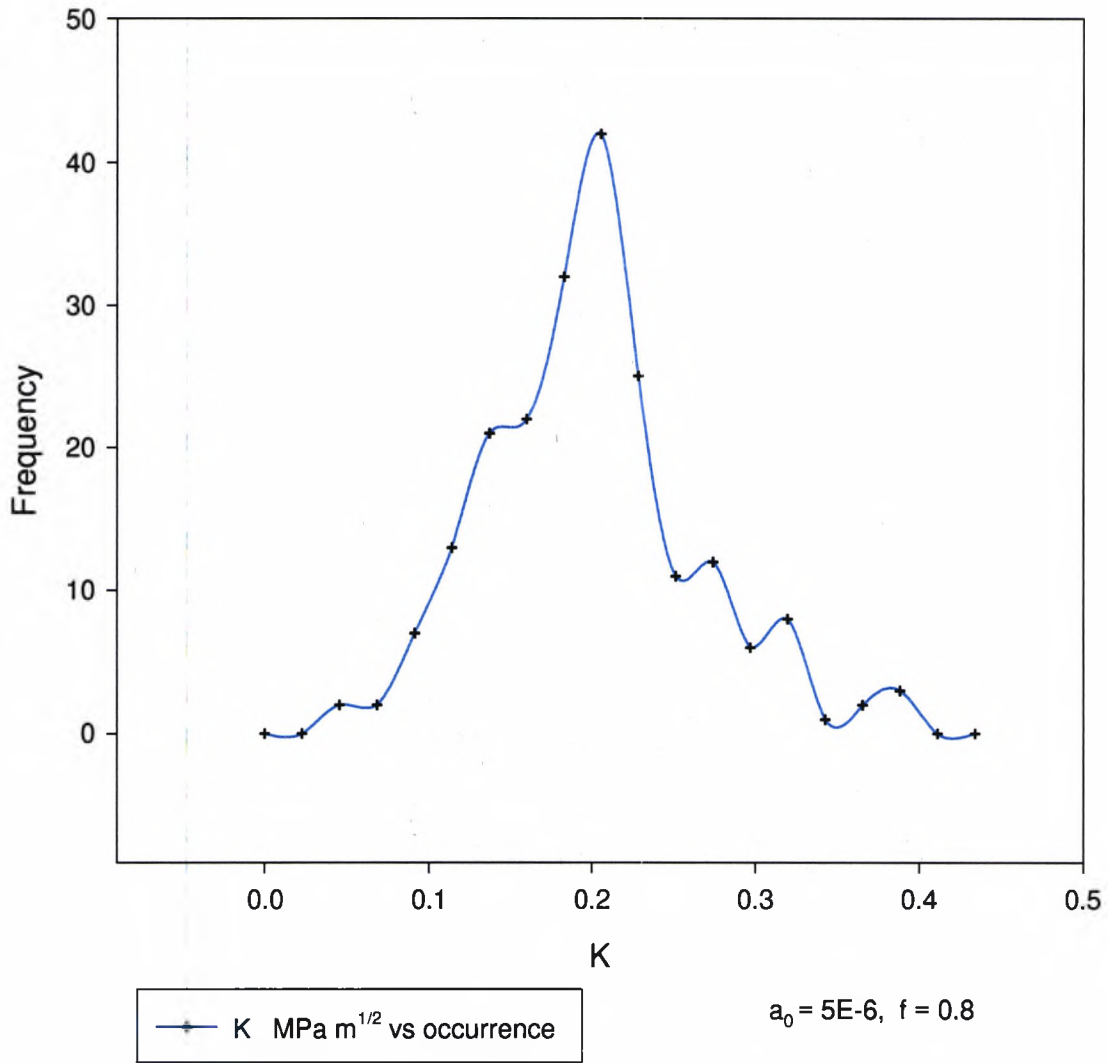
Graph of f v. m
with upper and lower 95% confidence intervals
Figure 145



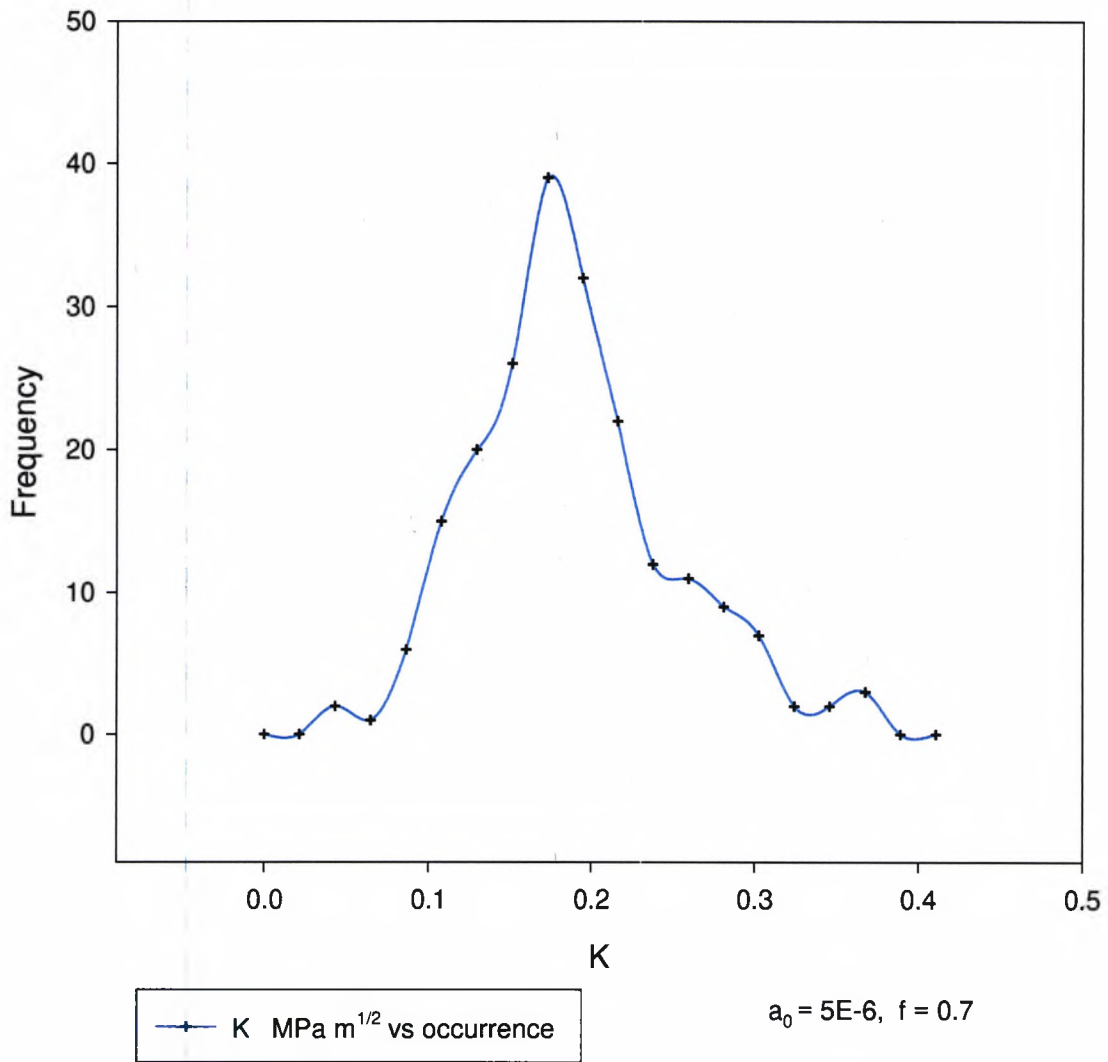
Stress Intensity Factor, K v. Frequency
Figure 146



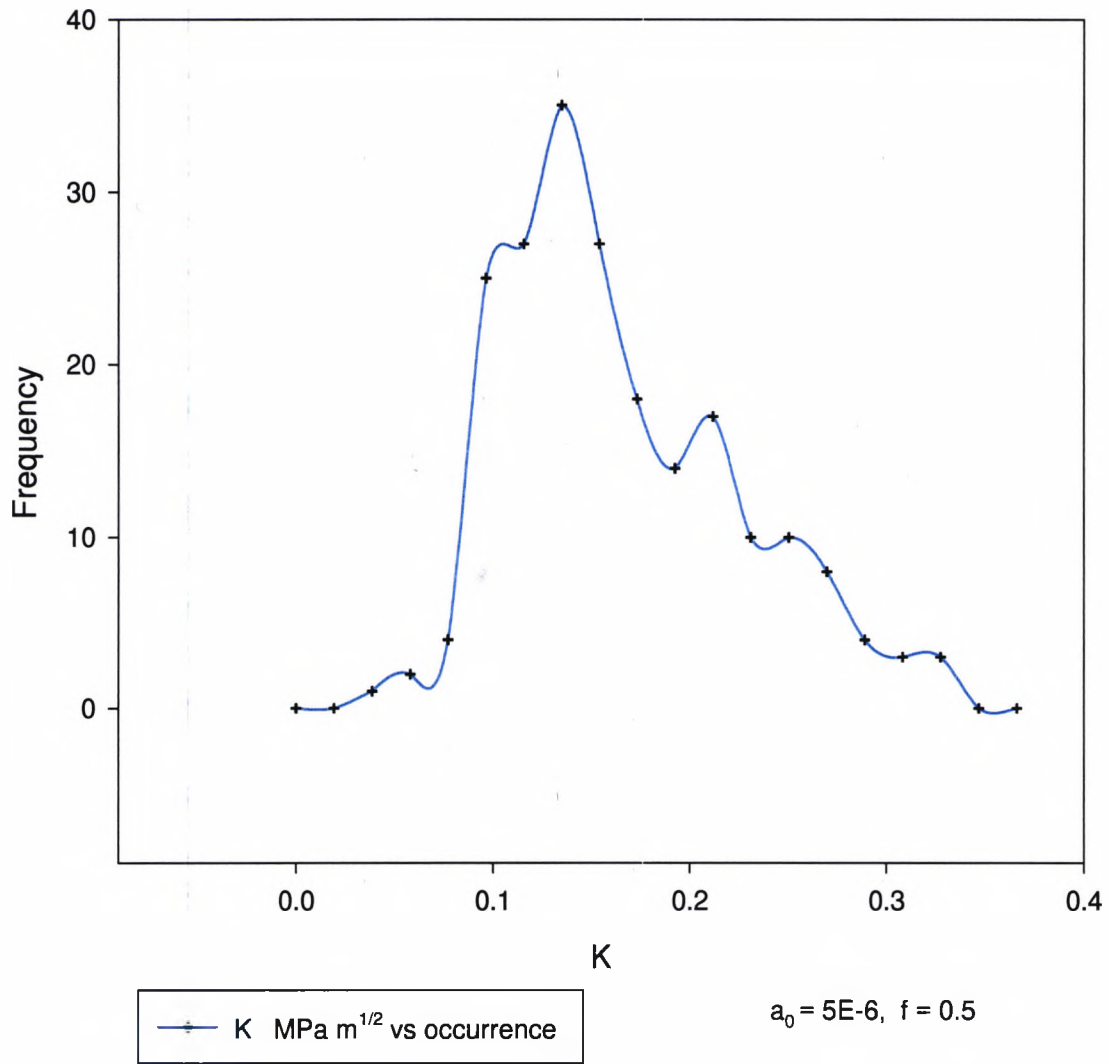
Stress Intensity Factor, K v. Frequency
Figure 147



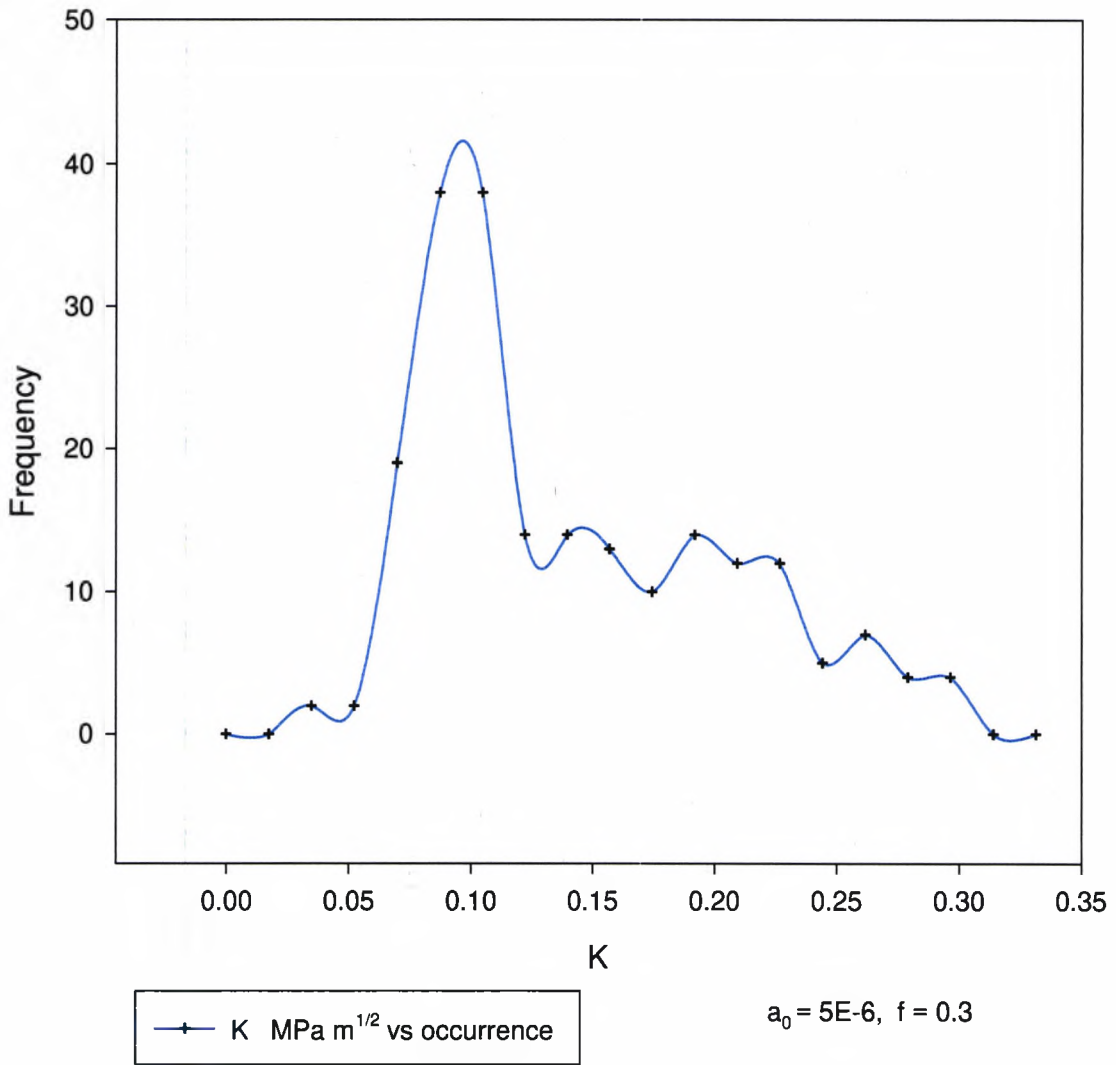
Stress Intensity Factor, K v. Frequency
Figure 148



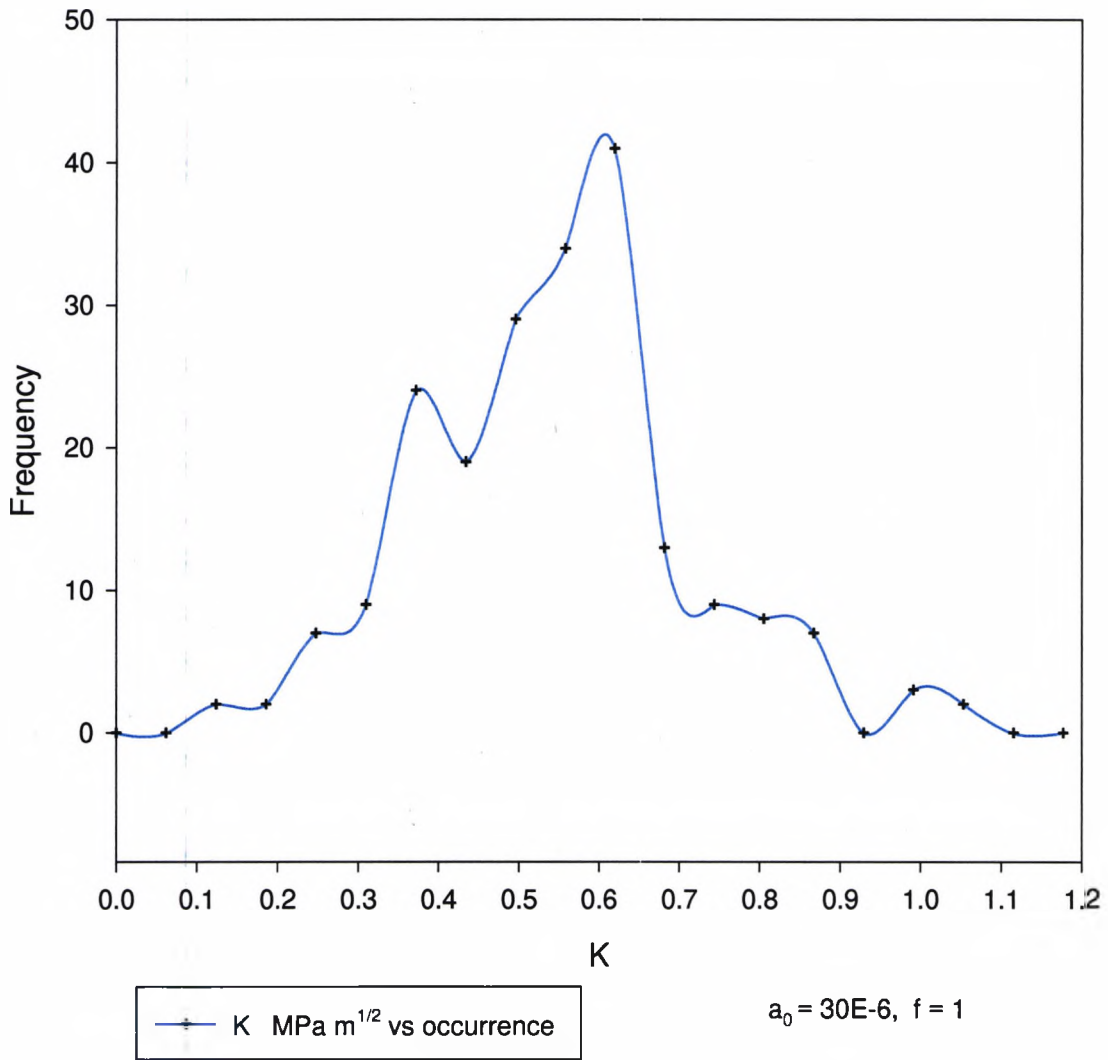
Stress Intensity Factor, K v. Frequency
Figure 149



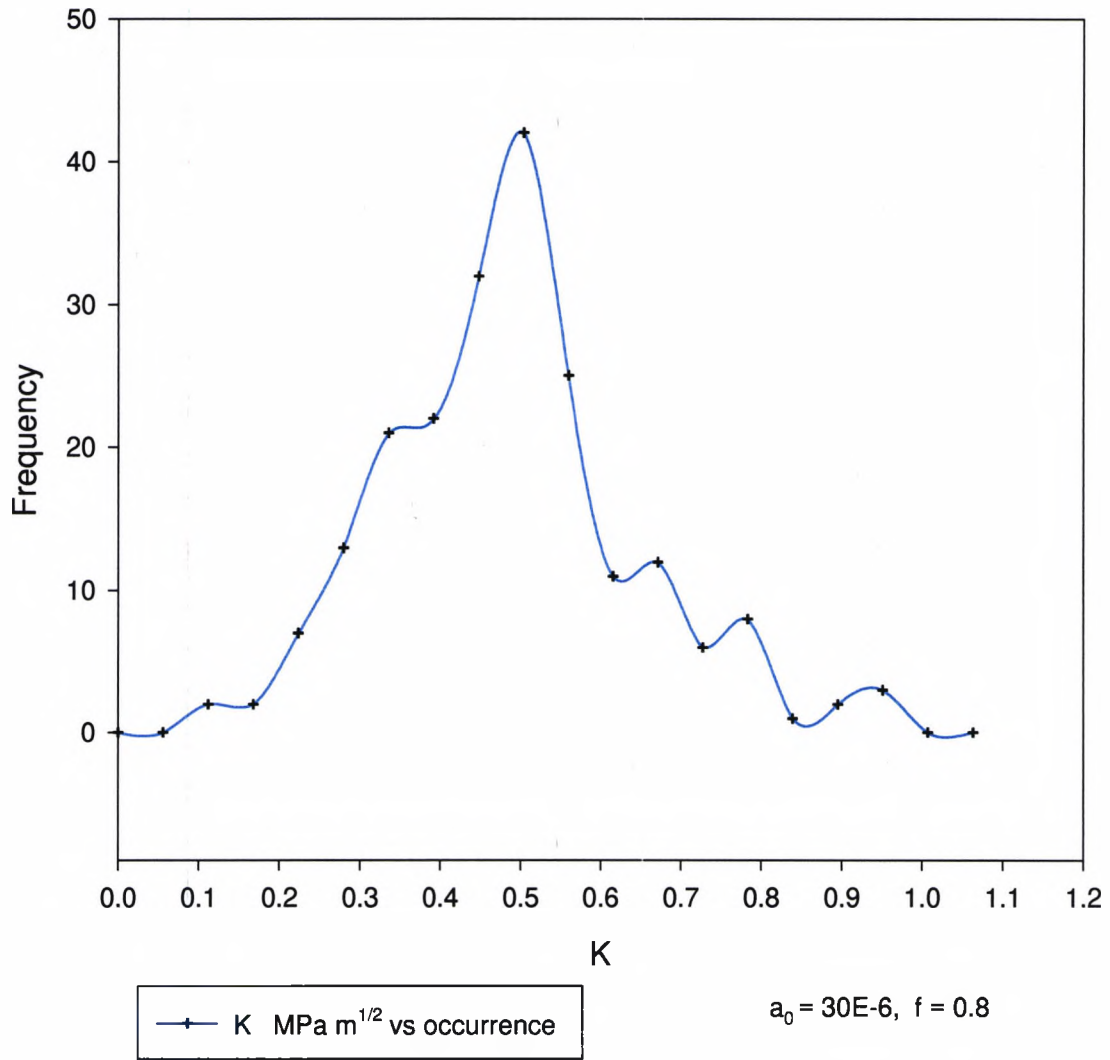
Stress Intensity Factor, K v. Frequency
Figure 150



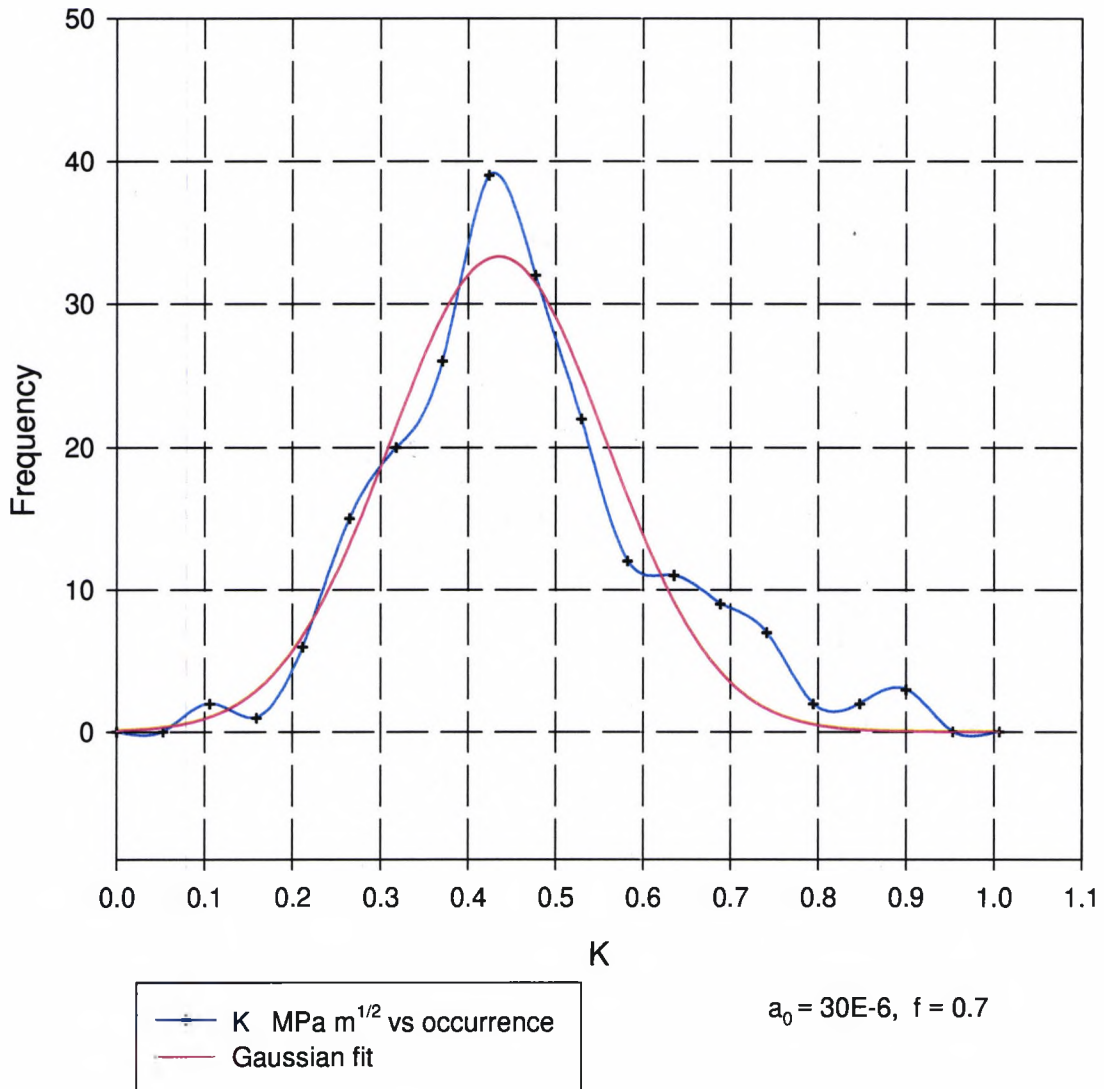
Stress Intensity Factor, K v. Frequency
Figure 151



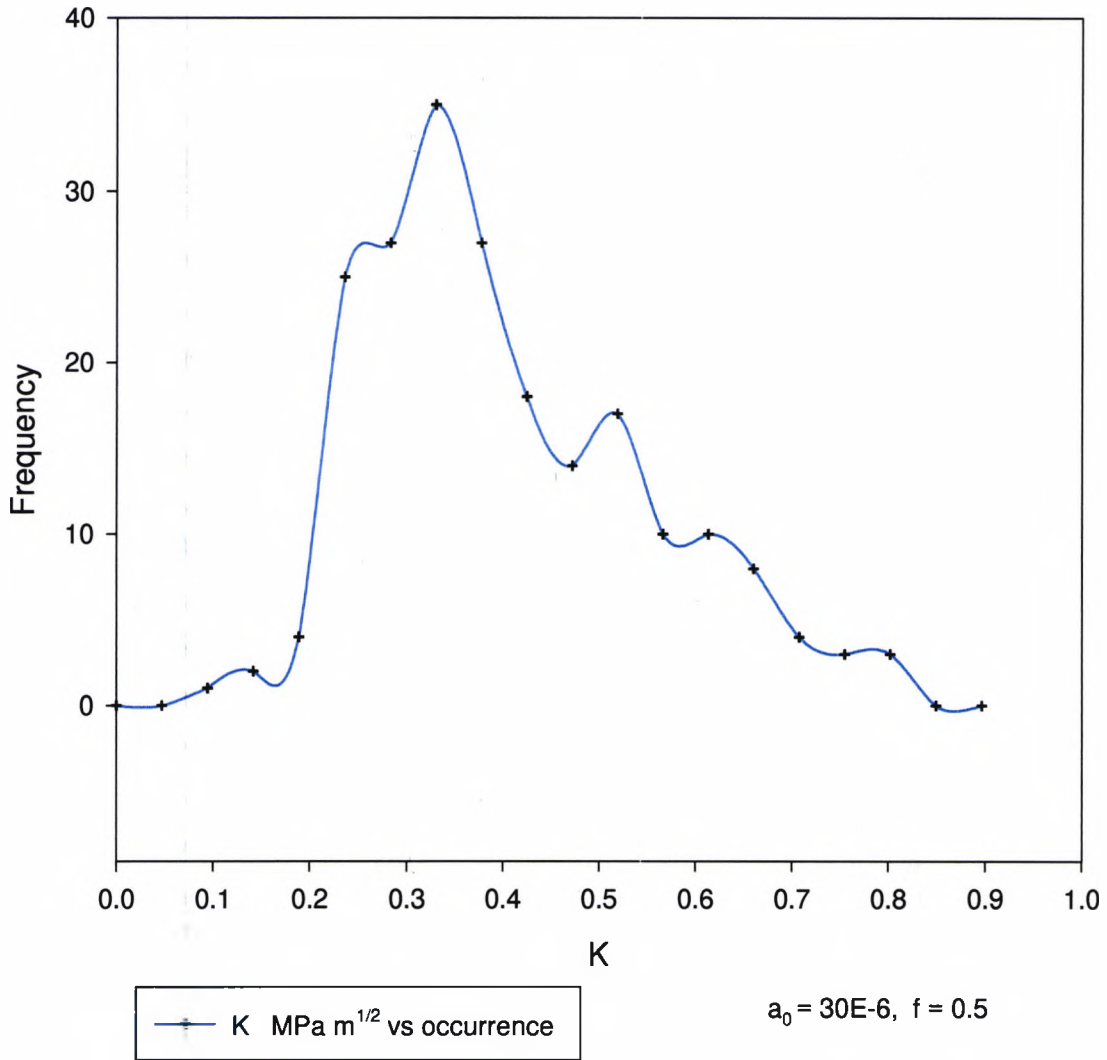
Stress Intensity Factor, K v. Frequency
Figure 152



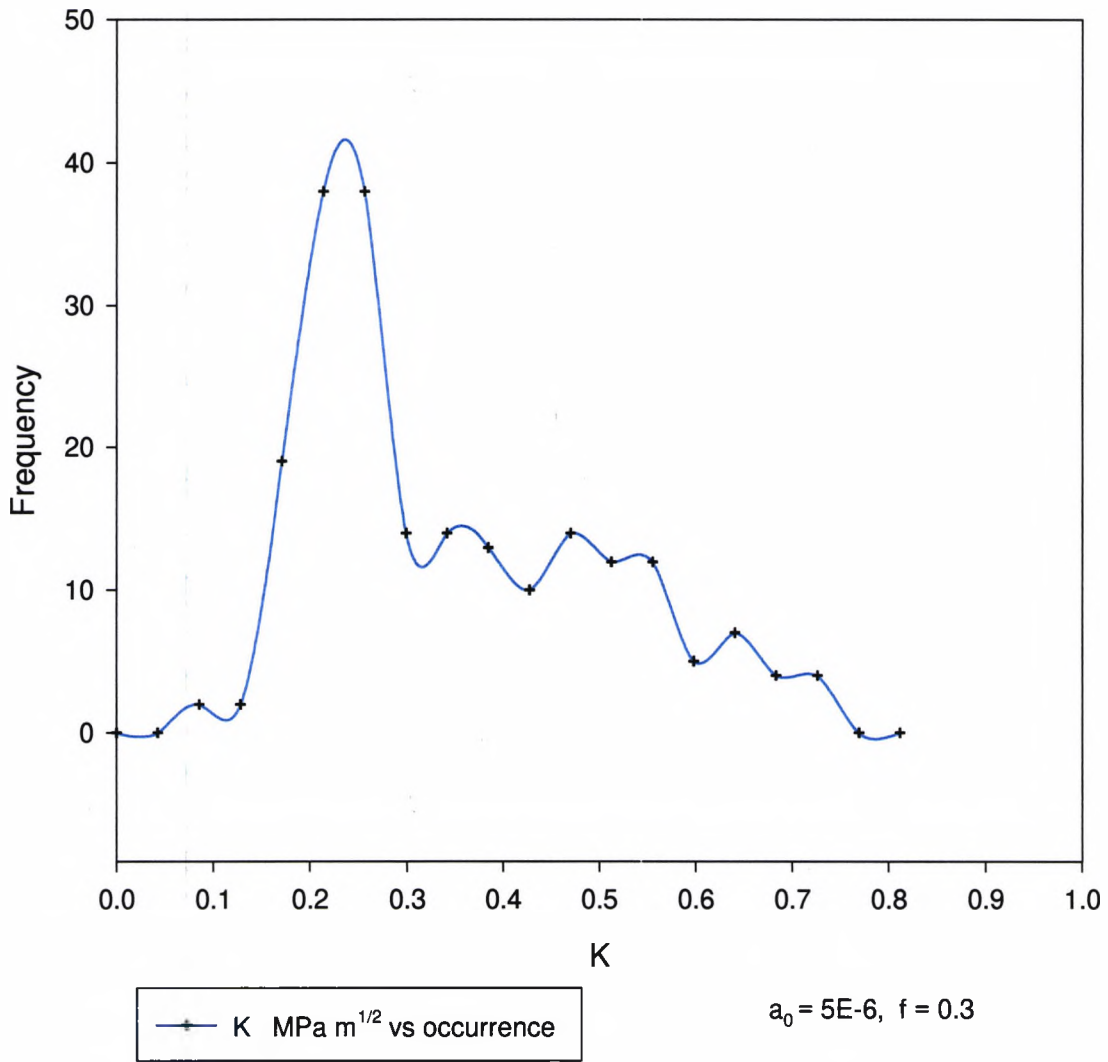
Stress Intensity Factor, K v. Frequency
Figure 153



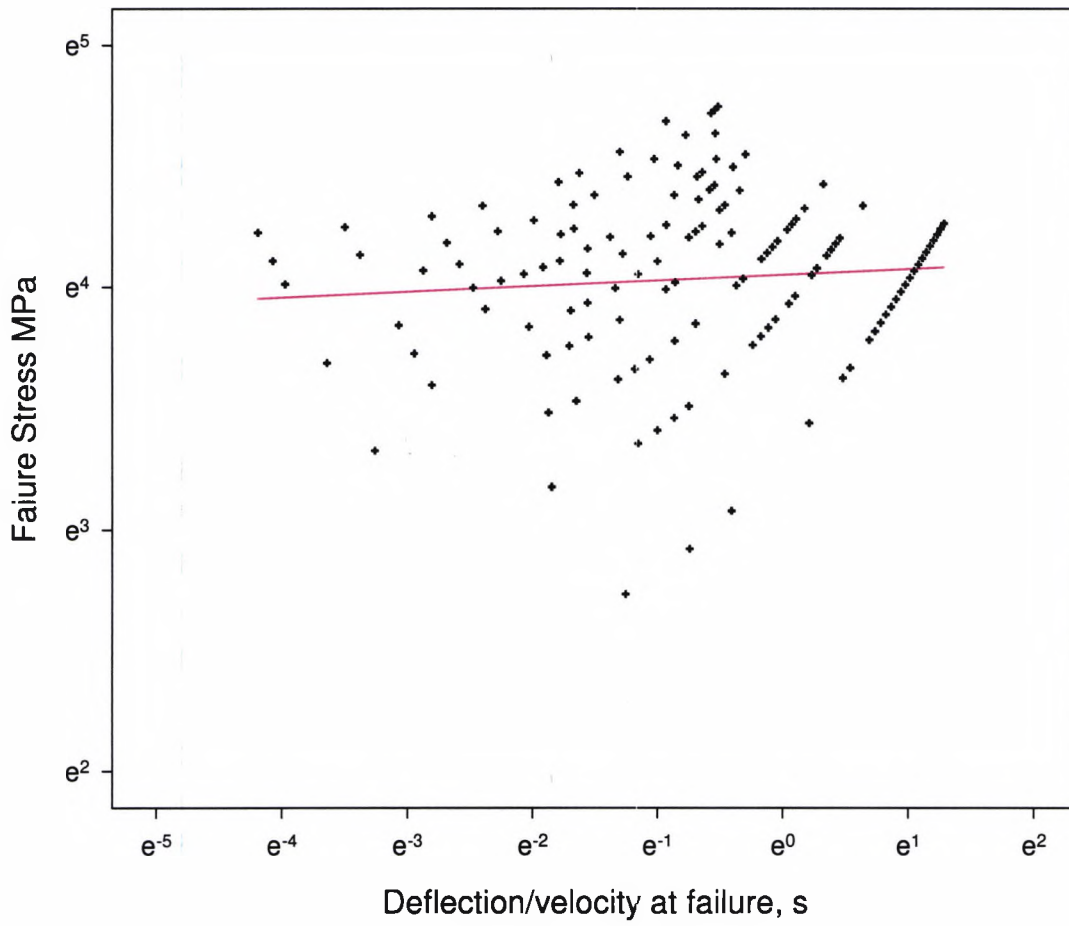
Stress Intensity Factor, K v. Frequency
Figure 154



Stress Intensity Factor, K v. Frequency
Figure 155



Graph of deflection/velocity at failure versus failure stress
Figure 156



Stress combination f actor, $f = 1$

References

- ACHENBACH, J.D., (1975) Wave propagation in elastic solids. North Holland, Amsterdam
- ADDIS, W. (1999) A history of using glass in buildings and some thoughts about the future. Glass in buildings conference, University of Bath
- ALLEN, H.G., (1969) Analysis and design of structural sandwich panels. Pergamon Press Oxford.
- ANDERSON, T.L., (1995) Fracture Mechanics, 2nd edition. CRC Press Boca Raton
- ASHBY, M.F., JONES, D.R.H., (1996) Engineering Materials 1, Butterworth, Oxford.
- AUERBACH, F (1891) Measurement of hardness. Ann. Phys. Chem., 43, 61.
- CASE, J., CHILVER, A.H. (1971) Strength of materials and structures. Edward Arnold, London
- CHATFIELD, C., (1983) Statistics for Technology, 3rd Edn., Chapman and Hall, London
- CHAUDHRI, M.M., WALLEY, S.M., (1978) Damage to glass surfaces by the impact of small glass and steel spheres. Philosophical Magazine A, Vol. 37, No.2, 153-165
- CHAUDHRI, M.M., YOFFE, E.H., (1981) The area of contact between a small sphere and a flat surface. Philosophical Magazine A, 1981, Vol. 44, No. 3, 667-675.
- COLVIN, J.B. (1993). Pilkington Glass. Personal communication.
- COTTRELL, A.H. (1964) The mechanical properties of matter. John Wilkey, London
- DALGLIESH, W.A., TAYLOR, D.A., (1989) The strength and testing of window glass. Canadian Journal of Civil Engineering, 17, 752-762
- DAVID, D.J., WITTEBERG, T.N. (1984) Journal of Adhesion, 17: 231
- DOREMUS, R.H. (1994) Glass Science 2nd ed. John Wiley, New York
- ERNSBERGER, F.M. (1962). Advances in glass technology. Plenum Press, New York
- FRANK, F.C., LAWN, B.R. (1967) Proc. Roy. Soc. A299, 291
- FRECHETTE, V.D., (1990) Failure analysis of brittle materials. The American Ceramic Society, Ohio.

- GLATHART, J.L., PRESTON, F.W., (1968) The behaviour of glass under impact: theoretical considerations. *Glass Technology* Vol 9 No. 4.
- GRIFFITH, A.A. (1921). The Phenomena of rupture and flow in solids. *Transactions of Royal Society of London* 221: 163-198.
- HAMILTON, B., RAWSON, H., (1970) The determination of the flaw distributions on various glass surfaces from Hertz fracture experiments. *J.Mech Phys. Solids* Vol 18 p 127.
- HARRIS, B.,(1998).Kempe's engineering year-book, the science of engineering materials.Morgan Grampian, London
- HERTZ, H. (1882) Über die Berührung fester elastischer Körper (on the contact of elastic solids)*J. reine angew. Math.*, 92, 156
- HERTZ, H.R. (1895) *Gesammelte Werke* 1,155.
- HUNTER, S.C. (1957) Energy absorbed by elastic waves during impact. *Journal of the mechanics and physics of solids*, 5, 162.
- INGLIS, C.E., (1913) *Trans.Inst.Nav.Arch.* 55, 219-229
- JOHNSON, K.L.(1987) *Contact Mechanics*. Cambridge University Press
- JOHNSON, K.L., O'CONNOR, J.J., AND WOODWARD, A.C., (1973) *Proc.R.Soc. A* 334, 95
- JOHNSON, W. (1972) *Impact Strength of Materials*. Edward Arnold, London
- KAMAL,M.R., SAMAK,Q., PROVAN,J., AHMAD,V. (1987) *Instrumented Impact testing*, Edited Kessler, Adams, Driscoll, Ireland. ASTM, Philadelphia
- KOLSKY, H. (1963) *Stress waves in solids*. Dover Publications, New York.
- LANGITAN,F.B., LAWN,B.R. (1969) Hertzian fracture experiments on abraded glass surfaces as definitive evidence for an energy balance explanation of Auerbach's law. *Journal of Applied Physics*. 40 4009.
- LAWN,B, (1993) *Fracture of brittle solids*, 2nd ed.Cambridge University Press
- LEVY, M., (1899) *Compt. rend.*, vol.129, pp. 535-539, 1899
- LOVE, A.E.H., (1927). *A treatise on the mathematical theory of elasticity*. Cambridge University Press.
- LUSH, P., (1999) private communication.
- MEGSON, T.H.G., (1990) *Aircraft Structures*. Edward Arnold, London.

- MICHALSKE, T.A., BUNKER, B.C., (1987) The fracturing of glass. Scientific American, December, 122-129.
- MOULD, R.E. (1961) J.Am.Ceram. Soc. 44, 481.
- NOLLE, A.W. (1950). Journal of polymer science. 5: 1
- NORVILLE, H.S., BOVE, P.M., SHERIDAN, D.L., (1991) The strength of new thermally tempered window glass lites. Glass Research and Testing Laboratory, Texas Tech University
- OH, H.L., FINNIE, I. (1967) The ring cracking of glass by spherical indenters. J.Mech. Phys Solids vol 15, 401
- OLIVER, D.S., (1975) The use of glass in engineering, Design Council
- OVEREND, M., BUHAGIAR, D., PARKE, G.A.R. (1999). Failure prediction - what is the true strength of glass ? Glass in Buildings Conference, University of Bath 1999.
- PAUL, A. (1990). Chemistry of glasses, 2nd ed. Chapman and Hall, London.
- PEARSON, E.S., HARTLEY, H.O., (1966). Biometrika Tables for Statisticians. Cambridge University Press, 3rd edn.
- PRESTON, F.W. (1931) The Impact modulus of glass. Journal of American Ceramics
- PYE, A.J., LEDBETTER, S.R., (1999) Realising composite glass-adhesive beams in practice. Glass in Buildings Conference, University of Bath 1999.
- RAMAN, C.V. (1920) On some applications of Hertz's theory of impact. Physical Review 15 277.
- RAYLEIGH (1887) London Math.Soc. Proc. 17
- ROESLER, F.C. (1956) Proc. Phys. Soc. B69, 55
- RUIZ, C., (1989) Overview of impact properties of monolithic ceramics. Inst.Phys Conf. Ser. No 102 session 7
- SCHOLZE, H. (1990). Glass. Translated by LAKIN, M.J. Springer Verlag, New York.
- SCHONBERG, W.P., KEER, L.M., WOO T.K., (1987) Low velocity impact of transversely isotropic beams and plates. Int. J. Solids Struct 23 871
- SNOWDON, J.C. (1968). Vibration and shock in damped mechanical systems. John Wiley & Sons, New York.

SOBEY, A.J., (1990) Impact modelling: some recent developments and their appraisal. Private report prepared for the Post Office by Systems Studies Ltd.

TILLET, J.P.A. (1954) A study of the impact on spheres of plates. Proc. Phys Soc London

TIMOSHENKO, S, WOINOWSKY-KRIEGER, S., (1959) Theory of Plates and Shells. 2nd Edition. McGraw-Hill.

TIMOSHENKO, S. (1934) Theory of elasticity. McGraw-Hill, New York & London.

TIMOSHENKO, S. GOODIER, J.N., (1951) Theory of elasticity. 2nd ed. McGraw-Hill, New York & London.

TSAI, Y.M., (1971) Dynamic contact stresses produced by the impact of an axisymmetrical projectile on an elastic half space. Int. J. Solids Structures vol7 p543

TSAI, Y.M., KOLSKY, H. (1967) A Theoretical and Experimental Investigation of the Flaw Distribution on Glass Surfaces. J. Mech Phys. Solids 15, 29

UHLMANN, D.R., KREIDL, N.J., ed (1980) Glass: Science and Technology, Volume 5, Elasticity and Strength in Glasses. Academic Press, Inc. New York.

WARREN, B.E. (1941). Summary of work on atomic arrangement in glass. Journal of American Chemical Society 24: 256-261.

WEIBULL, W. (1939) Ingvetskakad. Handl. (Stockholm), No.151.

YOUNG, W.C., (1989) Roark's formulas for stress and strain. 6th Edition. McGraw-Hill

ZACHARIASEN, W.H. (1932). The atomic arrangement in glass. Journal of American Chemical Society 54: 3841- 3851.

ZUKAS, J.A., et al (1982). Impact Dynamics. Wiley, New York.